Search for Upsilons in Heavy-Ion Collisions with the STAR Detector

Dissertation
zur Erlangung des Doktorgrades
der Naturwissenschaften

vorgelegt beim Fachbereich Physik
der Johann Wolfgang Goethe – Universität
in Frankfurt am Main von

Thorsten Kollegger
aus Frankfurt am Main

Frankfurt am Main 2005
(D30)

vom Fachbereich Physik der
Johann Wolfgang Goethe – Universität als Dissertation angenommen.

Dekan:	Prof. Dr. W. Aßmus
Gutachter:	Prof. Dr. Dr. h.c. R. Stock, JProf. Dr. C. Blume
Datum der Disputation:	26. April 2006

Zusammenfassung

Die Struktur der uns umgebenden Materie sowie die zwischen ihren Bestandteilen wirkenden Kräfte waren schon immer eine der zentralen wissenschaftlichen Fragestellungen. Nach den gegenwärtigen Erkenntnissen ist die uns umgebende Materie aus einigen wenigen Elementarteilchen aufgebaut; sechs Quarks und sechs Leptonen. Zwischen ihnen wirken vier fundamentale Kräfte; die starke, die schwache, die elektromagnetische und die Gravitationskraft.

Dominierende Kraft zwischen Quarks ist auf kleinen Skalen, wie im Inneren von Nukleonen, die starke Kraft. Die sie beschreibende Theorie ist die Quantum Chromo Dynamic (QCD). Eine besondere Eigenschaft der QCD ist die Vorhersage, dass Quarks nur in gebundenen Zuständen auftreten, entweder als Paar (Mesonen) oder als Kombination aus drei Quarks (Baryonen). Tatsächlich wurden bisher keine freien Quarks experimentell gefunden. Dieses Phänomen wird als "confinement" bezeichnet. Es stellt sich die Frage, ob es möglich ist, einen Materiezustand zu erzeugen in welchem sich die Quarks in einem ausgedehnten Volumen wie freie Teilchen verhalten. Tatsächlich sagen theoretische Berechnungen einen solchen Zustand, das Quark-Gluon-Plasma, für sehr hohe Temperaturen und/oder Dichten voraus.

Ultrarelativistische Schwerionenkollisionen sind die einzige derzeit bekannte Möglichkeit, die nötigen Temperaturen und Dichten im Labor zu erreichen. Erschwert wird die Interpretation des hierbei erzeugten Materiezustandes durch die Tatsache, dass im Experiment nur der hadronische Endzustand der Kollision beobachtet werden kann, auf Grund der sehr kurzen Zeitskala jedoch nicht die erzeugte Materie selbst. Trotzdem wurden inzwischen einige Observablen gemessen, die einen Rückschluss auf den Materiezustand in den frühen Phasen der Kollision zulassen. Die kombinierte Information legt die Bildung eines "deconfinten" Zustandes nahe. Eine dieser Proben ist die Produktion von schweren Quarkonia, d.h. Mesonen, die aus charm-anticharm (bzw bottom-antibottom) Quarkpaaren bestehen. Wie in Kapitel 2 näher erläutert, kann von ihrer Produktion möglicherweise auf die in der Kollision erreichte Temperatur geschlossen werden.

Das bisherige experimentelle Programm konzentrierte sich auf die Messung des J/ψ Mesons, dem 1S Zustandes des charm - anticharm Systems. Wie von der Theorie vorhergesagt, wurde eine Unterdrückung seiner Produktion in Schwerionenkollisionen relativ zur Produktion in Proton-Proton-Kollisionen beobachtet, z.B. vom Experiment NA50 am SPS Beschleuniger des Europäischen Zentrums für Teilchenphysik CERN, wie in Abbildung 2.2 gezeigt.

Die Deutung dieser Meßdaten ist jedoch umstritten. Neben einer Interpretation im Rahmen des oben beschriebenen Modells können die Daten sowohl von hadronischen Modellen als auch von statistischen Hadronisierungsmodellen, die eine Bildung des $c\bar{c}$ Zustandes nicht in den initialen Partonkollisionen, sondern erst beim Übergang zum hadronischen Endzustand annehmen, beschrieben werden. Eine

Möglichkeit, einzelne Modelle zu falsifizieren bzw. einige der Modellparameter weiter einzuschränken, besteht in der Messung anderer Quarkonia Zustände als dem J/ψ Meson. Hier wären zum einen die anderen Zustände der $c\bar{c}$ Familie zu nennen, z.B. das $\chi_c(1P)$. Dieses ist jedoch durch seine Zerfallskanäle experimentell nur schwer nachzuweisen. Eine andere Möglichkeit bietet die Messung von Bindungszuständen zwischen bottom Quarks. Das $b\bar{b}$ System hat durch die grössere Massendifferenz zwischen dem ersten Bindungszustand, dem $\Upsilon(1S)$, und der für die Erzeugung zweier Hadronen mit jeweils einem bottom und einem leichten Quark, wesentlich mehr Zustände als das $c\bar{c}$ System. Experimentell sind durch den Zerfallskanal in zwei Leptonen insbesondere die Upsilon gut nachzuweisen.

Die Messung von Upsilons in ultrarelativistischen Schwerionenkollisionen ist jedoch experimentell äusserst herausfordernd. Durch die große Masse von circa 10 GeV/c^2 ist die Produktionswahrscheinlichkeit sehr klein im Vergleich zu leichteren Teilchen, zum Beispiel dem nur 3.14 GeV/^{2} schwerem J/ψ. Der im Jahr 2000 in Betrieb genommene Relativistic Heavy Ion Collider (RHIC, siehe Kapitel 3.1) des Brookhaven National Laboratories (BNL) auf Long Island in der Nähe von New York erreicht zum ersten Mal eine ausreichend grosse Schwerpunktsenergie und Luminosität, welche eine Upsilon Messung möglich erscheinen lassen. Die Entwicklung des experimentellen Programms zur Messung von Upsilons mit dem STAR Detektor am RHIC und erste Ergebnisse aus der Strahlzeit der Jahre 2003/2004 werden in dieser Arbeit beschrieben.

Herzstück des STAR Detektors, der in Kapitel 3.2 näher beschrieben wird, ist eine Time Projection Chamber (TPC) welche die Rekonstruktion geladener Teilchen in einem grossen Phasenraumbereich bei mittlerer Rapidität erlaubt. In den Jahren 2001 bis 2005 wurde das Experiment um elektromagnetische Kalorimeter (BEMC, EEMC) erweitert, mit welchen zusätzlich die Energie von Photonen und Elektronen bestimmt werden kann.

Die verschiedenen Detektoren des STAR Detektorsystems können in zwei, durch ihre mögliche Ausleserate definierte, Klassen eingeteilt werden. Ein Teil der Detektoren wird bei jedem RHIC Bunch Crossing ausgelesen, d.h. mit einer Frequenz von 9.3 MHz. Zu dieser Klasse der sogenannten Triggerdetektoren gehören unter anderem das schon erwähnte elektromagnetische Kalorimeter, der Central Trigger Barrel (CTB), die Zero Degree Calorimeter (ZDC) und die Beam-Beam Counter (BBC). Die Time Projection Chamber und einige andere Detektoren, wie z.B. der Silicon Vertex Tracker (SVT), können im Gegensatz dazu nur mit maximal 100 Hz ausgelesen werden.

Offensichtlich ist es sinnvoll, die Daten der Triggerdetektoren zu nutzen, um die langsamen Detektoren für möglichst "interessante" Kollisionen auszulesen. Diese Aufgabe wird in STAR vom Trigger System übernommen, welches in vier verschiedene Stufen aufgeteilt ist. Die erste Stufe des Triggersystems ,"Level 0" (L0), ist als DSM Entscheidungsbaum aufgebaut. Eine L0 Entscheidung wird für jedes Bunch Crossing generiert, d.h. mi 9.3 Mhz. Die Komplexität der möglichen Entscheidungen auf L0 ist allerdings durch die zu garantierende schnelle Antwortzeit und den Aufbau aus speziell entworfenen VME Modulen stark limitiert. Daher wird ein Teil der Berechunungen bereits auf der Detektor Frontend-Elektronik durchgeführt, welche sogenannte Trigger Primitive für die eigentliche Entscheidungsfindung auf L0 bereitstellt. Ein solcher Trigger Primitiv ist z.B. die Summe über alle Streifen des CTB, welche proportional zur totalen Ereigniss Multiplizität ist, oder die Zeitdifferenz zwischen der Registrierung von Pulsen in den beiden ZDCs, welche Rückschlüsse auf die longitudinale Position des Ereignisses zulässt.

Von besonderer Bedeutung für diese Arbeit sind die Trigger Primitive, welche vom BEMC bereitgestellt werden. Dies ist zum einen der höchste ADC Wert in 4×4 Tower Patches, welche 0.2 Einheiten in Pseudorapidität und azimuthalen Winkel abdecken, zum anderen die ADC Summe eines solchen Patches.

Sobald ein Ereigniss durch L0 akzeptiert wird, startet die Auslese der langsamen Detektoren, die ca. 10 ms in Anspruch nimmt. Während dieser Zeit können die Daten der Triggerdetektoren auf den nächsten Trigger Stufen L1 und L2 weiter analysiert werden. Das grössere Zeitbudget erlaubt komplexere Berechungen als auf der ersten Trigger Stufe. Von besonderem Interesse ist hier L2, dem alle Rohdaten der Triggerdetektoren zur Verfügung stehen und welches auf einem üblichen PC läuft, womit die Komplexität der Triggeralgorithmen im wesentlichen nur durch die Ausführungszeit beschränkt ist. Typischerweise sollte eine L1 Entscheidung nach 100 μs und eine L2 Entscheidung in ca. 1 ms gefällt werden. Entscheidet einer dieser beiden Level aufgrund der detallieren Analyse, dass das Ereigniss doch nicht so "interessant" ist, dass es Sinn macht, die langsamen Detektoren auszulesen, so wird der bereits gestartete Auslesevorgang abgebrochen. Die ist insbesondere interessant, da während des Auslesens der langsamen Detektoren kein neues Ereigniss von L0 akzeptiert werden kann, d.h. selbst besonders interessante Ereignisse können in den 10 ms Auslesezeit nicht gespeichert werden. Durch das Abbrechen weniger interessanter Ereignisse stehen die langsamen Detektoren wieder schneller für neue Ereignisse bereit und mehr "interessante" Ereignisse können aufgezeichnet werden.

Die Daten von L0 akzeptierter Ereignisse, die nicht von den nachfolgenden Trigger Stufen L1 und L2 abgebrochen wurden, werden vom Data Acquisition System (DAQ) gesammelt und für die permanente Speicherung auf Magnetbändern vorbereitet. An dieser Stelle tritt durch die von den Magnetbandlaufwerken, bzw. der vorgeschaltenen Festplattencaches, maximal ausgehaltenen Datenrate eine weitere Limitation der Ereignissrate auf. Das ursprüngliche STAR Konzept sah eine Magnetbandrate von einem Ereigniss, dessen komprimierte Rohdaten ca. 80 MByte umfassen, pro Sekunde vor. Durch Fortschritte in der Magnetbandgeschwindigkeit, der Netzwerkanbindung und Parallelisierung konnte dies bis zum Jahr 2002 auf 10 Hz gesteigert werden.

Zwischen der durch die Frontendelektronik der langsamen Detektoren bestimmten Ausleserate und der Magnetbandaufzeichnungsrate besteht also ein Faktor 100 bis 10 Unterschied. Offensichtlich macht es auch hier Sinn, möglichst "interessante" Events auszuwählen, welche endgültig gespeichtert werden. Dies ist die Aufgabe des L3 Systems, welches in Kapitel 3.2.4 detailliert beschrieben wird.

Auf L3 stehen sowohl die Rohdaten aller Detektoren von STAR zur Verfügung (in der derzeitigen Implementierung werden nur die Daten der TPC, des BEMC und EEMC sowie der Triggerdetektoren verwendet, prinzipiell könnten jedoch die Daten aller Detektoren verwendet werden). Ziel des L3 Systems ist eine möglichst vollständige Rekonstruktion des Events, inklusive der Spurverfolgung in der Time Projection Chamber. Die technische Herausforderung liegt hier insbesondere im zur Verfügung stehenden Zeitbudget von ~ 100 ms; deutlich wird dies im Vergleich zu den typischerweise 2-4 Minuten, welche die Rekonstruktion eines Ereignisses während der späteren "normalen" Datenanalyse braucht.

Das STAR L3 System ist die erste Implementation eines solchen Systems in einem Schwerionenexperiment. Verschiedene Betriebsmodi und Strategien wurden mit ihm getestet, um die nötige Reduktion des Datenrate zu erreichen. Hier wäre zunächst der sogennante "Event Selection" oder Triggermodus. In ihm arbeitet

L3 wie die L1 und L2 Systeme, erscheint ein Ereigniss wenig "interessant", so wird DAQ signalisiert, es nicht auf Magnetband zu schreiben und das Ereigniss zu verwerfen. Der Nachteil dieses Betriebsmodus liegt in der Auswahl, was "interessante" Ereignisse sind. Die verschiedenen Observablen, die gleichzeitig mit dem STAR Experiment untersucht werden, machen die genaue Definition "interessanter" Ereignisse schwierig; Ereignisse, die für eine Observable essentiel sind, können oft für andere Messungen nicht verwendet werden. Der Triggermodus steigert daher nur die Aufzeichnungsrate für Ereignisse, für welche ein hinreichend selektiver L3 Entscheidungsalgorithmus definiert werden kann.

Eine Variation des Trigger Modus ist der "Event Tagging" Modus. In ihm werden interessante Events von L3 markiert, die dann durch das DAQ System auf Grund der Markierung gesondert behandelt werden können. Interessant ist hier insbesondere die Möglichkeit, markierte Events in spezielle Dateien zu schreiben ("express streams"), die dann gesondert analysiert werden können. Ergebnisse aus der Analyse dieser Dateien stehen deutlich schneller nach Ende der Datennahme zur Verfügung. Im Fall der in dieser Arbeit analysierten $Au + Au$ Daten dauert die Rekonstuktion aller Daten ein bis zwei Jahre, während die Rekonstruktion der Express Streams zwei Tage dauerte.

Eine weitere Möglichkeit, die aufzuzeichnende Datenmenge zu reduzieren, ist der Einsatz von Kompressionstechniken. L3 eröffnet die Möglichkeit, Zwischenergebnisse der TPC Spurrekonstruktion zu einer verlustbehafteten Komprimierung der TPC Daten zu nutzen. Hierzu eignen sich insbesondere die rekonstruierten Spurpunkte in der TPC. Durch ausschliessliches Speichern der Spurpunkte und Verwerfen der Rohdaten reduziert sich die typische Grösse eines Ereignisses um ca. einen Faktor 10, abhängig von der Multiplizität. Im Fall von STAR ist dieser Faktor ausreichend, dass DAQ Ereignisse mit bis zu 100 Hz auf Magnetband schreiben kann. Da dies auch die Ausleserate der langsamen Detektoren ist, kann damit jedes von L0 akzeptierte und nicht von L1 oder L2 abgebrochene Ereignis auf Band geschrieben werden. Der Vorteil dieses L3 Betriebsmodus liegt in der Tatsache begründet, dass sämtliche Analysen profitieren, während bei den bisher diskutieren Modi nur Analysen, für die ein L3 Trigger Algorithmus möglich ist, aus L3 Nutzen ziehen können. Auf Grund der offensichtlichen Vorteile wurde dieser Betriebsmodus vom STAR Experiment beginnend mit der 2003/2004 Strahlzeit als Standardmodus gewählt. TPC Rohdaten werden nur noch für einige wenige Ereignisse zu Qualitätssicherungszwecken auf Band geschrieben.

Die geringe Produktionswahrscheinlichkeit von Upsilons macht eine Nutzung sämtlicher Möglichkeiten des Trigger Systems nötig. Die Entwicklung der hierfür notwendigen Triggeralgorithmen ist in Kapitel 4.3 detailliert beschrieben. Hierbei sind verschiedene Punkte zu beachten. Zum einen müssen natürlich die durch das Detektorsystem gegebenen technischen Einschränkungen beachtet werden. Hierzu zählen z.B. die maximale Zeit, bis ein L2 Trigger Entscheidung gefällt sein muss, oder die beschränkte mögliche Komplexität auf L0. Ebenso wichtig sind jedoch auch die Integration in das STAR Datennahme Schema. Verschiedene Messprogramme konkurrieren hier um die verfügbare Bandbreite. Die hierdurch entstehenden Einschränkungen müssen bereits in der Algorithmenentwicklung berücksichtigt werden.

Wie bereits erwähnt, ist der Upsilon Zerfall in ein Leptonenpaar experimentell besonders gut rekonstruierbar. Eine gute Identifizierung der Leptonen ist durch die gewählte Rekonstruktionstechnik essentiel. Durch die Kombination des Elektromagnetischen Kalorimeters BEMC und der TPC hat STAR eine exzellente Elektronidentifikation, weshalb sich diese Analyse auf den Upsilon Zerfall in ein Elektron-

Positron Paar konzentriert. Die TPC erlaubt die Bestimmung des Impulses, über die Messung der Ablenkung des Teilchens im Magnetfeld des Experiments, und eine Messung des spezifischen Energieverlustes im TPC Gas. Die Geschwindigkeitsabhängigkeit des Energieverlustes im TPC Gas erlaubt zusammen mit der Impulsmessung eine statistische Trennung der verschiedenen Teilchensorten.

Die Elektronidentifikation mit dem BEMC nutzt die unterschiedliche Schauerentwicklung von Hadronen und Elektronen im Kalorimetermaterial. Während das Kalorimeter Schauer von Elektronen nahezu vollständig erfasst, wird nur ein Bruchteil der Energie von Hadronschauern gemessen, da die longitudinale Grösse des BEMC in der Regel nicht ausreichend ist, um den Schauer vollständig zu erfassen. Kapitel 4.1 geht auf die hierdurch eröffneten Identifikationsmöglichkeiten näher ein. Durch Kombination von TPC und BEMC Messungen werden bei einer Elektronidentifikationswahrscheinlichkeit von 80% nur ca 0.01% aller Hadronen fälschlicherweise auch als mögliche Elektronen identifiziert.

Die Verfügbarkeit der BEMC Daten bereits auf dem ersten Trigger Level L0, und damit einer Möglichkeit die Zerfallselektronen zu identifizieren, ermöglicht überhaupt erst die Entwicklung eines Upsilon Triggers. Es wurden zwei verschiedene Algorithmenvarianten entwickelt und getestet. Der erste Algorithmus basiert auf einer Messung der Energie des Upsilon-Zerfallselektrons, welche in L0 als höchster ADC Wert in einem BEMC Patch verfügbar ist. Die Akzeptanzbedingung dieses Algorithmus ist eine ausreichend hohe Energiedeposition im BEMC. Der zweite Algorithmus benutzt die Energiemessung beider Zerfallselektronen und zusätzlich ihre relative Position zueinander. Ein Öffnungswinkel von mehr als 60^o ist nötig, damit das Ereigniss akzeptiert wird. Beide Algorithmen wurden implementiert und während der 2003/2004 Datennahme getestet. Die Performance des ersten Algorithmus erwies sich als besser, wie bereits von Simulationen erwartet. Er wurde daher als Standardtrigger gewählt.

Die auf L0 getroffene Entscheidung kann auf L2 durch die Verfügbarkeit der BEMC Rohdaten weiter verfeinert werden. So ist zum einen eine genauere Bestimmung der Zerfallselektronenenergien möglich, zum anderen eine bessere Messung des Öffnungswinkels. Wie in Kapitel 4.3 gezeigt sind diese Informationen ausreichend um den Zerfall vollständig zu rekonstruieren und damit Upsilons zu rekonstruieren. Durch zufällige Kombinationen werden jedoch auch eine Reihe von Ereignissen fälschlicherweise akzeptiert. Die Spurinformationen von L3 erlauben eine weitere Reduzierung dieser fälschlicherweise akzeptierten Ereignisse.

Zum ersten Mal eingesetzt wurde der in dieser Arbeit entwickelte Trigger während der $Au+Au$ Datennahme in den Jahren 2003 und 2004. Der Betrieb wurde erschwert durch die erstmalige Inbetriebnahme sowohl des Elektromagnetischen Kalorimeters als auch der L2 Trigger Stufe. Die hierbei aufgetretenen experimentellen Schwierigkeiten werden in Kapitel 5 ausführlich erläutert. Auf die Benutzung von L2 musste schliesslich verzichtet werden, da die Ausleseelektronik einiger Detektoren einen Abbruch der Auslese nicht korrekt verarbeiten konnte. Die nicht vollständig mögliche Inbetriebnahme des BEMC reduzierte die Elektronidentifikationsmöglichkeiten von STAR.

Die Suche nach Upsilons in den Daten der Jahre 2003 und 2004 ist im Detail in Kapitel 5 beschrieben. Die akkumulierte Statistik erlaubte lediglich die Bestimmung einer oberen Grenze der Upsilonproduktionswahrscheinlichkeit bei mittlerer Rapidität von $\mathcal{B}\frac{\mathrm{d}\sigma}{\mathrm{d}y}\mid_{y=0} = 7.6\ \mu\mathrm{b}$ für 90% C.L. Dieses Limit liegt im Bereich der theoretischen Vorhersagen, ist jedoch nicht ausreichend, um die Parameter der verschiedenen Modelle einzuschränken bzw einzelne zu falsifizieren.

Es wurde jedoch gezeigt, dass eine effiziente Identifikation von Upsilons auf dem Triggerlevel in STAR möglich ist. Die Detektorkomponenten, welche die Schwierigkeiten während der in dieser Arbeit analysierten Datennahme verursachten, wurden in der Wartungsperiode des Jahres 2004 behoben. Während der Datennahme in den Jahren 2004 und 2005 konnte der Trigger wie ursprünglich in dieser Arbeit entwickelt verwendet werden. Die hierdurch mögliche Erhöhung der Sensitivität um mindestens einen Faktor 20 wird STAR aller Wahrscheinlichkeit nach eine erfolgreiche Upsilon Messung in künftigen Jahren erlauben. Des weiteren wurde innerhalb der Kollaboration ein Ausbauprogramm gestartet, welches in einigen Jahren eine weitere Verbesserung der Senitivität erwarten lässt.

Search for Upsilons in Heavy-Ion Collisions with the STAR Detector

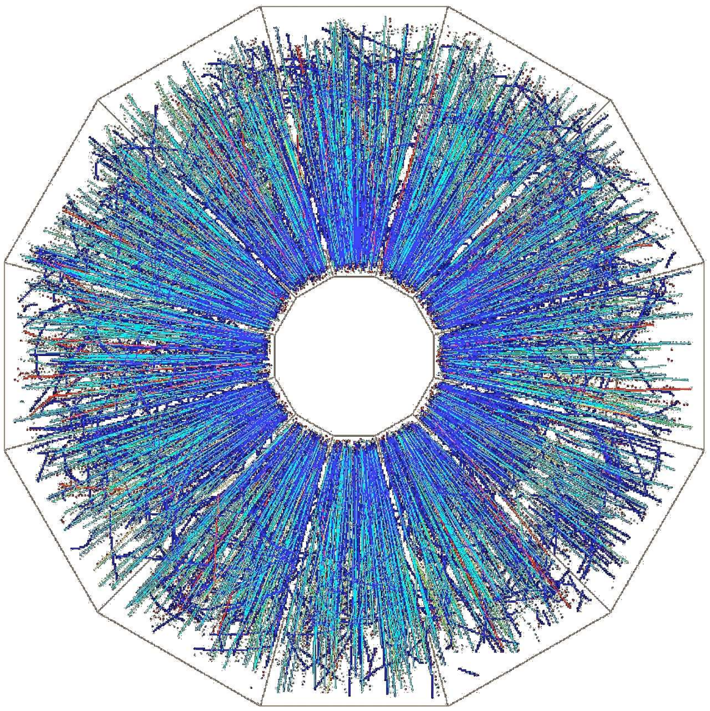

A Dissertation Presented to the
Johann Wolfgang Goethe – Universität
Frankfurt am Main

By
Thorsten Kollegger

December 2005

Damit das Mögliche entsteht,
muss immer wieder das Unmögliche versucht werden.

(Hermann Hesse)

Contents

1 Introduction

Understanding the structure of matter and the forces between its constituents has always been one of the main questions in science. The answers evolved with time, cumulating in our current knowledge at the beginning of the 21^{st} century. According to it, all matter is build from few elementary particles; six quarks and six leptons. Four fundamental interactions between them were identified: the strong, weak, electromagnetic and gravitational forces, the first three constituting the Standard Model.

All forces are mediated by exchange particles and their relative "strength" determined by a characteristic "coupling" to a "charge", which each particle carries. The weakest is the gravitational force, acting between all particles with mass as "charge" and a yet unidentified exchange particle. All particles carrying electric charge obey the electromagnetic force with the photon as mediating particle. Closely related is the weak force, acting on flavor "charges", with the $W^{\pm}$ and Z^0 mesons as exchange particles.

The dominant interaction on small scales, like inside a nucleon, is the strong force which acts between the quarks with gluons as exchange particles. What makes it different from all other forces is the fact, that also the exchange particles themself carry color, the "charge" of the strong force, and thus themself interact strongly. The theory describing the strong force is called Quantum Chromo Dynamics (QCD).

One of the most challenging aspects of QCD is the running coupling constant which is large at low energies and becomes small only at high energies, a principle called *asymptotic freedom* [GW73, Pol73]. A consequence of this and the previously mentioned fact that the gluons themself carry color is the phenomenon that no free quarks can be observed in nature, they are always *confined* into color-neutral hadrons. So far all experimental searches for free quarks have failed, supporting this prediction. But it is still possible to proof the existence (and even measure the distribution) of quarks inside the hadron in experiments with high momentum transfer, e.g. deep inelastic scattering experiments, due to the principle of asymptotic freedom.

An interesting question follows immediately from the above: Even if one can not isolate quarks in the vacuum, is there a way to create a state where a parton acts like deconfined over a large volume, i.e. larger than the size of a nuclei? Such a state would allow to test QCD predictions even in the low-energy regime and greatly improve the understanding how hadrons are formed.

Indeed theoretical calculations show that such a state might be created with matter at high temperature and/or density [CP75b, CP75a], as shown in figure 1.1. A new state of matter, the Quark-Gluon-Plasma (QGP), is expected, in which hadrons cease to exist and quarks and gluons act like free particles over a large volume. Current estimates from lattice QCD predict the transition from the hadron dominated phase into the QGP at an energy density of order 1 GeV/fm^3 or, for baryon symmetric matter, at the temperature $T_c = 165 \pm 10$ MeV [Kar02]. This coincidences with the Hagedorn temperature, where, due to the exponentially growing mass spectrum of hadronic resonances, divergences in thermodynamic quantities like energy density are expected [Hag65]. The phase transition at zero net baryon density is expected to be not a true (discontinuous) one but rather a rapid crossover, becoming a first order transition at a critical point. The theoretical calculations have however still large uncertainties. The exact location of the critical point and even the order of the phase transition expected to happen are far from certain. This points to the need of experimental measurements to clarify this picture. But how can the necessary temperature and density be achieved experimentally?

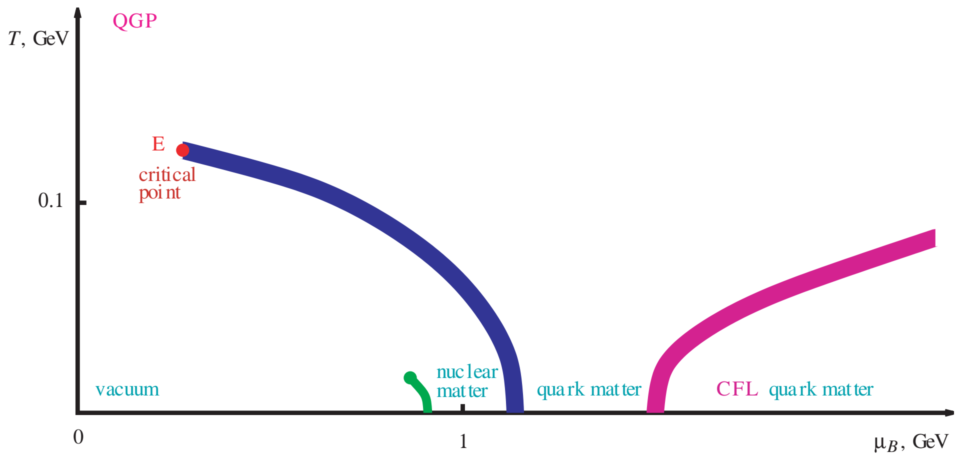

Figure 1.1: Sketch of the phase diagram of QCD matter [Ste04].

1.1 Relativistic Heavy Ion Collisions

The only known possibility so far to create QCD matter at high temperature and density in the laboratory is provided by relativistic heavy ion collisions. Heavy nuclei like gold or lead are accelerated to relativistic energies, i.e. close to the velocity of light, and brought to collision with each other. In the overlap region a large number of interactions between the incoming quarks and gluons happens, transforming part of the energy into other particles, resulting in a very large number of high-energetic partons in a, for elementary particle physics large, volume. The quest of relativistic heavy ion physics is to develop methods and detectors to measure the properties of this overlap region.

This task is extremely challenging due to the short timescales which a possibly created QGP is expected to exist. What makes measurements even more complicated is the fact, that the partonic state can not be directly detected. Measurable in present experiments is only the hadronic final state, to which confinement forces the collision fireball to evolve. Therefore any evidence for a deconfined state has to be gained indirectly by analysis of the observed final hadronic system. Several recent assessments of the available experimental data show that evidence for a deconfined state exists [HJ00, BM04, A+05a, A+05b, A+05f, B+05, Sto05], but further work is required for a real understanding. Some of the available evidence is briefly discussed in the following paragraphs, before turning to a more detailled description of one proposed signal in chapter 2 whose measurement is the objective of this work.

An important property to show is that the partons in the overlap region act collectively, i.e. that the created state is not just a superposition of independent collisions. A result pointing in this direction is the applicability of grand-canonical statistical models to describe the measured hadron yield ratios over a broad range in collision energy [BGK$^+$04, BMMRS01, BCK$^+$01]. Assuming equilibrium of the fireball constituents, the model parameters can be identified with the corresponding thermodynamic quantities, i.e. temperature, baryo-chemical potential and volume.

An interesting result is that the extracted temperature for high collision energies is close to the phase transition temperature calculated in lattice QCD, i.e. coincidences with the hadronization temperature. The hadronic state seems to be "born into equilibrium" out of a partonic state [Sto99a]. This picture is futher supported by calculations showing that equilibrium cannot be reached in a hadronic medium, considering collision rates and time scales of the hadronic fireball expansion [BMSW04].

However these models do not describe the collision dynamics, i.e. how the system has achieved equilibrium (if at all). It has been pointed out [Koc03] that the essential condition for the applicability of statistical models is phase-space dominance. The success of statistical models thus does not necessarily mean that the system has been equilibrated via a thermodynamic process in the sense of Boltzmann. Indeed statistical model fits, in the microcanonical and canonical formulations, describe the observed particle ratios in p+p, e^+e^- and p+A collisions [BH97]. On the other hand the applicability of a grand-canonical model, which does not need exact quantum number (e.g. strangeness) conservation, shows that the produced state is not simply a superposition of independent collisions. This is further supported by the observed strangeness enhancement, i.e. that (multi-)strange hadron production is significantly enhanced compared to elementary collisions and reaches the grand-canonical equilibrium value.

More insights into the collision dynamic can be gained by the application of hydrodynamic models. Assuming that the initial interactions among the constituents are sufficiently strong to rapidly establish local thermal equilibrium and to maintain it over a significant evolution time, the resulting matter may be treated as a relativistic fluid undergoing collective, hydrodynamic flow.

Indeed the hadron spectra at low momenta are well described by hydrodynamic-motivated fits (Blast-Wave fits [RL04]). The model parameters may thus reflect the characteristics of the system at kinetic freezout, i.e. when no futher elastic interactions happen. The decreasing freezout temperature and stronger collective flow may indicate a more rapid expansion after chemical freezout with increasing collision centrality. Multistrange baryons spectra, however, seem to reflect a higher freezout temperature. It has been suggested that they accumulate their substantial radial flow velocity prior to the chemical freezout, giving them an increased sensitivity to the earlier partonic stages of the system evolution. However the extracted fit parameters are quite sensitive to model assumptions like the used velocity profile and the fitted momentum range, making it difficult to draw strong conclusions without a full hydrodynamic calculation.

All these studies using low momentum hadrons, despite some caveats in their interpretation, point in the same direction: heavy ion collisions produce some new form of matter. It is very likely that (at least local) equilibrium is attained and collective flow established in the early collision stage when sub-hadronic degrees of freedom dominate the matter. The temperature extracted from statistical models coincidences with the phase transition temperature of lattice QCD. It remains the challenge to characterize the properties of the created matter and the phase transition back to to normal hadronic matter.

Several proposals for observables exist which might allow a deeper understanding of the medium properties. They can be roughly divided into two classes, one based on the interaction of well defined probes (*hard probes*) with the medium, the second based on modifications of bulk final state particle properties relative to model expectations.

Focusing on the later class first, it has for example been proposed that the number of strange quarks (and hence also the number of hadrons with strange quarks) is smaller for a final state originating from a deconfined state then for one from purely hadronic production [GG99b], resulting in a non-monotonic behavior when the phase boundary is crossed. Indeed indications for such a behavior have been observed by the NA49 experiment at the CERN SPS [A$^+$02c]. However also other models based solely on hadronic production mechanisms can reproduce the generel trend of the data [BMCOR02].

Fluctuations [SRS98, Sto99b, VKR99, Hei01] are another example of this class of observables, e.g. net charge [JK00, AHM00] or transverse momentum [GM92] fluctuations. The interpretation of the measured results remains difficult due to different model predictions and analysis details. Especially the influence of the hadronization process and of the created hadronic state itself on the observables remains disputed.

To avoid the problems associated with the hadronization process it has been proposed to study the production of non-strongly interacting particles, i.e. photons and leptons (*electromagnetic probes*). Due to their large mean free path they leave the medium without final-state interactions, and thus carry direct information about the medium's conditions and properties. One of the most interesting observables of this class is thermal radiation emitted by the quark-gluon plasma via quark-antiquark annihilation. The spectral shape of the observed distribution can then be directly related to the plasma temperature.

However analyzes based on these non-strongly interacting probes suffer from the fact that photons and leptons are not only produced during the initial stage of the collision but also later in time, e.g. by decaying hadrons. Distinguishing these background particles from the signal particles is experimentally very challenging and so far no conclusive evidence has been obtained [TRG04].

The other class of observables mentioned above which might allow a deeper understanding of the medium properties are hard probes. This class is defined by the involved production process, hard probes are those which are expected to be only produced in the initial parton-parton collisions due to the necessary large energy transfer. A characteristic feature of these probes is the expected scaling with the number of initial parton-parton collisions, often refered to as binary collision scaling. This is in contrast to the observed number of participant scaling for soft probes. This scaling assumption can be checked by analyzing hard probes which do not interact with the medium, i.e. the electromagnetic probes mentioned above. Indeed hard (i.e. high energy) photon production, from e.g. the process $g + q \rightarrow \gamma + q$, has been observed to scale with the number of binary collisions [A$^+$05c].

Strongly interacting hard probes might allow to study the early phase of the produced medium. If the hard probes are indeed only produced in the initial collisions, any differences to the scaled production cross-section or phasespace distribution from elementary collisions must be attributed to the propagation through the medium created in the collision. Examples for such probes are jet production and heavy flavor production.

The Relativistic Heavy Ion Collider (see section 3.1 for a more detailled description) reaches for the first time in heavy ion collisions the necessary energy to allow an efficient study of hard probes. The first published results on hard probes concentrated on jet production and recieved significant attention.

Jets at RHIC have so far been studied by measuring particles with high transverse momentum and also by analyzing correlations between these particles. The observed transverse momentum distributions show strong modifications compared to the expectations from binary scaling. High transverse momentum hadrons are suppressed relative to binary scaling by nearly a factor 5 in central collisions, with the observed modification factor decreasing for more peripheral collisions [A+02b, A+03d].

As a cross-check that this is indeed due to interactions with the medium produced in nucleus-nucleus collisions, the same observable has alos been studied in deuteron-gold collisions in which no medium is expected to be formed. In these collisions the suppression observed in nucleus-nucleus collisions is not present, also the shape is modified compared to the scaled reference from elementary collisions by the Cronin effect [A+03b, A+03h].

These observations have been interpreted as energy loss via gluon radiation by the partons traversing a partonic medium [BDM+97, Wie00]. The validity of this interpretation is based on the assumption that the standard factorization scheme is still valid, i.e. that the parton fragmentation into hadrons is not modified by the medium (vaccum fragmentation). While this might be valid in the high energy limit, when the dilated fragmentation time should exceed the traversal time of the parton through the medium, it seems questionable for partons at intermediate momenta. Indeed there is ample experimental evidence that the hadronization process at intermediate transverse momenta is modified, a phenomenon commonly described by recombination models [FMNB03, GKL03, MV03]. However the data in the range of validity of the energy loss models might be used to constrain the initial gluon density in the collision [VG02].

The sensitifity of the observed leading hadron spectra to the initial density is however small at high energy densities [EHSW05]. A higher sensitifity might be gained by studying jet production via correlation measurements. The first experimental results [A+03e] showed a large suppresion of the away side partner of dijets in nuclear collisions. Another possibility to gain higher sensitivity is the study of heavy quark jets or γ-jets. The above discussion of jet production shows exemplarely the power of hard, penetrating probes to study the early phase of heavy-ion collisions.

2 Probing the Early Phase of Heavy Ion Collisions: Heavy Quarkonia in the Medium

Another hard probe proposed to study the early phase of a heavy ion collisions are heavy quarkonia, i.e. bound charm-anticharm and bottom-antibottom pairs. In the standard picture, the large mass of the charm (1.15 to 1.35 GeV) and bottom (4.1 to 4.4 GeV) quarks allows to calculate heavy quark production pertubatively, with production timescales $\tau \propto 1/m_Q$ short enough to be sensitive to the early phase of an heavy-ion collision. The $Q\overline{Q}$ pair created may become a full physical resonance (i.e. a quarkonium state) close to the formation point for low pair velocities (typical formation times are one the order of one fermi) and then traverse the medium as a color singlet state. The intrinsic spatial scales of the quarkonia states remain however much smaller than the hadronic size $1/\Lambda_{\mathrm{QCD}}$, in contrast to hadrons containing a light (u, d, s) quark. Heavy quarkonia are thus able to probe the partonic state of the medium. Additionally the bound quarkonia states decay electromagnetically at time scales far larger than the typical fireball lifetime. Their decay daughters are thus not influenced by the medium, making the quarkonia production cross section experimentally accessible.

So far experimental studies have been concentrated on the charmonium states (see figure 2.1) and here on the $1S$ ground state, the J/ψ, mainly because of its relatively large production cross section. $J/\psi(1S)$ production in nuclear collisions has been studied at the CERN SPS in $p+p, p+A$ and $A+A$ collisions up to central $Pb+Pb$ collisions, at the Fermilab fixed target beam in $p+p$ and $p+A$ collisions and more recently at the Relativistic Heavy Ion Collider RHIC (see next chapter 3) in $p+p, d+Au$ and $A+A$ collisions up to central $Au+Au$ collisions.

Figure 2.2 shows the combined results of the NA38, NA50 and NA51 experiments at the CERN SPS. The ratio of the J/ψ cross section over the Drell-Yan pair cross section decreases approximately linear with the length L of nuclear matter traversed up to $L \approx 7$ fm. The normailzation to Drell-Yan pairs has been choosen since they have been observed to scale with the number of binary collisions, as caracteristic for hard probes. A decrease below the one expected from this approximately linear extrapolation is observed at larger pathlengths.

2.1 Models of Quarkonia Production in Heavy Ion Collisions

Several theoretical models have been developed to describe the observed $J/\psi(1S)$ suppression pattern. The standard approach is based on the assumption that quarkonia are only produced in the initial hard scattering. The observed suppression

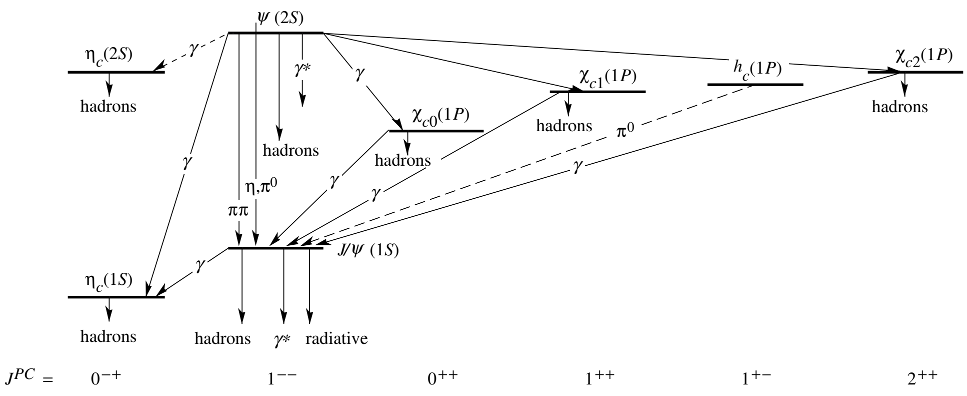

Figure 2.1: The charmonium system [E+04].

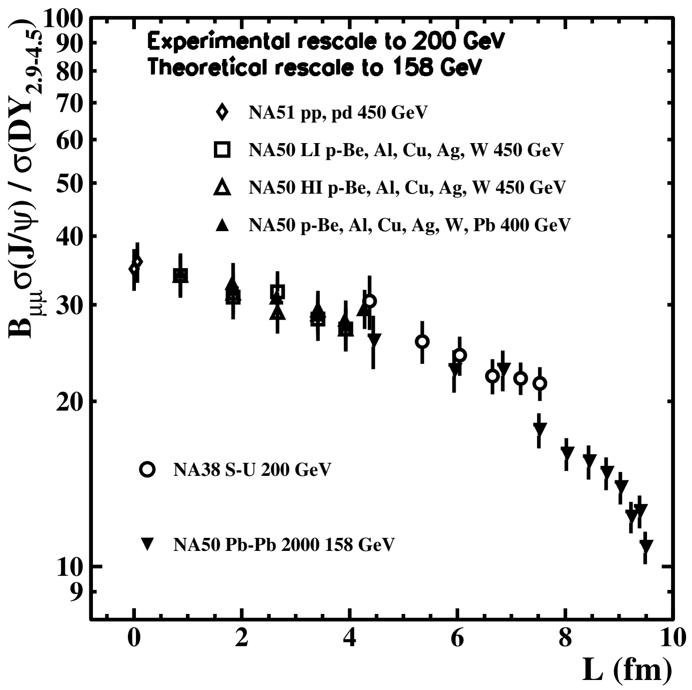

Figure 2.2: Ratio $\mathcal{B}_{\mu\mu}\sigma\left(J/\psi\right)/\sigma(DY)$ of the $J/\psi(1S)$ cross section (times the branching ratio $\mathcal{B}_{\mu\mu}$ to muons) to the cross section $\sigma(DY)$ of Drell-Yan pairs with mass 2.9 GeV/c^2 $< m <$ 4.5 GeV/c^2 as function of the averaged length L of nuclear matter traversed. [A+05e]

is therefore a result of the interaction between the quarkonia state and the medium created in the collision. Another class of models not based on this assumption was developed a few years ago. Quarkonia production in these models takes place at hadronization and does thus not provide any direct information on the early stage of the collision. In the following sections the ideas behind the different models and their implications on the interpretation of the experimental data will be discussed.

2.1.1 Color Screening

The experimental study of quarkonia production was mainly motivated by a prediction of Matsui and Satz [MS86] that quarkonia should be strongly suppressed by color screening if a QGP is indeed created in heavy ion collisions. It belongs to the class of models which assume that the J/ψ is produced early in the collision and then traverses the medium.

In the absence of any medium, the masses and radii of the different quarkonia states can be well described by a non-relativistic potential theory [EGK$^+$78, EGK$^+$80, JOS86, EQ95] based on the Schrödinger equation

$$\left[2m_Q + \frac{1}{m_Q}\bigtriangledown^2 + V_1(r)\right]\phi_i^Q = M_i^Q\phi_i^Q \tag{2.1}$$

where in the case of the J/ψ Q stands for a charm quark, i denotes the $1S$ state of the J/ψ and r is the separation of the c and $\overline{c}$ quarks. The confining color singlet potential V_1 in the vacuum can be to first order parametrized in terms of a linear confining term with the string tension σ and a $1/r$ contribution containing Coulomb-like one-gluon exchange effects

$$V_1(r) = \sigma r - \frac{\alpha}{r} \tag{2.2}$$

More complex forms for the potential have also been developed [DPS01b, EQ95] however the basic idea behind the model can already been studied with the simple form.

In a high temperature, deconfined medium, screening effects due to the large density of charge carriers may become important and thus the form of the potential changes to

$$V_1(r) \sim -\frac{\alpha(T)}{r}e^{-\mu(T)r} \tag{2.3}$$

where $\mu(T)$ is the temperature T dependend effective screening mass in the deconfined medium. The screening mass $\mu(T)$ can be calculated by a variety of methods, pure SU(2) and SU(3) gauge theory [HKR95, HKR98, CKP01] and lattice QCD calculations [KLP01, BLP$^+$89, Won99], and is increasing with temperature T.

For a given temperature, the screened potential 2.3 gets constant at some radius r_0, indicating that the $Q\overline{Q}$ interaction potential vanishes. Thus r_0 sets a natural upper limit on the radius of a bound state produced in a deconfined medium.

Using probes with a known radius r allows to test the temperature of the deconfined medium. If the radius is larger than r_0 the particle get dissociated and can not any longer be experimentally observed, while particles with a radius smaller then r_0 survive. Calculations have shown that the radius of the quarkonia, as they can be calculated from equation 2.1 and the relevant potential, are of the same order as

r_0 at the deconfinement temperature $T_C \approx 170$ MeV. For the J/ψ a dissociation temperature T_D of $T_D/T_C = 1.1$ has been calculated [DPS01a].

The J/ψ interaction cross section with hadrons are believed to be rather small [KS94] (see the discussion in the following sections 2.1.2, 2.1.3 and 2.1.4) and thus the J/ψ yield in a hadronic medium should not be modified too much. Measuring the J/ψ yield should thus be sufficient to distinguish between a hadronic and a deconfined medium with a temperature $T > T_D$. Indeed the observed J/ψ suppresion in the NA38/NA50 data at the CERN SPS has been interpreted along these lines, extending the model from the static picture presented here to the more realistic one of an extending medium.

2.1.2 Quarkonia Suppresion by Gluon Dissociation

A dynamic mechanism to dissociate a quarkonium state in a QGP are collisions with gluons, i.e. the process $g + \left(Q\overline{Q}\right) \to Q + \overline{Q}$. If the energy of the gluon is higher then the binding energy E_B of the quarkonium state, i.e. the energy difference between the quarkonium mass and the open charm (bottom) threshold $2m_D$ ($2m_B$), it dissociates into two open charm (bottom) mesons. The gluon-quarkonium cross section has been calculated as

$$\sigma_{g\left(Q\overline{Q}\right)(k)} = \frac{2\pi}{3}\left(\frac{32}{3}\right)^2\left(\frac{m_Q}{E_B}\right)^{1/2}\frac{1}{m_Q^2}\frac{\left(k/E_B - 1\right)^{3/2}}{\left(k/E_B\right)^5} \tag{2.4}$$

with k denoting the momentum of the incident gluon on a stationary quarkonium [KS95, Pes79, BP79]. It vanishes until the gluon momentum passes the binding energy E_B, peaks just a little bit later and then vanishes again when sufficiently hard gluons just pass through the quarkonium.

In a thermalized QGP the gluons have a Bolzmann distribution $f(k) \sim e^{-\frac{|k|}{T}}$ and hence average momenta of $<| k |>= 3T$. The necessary gluon momentum to dissolve a J/ψ is on the order of 0.7 to 1.7 GeV. Given that a deconfined medium is expected only above the critical temperature $T_C = 170$ MeV, i.e. a minimal expected average gluon momentum $<| k |>= 3T = 0.51$ GeV/c, the process should be quite efficient and no (few) J/ψ should survive.

The gluon-quarkonium cross section $\sigma_{g\left(Q\overline{Q}\right)(k)}$ can be used to calculate the light hadron-quarkonium cross section $\sigma_{h\left(Q\overline{Q}\right)}$ by convoluting it with the gluon distribution in the light hadron (e.g. a pion)

$$\begin{aligned}\sigma_{h\left(Q\overline{Q}\right)} &= 2\pi^{3/2} g_2 \left(\tfrac{16}{3}\right)^2 \left(\tfrac{16\pi}{3g^2}\right) \tfrac{1}{m_Q^2} \tfrac{\Gamma(k+2)}{\Gamma(k+\frac{7}{2}}) \left(1 - \tfrac{\lambda_0}{\lambda}\right)^{k+5/2} \\ &\simeq \sigma_{\text{geom}} \left(1 - \lambda_0/\lambda\right)^{n+3.5}\end{aligned} \tag{2.5}$$

with $\lambda \simeq (s - m_{Q\overline{Q}})^2/m_{Q\overline{Q}}$ and $\lambda_0 \simeq (m_h + E_B)$; s is the squared $(Q\overline{Q}) - h$ collision energy and $g_2 \simeq 0.5$ the fraction of the hadron momentum carried by gluons. The gluon distribution in the hadron has been assumed to be $xg(x) \simeq g_2(1-x)^{1+n}$. To dissolve the J/ψ hadron momenta of 3-4 GeV would be necessary. Again assuming a temperature of 170 MeV and a Boltzmann distribution for the hadrons, the average hadron momentum is $<| p |>= 3T = 0.51$ GeV/c, i.e. quite low compared to the energy necessary to dissolve the J/ψ in hadronic collisions. Most of the J/ψ produced in the collision should therefore survive in an hadronic medium, in contrast to a deconfined medium as discussed above.

2.1.3 Quarkonia Absorption in Nuclear Matter

So far it has been assumed that the initial quarkonium production mechanism is not modified in nuclear collisions. In this case the quarkonia yield in nuclear collisions scales with the number of binary collisions which can be easily calculated in the Glauber framework. For $p + A$ (minimum bias $A + A$) collisions the expected quarkonium production cross-section $\sigma_{Q\overline{Q}}$ is expected to scale like A (A^2) and thus the baseline for all these models is $\sigma_{Q\overline{Q}}(A + B) = \sigma_{Q\overline{Q}}(p + p)AB$.

However in $p + A$ collisions, both at the CERN SPS and at the Fermilab fixed target beam, deviations from this scaling have been observed, as is obvious from figure 2.2. This has been attributed to the interaction of the quarkonia itself or pre-resonance $\left(Q\overline{Q}g\right)$ states [KS96] with the nucleons of the nuclei. If pre-resonance absorption is the dominant mechanism, the absorption should be independent of the formed quarkonium state as the transition of the pre-resonance state to the physical resonance state $Q\overline{Q}$ happens outside the nucleus, e.g. for the $c\overline{c}$ system the absorption should be the same for J/ψ and $\psi(2S)$. Indeed such a behavior has been observed [B$^+$95, A$^+$99a], favoring the pre-resonance absorption interpretation.

To include these effects into the baseline of the models, the scaling equation is extended to

$$\sigma_{Q\overline{Q}}(A + B) = \sigma_{Q\overline{Q}}(A + B)\,(AB)^{\alpha} \tag{2.6}$$

with α a phenomenological factor determined from fits to $p + A$ data. While this equation is sufficient to describe the expected yield in minimum bias $A+A$ collisions, it can not model the centrality dependence. To calculate it an effective absorption cross section σ_{abs} is introduced which can be related to α in $p + A$ collisions as

$$\sigma_{\text{abs}} = \frac{16\pi r_0^2}{9}\,(1 - \alpha) \tag{2.7}$$

for large targets ($A > 50$) [Vog99] using the Glauber model with a Wood-Saxon parametrization of the nuclear density to describe the collision geometry. The survival probability $S^A_{Q\overline{Q}g}$ of a $\left(Q\overline{Q}g\right)$ pair formed at point z_0 in the target nucleus A is then

$$S^A_{Q\overline{Q}g} = \exp\left\{-\int_{z_0}^{\infty} \mathrm{d}z\rho_A(z)\sigma_{\text{abs}}\right\} \tag{2.8}$$

where ρ_A is the Wood-Saxon density distribution of the nucleus A and the integral covers the path from the production point z_0 out of the nucleus.

Fits to the CERN SPS data give $\sigma_{\text{abs}} = 4 - 7$ mb [C$^+$03a, GFS$^+$98, Vog99, KLNS97, CCP$^+$88]. In [B$^+$03b] is has been argued that the absorption cross section should scale with the center of mass energy $\sqrt{s_{NN}}$ as

$$\sigma_{\text{abs}}\left(\sqrt{s_{NN}}\right) = \sigma_{\text{abs}}\left(\sqrt{s_{NN_0}}\right)\left(\frac{s_{NN}}{s_{NN_0}}\right)^{\Delta/2} \tag{2.9}$$

where σ_{abs}(17.3GeV) has been fixed to 5 ± 0.5 mb and Δ is 0.125. Using this relation, the absorption cross section at RHIC σ_{abs}(200GeV) should increase to ≈ 6 mb. However it has been pointed out by several authors that the absorption processes at RHIC might be completely different than the ones at SPS; both an increasing of the absorptions with energy [CS01] as well as an decrease with energy [GFS$^+$01] have been predicted. The recently measured absorption cross section in $d + Au$ collisions is 1-3 mb [A$^+$05d], i.e. much smaller than most predictions.

After fixing the nuclear absorption cross section, the survival probability of the quarkonium $S_{Q\overline{Q}}(b)$ in a heavy ion collision $A+B$ can be calculated by modifying equation 2.8 to take the second nucleus into account

$$S^{(A+B)}_{Q\overline{Q}g}(b) = \exp\left\{ - \int_{z_0^A}^{\infty} \mathrm{d}z \rho_A(z) \sigma_{\mathrm{abs}} \int_{z_0^B}^{\infty} \mathrm{d}z \rho_B(z) \sigma_{\mathrm{abs}} \right\} \tag{2.10}$$

where z_0^A (z_0^B) is the production point of the $\left(Q\overline{Q}g\right)$ state in the nucleus A (B) and ρ the respective density calculated in the Wood-Saxon parametrization.

2.1.4 The Comover Interaction Model

Interactions of the formed resonance with other comoving particles produced in the collision might also reduce the number of observable J/ψ [GGJ88, BO89, AC98, S+99, GGB+99], e.g. $J/\psi + \pi \rightarrow \eta_c + \pi + \pi$ or the reaction $J/\psi + \pi \rightarrow D + \overline{D}$. In the environment of a heavy-ion reaction, where a lot of resonances are formed, also exothermic reactions like $J/\psi + \rho \leftrightharpoons \eta_c + \pi$, $J/\psi + \omega \leftrightharpoons \eta_c + \pi + \pi$ and $J/\psi + \eta \leftrightharpoons \eta_c + \pi + \pi + \pi$ and reactions of the J/ψ with resonances like $J/\psi + \rho \rightarrow D + \overline{D}$ are possible. The combined cross section for these processes is expected to be non-negligible and has been estimated to be $\sigma_{\mathrm{co}} \approx 1 - 2$ mb.

The survival probability of the J/ψ can then be calculated as

$$S^{\mathrm{co}}_{J/\psi}(b,s) = \exp\left[-\sigma_{co} N_y^{co}(b,s) \ln\left(\frac{N_y^{c0}(b,s)}{N_f} \right) \Theta\left(N_y^{co}(b,s) - N_f \right) \right] \tag{2.11}$$

where $N_y^{\mathrm{co}}(b,s)$ is the initial density of comovers per unit transverse area $\mathrm{d}^2 s$ and per unit rapidity at impact parameter b and N_f the corresponding freeze-out density [ACF99]. The logarithmic factor accounts for the decrease in density from the initial formation time of the J/ψ to the freeze-out time when the density $N_f \approx 1$ GeV/fm^3 is reached.

The main parameter of the model is the density N_{co} of the comovers. It is commonly calculated using the Wounded Nucleon Model in which the comover density is proportional to the number of participating (wounded) nucleons. The model however neglects the part of the multiplicity coming from hard interactions, whose fraction of the total multiplicity is expected to increase with increasing collision energy. Other models like the Dual Parton Model [AC98, ACF99] include this cross section and give similar results at SPS energies.

While the comoving particles are commonly identified as hadrons, one might doubt that hadrons still have their vacuum properties in the high density environment at the early stage of the collision, if hadrons exist at all. However the early phase of the collision contributes most to the quarkonium absorption in the comover model. The applicability of the cross sections estimated earlier is thus highly doubtfull. To elude this problem, some authors of the comover approach do not insist on the hadronic nature of the comoving medium[ACF99, Cap04], but instead treat σ_{co} as a free parameter, describing some sort of average cross section of the J/ψ with the matter created in nucleus-nucleus collisions, determined from fits to the data. Fitting the NA50 results on J/ψ production in $Pb + Pb$ collision gives $\sigma_{co} = 0.6$ mb.

2.1.5 Statistical Hadronization Model

The apparent success of statistical hadronization models to describe the light hadron (i.e. hadrons composed of u, d and s quarks) inspired an extension of these models to include also heavier quarks, e.g. the charm quark. In grand-canonical models the J/ψ yield is expected to scale with the volume, which should be proportional to the number of participants in the collision and thus also to the total hadron yield. Indeed for sufficiently central collision a constant $J/\psi/h$ ratio has been observed [GG99a].

However grand-canonical hadron-gas model calculations underestimate the measured J/ψ yield by factors 2-3 at SPS energies, indicating that charmed hadrons are not in full chemical equilibrium [BMS00]. This is not surprising given the small cross sections for charm production that rule out equilibration in hadronic models.

These observations have sparked the development of statistical coalescence models [GKSG01, GKSG02, ABMRS03, GKR04, GR01] for the description of charmed hadron abundances in heavy ion collisions. These models are based on the assumption that charm quarks are produced only in the initial hard collisions and none are formed at later stages. However the subsequent formation of charmonium states is assumed to not follow the production mechanisms in elementary collisions, on which the models discussed above where based. It is rather assumed that the distribution of the charm and anti-charm quarks to the finally formed charmed hadrons happens at hadronization time, according to the laws of statistical mechanics. The assumption that no charmonium states are formed in the early phases of the collision might be compatible with the assumption of total color screening.

Due to the small number of charm quarks, the production of charmed hadrons is generally treated with in the framework of canonical thermodynamics. The yield of open charm hadrons i and charmonia j can be then obtained from [ABMRS03]:

$$N_i = g_c N_i^{th} \frac{I_1\left(g_c N_{oc}^{th}\right)}{I_0\left(g_c N_{oc}^{th}\right)} \qquad \text{and} \qquad N_j = g_c^2 N_j^{th} \tag{2.12}$$

where I_n are modified Bessel functions, g_g a fugacity parameter which accounts for deviations of charm multiplicity from the value that is expected in complete chemical equilibrium and N_{oc}^{th} $\left(N_j^{th}\right)$ the total number of open charm hadrons (hidden charm mesons) computed from their grand-canonical densities. The sum over all states $N_{i,j}$ should be then equal to the number of directly produced charm-anticharm quarks $N_{c\bar{c}}^{dir}$ in the initial hard collisions. The model is expected to be valid only for sufficiently large numbers of participating nucleons [SSZ97, BMS00]. One of the main input parameters into the model is the total charm production cross section, which is not well measured at RHIC.

The most striking prediction of these models is a change of the centrality dependence between SPS, RHIC and LHC. While at SPS a decrease of the $J/\psi/N_{part}$ ratio with centrality is described, a slight enhancement at RHIC and a strong enhancement with increasing centrality at LHC is predicted.

2.2 Quarkonia Suppresion and the $\left(b\bar{b}\right)$ System

The apparent success of most models to describe the SPS data, involving completely different processes, obviously requires further studies to falsify at least some of them. One possibility is changing the collision energy, i.e. going to RHIC ($\sqrt{s_{NN}} = 200$ GeV) or even to LHC ($\sqrt{s_{NN}} = 5.5$ TeV). While the first results from RHIC on J/ψ production in $Au + Au$ collisions [A$^+$04b] were rather inconclusive due to the low statistics, recently high statistics data became available [DC05]. None of the models could correctly predict the data, also after model parameter adjustment some success was claimed. The interpretation of the data remains debated.

Another possibility to increase the insight into quarkonium production and modification in the medium is to examine also the production of other quarkonia states than the J/ψ. The only other state experimentally accessible in the quarkonium system show in figure 2.1 is the $\psi(2S)$ with a mass of 3.686 GeV[1]. However the binding energy $E_b \simeq 0.05$ GeV of the $\psi(2S)$ is quite small and it thus might dissociate already in a confined medium. Dissociation temperatures of $T_D/T_C \approx 0.1 - 0.2$ have been calculated [DPS01b]. Following the arguments of section 2.1.2 the hadron momentum sufficient to dissolve the $\psi(2S)$ is a few hundred MeV which has to be compared to the expected mean hadron momentum of 0.5 GeV. An additional challenge is the experimental measurement, the branching ratio into dilepton channels is an order of magnitude smaller than the one of the J/ψ and the $\psi(2S)/J/\psi$ production ratio is ≈ 0.14. Together this results in a factor 10^2 of more events needed for a $\psi(2S)$ observation and indeed the so far available data on it is rare.

However there exist another system of quarkonia states, the bottomonium family build of b quarks. The ground state $\Upsilon(1S)$ was first observed at in $p + A$ collisions at Fermilab [H$^+$77]. Our current understanding of the system is shown in figure 2.3. The larger energy difference between the ground state and the open bottom threshold results in a much more populated system. The properties of most states are quite well known from experiments at e^+e^- colliders which copiously produce the Υ states by running at the corresponding center of mass energy [A$^+$83, K$^+$92]. From an experimentalists view the most promising states are the ones decaying into dilepton pairs, the members of the Υ family. Table 2.1 lists their masses and dilepton branching ratios. In contrast to the members of the charmonium family the branching ratios are roughly equal. Their experimental observation thus depends only on the production ratios which will be discussed later in section 2.3. However the production cross section is several orders of magnitude ($\sim 10^3$ at RHIC) smaller than the one of charmonium states and so far Upsilons have not been measured in heavy ion collisions.

A first Υ measurement would provide a unique dataset to study quarkonia production and modification in the medium and to constrain the different models. In the color screening picture the dissociation of the $\left(Q\overline{Q}\right)$ states depends mainly on the radius of the quarkonium states which can be calculated with equation 2.1. The dissociation temperatures calculated in [DPS01a] are listed in table 2.2. As expected the Υ states dissociate at different temperatures, ranging from $\sim 0.75T_C$ for the $\Upsilon(3S)$ to $\sim 2.3T_C$ for the $\Upsilon(1S)$. Measuring the individual suppression factors (and additionally the one of the J/ψ) would allow to constrain the temperature reached in the collision.

[1]The (1P) states can not decay into lepton pairs and are thus experimentally difficult to reconstruct, especially in the high density environment of a heavy ion collision.

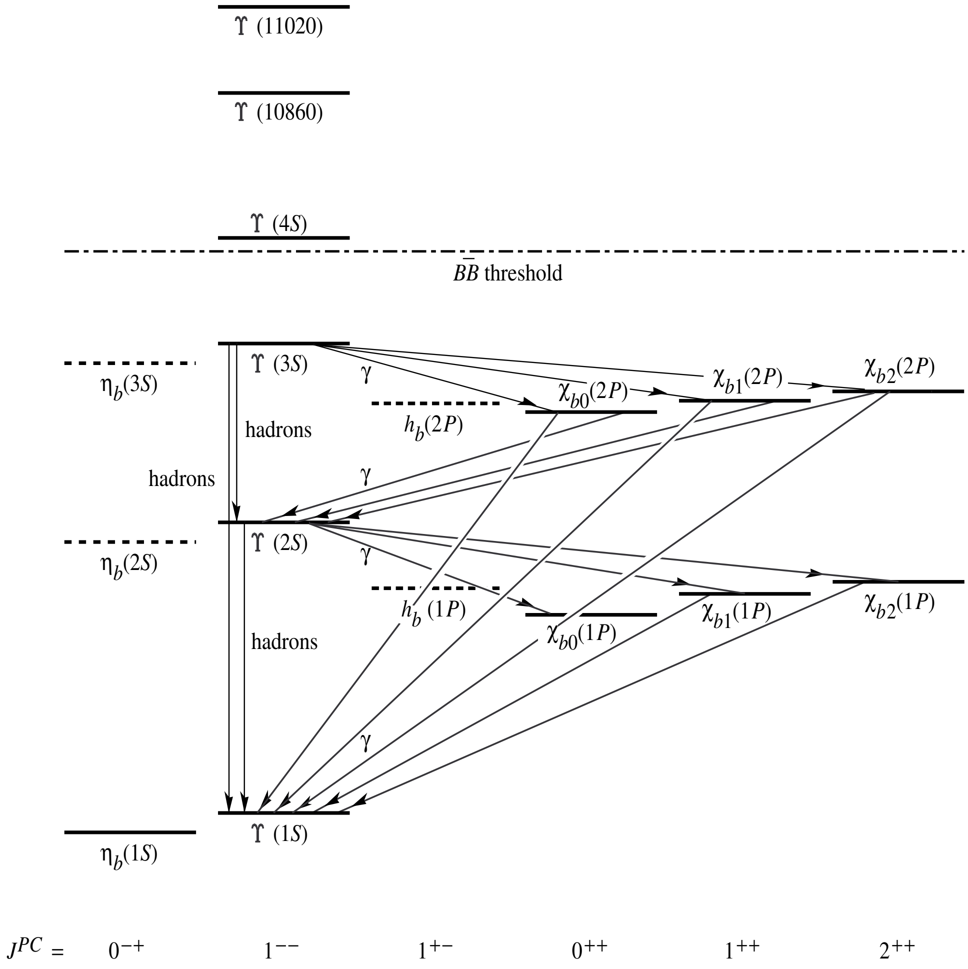

Figure 2.3: The bottomonium system [E+04].

	mass [E+04]	width [E+04]
$\Upsilon(1S)$	(9460.30 ± 0.26) MeV	(53.0 ± 1.5) keV
$\chi_{b0}(1P)$	(9859.9 ± 1.0) MeV	-
$\Upsilon(2S)$	(10023.26 ± 0.31) MeV	(43.0 ± 6) keV
$\chi_{b0}(2P)$	(10232.1 ± 0.6) MeV	-
$\Upsilon(3S)$	(10355.2 ± 0.5) MeV	(26.3 ± 3.4) keV

$\Upsilon(1S)$

decay mode	$\mathcal{B}$ [E+04]	$\mathcal{B}$ [A+04a]
e^+e^-	$(2.67^{+0.14}_{-0.16})$ %	
$\mu^+\mu^-$	(2.48 ± 0.06) %	(2.49 ± 0.09) %

$\Upsilon(2S)$

decay mode	$\mathcal{B}$ [E+04]	$\mathcal{B}$ [A+04a]
e^+e^-	$(1.18 \pm 0.20$ %	
$\mu^+\mu^-$	(1.31 ± 0.21) %	(2.03 ± 0.11) %

$\Upsilon(3S)$

decay mode	$\mathcal{B}$ [E+04]	$\mathcal{B}$ [A+04a]
e^+e^-	seen	
$\mu^+\mu^-$	(1.81 ± 0.17) %	(2.39 ± 0.17) %

Table 2.1: Selected $b\bar{b}$ particles and branching ratios.

State	$\psi(2S)$	$\chi_c(1P)$	$J/\psi(1S)$		
E_b (GeV)	0.05	0.23	0.64		
T_D/T_C	0.1-0.2	0.74	1.10		
State	$\Upsilon(3S)$	$\chi_b(2P)$	$\Upsilon(2S)$	$\chi_b(1P)$	$\Upsilon(1S)$
E_b (GeV)	0.2	0.3	0.54	0.67	1.1
T_D/T_C	0.75	0.83	1.10	1.13	2.31

Table 2.2: Binding energy and dissociation temperatures of the different quarkonia states [DPS01a].

2.2.1 Quarkonia Suppression and Feed-Down from Higher States

An aspect not considered so far is the feeddown between the different states. As can be seen from figure 2.3 the $\Upsilon(1S)$ contains contributions from essentially all other $b\bar{b}$ states. Its observed cross section will thus change if the cross section of one of the higher states changes. The dissociation of the $\Upsilon(3S)$ and the other states will therefore reduce the observed inclusive $\Upsilon(1S)$ cross section.

The inclusive cross section σ_{inc} of the bottomonium state H_i can be calculated as the sum of the directly cross section $\sigma_{\text{dir}}(H_i)$ and the feeddown from higher states

$$\sigma_{\text{inc}}(H_i) = \sigma_{\text{dir}}(H_i) + \sum_j \mathcal{B}\left(H_j \to H_i\right)\sigma_{\text{inc}}(H_j) \tag{2.13}$$

where $\sigma_{dir}(H_i)$ is the direct production cross section of the state H_i and $\mathcal{B}\left(H_j \to H_i\right)$ the branching ratio of the higher state H_j to H_i. The knowledge of the direct production cross sections of all states and the branching ratios would in turn allow to calculate the expected suppresion pattern.

Experimentally observable are of course only the inclusive cross sections. The ratio between the inclusive cross section of the Υ states times the branching ratios into leptons has been measured by a variety of experiments, the results are listed in table 2.3. The approximate energy independence of theses ratios between $\sqrt{s_{NN}} =$ 38.8 GeV and 1800 GeV allows to use the same ratio also at RHIC energies. Since the branching fraction to muons is included in the ratios, they have to be correct to get the ratio of the inclusive cross sections

$$\frac{\sigma_{\text{inc}}(nS)}{\sigma_{\text{inc}}(1S)} = \mathcal{R}\left(\Upsilon(nS)/\Upsilon(1S)\right) \times \frac{\mathcal{B}\left(\Upsilon(1S) \to \mu^+\mu^-\right)}{\mathcal{B}\left(\Upsilon(nS) \to \mu^+\mu^-\right)} \tag{2.14}$$

resulting in $\sigma_{\text{inc}}(2S)/\sigma_{\text{inc}}(1S) = 0.51$ and $\sigma_{\text{inc}}(3S)/\sigma_{\text{inc}}(1S) = 0.18$, using the branching ratios from [E+04], $\mathcal{R}\left(\Upsilon(2S)/\Upsilon(1S)\right) = 0.27$ and $\mathcal{R}\left(\Upsilon(3S)/\Upsilon(1S)\right) = 0.13$.

The CDF collaboration has also measured the fraction of $\Upsilon(1S)$ from decays of $\chi_b(1P)$ and $\chi_b(2P)$

$$F\left(\chi_b(nP)\right) = \frac{\sum_{j=0,1,2} \mathcal{B}\left(\chi_{bj}(nP) \to \Upsilon(1S)\right)\sigma_{\text{inc}}\left(\chi_{bj}(nP)\right)}{\sigma_{\text{inc}}\left(\Upsilon(1S)\right)} \tag{2.15}$$

The measured values are $F\left(\chi_b(1P)\right) = 27.1 \pm 6.9 \pm 4.4$ and $F\left(\chi_b(2P)\right) = 10.5 \pm 4.4 \pm 1.4$ [A+00]. The individual $\chi_{bj}(1P)$ and $\chi_{bj}(2P)$ states could not be experimentally distinguished, the measured fraction is the sum of all nP states.

$\mathcal{R}\left(\Upsilon(2S)/\Upsilon(1S)\right)$	$\mathcal{R}\left(\Upsilon(3S)/\Upsilon(1S)\right)$	$\sqrt{s}$	reference
0.27 ± 0.03	0.14 ± 0.02	38.8 GeV	[M+91]
0.32 ± 0.03	0.13 ± 0.03	400 GeV	[U+79]
0.28 ± 0.03	0.15 ± 0.03	1800 GeV	[A+95]
0.25 ± 0.02	0.13 ± 0.02	1800 GeV	[A+02a]

Table 2.3: Production ratios of the different Upsilon state measured in hadron+hadron collisions.

	$\Upsilon(3S)$	$\chi_{b2}(2P)$	$\chi_{b1}(2P)$	$\chi_{b0}(2P)$	$\Upsilon(2S)$
$\Upsilon(3S)$	1	11.4 ± 0.8	11.3 ± 0.6	5.4 ± 0.6	10.6 ± 0.8
$\chi_{b2}(2P)$		1			16.2 ± 2.4
$\chi_{b1}(2P)$			1		21 ± 4
$\chi_{b0}(2P)$				1	4.6 ± 2.1
$\Upsilon(2S)$					1

	$\chi_{b2}(1P)$	$\chi_{b1}(1P)$	$\chi_{b0}(1P)$	$\Upsilon(1S)$	
$\Upsilon(3S)$	0.6 ± 0.1	0.6 ± 0.1	0.4 ± 0.1	11.2 ± 0.5	
$\chi_{b2}(2P)$	1.1 ± 0.2	1.1 ± 0.2	0.7 ± 0.2	12.1 ± 1.3	
$\chi_{b1}(2P)$	1.4 ± 0.3	1.4 ± 0.3	0.9 ± 0.3	15.0 ± 1.8	
$\chi_{b0}(2P)$	0.3 ± 0.1	0.3 ± 0.1	0.2 ± 0.1	2.3 ± 0.9	
$\Upsilon(2S)$	6.6 ± 0.9	6.7 ± 0.9	4.3 ± 1.0	31.1 ± 1.6	
$\chi_{b2}(1P)$	1			22 ± 4	
$\chi_{b1}(1P)$		1		35 ± 8	
$\chi_{b0}(1P)$			1	< 6	
$\Upsilon(1S)$				1	

Table 2.4: Branching fractions (in %) between the different bottomonium states [BFL01].

	$\sigma_{\text{inc}}(H)$	σ_{dir}
$\Upsilon(3S)$	0.18	0.18
$\chi_b(2P)$	0.95	0.93
$\Upsilon(2S)$	0.51	0.35
$\chi_b(1P)$	1.17	1.03
$\Upsilon(1S)$	1	0.45

Table 2.5: Direct and inclusive cross sections of the bottomonium states, relative to the inclusive cross section of the $\Upsilon(1S)$ state.

To calculate the direct cross sections for all states more information, especially on the branching ratios between the different states, is needed. In the absence of experimental measurements input from theoretical models has to be used, table 2.4 lists the branching ratios between the different states with an NRQCD analysis [BFL01].

The same model [BFL01] also gives the ratio between the different $\chi_{bj}(nP)$ states, allowing to calculate an effective branching ratio to compare with the fractions measured by CDF. The ratios of the inclusive cross sections are $\chi_{b0}(1P) : \chi_{b1}(1P) : \chi_{b2}(1P) = 1 : 1.8 : 2.5$ and $\chi_{b0}(2P) : \chi_{b1}(2P) : \chi_{b2}(2P) = 1 : 1.2 : 2.2$, however with large errors. Using these ratios, one can calculate the effective branching ratios $\mathcal{B}\left(\chi_b(1P) \rightarrow \Upsilon(1S)\right) = 23\%$ and $\mathcal{B}\left(\chi_b(2P) \rightarrow \Upsilon(1S)\right) = 11\%$. Using these branching ratios one can calculate the inclusive cross section for $\chi_b(nP)$ states from the CDF measurement as $\sigma_{\text{inc}}\chi_b(1P) = 1.17\sigma_{\text{inc}}(\Upsilon(1S))$ and $\sigma_{\text{inc}}\chi_b(2P) = 0.95\sigma_{\text{inc}}(\Upsilon(1S))$.

The combined information is sufficient to calculate the direct production cross sections relative to the $\Upsilon(1S)$ cross section under the assumption that all $\Upsilon(3S)$ are directly produced, i.e. $\sigma_{\text{inc}}(\Upsilon(3S)) = \sigma_{\text{dir}}(\Upsilon(3S))$. The calculated direct and inclusive cross sections relative to $\sigma_{\text{inc}}(\Upsilon(1S))$ are listed in table 2.5.

The expected suppression pattern for the Υ states can now be calculated, assuming complete dissociation at the temperatures listed in table 2.2. Figure 2.4 shows the results for all Υ states. As will be shown later, it is experimentally not possible to distinguish the different states at RHIC with the present STAR detector. The expected suppresion pattern for the sum of all Υ states is therefore also shown in figure 2.4, where the dashed line shows the experimentally observable fraction including the different branching ratios to electrons.

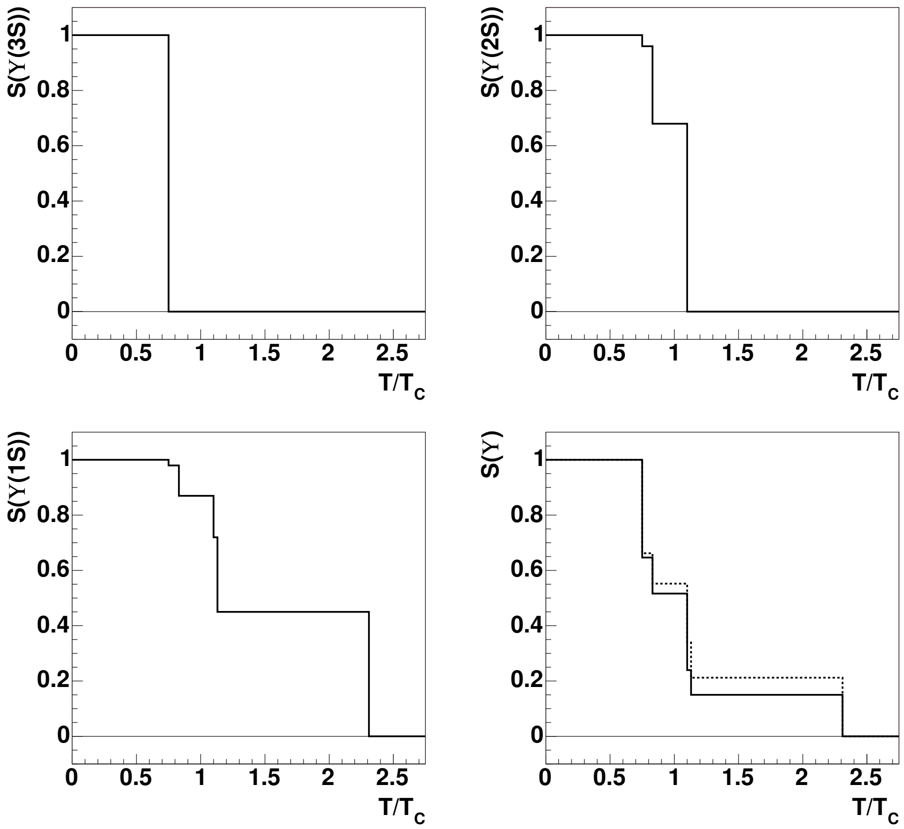

Figure 2.4: Expected suppression pattern for the $\Upsilon(3S)$ (upper left), $\Upsilon(2S)$ (upper right), $\Upsilon(1S)$ (lower left) and the sum of all Υ states (lower right) using the dissociation temperatures from [DPS01a]. The dashed line in the lower right plot includes the branching ratios to di-leptons.

2.3 Upsilon Production Cross-Section at RHIC Energies

A crucial input for all quarkonia models is the Υ production cross section in elementary collisions. No data at the RHIC energy of $\sqrt{s_{NN}} = 200$ GeV exist so far. The expected cross section has thus to be approximated by using either theoretical calculations or an extrapolation from data taken at different energies.

A compilation of the existing measurements is shown in table 2.6. Most of the data was obtained at the CERN ISR $p+p$ collider and at the Fermilab fixed target p beam. Results at higher collision energies are available from the CERN S$p\overline{p}$S collider and the Fermilab $p\overline{p}$ collider. A linear dependence on the target mass number was assumed for $p+A$ experiments, i.e. $\alpha = 1$ in equation 2.6. Most of the experiments were not able to resolve the different Υ states due to their limited resolution and thus only the cross section for all Υ states is given:

$$\mathcal{B}\frac{\mathrm{d}\sigma_\Upsilon}{\mathrm{d}y} = \mathcal{B}_{\Upsilon(1S)}\frac{\mathrm{d}\sigma_{\Upsilon(1S)}}{\mathrm{d}y} + \mathcal{B}_{\Upsilon(2S)}\frac{\mathrm{d}\sigma_{\Upsilon(2S)}}{\mathrm{d}y} + \mathcal{B}_{\Upsilon(3S)}\frac{\mathrm{d}\sigma_{\Upsilon(3S)}}{\mathrm{d}y} \tag{2.16}$$

The $\sqrt{s_{NN}}$ dependence of $\mathcal{B}\frac{\mathrm{d}\sigma_\Upsilon}{\mathrm{d}y}$ is shown in figure 2.5. The low energy data was fitted to the function

$$\mathcal{B}\frac{\mathrm{d}\sigma_\Upsilon}{\mathrm{d}y}\,|_{y=0} = C exp\left(-14.7m/\sqrt{s_{NN}}\right) \tag{2.17}$$

which was first used by Craigie to describe the low energy J/ψ data. The parameters obtained in the fit were $C = 120$ pb and $m = 10 \pm 0.5$ GeV, close to the expected mass for a combination of all Υ states. The parametrization obviously misses the high energy data. The expected cross section at $\sqrt{s_{NN}} = 200$ GeV is $\mathcal{B}\mathrm{d}\sigma_y/\mathrm{d}y\,|_{y=0} = 58$ pb. A NLQ Color Evaporation Model calculation [Vog99] describes the data, both at low energy where the dominant production process is $q+\overline{q} \rightarrow \left(Q\overline{Q}\right)$ and at higher energies where $g+g \rightarrow \left(Q\overline{Q}\right)$ becomes dominant. The calculated cross section at $\sqrt{s_{NN}} = 200$ GeV is $\mathcal{B}\mathrm{d}\sigma_y/\mathrm{d}y\,|_{y=0} = 86$ pb. The results from the parametrization and from the NLO QCD calculation will be used as lower respectively upper bound of the expected Υ cross section at RHIC as indicated by the shaded area in figure 2.5.

The expected cross sections for the individual Υ states can be calculated from equation 2.16 since the observed production ratios

$$\mathcal{R}\left(\Upsilon(2S)/\Upsilon(1S)\right) \equiv \left(\mathcal{B}\mathrm{d}\sigma_{\Upsilon(2S)}/\mathrm{d}y\,|_{y=0}\right) / \left(\mathcal{B}\mathrm{d}\sigma_{\Upsilon(1S)}/\mathrm{d}y\,|_{y=0}\right)$$

and

$$\mathcal{R}\left(\Upsilon(3S)/\Upsilon(1S)\right) \equiv \left(\mathcal{B}\mathrm{d}\sigma_{\Upsilon(3S)}/\mathrm{d}y\,|_{y=0}\right) / \left(\mathcal{B}\mathrm{d}\sigma_{\Upsilon(1S)}/\mathrm{d}y\,|_{y=0}\right)$$

are approximately energy independent as shown in table 2.3 which summarizes the available measurements. Using $\mathcal{R}\left(\Upsilon(2S)/\Upsilon(1S)\right) = 0.27$ and $\mathcal{R}\left(\Upsilon(3S)/\Upsilon(1S)\right) = 0.13$ equation 2.16 becomes

$$\begin{aligned}\mathcal{B}\tfrac{\mathrm{d}\sigma_\Upsilon}{\mathrm{d}y}\,|_{y=0} = \;& \mathcal{B}_{\Upsilon(1S)}\frac{\mathrm{d}\sigma_{\Upsilon(1S)}}{\mathrm{d}y}\,|_{y=0} + \\ & +\mathcal{R}\left(\Upsilon(2S)/\Upsilon(1S)\right)\mathcal{B}_{\Upsilon(1S)}\frac{\mathrm{d}\sigma_{\Upsilon(1S)}}{\mathrm{d}y}\,|_{y=0} \\ & +\mathcal{R}\left(\Upsilon(3S)/\Upsilon(1S)\right)\mathcal{B}_{\Upsilon(1S)}\frac{\mathrm{d}\sigma_{\Upsilon(1S)}}{\mathrm{d}y}\,|_{y=0}\end{aligned} \tag{2.18}$$

Target	$\sqrt{s_{NN}}$ (GeV)	$\mathcal{B}\mathrm{d}\sigma_\Upsilon/\mathrm{d}y\,\|_{y=0}$ (pb/N)	ref.
Pt	19.4	0.038 ± 0.032	[B+79]
A	23.7	0.14 ± 0.03	[Y+78]
A	27.3	0.42 ± 0.13	[Y+78]
Pt	27.4	0.44 ± 0.06	[U+79]
Fe	27.4	0.48 ± 0.06	[C+85]
Be	38.7	2.3 ± 0.4	[Y+89]
Cu	38.8	2.21 ± 0.14	[M+91]
p	44	6 ± 3	[Cam79]
p	53	13.5 ± 7.4	[K+80]
p	62	10 ± 4	[Cam79]
p	62.4	9 ± 2.2	[A+79]
p	63	15.2 ± 5.5	[Cam79]
$\bar{\mathrm{p}}$	630	290^{+57}_{-114}	[A+87]
$\bar{\mathrm{p}}$	1800	1037 ± 189	[A+95]
$\bar{\mathrm{p}}$			[A+02a]

Table 2.6: $\Upsilon(1S) + \Upsilon(2S) + \Upsilon(3S)$ cross sections in p+A collisions [G+95, Vog99].

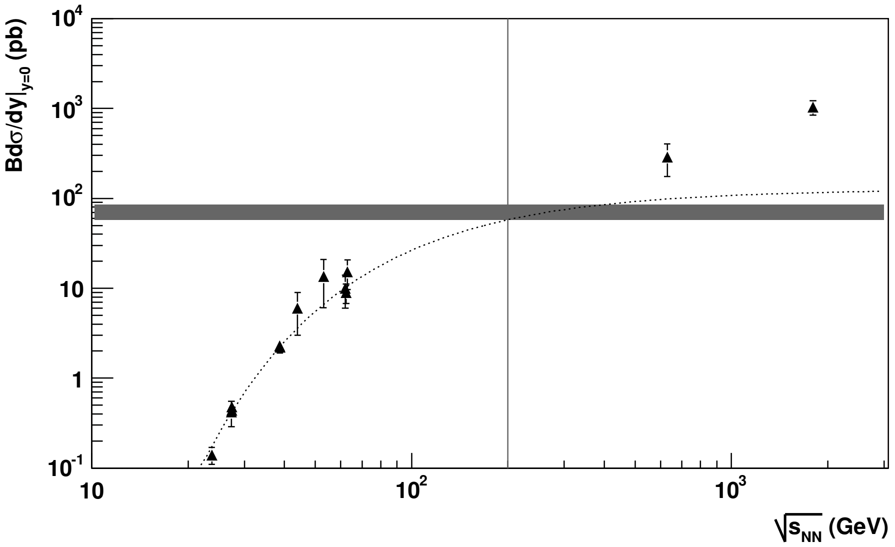

Figure 2.5: Energy dependence of the $\Upsilon(1S) + \Upsilon(2S) + \Upsilon(3S)$ cross section at midrapidity (decaying into $\mu^+\mu^-$) [Vog99]. The vertical gray line shows the RHIC energy $\sqrt{s_{NN}} = 200$ GeV, the gray box the range of expected production cross sections at this energy. The dashed line shows the predictions of the Craigie parametrization [Cra78], fitted to the low energy data.

resulting in $\mathcal{B}\frac{d\sigma_{\Upsilon(1S)}}{dy}\ |_{y=0}= 41(61)$ pb for the total cross section calculated by the Cragie parametrization (NLO QCD calculation). The same branching ratio for all Υ states to electrons was assumed, following the latest results from CLEO for the branching ratio into muons shown in table 2.1. Using the PDG values for the branching ratios results in slightly different results. The expected production cross sections from the different assumptions are summarized in table 2.7.

	$\mathcal{B}\frac{d\sigma_{\Upsilon}}{dy}$	$\mathcal{B}_{\Upsilon(1S)}\frac{d\sigma_{\Upsilon(1S)}}{dy}$	$\mathcal{B}_{\Upsilon(2S)}\frac{d\sigma_{\Upsilon(2S)}}{dy}$	$\mathcal{B}_{\Upsilon(3S)}\frac{d\sigma_{\Upsilon(3S)}}{dy}$
Cragie	58 pb	41 pb	11 pb	5 pb
CEM	86 pb	61 pb	16 pb	8 pb

Table 2.7: Expected Υ cross section at midrapidity in $p+p$ collisions at $\sqrt{s_{NN}} = 200$ GeV.

2.3.1 Scaling to (AB) Collisions

Having calculated the Υ cross section in $p+p$ collisions, it is now possible to estimate the expected cross section in heavy ion collisions. As mentioned in the introduction to this chapter, hard processes like Υ production are expected to scale with the number of binary collisions, i.e. for minimum bias $A + B$ collisions the expected cross section is $\sigma_{(A+B)} = \sigma_{(p+p)}\,(AB)$.

This equation assumes that the production is not modified by any nuclear effects, including the absorption in cold nuclear matter discussed in section 2.1.3. However from the underlying physics nuclear absoption is certainly expected to be present and equation 2.6 has to be used

$$\sigma_{(A+B)} = \sigma_{(p+p)}\,(AB)^{\alpha}$$

with the phenomenological factor α describing the absorption strength.

The so far only available measurement of Υ production in cold nuclear matter was made by the Fermilab E772 experiment in collisions of protons with ^{2}H, C, Ca, Fe and W ions at $\sqrt{s_{NN}} = 38.8$ GeV. Figure 2.6 shows the ratio of the yield per nucleon A for $\Upsilon(1S)$ and the sum $\Upsilon(2S) + \Upsilon(3S)$, together with the expectations for $\alpha = 0.92$, 0.96 and 0.97. The values extracted from a fit to the data are $\alpha = 0.962 \pm 0.006$ the $\Upsilon(1S)$ and $\alpha = 0.948 \pm 0.012$ for the $\Upsilon(2S) + \Upsilon(3S)$ data [A$^+$91].

The E772 experiment has also measured the transverse momentum p_T (figure 2.7) and x_F (figure 2.8) dependence of the phenomenological factor α. The transverse momentum dependence is weak below 2.5 GeV with values of α between 0.92 and 1. At higher p_T a strong increase is observed with ratios larger than 1, i.e. more $\Upsilon(1S)$ are produced in nuclear collisions than expected from binary scaling. The dependence of the α values on x_F (or rapidity) is weak in the the forward hemisphere where again α is between 0.92 and 1. In the backward hemisphere a strong decrease to $\alpha \approx 0.85$ is observed, however with quite large errors.

From the E772 measurements it seems reasonable to assume a common factor $\alpha = 0.96$ to describe the available data on Upsilon absorption at $\sqrt{s_{NN}} = 38.8$ GeV, independent of transverse momentum or rapidity. The huge increase at high transverse momentum as well as the strong decrease in the backward hemisphere are neglected.

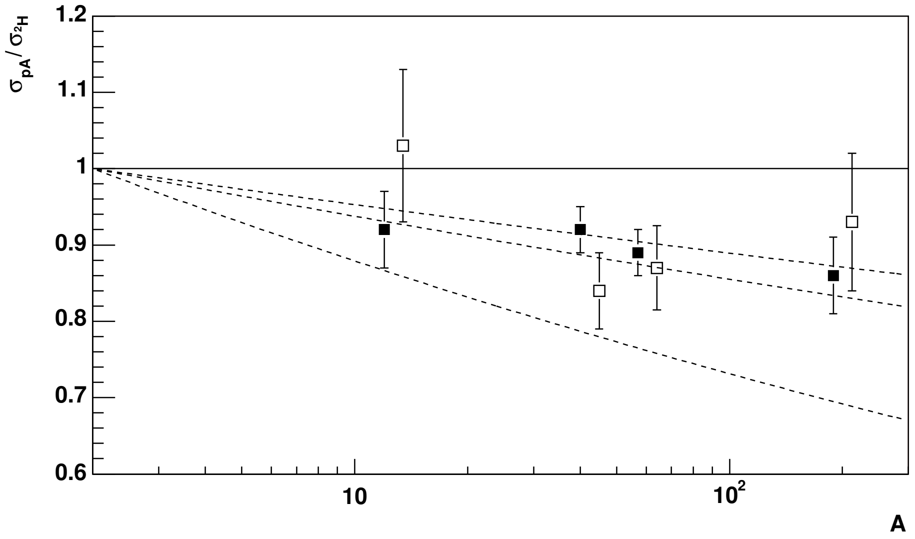

Figure 2.6: Ratio of the $\Upsilon(1S)$ (solid symbols) and $\Upsilon(2S) + \Upsilon(3S)$ (open symbols) yield per nucleon A in p+A collisions to the one in p+^{2}H collisions. The dashed lines show the expected nuclear absorption dependence $\sigma_{pA} = \sigma_{p+p}A^{\alpha}$ for $\alpha = 0.92$, 0.96 and 0.97 [A+91].

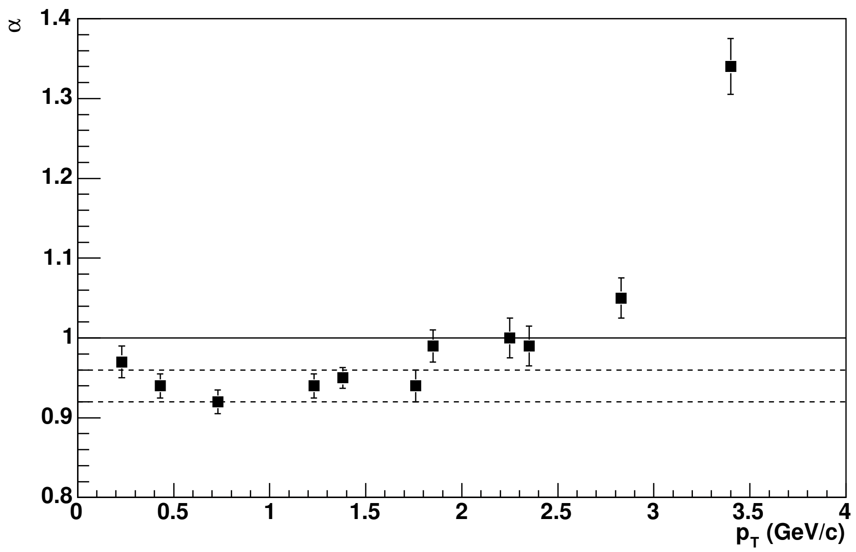

Figure 2.7: Transverse momentum dependence of the fitted factor α [A+91].

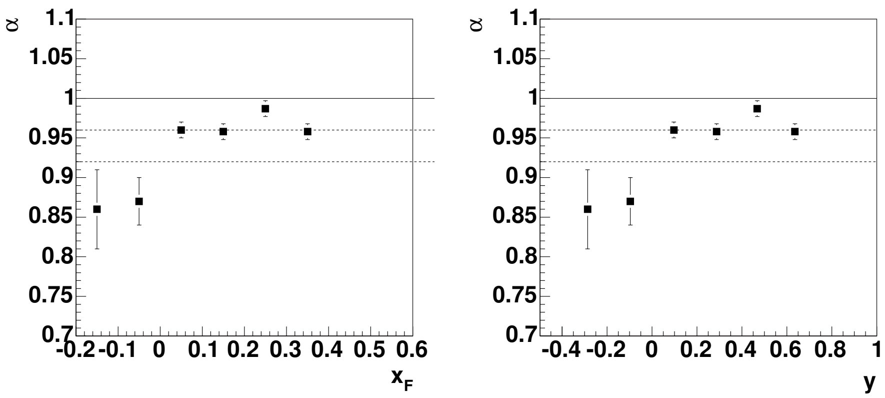

Figure 2.8: Feynman x_F (left) and rapidity y (right) dependence of the fitted factor α [A+91].

It remains to extrapolate the absorption cross section from $\sqrt{s_{NN}} = 38.8$ GeV to $\sqrt{s_{NN}} = 200$ GeV for the application at RHIC. The energy dependence was already discussed in section 2.1.3. No clear picture emerged, depending on the theoretical calculation both an increasing absorption cross section as well as a decreasing one were expected. The data on J/ψ production at SPS and RHIC prefers a decreasing energy dependence, with the absorption cross section at RHIC nearly a factor 2 smaller than the one at SPS. In spite of this no energy dependence of α is assumed, i.e. $\alpha = 0.96$ is used for the further extrapolations.

When extrapolating in energy and making comparisons with the J/ψ one has to be cautious because different x ranges in the nucleus are probed. The x range probed by Υ production at RHIC can be calculated for the leading order production process $gg \to Q\overline{Q}$ as

$$m_{\Upsilon}^2 = \hat{s} = x_1 x_2 s \tag{2.19}$$

where x stands for the momentum fraction carried by the incident gluon. To ratio x_1/x_2 determines the Υ rapidity as

$$y = \frac{1}{2} \ln \left(\frac{x_1}{x_2} \right) \tag{2.20}$$

As will be shown later in section 4.2.1 STAR will be mainly sensitive to Upsilons produced in the interval $-1 \leq y \leq 1$. Combing both equations, the x range probed will be $\sim 5 \cdot 10^{-2}$ for midrapidity Upsilons and $10^{-2} < x < 10^{-1}$ for $y = 1$ Upsilons while the values probed by the J/ψ will be significantly smaller. This might become important because modifications of the parton distribution function (PDF) in nuclei compared to the ones in protons are expected. The EKS98 parametrization [EKS99] predicts a small anti-shadowing of the gluon PDF in the x and Q^2 region of interest.

To finally calculate the expected cross section in $Au + Au$ collisions at RHIC the following case are considered based on the discussion above: no nuclear effects ($\alpha = 1$), absorption as measured by E772 ($\alpha = 0.96$) and $\alpha = 0.92$ as a reasonable lower bound. The calculated cross sections, based on table 2.7 and equation 2.6, are given in table 2.8.

$\frac{d\sigma_{(p+p)}(\Upsilon)}{dy}\|_{y=0}$		$\frac{d\sigma_{(Au+Au)}(\Upsilon)}{dy}\|_{y=0}$		
		$\alpha = 0.92$	$\alpha = 0.96$	$\alpha = 1$
Craigie	58 pb	1.0 μb	1.5 μb	2.2 μb
CEM	86 pb	1.4 μb	2.2 μb	3.3 μb

Table 2.8: Expected Υ cross section in $Au + Au$ collisions at RHIC (summed over all Upsilon states).

3 The STAR Detector at RHIC

The cross section for heavy flavor production depends strongly on the collision energy as described in the previous chapter. The Relativistic Heavy Ion Collider (RHIC) [HLO03] at the Brookhaven National Laboratory (BNL) on Long Island, New York, currently provides the highest collision energy. The achieved energy of $\sqrt{s_{NN}} = 200$ GeV allows for the first time in heavy ion collisions the production of multiple charm quarks in each collision and a first look at bottom quark production. In addition to the heavy ion program, RHIC provides the unique capability to accelerate polarized protons.

Four different detectors were build at RHIC to provide complementary measurements [Lud03], two large ones, called STAR and PHENIX and two small ones (BRAHMS and PHOBOS). The STAR (Solenoid Tracker At RHIC) detector provides identification of hadrons and leptons over large phasespace regions and is therefore ideally suited to measure the different heavy flavor particles. The relevant detector subsystems for these measurements are described in section 3.2.

3.1 The Relativistic Heavy Ion Collider

The design of the Relativistic Heavy Ion Collider (RHIC) [H$^+$03] started in 1987, its construction in 1990 and first collisions were achieved in 1999. The Brookhaven National Laboratory was chosen as construction site due to the existence of the necessary civil structures from the earlier ISABELLE/CBA project and lower energy accelerators as injectors. Figure 3.1 shows a schematic view of the accelerator complex.

RHIC consists of two quasi-circular concentric accelerator/storage rings with 3.8 km circumference, the "blue" ring for clockwise and the "yellow" ring for counter-clockwise beams. The beams are brought to head-on-head collisions at six interaction regions around which the detectors were build. Both rings are formed by various superconducting magnets, cooled to 4.3K with liquid helium.

The acceleration scenario for heavy ions (i.e. Au A=197,Z=79) is shown in figure 3.2. The initial acceleration begins in the Tandem Van de Graaff accelerator. The ions coming from the source with charge -1 are accelerated from ground to $+14$ MeV potential. Passing the stripping foil in the high-voltage terminal the then positive ions are accelerated again from $+14$ MeV to ground potential. After passing through an additional stripper foil, the then $+32$ charged gold ions with an energy of ≈ 1 MeV/u are transferred to the Booster synchrotron.

The Booster groups the Au ions into six bunches and accelerates them to 95 MeV/u. Leaving the Booster the ions pass another stripping foil which changes their charge to $+77$. The next step in the acceleration chain is the Alternate Gradient Synchrotron (AGS). Four Booster cycles fill the AGS which 24 bunches, which are then

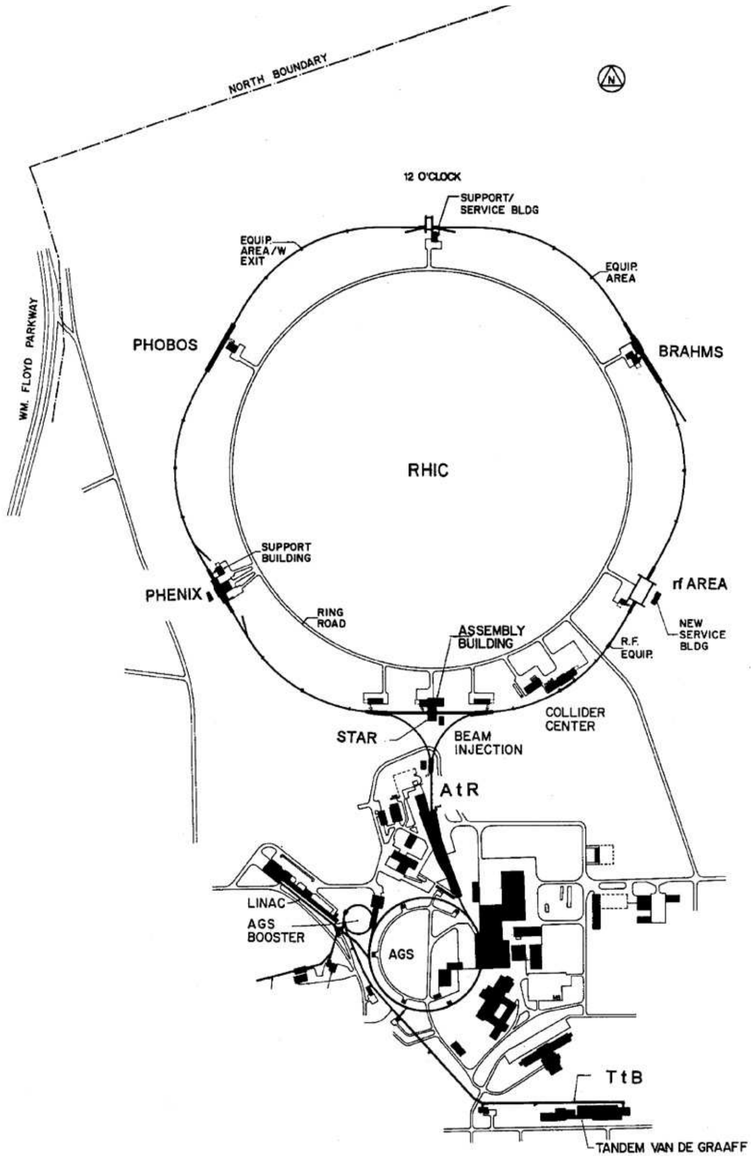

Figure 3.1: The RHIC accelerator complex [H$^+$03]

debunched and regrouped into four final bunches which are accelerated. Leaving the AGS, the gold ions have an energy of 8.86 GeV/u and get fully stripped to a charge of +79.

These ions are filled into the RHIC rings. A total of 14 AGS cycles is necessary to fill a ring with the nominal 56 bunches (plus four empty buckets as abort gap). The ions are then accelerated up to the top energy of 100 GeV/u and transferred to the storage RF system and brought to collisions at six interaction points.

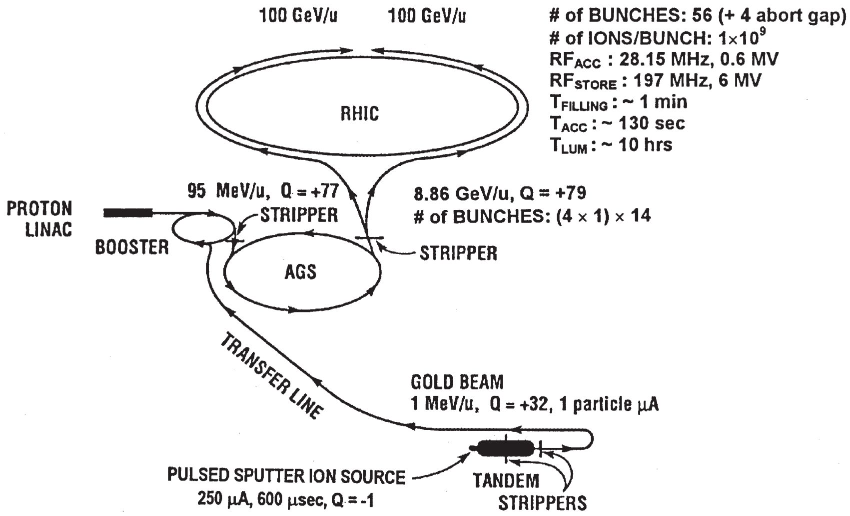

Figure 3.2: RHIC acceleration scenario for Au beams [H+03]

The other figure of merit beside the collision energy relevant for the experiments is the achieved luminosity which is defined as

$$\mathcal{L} = f\frac{n_1 n_2}{4\pi\sigma_x\sigma_y} \tag{3.1}$$

where f is the frequency of the collisions and n_i the number of particles in the colliding bunches. σ_x and σ_y characterize the Gaussian transverse beam profiles. Another way to define the luminosity is by expressing the beam size in terms of two quantities, the transversed emittance ϵ and the amplitude function β. Equation 3.1 becomes then

$$\mathcal{L} = f\frac{n_1 n_2}{4\sqrt{\epsilon_x\beta_x^*\epsilon_y\beta_y^*}} \tag{3.2}$$

where β^* is the value of the amplitude function reached at the interaction point. For a multibunch collider like RHIC and assuming common transverse emittance $\epsilon_N = \epsilon_x = \epsilon_y$ and amplitude values at the interaction point $\beta^* = \beta_1^* = \beta_2^*$, equation 3.2 becomes

$$\mathcal{L} = f\frac{Bn_B^2}{4\epsilon_N\beta^*} \tag{3.3}$$

with B the number of bunches and n_B the number of particles per bunch.

The achieved luminosity determines the event rate R at which interactions occur

$$R = \mathcal{L}\ \sigma_{int} \tag{3.4}$$

where σ_{int} is the interaction cross section. For Au ions colliding at RHIC, this cross section is ≈ 11 barn[1].

Following from equation 3.4 is that one can measure the luminosity by measuring the event rate. This is done at all RHIC interaction points with the help of the common Zero Degree Calorimeters (ZDC) [A+03f] or experiment specific counters, i.e. for STAR with the Beam Beam Counters (BBC) [LB+05]. Figure 3.3 shows the ZDC rate versus time for a typical day during the 2003/2004 Au+Au run for the four different experiments.

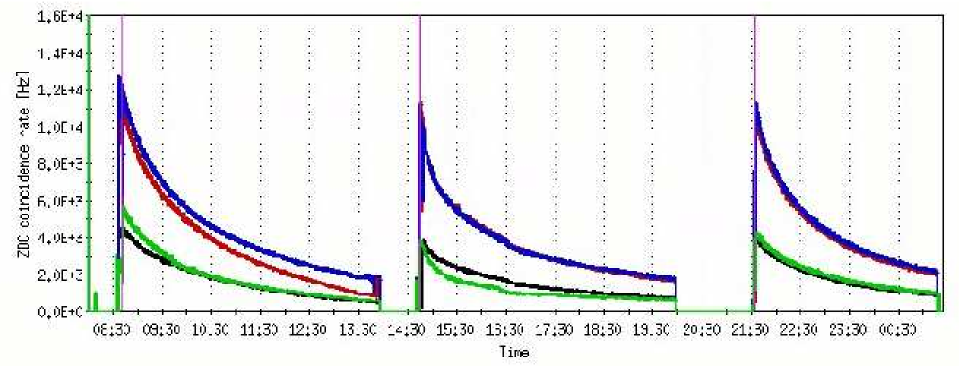

Figure 3.3: ZDC coincidence rate versus time for a typical day during the 2003/2004 Au+Au run. The coincidence rate at STAR is shown in red, the one at PHENIX in blue, PHOBOS in black and BRAHMS in green. Three runs of ~ 5 h are shown.

One can immediately distinguish two different classes in figure 3.3, STAR and PHENIX with high coincidence rates and BRAHMS and PHOBOS with lower ones. This is caused by limitations in the RHIC beam optic which allow a β^* of 1 m only at a few interaction regions while the others have $\beta^* = 3$ m. The slight difference between STAR and PHENIX is caused by the position of the empty abort gaps. In PHENIX the abort buckets "collide" with the abort buckets of the other ring while in STAR they "collide" with filled bunches. Since no collisions are happening in this case, the interaction rate in STAR is lower than the one in PHENIX. The same effect causes the difference between BRAHMS and PHOBOS.

Table 3.1 lists the main parameters achieved by RHIC during the 2003/2004 Au+Au run [Ros04]. Shown are the peak luminosity in PHENIX, the corresponding maximal interaction rate, the luminosity averaged over a typical three hour store and the luminosity delivered during a week[2].

$\mathcal{L}_{\max}$	12×10^{26}	$\mathrm{cm}^{-2}\ \mathrm{s}^{-1}$
$R_{\max}$	12	kHz
$\mathcal{L}_{\mathrm{avg}}$	4×10^{26}	$\mathrm{cm}^{-2}\ \mathrm{s}^{-1}$
$\mathcal{L}_{\mathrm{week}}$	160	$\mu\mathrm{barn}^{-1}\ \mathrm{week}^{-1}$

Table 3.1: RHIC performance during the 2003/2004 Au+Au run.

[1] Note that this is the total interaction cross section and not the hadronic cross section σ_{had} which is ≈ 6.9 barn [A+03c].

[2] We used the relation 1 barn $= 10^{-28}$ m^2 to get to a more common quantity to describe the accelerator performance for physics measurements.

3.2 The STAR Detector

The STAR (Solenoid Tracker At RHIC) detector is one of the two large detector systems at RHIC, located at the 6 o'clock position. Its design was chosen to achieve the goal of hadron measurements over a large rapidity region. It consists of several different detector (sub-)systems as shown in the cutaway side view in figure 3.4. A brief description of these subsystems will be given in the next paragraphs, followed by a more detailled description of the subsystems used for this thesis. More details on the other subdetectors can be found in [A$^+$03a] and the references therein.

The main subdetector is the Time Projection Chamber (TPC) providing charged particle tracking in the central rapidity region, installed inside a room temperature solenoidal magnet with a uniform field of 0.5 T and described in more detail in the next section 3.2.1. Its tracking capabilities are supplemented by the Silicon Vertex Tracker (SVT) and the Silicon Strip Detector (SSD) which allow charged particle tracking close to the interaction region. Additional charged particle identification will be provided by the planned Time of Flight (TOF) system of which prototypes were already installed. The Forward Time Projection Chambers (FTPC) allow charged particle tracking in more forward rapidity regions.

In addition to its tracking detectors, STAR has several electromagnetic calorimeters which provide photon and (additional) electron identification, allowing also the measurement of electromagnetically decaying hadrons. Both, the Barrel Electromagnetic Calorimeter (BEMC) and the Endcap Electromagnetic Calorimeter (EEMC), include Shower Maximum Detectors (SMD) providing a measurement of the shower profile in addition to the energy measurement of the calorimeter itself. A more detailled description of the BEMC can be found in section 3.2.2.

Both electromagnetic calorimeters provide also input signals into the STAR trigger system. The other detector which signals are used in the trigger system are the Central Trigger Barrel (CTB), a coarse array of scintillator counters providing a multiplicity measurement, the Zero Degree Calorimeter (ZDC), measuring the energy deposited by very forward neutrons, and the Beam Beam Counters (BBC). The trigger system itself consists of four levels, the first three (Level 0 to Level 2) using only the trigger detectors for fast decisions. The third trigger level performs an online reconstruction of the complete event including the TPC. The lower trigger levels and the Data Acquisition System (DAQ), responsible for detector readout and storage of the triggered events, are discussed in section 3.2.3, while the third level trigger system is discussed in section 3.2.4.

3.2.1 The Time Projection Chamber

A schematic view of the STAR Time Projection Chamber[3] (TPC) [A$^+$03j] is shown in figure 3.5. It consists of two halves, each 210 cm long, divided by the central high voltage membrane. The inner field cage at 50 cm radius and the outer field cage at 200 cm radius around the beam pipe define the tracking volume of the TPC. These dimensions correspond to a pseudorapidity coverage of $| \eta | \leq 1.8$ and $| \eta | \leq 1$ when one requires the track to leave the TPC through the outer field cage.

A uniform electric field is defined by the parallel disks of the central membrane, the readout end caps and the concentric field cage cylinders. The operation voltage

[3]For a detailled description of the TPC functionality see [BR93].

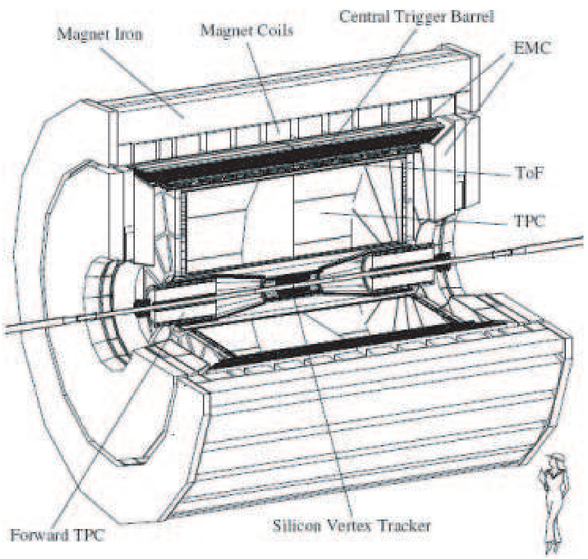

Figure 3.4: Cutaway side view of the STAR detector in its 2004 configuration.

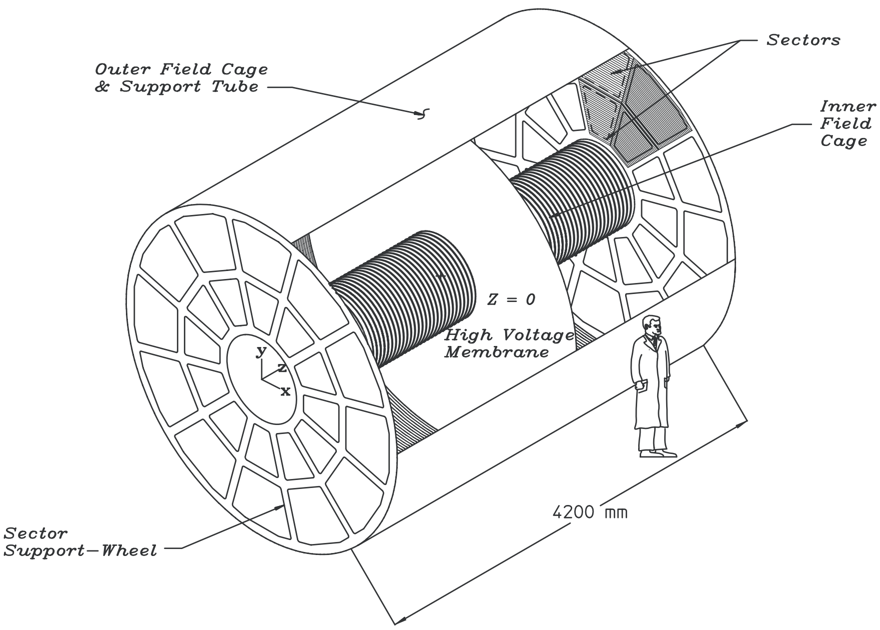

Figure 3.5: Schematic view of the STAR TPC.

of the central membrane is 28 kV while the endcaps are at ground, resulting in an electric field of $\approx$ 135 V/cm. The uniformity is guaranteed by the field cage cylinders, providing a series of 182 equi-potential, equally spaced rings. The rings are biased by resistor chains of 183 precision 2 MΩ resistors which provide a uniform gradient between the central membrane and the grounded readout end caps. During the 2003 pre-run testing a short between rings 169 and 170 on the east half was detected, resulting in a non-uniformity of the field. Since no repair was possible before RHIC startup, it was decided to introduce a similar short in the outer field cage as well to minimize the non-uniformity effects on the electric field. A correction for the different electric fields in the TPC halves was later applied in the offline reconstruction chain.

The TPC is filled with P10 gas, a mixture of 90% argon and 10% methane. The TPC gas system [K$^+$03] regulates the pressure to 2 mbar above athmospheric pressure. Figure 3.6 shows the dependence of the drift velocity in this gas mixture on the applied electric field. The electric field strength of 135 V/cm was choosen to allow operation on the peak of the velocity curve, making the drift velocity of $\approx$ 5.45 cm/μs stable and insensitive to small variations in temperature and pressure. Typical diffusion constants with this gas and a 0.5 T magnetic field are 230 μm/$\sqrt{\text{cm}}$ in transverse direction and 320 μm/$\sqrt{\text{cm}}$ in longitudinal (drift) direction.

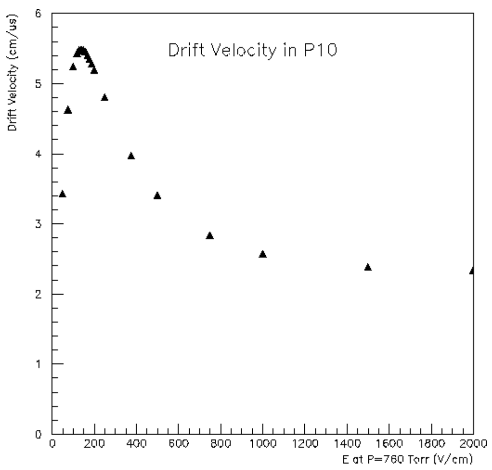

Figure 3.6: Drift velocity in P10 gas (90% Ar, 10% CH_4) as function of the electric field for a pressure of 760 Torr.

The TPC readout system in the end caps consists of MWPC[4] chambers with pad readout. The chambers have three wire planes: a gated grid, a ground plane and the anode wires. Both end caps are divided into 12 chambers (TPC sectors), the anode plane of one of these sectors is shown in figure 3.7.

Each TPC sector consists of two parts with different geometries. The design of the inner part with 13 padrows was optimized for good two-point resolution, while a good dE/dx resolution was the primary goal for the outer part with 32 padrows. The first padrow is $\approx$ 60 cm away from the center of the beam pipe. The total number of pads per sector is 5692, resulting in a total of 2 end caps $\times$ 12 sectors $\times$ 5962 pads $= 136,608$ pads.

[4]Multi Wire Proportional Chamber

The TPC readout system [A+03i] samples each pad 512 times with 10 bit precision for an event, with about 380 samples in the active drift time. Each TPC event has therefore a size of $136,608$ pads $\times$ 512 samples $\times$ 10 bits $\approx$ 83 MBytes before zero-suppression. The first part of the readout system are the front end electronic (FEE) cards with preamplifiers, shapers and analog to digital converters for 32 channels (pads). Up to 36 of the FEE cards are controlled and read out by the readout boards (RDO). The RDOs multiplex the digital signals from the FEE cards and send them to the data acquisition system.

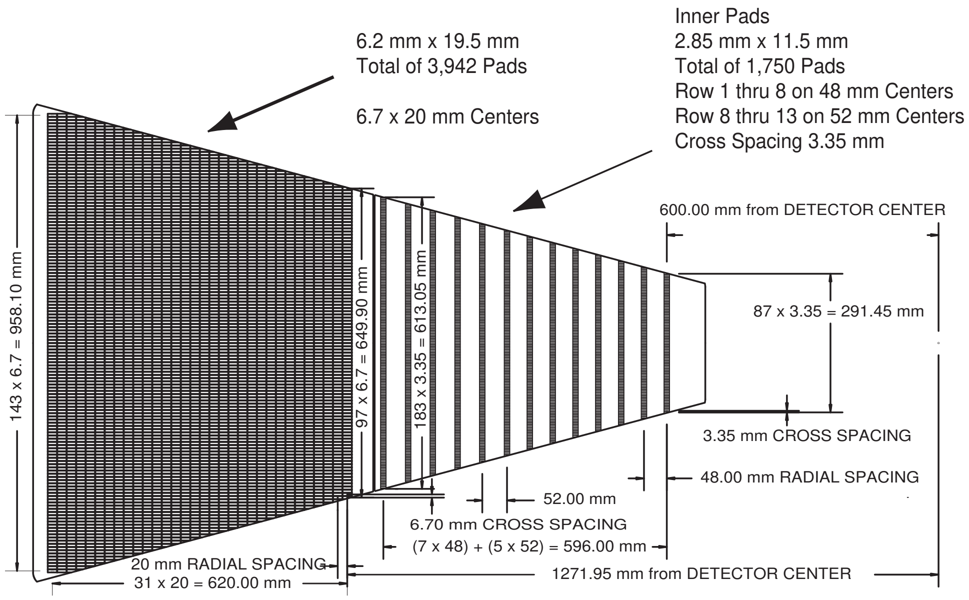

Figure 3.7: The anode pad plane of one full sector [A+03j].

3.2.2 The Barrel Electromagnetic Calorimeter

The Barrel Electromagnetic Calorimeter (BEMC) [B+03a] is located at a radius of ≈ 225 cm from the beam pipe next to the magnet coils. In its final configuration it will cover $| \eta | \leq 1$ and the full azimuth of 2π, matching the acceptance for full TPC tracking.

The BEMC is divided into two halves in pseudorapidity and 60 divisions in azimuth for each half, resulting in a total of 120 so-called modules. Each module covers therefore 1 unit in η and $6°$ in $\Delta\phi$. The modules themselves are segmented into 40 towers each, covering an area of 0.05 in $\Delta\phi$ ($3°$) times 0.05 in $\Delta\eta$, resulting in a total of 4800 towers for the complete calorimeter. The design choice of equal spacing in $\Delta\eta$ requires the towers to grow in Δz with increasing z. This projective nature in $\Delta\eta$ is illustrated in figure 3.8, which shows a schematic side view of a module.

The construction of the calorimeter was staged over ~ 4 years, with 60 modules (one half) installed for the 2002/2003 run, 72 modules mechanically installed for the 2003/2004 run and all modules installed during the 2004 shutdown. Due to failing high voltage supplies for the detector electronics not all of the installed modules could be used for data tacking. The available acceptance during the 2003/2004 run will be discussed in section 5.1.1.

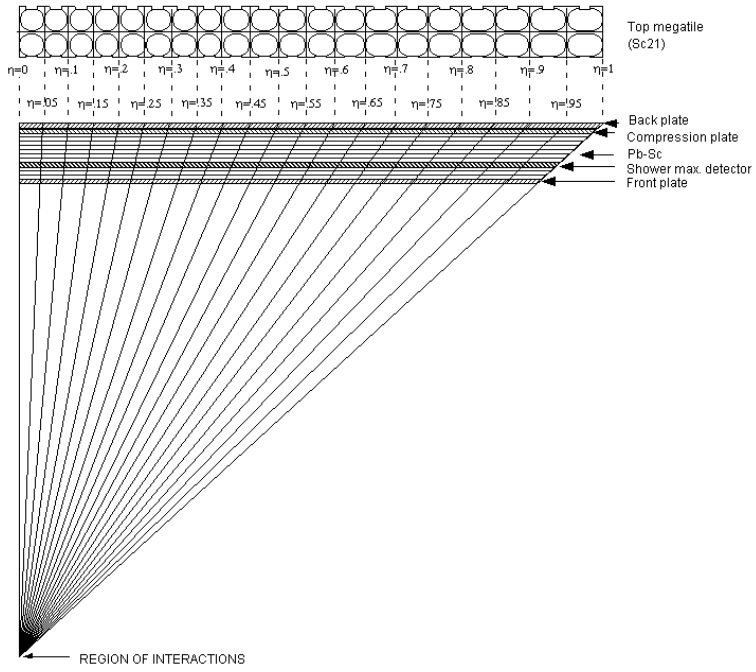

Figure 3.8: Schematic side view of a BEMC module [B+03a].

Figure 3.9 shows the mechanical structure of a BEMC module seen from the front. The sandwich structure of the calorimeter is easily seen, consisting of 21 active scintillating layers and 20 lead absorber plates. Between the 5th and 6th stack are two proportional wire chambers installed, the Barrel Shower Maximum Detectors (BSMD). The total depth of the calorimeter is approximately 20 radiation lengths ($20X_0$)[5] at midrapidity. Each scintillator layer is divided into 40 optically isolated 'tiles'. The 21 light signals of matching tiles (one tile per layer) are merged onto a single photomultiplier tube[6], compromising a single tower and providing a measurement of the energy deposited in the calorimeter.

The design of the readout electronics is driven by the requirement to provide trigger signals for the STAR trigger system at each RHIC bunch crossing, i.e. with a rate of 9.37 MHz. A schematic view of the readout system is shown in figure 3.10. One front end electronic (FEE) card digitizes the signals of four photomultipliers with 12 bit resolution. The FEE cards from 3 + 0.5 + 0.5 = 4 BEMC modules (160 towers) are mounted in the Tower Digitizer Crates (TDC). These crates provide measurements of the energy deposition in the towers to the L0 trigger electronics which will be discussed in section 3.2.3. The recorded data is pipelined until a L0 trigger decision is made. The data of accepted events is then sent to the Tower Data Collector over a serial link. The collector merges the contribution of all 30 BEMC tower crates and prepares the data for transfer to the data acquisition system.

In addition each of the first two scintillating layers is readout by a second fiber. While the signal of the first fiber goes into the sum of all layers discussed in the previous paragraph, resulting in the tower signal, the second fiber signal is merged

[5] The radiation length X_0 is the mean distance over which a high-energy electron loses all but 1/e of its energy by bremsstrahlung.
[6] A detailled description of optical readout structure can be found in section 4 of [B+03a].

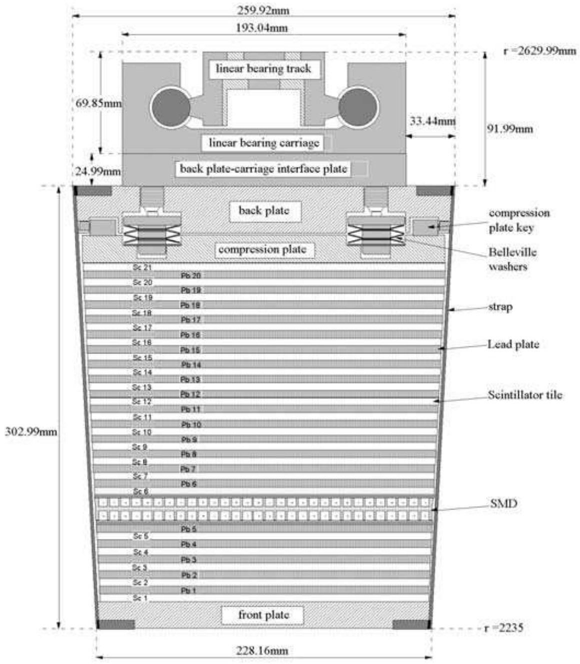

Figure 3.9: Front view of a BEMC module [B+03a].

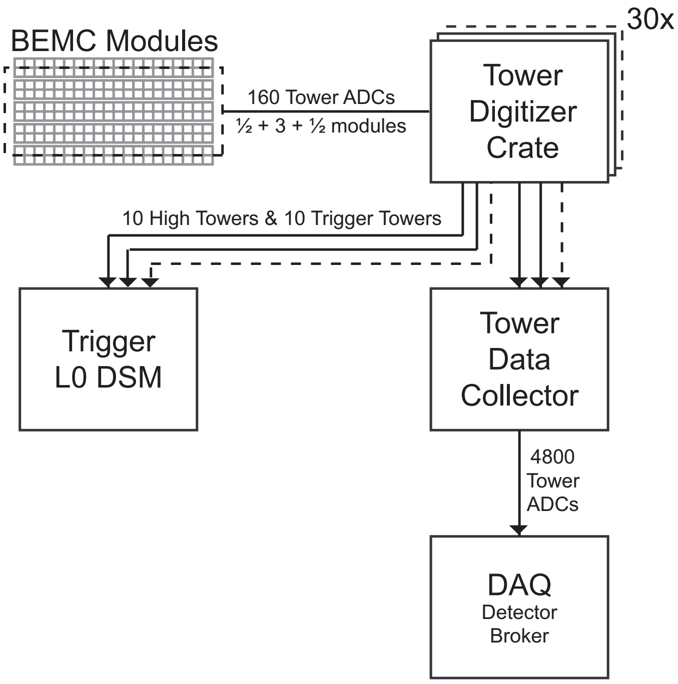

Figure 3.10: Schematic view of the BEMC readout electronics.

with the corresponding signal of the other layer and readout by an own photomultiplier. These 4800 signals of the first two layers compromise the Barrel Preshower Detector (BPRS), providing a measurement of the longitudinal shower development after $(1-1.5)\,X_0$. Since the light delivered by each fiber was found to be reduced by 20% compared to a single fiber, the thickness of the first two scintillating layers was increased to 6 mm from the 5 mm of the other 19 ones.

The Barrel Shower Maximum Detector (BSMD) between the 5^{th} and 6^{th} stack was already mentioned. It provides a measurement of the shower profile in the $\eta-\phi$ plane. It consists of two independent detectors, one measures the shower profile in the η direction and one measures the profile in the ϕ direction. Both are proportional wire chambers with strip readout. A schematic view of the BSMD is shown in figure 3.11.

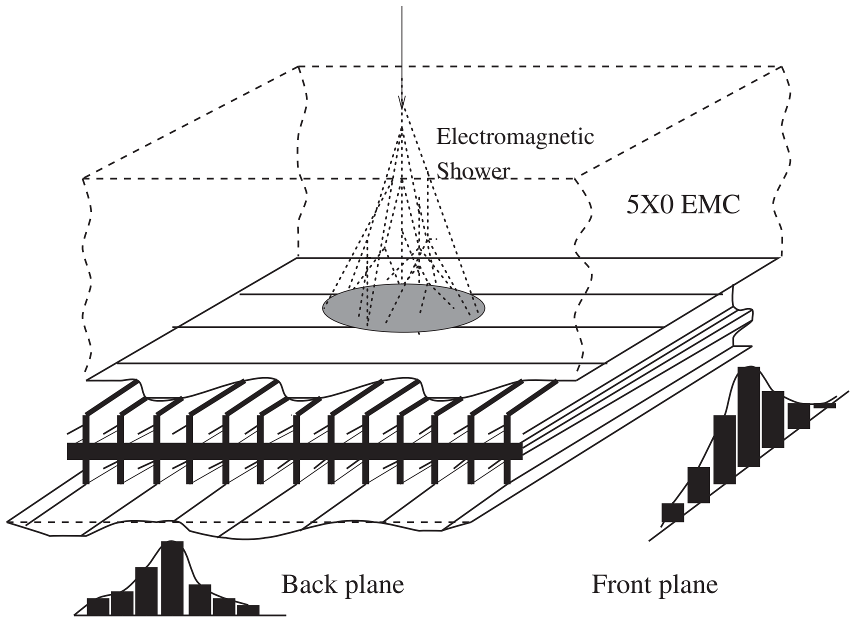

Figure 3.11: Schematic view of the Barrel Shower Max Detector.

Both wire chambers share a common support structure, an aluminum extrusion which is on ground potential. A total of 30 wires per module run along the η direction. The signal is read out via the induced charge on the strips. The strips on the front layer measure the shower profile in the η direction. They span the whole module in ϕ ($\Delta\phi = 0.1$) and have a width of 0.0064 in η, resulting in a total of 150 channels per module. The shower profile in the ϕ direction is measured by the strips on the back layer. These strips have a length of 0.1 in η and a width of $\Delta\phi = 0.006$, again for a total of 150 channels per module. The total number of channels from the BSMD for the complete calorimeter (i.e. 120 modules) will therefore be 36,000. During the 2003/2004 run the 18,000 channels from the 60 instrumented modules (one half) were used.

3.2.3 The Trigger and Data Acquisition System

The STAR trigger system [C+03b] determines whether to start the amplification-digitization and data acquisition process of the slow detectors, i.e. TPC and SVT. Both can operate at a maximum rate of ~ 100 Hz due to limitations in the readout electronics and data acquisition while the typical bunch crossing rate is 9.37 MHz, a factor 10^5 higher. The decision when to start the readout cycle is based on the fully pipelined data of the fast or trigger detectors. The Central Trigger Barrel (CTB), the Zero Degree Calorimeters (ZDC), the Beam Beam Counters (BBC) and the tower data from the electromagnetic calorimeters (BEMC,EEMC,FPD) belong to this group. In addition the slow detector status is used, e.g. the TPC signals that it is ready for a new event (live).

The trigger itself is divided into four successive trigger levels (L0-L3). The last trigger level L3 differs from the lower ones by the fact that it can also use data of the slow detectors and issues a decision only after the readout cycle is finished. It will be discussed in more detail in section 3.2.4, while we focus here only on the lower trigger levels.

L0 consists of four types of custom designed VME boards: the Data Storage and Manipulation boards (DSM), the Trigger Control Unit (TCU), the Trigger Clock Distribution (TCD) and the RHIC Clock and control boards (RCC). Data analysis in L0 uses a tree of DSM boards. Each one receives new input data at each bunch crossing, performs a simple calculation and passes the data to the next level of DSM boards in the tree in time for the next bunch crossing. It narrows to the output of one DSM board which is sent to the TCU. The TCU then combines the DSM tree output and the live/busy status bits from the slow detectors and maps them to a 16-bit Trigger Word using a look-up table, allowing different combinations of the input data which all result in an accepted event.

The Trigger Word itself is used as input for the prescale system and the Action Word look-up table, which is loaded with a list of detectors which should be triggered for this Trigger Word. This design allows to read out events with fast detector data only while the slow detectors are still busy with a previous events, thus increasing the statistics for analyzes which do not need the slow detector data. The pre-scale system plays an important role in sharing the available lifetime of the slow detectors between the different triggers. It allows to select only a pre-determined fraction of the each trigger type. At the start of each run this fraction is determined using the (time-in-store-depended, un-prescaled) L0 rate of each Trigger Word and the desired output rate, thus guaranteeing a minimum slow detector lifetime for the other triggers.

After passing the pre-scale system a trigger is issued. It is labelled with a 12-bit token which stays with it until the event is completely processed by the DAQ system or aborted by a higher trigger level. The Trigger and Action Word as well as the token are passed on to the TCDs for distribution to the detector subsystems. The TCD boards from the interface between the trigger system and the detector electronics. Once a L0 trigger arrives, the amplification, digitization and read-out process is started.

The DSM tree used during the 2004/2005 run is shown in figure 3.12. Four levels of DSMs are visible in the tree, they can be roughly grouped into four subtrees as can be seen on the third DSM level: data on the event multiplicity, the vertex position and the energy deposition in the electromagnetic calorimeters, divided into two subtrees, one for the BEMC and EEMC data, the other one for the FPD data.

The input to the multiplicity subtree comes from the Central Trigger Barrel (CTB), consisting of 240 scintillator slats arranged in four cylindrical bands, each covering half a unit of pseudo-rapidity η. The light in each scintillator slat is proportional to the number of particles hitting it and thus provides a multiplicity measurement. The output of the PMTs attached to each slat is digitized and the 8-bit output is sent to the first level of DSMs.

Information on the event vertex position, i.e. the position where the primary collision occurred, is provided by two detectors, the Zero Degree Calorimeters (ZDC) and the Beam-Beam-Counters (BBC). In addition both detectors provide a further multiplicity measurement. The two ZDCs are small transverse area hadron calorimeters located behind the first bending magnets in the collider line. Each consists of three modules comprised of tungsten plates alternating with layers of wavelength shifting fibers that route Cherenkov light to PMTs. The measured energy in the ZDCs is proportional to the number of spectator neutrons in nuclear collisions and thus determines the collision centrality. In addition the time difference between the two ZDC measures the vertex position with a centrality dependent resolution of ≤ 15 cm [Dun04]. The BBCs consist of two rings of hexagonal scintillator tiles, an outer ring composed of large tiles and an inner ring composed of small tiles. Each of the rings is further divided into two subrings of 6 and 12 tiles each. The number of counts in the BBCs is proportional to the number of charged particles hitting its scintillator tiles, resulting in another multiplicity measurement. The timing difference between the hits in both counters locates the vertex position without centrality dependence. The BBC is the main interaction trigger for p+p collisions.

The other two subtrees use the energy deposition in the electromagnetic calorimeters. The tower digitizer crates (TDC) of the BEMC and EEMC described in section 3.2.2 calculate two trigger primitives for use in the EMC subtree. The first ones from the BEMC are 300 high tower values of 6 bits. They are the largest tower signal in a 0.2 by 0.2 patch in $\eta - \phi$ (16 towers). The 12-bit data from the ADCs is shifted to adjust to the trigger range of interest and a pedestal can be subtracted. The second primitive from the BEMC is the sum of the energy deposition in each 0.2×0.2 patch, digitized to 6 bits. The EEMC provides similar trigger primitives for 90 patches. Triggering on the electromagnetic energy deposition will allow to select (high-p_T) electrons and photons and thus to increase the available statistics. It will be discussed in chapter 4 how this information is used to select events containing an Υ.

Once the TCU has issued a trigger to the TCDs there is a period of several milliseconds during which the selected detectors (e.g. TPC and SVT) are busy digitizing their data and transmitting it to the DAQ. The next two trigger levels L1 and L2 can use this time for a more detailled analysis of the trigger data. The L1 decision has to arrive within $\sim 100\mu$s while the L2 decision can take up to ~ 5 ms with a typical decision time of ≤ 1 ms. Both levels work on the trigger detector data, but due to the larger time budget more complex operations are possible. The data is also more finely grained, e.g. L2 has the 12-bit ADC values for each tower of the BEMC available.

Both trigger levels can abort the digitization or read-out of the slow detectors, e.g. the TPC if they decide no to accept the event. In this case they send their abort

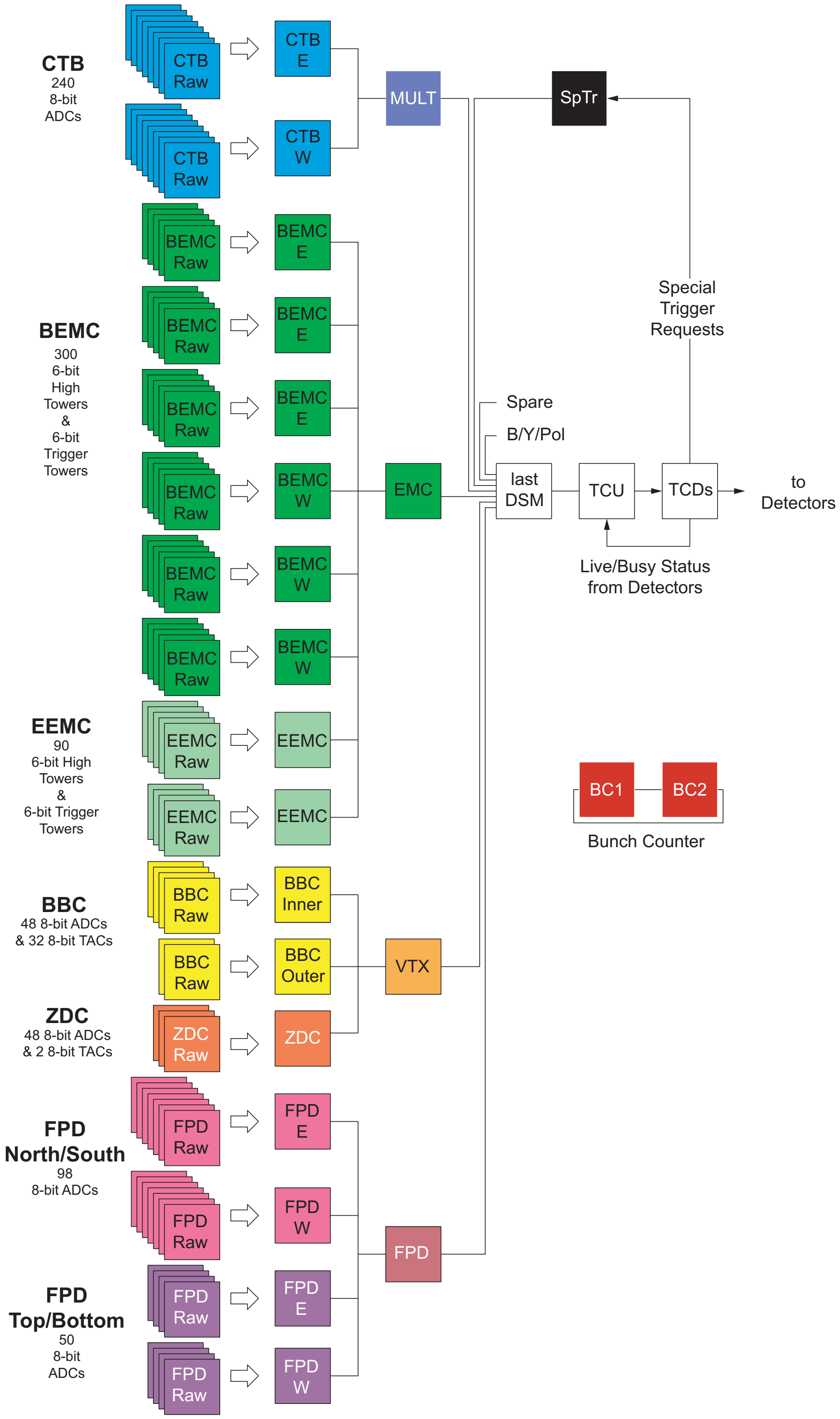

Figure 3.12: L0 DSM tree in its 2004/2005 configuration [C+04].

decision to the TCU which distributes it over the TCDs to the detectors, freeing them for a new trigger and thus increasing the slow detector livetime. When an event is accepted by L2, the DAQ system is notified by the trigger system and control of the proto-event relinquished to it.

In the case of an accept the DAQ system [L$^+$03] then collects the data contributions from all detectors, formats them and sends them over Gigabit Ethernet links to the RHIC Computing Facility (RCF) for storage on tapes using HPSS. The detectors are read-out with rates up to 8,000 MByte/s (80 MByte/event times 100 Hz read-out rate). This large input rate demands a parallel processing through DAQ. The dataflow through the system is controlled by the Global Broker (GB) which steers the read-out and data transport in DAQ for every token sent from the trigger.

The front end to the detector electronics uses multiple receiver boards (RB) [L$^+$00] receiving data on separate optical fibers from the detector electronics. Each RB holds three Mezzanine Boards (MZ) which have each an i960 processor and 6 ASICs. For the TPC data the ASICs perform a compression of the ADC values from 10-bit to 8-bit, apply a gain correction and subtract pedestals. To further reduce the data size the data get zero suppressed. It is then formatted by the i960 CPU for further processing by DAQ. Part of the computing ressources of the MZs is used to perform two dimensional TPC cluster finding for the L3 trigger system, a task described more detailled in section 3.2.4. Similar tasks are performed on the MZs mounted on the RBs for the other detectors.

The receiver boards are grouped together in VME crates, each crate controlled by a Detector Broker CPU (DET). There are 12 DETs for the 144 RBs of the TPC, 2 for the 20 boards of the FTPC, 2 for the 24 boards of the SVT and some more for the EMCs and the other small detectors. The data is then sent over a Myrinet, a low-cost, high-performance, low-latency commercial network system, to the Event Buffer computers (EVBs). To enhance the availability and reduce the load multiple PCs are used, currently four. Once the contribution from all DETs has arrived, the EVBs format the data for the final transfer to RCF for storage on tape and signals the trigger system that the event identified by the token has been processed, freeing that token for further use in the trigger system. The data speed of 30 MByte/s for the transfer from the EVBs to the HPSS storage system limits the event rate to 3-6 Hz of zero-suppressed but not further processed Au+Au events[7]. The dependence on the availability of the RCF link and HPSS is reduced by the disk space in the EVBs which allows to buffer the data for some time. It also makes larger event rates possible since buffered data can be transfered as well in periods without data taking and thus during running the EVBs can accept more events from the detectors than they can write to the storage system.

3.2.4 The Level 3 Trigger System

Another important element of the STAR online systems is the Level 3 (L3) trigger system [A$^+$03g]. It can operate on the whole raw data produced by the various subsystems, allowing a much more sophisticated event analysis then on the lower trigger levels. A full online reconstruction of the event is made within ~ 100 ms, a challenging short time budget compared to the few minutes per event necessary for the final offline reconstruction for physics analysis.

[7] The STAR link to the RCF HPSS storage facility was upgraded to 80 MByte/s before the FY03 run, allowing event rates of 10-15 Hz for Au+Au collisions.

The labeling of L3 as a trigger system is partially misleading since it supports not only triggering but several other operating modes as well. Also all detectors have already finished their data read-out, digitization and transfer to DAQ cycle before the L3 issues a decision. They might have even performend this for several other, following events until the L3 processing of the original event has finished. The L3 trigger decision thus influences only the processing of the event in the DAQ system. For a "real" trigger system one would commonly expect some interaction with the detectors themself, which is not happening in the STAR L3 implementation. One thus better thinks of L3 as an online analysis system.

The reduction of the data written to tape by the DAQ system is the main goal of L3. In principle one can design a DAQ, permanent storage and offline reconstruction system capable of handling the data from all detectors operating at the maximum speed of currently 100 Hz. In practice however financial cost considerations make the construction of such a system difficult if not impossible. The data reduction by L3 allows to get the equivalent of such a "full-speed" DAQ, storage and reconstruction system for at least some, if not all, physics signals one wants to analyze and this at much lower cost.

L3 as the first ever such system in heavy ion collisions has tried several strategies to achieve the necessary data reduction, defining the different non-exclusive operation modes:

- **Event Selection (Triggering):**
  The online reconstructed event is analyzed for some specific physics signals. Examples for such signals include high transverse momentum tracks pointing to some detector (RICH) [Ber03], $\overline{^4\mathrm{He}}$ [Str03], high momentum π^0s [Die05] and Υs. DAQ writes then only events with have at least one of these signals to the storage system, all others get discarded. The number of events which are written to tape stays the same, but the fraction of events with specific physics signals gets enhanced. For these special events the system is equivalent a the "full-speed" DAQ.

  The applicability of this strategy depends of course how often events with such a special signal happen. In STAR the DAQ speed to storage is 3-5 events per second while the detectors can operate with up to 100 Hz. Since some of the storage bandwidth has to be given to unbiased events the maximum rate of events accepted by L3 should be less than 1 out of 100. This limits us to a small subset of all physics signals called "rare probes" in the following. In addition this maximum rate has to be shared by all concurrently running algorithms, putting further constraints on the frequency of selected events. A rule of thumb for an algorithm in the STAR context is therefore to select at most 1 out of 1000 events. A disadvantage of this strategy is that the data size of unbiased events does not get reduced, thus resulting in a gain for only some physics signals.

- **Event Tagging:**
  This operation mode is a special case of the event selection mode just described, it mainly differs in the DAQ handling of the L3 decision. Again every event gets analyzed for some physics signals as above. However DAQ does not discard these events, it only flags them as "special". The number of events to the storage system is thus not reduced and obviously nothing is gained beside the fact that we know that these are special events.

  However this information opens several possibilities in the DAQ and offline reconstruction event handling which make this mode quite usefull. A first application focuses on the offline reconstruction of the recorded data, a quite time consuming process. As an example the production of the FY04 Au+Au data taken by STAR is estimated to take 1 to 1.5 years. This time gets even further enhanced by the fact that typically the production is run more than once due to improved calibrations and reconstruction software. Obviously the reconstruction time span poses a serious problem for timely physics analysis. The knowledge from the L3 online analysis that an event contains an interesting physics signal allows DAQ and offline a priority reconstruction of these events, thus leading to much shorter timescales for physics signals recognized by L3. This priority path is called *express stream*. A variation of the express streams are special streams for calibration triggers.

Another application exists in connection with the data compression operation mode described next. There might be special cases where the chosen data compression algorithm is not applicable for events containing a specific physics signal or where the physic signal depends strongly on details of the raw data which one thus does not want to loose. In this case the information that the event contains one of these signals allows DAQ to additionally write out the raw data and not only the processed data. An example for such events are events containing $\overline{^{4}\mathrm{He}}$ which gets identified by the energy loss in the TPC gas. The availability of the TPC pixel data and not only the cluster data might help to assure the quality of the analysis.

As in the event selection mode, only analysis benefit for which an L3 algorithm can be designed. But one does not face the same rate restrictions since every event is anyhow written to tape and a smaller selectivity is sufficient, making this mode applicable for more physics signals. The limitations are now only set by the desired offline processing time and/or data volume, a "soft" factor which can be freely determined.

- **Data Compression:**
  The raw ADC values from the detector electronic are not necessarily in a data format which takes the least space on tape. In addition not all of the recorded data is relevant for later physics analysis. Further processing on the DAQ/L3 level can thus significantly reduce the needed tape space.

  One possibility would be the use of lossless compression algorithms. These algorithms use e.g. entropy encoding to compress the raw data. Such an algorithm was used successfully by the NA49 experiment [A$^+$99b] at CERN, which used Huffman encoding [Huf52] to compress the TPC raw data in the 2000 heavy ion run. Altough these methods have been studied in STAR [B$^+$02] they are not yet used.

  Another possibility to compress the data is to process the data online and save only the results to tape. However all the methods of this group are not losseless and thus the impact on the physics analysis has to be carefully evaluated. A first algorithm of this type was already discussed in the description of the DAQ receiver boards. The TPC zero suppression removes all ADC values below some threshold, thus reducing largely the number of empty or noisy TPC pixels.

  The computing and analysis power of L3 allows for much more sophisticated algorithms. Saving just the online found tracks would achieve the maximum possible data reduction. An intermediate step is the saving of online found TPC clusters. The data reduction factors achievable with these methods range from 5 for saving of clusters to 20 for saving of tracks compared to standard, zero-suppressed central Au+Au events.

What makes this operation mode especially interesting is the fact that all analysis profit from it. Even the factor 5 achieved for TPC cluster saving is sufficient to reach the goal of a "full-speed DAQ". However one has to carefully evaluate the impact on the later physics analysis. There is no way to recover the data if there was a bug in the compression algorithm.

- **Quality Assurance and Detector Calibration:**
  All the operation modes discussed so far have been focused on reaching the goal of a "full-speed DAQ" equivalent. However the availability of a full online reconstructed event influences also other areas of the STAR detector operation which we will discuss here as an own L3 operation mode.

  First of all L3 allows a quick check of the data quality. Several key observables are reported to the shift crew operating the detector. The most impressive feedback is the online event display (see figure 3.15) but also more quantitative values get reported. Examples are the main vertex position and multiplicity distributions.

  Another application is the use for detector calibration. Several detectors, i.e. the CTB and the BEMC, depend on track information from the TPC for a proper calibration of the individual detector parts. The availability of TPC tracks from L3 largely reduces the turn-around time for these calibrations. These quick turn-around times are especially important since both the CTB and the BEMC are trigger detectors. Without proper calibration physics data taking using these detectors in the trigger is impossible.

All the operating modes just described have been or are used in STAR. Quality assurance and detector calibration was used from day one and proved quite usefull to immediately detect detector failures, operator errors or changing beam conditions and especially during the initial commissioning periods at the begin of each run. During the FY01 and FY02 runs (2000-2002) L3 was used in the trigger or event selection mode to enhance the number of usefull events for specific physics signals. Starting with the FY03 (2002/2003) run data compression was used and only online found TPC clusters are written to tape. This now standard STAR operation mode allows to write every event to tape which one can take with the present detector electronics. This was supplemented by event flagging for express and calibrations streams beginning with the FY04 and FY05 runs (2003/2004 and 2004/2005 respectively).

Common to all operating modes described is the reconstruction of the full event. The full event reconstruction splits naturally into reconstruction of the subsystem data, e.g. TPC track reconstruction, EMC hit reconstruction and further processing of the trigger detector data. The TPC track reconstruction can be further splitted into two tasks, cluster finding and track finding. The final task is obviously the combination of all the data to the full event and the trigger decision making of the various algorithms. All these steps will be briefly described later.

A constraining factor for the algorithm complexity is computing time. In the original L3 implementation it was given by the readout rate of the slow detectors and the available buffers in the DAQ system. The DAQ detector brokers can buffer 12 events, together with the slow detector readout rate of 100 Hz this gives $1/100\ \text{Hz} \cdot 12 = 120$ ms as the average time budget for a L3 decision.

A possible way to deal with this challenging short time budget is parallelization. Two possible strategies exist: splitting of the different reconstruction tasks of one event over many computers (intra-event parallelization) and working on many events in parallel (event parallelization). Intra-event parallelization reduces the time for a single event, while event parallelization reduces the time until a decision is issued for subsequent events.

L3 used a combination of both methods. Intra-event parallelization was chosen for the TPC data reconstruction, for both cluster and track finding as can be seen in the schematic L3 data flow shown in figure 3.14. The data of each of the 12 TPC supersectors is read out by one DAQ detector broker (DET) as already explained in section 3.2.3. The DETs contains 6-12 receiver boards (RB) with three mezzanine cards each. The input data needed for the cluster finding algorithm is already available on the RB level. It was therefore decided that the i960 CPUs on the RBs handle the TPC cluster finding, resulting in a total of 432 parallel working CPUs.

The splitting of the TPC data into 12 supersectors at the DAQ level is another natural technically motivated intra-event parallelization opportunity for the track finding. However this imposes a first compromise on the track reconstruction quality, tracks crossing supersector boundaries will not be fully reconstructed. Mainly low transverse momentum tracks have a large enough curvature to cross supersector boundaries. However most of the envisioned algorithms focus on the high transverse momentum part. The degradation of reconstruction quality was thus deemed acceptable. The data of each of the 12 TPC supersectors is processed by an Alpha 21264 CPU, build into Compaq workstations. Track finding is thus done by 12 CPUs in parallel, the so called *Sector Level 3* (SL3) CPUs.

Neither of the other reconstruction and analysis tasks has similar parallelization opportunities as the TPC and thus no intra-event parallelization was implemented. All of them are handled on a single CPU, the *Global Level 3* (GL3).

To further enhance the throughput rate of the system, the SL3s, i.e. track finding, and the GL3, i.e. global event analysis, were parallelized on the event level. In total 48 SL3s with Alpha processors are available, allowing to work in parallel on 4 events (each with 12 supersectors). For the global event analysis 3 GL3s (1 Alpha, 2 Pentiums) are used, allowing to process 3 events in parallel.

Additional time is gained by additionally parallelizing the individual tasks themself. Each of the tasks splits into three parts, receiving of the input data from the previous level, performing the analysis task, e.g. track finding, and sending the output data to the next level. All these subtasks are executed in parallel, e.g. while the found tracks are send to from the SL3 to the GL3 for further processing, the supersector of another event is tracked while the supersector of yet another event is received from the DET. This results in a high usage efficiency of the available CPU and network ressources.

The data transfer network plays a critical role in the system. Low latency and high data transfer rates are mandatory. Myrinet fullfills these requirements and is used for the DAQ and L3 data transfers. A schematic view of the L3 network architecture is shown in figure 3.13 and communication.

The L3 computing system is augmented by several other auxiliary computers and network systems. In addition to Myrinet all computers are connected to an Ethernet network which is used for system file transfer and process control. A serial console terminal server allows low-level control and surveillance, e.g. remote power down/up of the power supplies. Another Alpha computer (L3EVP) serves as local storage system, allowing L3 to save the processed data independent of DAQ for quick quality

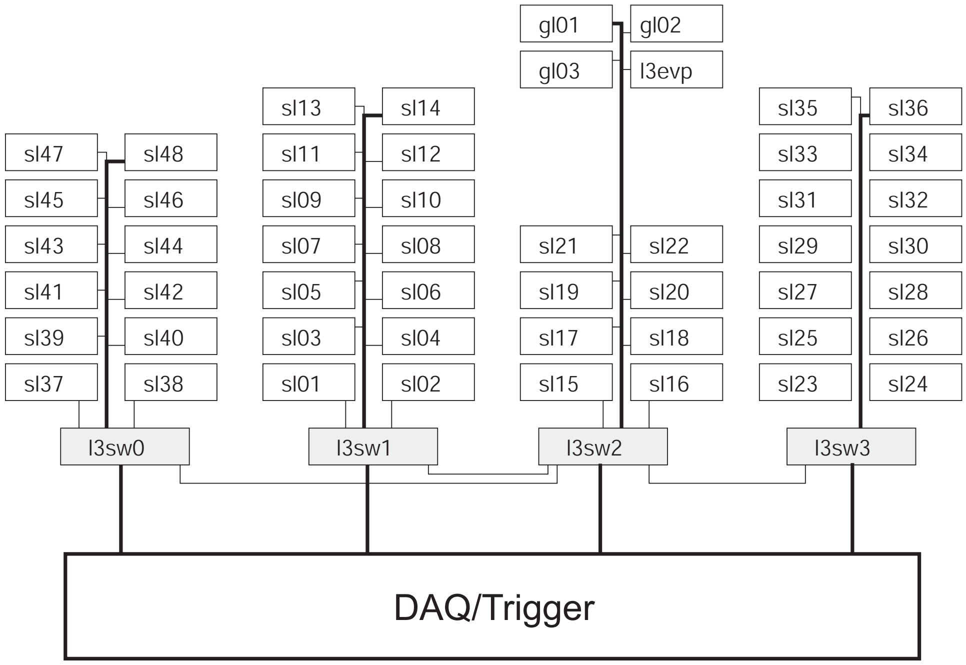

Figure 3.13: The architecture of the Level 3 trigger network.

checks. The online event display is controlled by another computer, L3DISP. More details on the L3 hardware and software design can be found in [Adl03].

As explained before this massive parallel design including intra-event parallelization was chosen to meet the 120 ms time limit set by the DAQ buffers on the receiver boards. No further buffers were envisioned in the original DAQ concept. However in 2002 the DAQ concept evolved and a huge buffer capacity on the event builders (EVBs) became available. Also the responsibility for the data transfer from the individual DETs to the event builders shifted from the global broker (GB) to the EVBs as explained in section 3.2.3. This relaxes the time limit by quite a bit, since now only the number of free trigger tokens identifying the event matters. As discussed below the splitting of the tracking on several machines causes some limitations, so a future L3 implementation might forgo the intra-event tracking parallelization on the trigger level.

A side effect of this massive parallel design is the built-in fault tolerance. Since each task and event can be handled by one of several computers no single point of failure exist. This is crucial for an online system since every non-recoverable fault would stop the data taking of the experiment and require an expert operation. This is also reflected in the software design which traps most of the possible errors and automatically resets the program to an healthy state. During the first years failures of L3 nodes would still stop the run, requiring the shift crew to manually remove the system from the configuration before resuming data taking. Before the FY04 run the procedure got completely automated. The DAQ Global Broker periodically checks the L3 computers. Broken nodes get automatically removed without stopping the run. A notice is send to the L3 bug tracking system to record the incident. The bug tracking system allows a failure frequency analysis to detect the most common failure modes. A concentrated effort to solve or circumvent these modes resulted in a pretty stable system, with typically < 1 failure/month were a

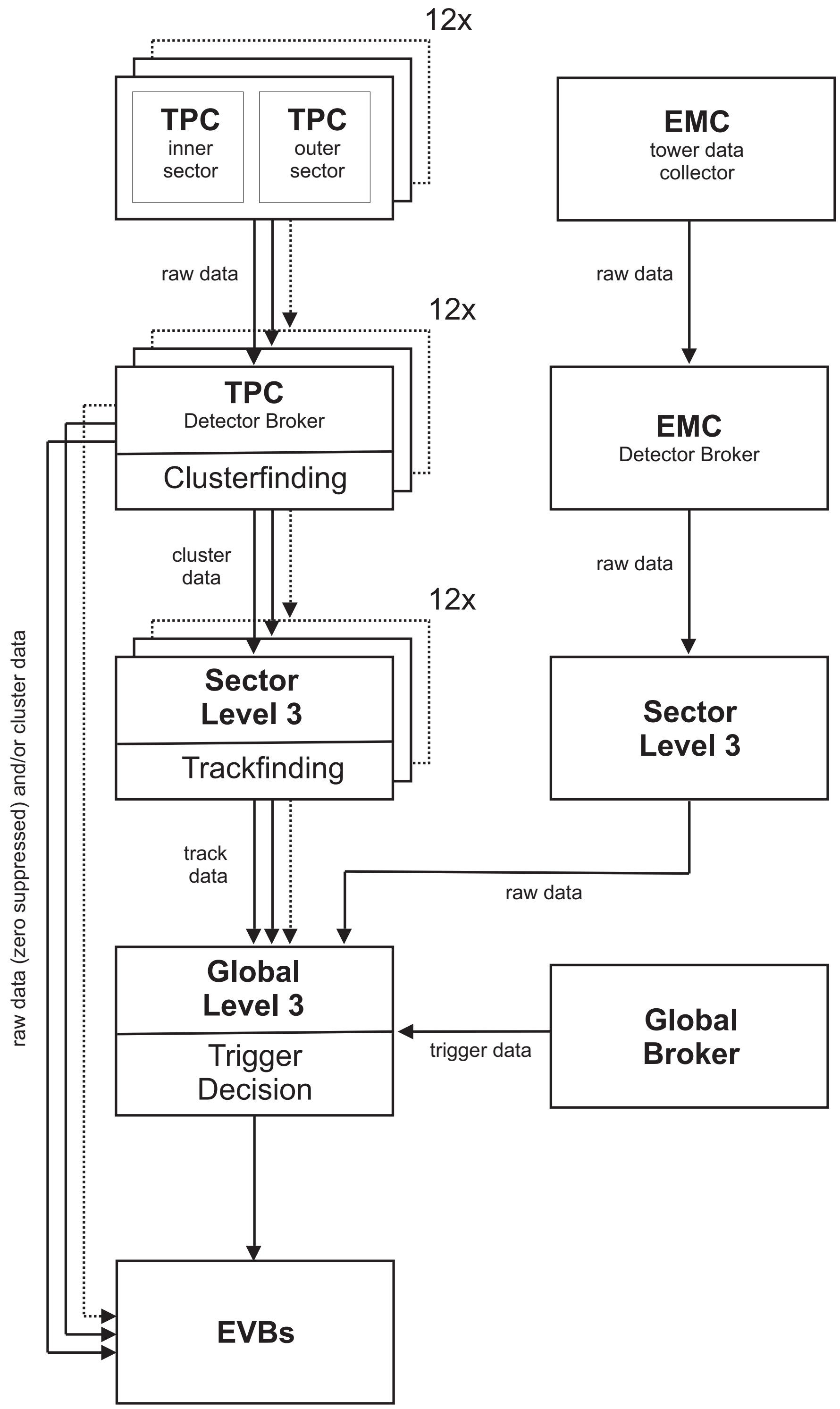

Figure 3.14: Dataflow in the Level 3 system.

node had to be removed from the run and 0 non-recoverable errors which caused run stops during the whole run period.

After this excourse to the L3 hard- and software implementation we now come back to the reconstruction algorithms. Four different main tasks were identified, the TPC cluster and track finding, the EMC data processing and the global event analysis which will be discussed in the following paragraphs.

- **TPC Cluster Finding**

  As first step of the TPC cluster finding process ADC sequences above the zero-suppression threshold in time direction (i.e. the drift or z direction) are identified for each TPC pad. Before the threshold comparison pedestal and gain correction are applied to the ADC data, yielding comparable ADC signals for each pad. To qualify as sequence, two additional criteria have to be fullfilled:

  1. More than n_l ADC values in sequence above the zero-suppression threshold
  2. More than n_h ADC values in sequence above an higher ADC threshold ADC_h

  The first condition rejects one-pad clusters which might be created by electronic noise in the TPC FEEs. Sequence candidates with a too low total charge are rejected by the second condition, reducing the influence of pedestal fluctuations. Pointers to the ADC sequences are saved for further processing by the i960 processors.

  The task of the clusterfinder is to match the ADC sequences in pad direction to reconstruct the cluster in the two dimensional padrow-time plane. For each found ADC sequence the cluster finder searches the adjacent pads for an ADC sequence with a matching position in the time direction. If one is found it is added to the cluster. For each cluster the position and width in the pad and time direction are saved for further processing as well as the total charge. In addition a quality flag is set. The achieved position resolution are $\sigma_{r\phi} \sim 830\mu\mathrm{m}$ in the pad direction and $\sigma_z = 1130\mu\mathrm{m}$ in the time direction[8].

  A possible complication for the cluster finding are overlapping clusters, especially in the high-density environment of central heavy ion collisions. The algorithm tries to identify and deconvolute these overlapping clusters. However the splitting of the total charge between the two deconvoluted clusters remains challenging. The quality flag is thus set to a different value for these clusters. Later calculations which are sensitive to the total charge, e.g. the calculation of the particle energy loss in the TPC gas ($\mathrm{d}E/\mathrm{d}x$), can thus identify and discard these clusters.

  The quality of this online cluster finder has been compared to the more advanced STAR offline cluster finder [Lis96] in the L3 context[Fli03]. The differences in the position resolution, reconstructed cluster charge and efficiency turned out to be negligible. A further comparison of both cluster finders by all physics working groups in STAR confirmed this encouraging result. It was thus decided to use one of the L3 Data Compression modes and just write

[8] The position resolution values were determined for a magnetic field of 0.25 T (half field). The position resolution at nominal field strength (0.5 T) are significantly better due to the reduced diffusion of the electron cloud during the drift process)

clusters to tape starting in the 2003/2004 run. The raw TPC data is also written out every nth event (with typically $n \approx 10$) for offline quality check purposes.

- **TPC Track Finding**

  The clusters are then used by the track finder to reconstruct the trajectory of the charged particles through the TPC. L3 uses a pattern recognition algorithm tuned to speed [Yep96]. It uses a "nose-following" method for the actual pattern recognition. Starting from a *seed*, i.e. three to five TPC clusters in the outermost padrows of the TPC, the track gets extrapolated towards the center and clusters along the path are added to the track.

  To speed up the extrapolation a conformal mapping is used to transfrom the particle trajectories into straight lines. As will be explained in section 4.1.1 the path of charged particles in the STAR magnetic field can be described well with an *helix*, i.e. an circular path in the $x - y$ plane perpendicular to the magnetic field. Applying the conformal mapping allows the pattern recognition algorithm to search for lines instead of circles in the $x - y$ plane, resulting in a much faster algorithm. Assuming that all tracks originate from the collision vertex[9] (*vertex constraint*) allows to apply the conformal mapping at initialization time, further speeding up the pattern recognition.

  Essential for a fast algorithm is the organization of the cluster data. Searching all clusters during the track extrapolation would be quite inefficient. To avoid this the TPC clusters are organized in sub-volumes, i.e. slices in azimuthal angle and pseudorapidity. Matching points are then just searched in these sub-volumes, resulting in a significant speed gain.

  To recognize also tracks without hits in the outermost padrows, the seed finder also produces seeds from more inward padrows. To reduce the combinatoric, an iterative procedure is used: First only seeds using clusters from the outermost padrow are calculated and tracked. The seed finding using clusters from the second-to-last padrow as starting points then uses only clusters which have not been assigned to an valid track and so on. To also recognize tracks without hits in some intermediate padrows, the pattern recognition algorithm accepts up to two padrows without clusters before stopping the extrapolation.

  Crucial for physics applications is the quality of the track finding process relative to the offline results (cf. section 4). It can be measured by two main criteria, the track finding efficiency and the momentum resolution.

  The relative track finding efficiency relative to offline is on the 80-95% level, depending on the momentum and vertex position[Adl03]. The rather large dependence on the vertex position is an artefact of the cluster ordering (pseudorapidity slices) used to speed up L3. The low efficiency at low transverse momentum is caused by the segmentation of the L3 tracking into supersectors. Tracks which cross the supersector boundaries can not be tracked since the clusters are assigned to different SL3 processors. Low transverse momentum tracks have a large curvature and therefore a large probablility to cross different sectors than the rather straight high transverse momentum tracks (c.f. figure 4.1). A possible track piece matching for these tracks on the GL3 level was never implemented since the running algorithms focus anyway on high momentum tracks.

[9]The current L3 implementation assumes the collision vertex to always at $(0, 0, 0)$. The position of the vertex in the $x - y$ plain is determined by the beam size and position and on the order of ≤ 2 cm. This leads to a not fully correct transformation (i.e. not completely straight lines). But for all practical tracking purposes this can be ignored.

More challenging for a fast reconstruction algorithm is the transverse momentum (p_T) resolution. The tracks found in conformal space are refitted in real space with an helix to determine the curvature and thus the transverse momentum. The offline reconstruction uses the vertex position as an additional fit point to improve the p_T resolution. The results obtained with L3 using this assumption as well are within 10% of the offline results. However as mentioned above the transverse vertex position is not know precisly in L3 and additionally changes from store to store. To avoid any bias by this it can not be used in the online tracking, resulting in a significantly reduced resolution. It is a factor ≈ 3 larger than the one achieved in offline tracking using the vertex and a factor ≈ 2 than offline tracking not using the vertex.

A huge challenge for the momentum determination is the exact cluster position in the TPC. Several *distortions* (cf. section 4) influence the drift of the electrons in the TPC, resulting in a shift in the reconstructed cluster position. For speed reasons the distortion correction in L3 had to be implemented as a static, combining the effect of all different distortions. The granularity of this table is 16 pads times 16 timebins, a linear extrapolation is used for positions in between. The conversion from drift time to the z-position using the drift velocity is also included in this table.

A remaining problem is the time-dependence of several corrections. The drift velocity for example depends on temperature and pressure. The changes are however small enough to not influence the momentum determination since STAR operates at the maximum of the drift velocity curve (see section 3.2.1 and figure 3.6). In addition it does not distort the curvature measurement, only the dip angle of the track.

A dynamic distortion which influences the cluster position in the transverse plane is the space charge correction. It depends on the luminosity and beam intensity. Both quantities can not be measured with a good enough precision during online data taking, making a correction like the one in offline impossible. During the FY04 data taking period the achieved luminosities were for the first time high enough to cause sizeable space charge effects. The p_T resolution of L3 for high p_T tracks was severely influenced by this, making it basically unusable for any physics purposes (i.e. 100% p_T resolution, no clear determination of particle charge).

In principle this can be solved by implementing dynamic correction tables. However in reality this turns out to be difficult since as mentioned above no sufficient luminosity and/or beam intensity information is available. In addition the space charge correction changes on the order of seconds or less, making it even more challenging to come up with precise enough distortion tables. While these (technical) problems could be overcome, the main problem was the time scale necessary for the implementation. The offline understanding of the different space charge effects converged only months after data taking, i.e. half a year to late for an online implementation at the beginning of the run. Reaching higher and higher luminosities year by year changes the relative importance of the different corrections and thus also the needed precision. It remains unclear how such the implementation time problem could be overcome. This is especially true since one wants to avoid too many periods with different biases from the online trigger for practical analysis purposes.

- **EMC Data Processing**

The EMC data reconstruction is much less computing intensive than the TPC cluster and tracking algorithms. The basic algorithm just requires one subtraction and one multiplication operation for each of the 4800 towers (cf. 4.1.2). No more advanced algorithms like clustering were implemented. If they are required to issue a trigger decision these advanced algorithms have to be implemented in the trigger decision algorithm.

The basic algorithm is run on the global event analysis level, i.e. on the GL3 computers. Nevertheless it was decided to route the EMC data like the TPC data, including the transfer from the DET over a SL3 to the processing GL3 (see the EMC L3 data flow in figure 3.14). This was done to keep the same messaging interface to the DAQ system. The additional load on the SL3s by transferring the data is small and thus not impacting the supersector tracking on the nodes.

The timely availability of the calibration and status tables is again a major problem. The staged construction of the BEMC required each year new calibration tables which were typically only available after 10 weeks, half-way through the run. Even more challenging were the tower status tables. These tables play a crucial role since they remove hot or non-working towers from further analysis. They cause some trigger algorithms to trigger every event, braking L3 triggering or event flagging. In these cases L3 is normally removed from the run by the shift crew. An automatic generation of these tables from EMC information was impossible during the first years since the EMC group was not able to provide an interface. This changed in the FY05 run where a database interface became available and was used by L2. Also the frequency of EMC failures was reduced due to new power supplies, reducing the severity of the problem.

- **Global Event Analysis**

The global event analysis of the decision algorithms is based on a common framework. It collects the TPC and EMC data from all SL3s and the trigger detector data from the DAQ global broker. Some simple algorithms whose results might be used by different decision algorithm are run, e.g. the EMC data processing just described or ZDC based z-vertex determination.

An important task of the global event analysis is *prescaling*. In this mode only every nth accept decision of an algorithm is accepted, all the other accepted events are discarded. This allows to run also algorithms which can not be made sensitive enough to meet the DAQ bandwidth allocated for them. This system was first developed in the L3 framework, with several different strategies [Adl03, Str03]. It was later extended to all trigger levels (L0-L3). The L3 input rate can thus be determined trigger dependend by the L2 prescale[10]. Coupled to this is the task of proper bookkeeping, i.e. which trigger accepted and aborted how many events, prior to and after prescaling. This bookkeeping scheme was also developed in L3 [Str03]. It was later on extended and implemented in trigger and DAQ for all trigger levels as already discused in section 3.2.3.

[10] In practice the L2 output rate is limited by the TPC readout rate. Since L3 can handle the full TPC rate, there is no need to use L2 prescales to limit the L3 input rate.

An online reconstructed event is shown in figure 3.15. The reconstructed tracks as well as BEMC towers above pedestal of the instrumented are clearly visible. Similar pictures are displayed every few seconds in the counting house to the shift crew for quick quality checks.

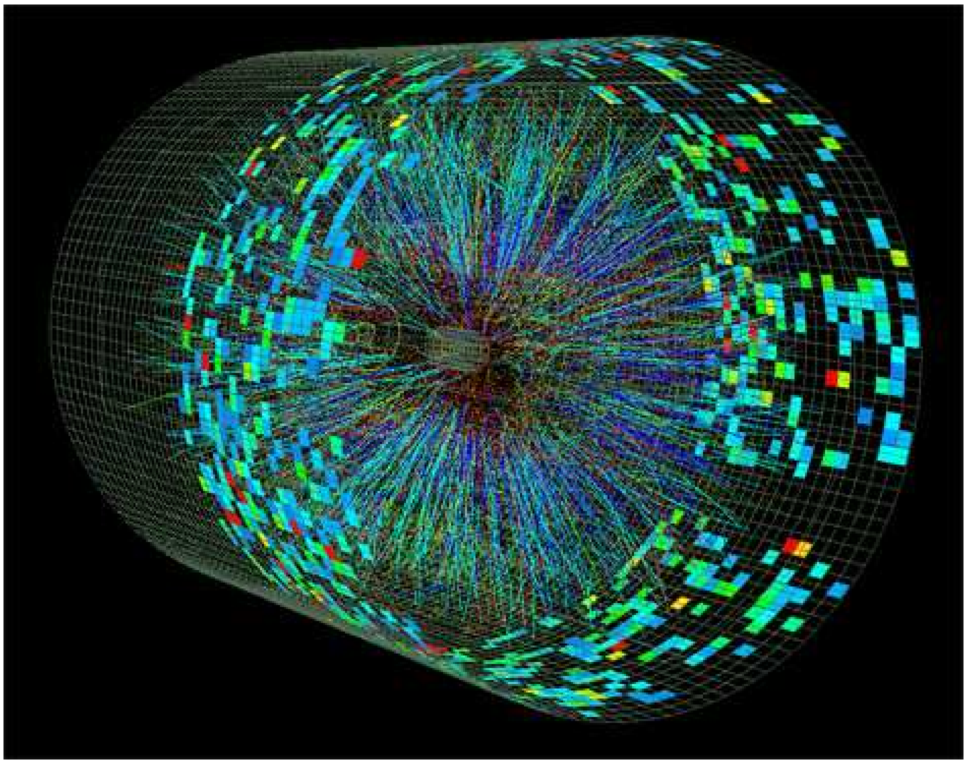

Figure 3.15: A Au+Au event at $\sqrt{s} = 200$ GeV reconstructed by L3.

Overall the STAR Level 3 system has demonstrated for the first time that a high level trigger using TPC tracking based decisions is technically feasible and significantly enhances the physics potential of an experiment. Several insights for future implementations of a track and especially TPC (or any drift detector) based high level trigger system (e.g. the ALICE HLT [ALI95, ALI04])several have been gained.

The by far most effective operation mode is data compression. The whole experimental physics program benefits if high enough compression factors are reached by a combination of lossless compression algorithms, cluster finding and possibly also tracking. The saved DAQ bandwidth and tape space result in a significant cost reduction compared to a conventional system with the same capacity. This is ideally supplemented by event tagging, allowing to concentrate the offline computing and analysis capacities on the most "promising" physic signals in a time effective way. One should note here that such a tagging might be provided as well by lower trigger levels.

However the potential of using track information is severely limited by the availability of sufficient (TPC) calibrations. STAR did not manage to reach the necessary quality fast enough to allow a meaningfull use of the track information for trigger decisions. The problem here is not the track finding process itself but rather the momentum determination which is too sensitive on the proper cluster position. Based on the STAR and NA49 experiences it is highly doubtful in the authors opinion that a fast enough TPC calibration is possible with a reasonable amount of resource allocation (runtime, computing and manpower). This does not exclude the usefullness of track recognition for advanced data compression modes or certain algorithms where the momentum information is not the primary decision criteria.

It is important to realize that such a high level trigger system is mainly a DAQ and not a trigger system. The HLT design and performance benefit from a close integration with DAQ and especially the event building process. An improved event identification would allow to relax the time constrains on the HLT. This allows to concentrate the processing of an event on a single node, avoiding the intra-event parallelization of the STAR implementation and simplifying the software design and communication protocol. The restriction to one node per event enhances the scalability of the system. The throughput scales linearly with the number of HLT nodes, resulting in a greater flexibility. This reduces also the demands on the CPU speed. The use of ”standard” and not high-end hardware results in significant cost savings, still achieving the same throughput.

The relaxed time limits also allow to avoid several compromises necessary in the STAR tracking implementation. Most notably is here the limitation to only one tracking pass. An iterative vertex finding followed by an refit of the found tracks can increase the momentum resolution close to the offline level if the correction problem mentioned above gets solved.

A very usefull by-product of a high level trigger system are the enhanced quality assessment capabilities, both visual ones like the event display and quantitative ones. Also (trigger) detector calibration benefits from the fast availability of track data. These applications themself however do not justify a high level trigger system since similar capabilities can be achieved with fewer ressources and sufficient allocation of offline computing time.

4 Upsilon Measurement with STAR

After describing the STAR experiment and the accelerator in the previous chapter; it is now time to come to the main quation of this thesis: Can STAR achieve a first measurement of Upsilon production in heavy ion collisions at RHIC?

To answer this question the first obvious thing to do is to choose one of the Upsilon decay channels. The most relevant ones are listed in table 2.1. The expected huge background from other particles in heavy ion collisions limits the experimentaly accessible decay channels to two-body decays, i.e. the leptonic decay channels. To reduce the background from random particle combinations, good particle identification (PID) for the decay daughters is mandatory. From the description of the STAR detector in the previous chapter 3 it should already be obvious that the particle identification capabilities for electrons by far exceed the ones for muons, a claim which will be substantiated in section 4.1.

Having identified the decay into two electrons as the most promising one, one still faces the challenge of the very small Upsilon production cross section. The STAR detector design allows to measure electrons in the region around midrapidity. As shown in 4.2 $32\% \times (68\%)^2 = 15\%$[1] of the Upsilon decays into electons will be measurable in STAR, i.e. both electrons get detected, reconstructed and identified as electrons. The achieved daughter electron momentum resolution will however not allow a clear seperation of the different members of the Upsilon family.

The STAR acceptance for Upsilons together with the expected delivered luminosity per year from RHIC looks quite encouraging, several hundred Upsilon decays into electrons per year should be detectable. But how many of these decays can be recorded to tape? STAR is nominally a slow detector, limited by the readout speed of the TPCs and the SVT to approximately 100 events per second. Typical collision rates for Au+Au provided by RHIC are ≈10 kHz, i.e. a factor 100 higher! Randomly selecting collisions for recording, i.e. a minimum bias trigger, will thus result in only a few recorded Upsilons per year, making a measurement impossible.

An effective way to select the collision containing an Upsilon decaying into electrons, enhancing the fraction of recorded events with a signal present, will be crucial for a successful Upsilon measurement with STAR. The event selection is the task of the STAR trigger system, described in 3.2.3 and 3.2.4. Section 4.3 will show how to use this system together with the BEMC to select most of the interesting events, enhancing the expected number of recorded Upsilons to a few hundred for Au+Au collisions.

[1] This number reflects the detection probablity for the full STAR detector. As discussed in 3.2 and 4.2 the detector construction was staged over several years, leading to a reduced detection probabilty until completion. See sections 4.2 and 5.1.1 for details.

4.1 Electron Identification

The detectors covering the phasespace region around midrapidity, i.e. TPC, SVT and BEMC, provide the best electron identification capabilities in STAR. The EEMC would allow to increase the acceptance to high pseudorapidities, but the decreasing TPC tracking capabilities in this phasespace region lead to small electron efficiencies, making its use difficult.

The main measurement needed to reconstruct the Upsilon decays is the energy (or the momentum with the assumption that the particle mass is the electron mass) of the decay electrons[2].

The momentum for charged particles like the electron is measured by track reconstruction in TPC and SVT. The usefullness of the SVT is limited by its small size in z, i.e. along the beam direction. It requires a collision vertex within $\mid z \mid \leq 10$ cm. The measured vertex distribution can be described by a Gaussian with $\sigma \sim 30$ cm, using the SVT would therefore reduce the number of useable collisions significantly. With the expected small Upsilon statistics one can not accept this reduction in usefull events and thus has to concentrate on the TPC information only.

Another measurement of the electron energy is obtained by the BEMC. The achieved energy resolution is however not as good as the momentum resolution of the TPC in the momentum region of the Upsilon decay daughters. The Upsilon reconstruction will thus use the TPC momentum as further discussed in 4.2.

The energy measurement of the BEMC will be however the key element in the Upsilon trigger as demonstrated in section 4.3. In addition the energy measured by the BEMC, together with the TPC momentum, allows to distinguish between electrons and hadrons as will be shown in section 4.1.2. This discrimination between hadrons and electrons is based on the different shower development in the BEMC material. Electromagnetic particles like the electron have short showers which are contained in the BEMC, which therefore measures the electron energy. The average shower length of a hadronic shower is much larger, an consequently only part of its energy is deposited in the BEMC. A comparison of the measured BEMC energy to the momentum information of the TPC gives therefore a tool to discriminate between hadrons and electrons.

The electron/hadron discrimination will be of importance to reduce the background from random particle combinations in the Upsilon mass region. Without particle identification random combinations of hadrons will dominate due to the low electron to hadron ratio $e/h \sim 10^{-3}$ in the momentum region relevant for Upsilon reconstruction. In addition to the combined BEMC/TPC information the TPC alone provides a further independent discrimination by measuring the energy loss $\mathrm{d}E/\mathrm{d}x$ of the particles in the detector gas as we will discussed in the following chapter.

4.1.1 Electron Identification with the Time Projection Chamber

Before discussion the electron identification capabilities provided by the energy loss in the TPC, the momentum measurement with the TPC is briefly discussed. The momentum information is determined by reconstructing the tracks of charged

[2]The invariant mass technique used to reconstruct the Upsilon from its decay daughters is described in section 4.2.

particles in the TPC. A charged particle moving in a uniform magnetic field $\vec{B} = (0, 0, B_z)$ is bend by the Lorentz force and its trajectory can be described by a helix equation of motion. In the xy-plane the trajectory can be described by a circle with radius

$$r = \frac{p \sin \lambda}{qB_z} \tag{4.1}$$

where p is the particle momentum and q its charge. λ is the angle between the particle direction and the xy-plane. Thus to measure the particle momentum we have to reconstruct its path trough the TPC, measure its curvature and dip angle which allow to calculate the momentum.

Particles passing through the TPC loose part of their energy in the TPC gas as described below. The cluster algorithm described in 3.2.4 determines the position of these energy deposits. The track path reconstruction is performed by a pattern recognition algorithm which uses these cluster positions as input data. The algorithm starts in the outer parts of the TPC by finding combinations of hits in the three outer padrows which overlap in the time direction, so called *track seeds*. A straight line fit to these three points seeds is then extrapolated inward to the next padrow. If another cluster is found in this padrow close to the extrapolated position, a *track segment* is formed and fitted with a helix. This helix is then extrapolated to the inner TPC field cage and clusters in the padrows along the extrapolation are added. After the algorithm has used the seeds from the outer most padrow, track seeds from clusters from the second to last padrow are calculated and extrapolated inwards as explained above, a process which continues inward until no more seeds can be found.

Once the pattern recognition step has finished, a helix is fitted to the found tracks to measure dip angle and curvature. The helix parametrization used in the STAR global Cartesian coordinates x, y, z as function of the path length s along the helix is:

$$\begin{aligned} x(s) &= x_0 + \tfrac{1}{\kappa}\left[\cos\left(\Phi_0 + hs\kappa\cos\lambda\right) - \cos\Phi_0\right] \\ y(s) &= y_0 + \tfrac{1}{\kappa}\left[\sin\left(\Phi_0 + hs\kappa\cos\lambda\right) - \sin\Phi_0\right] \\ z(s) &= z_0 + s\sin\lambda \end{aligned} \tag{4.2}$$

with x_0, y_0, z_0 the starting point at $s = s_0 = 0$, the dip angle λ, the curvature $\kappa = 1/R$, where R is the radius of the circle in the x, y plane, $h = -sign(qB_z) = \pm 1$ the sense of the rotation of the projected helix in the xy plane, with the particle charge q and the azimuthal angle Φ_0 of the starting point with respect to the helix axis. The actual fit is a two step process by first fitting the radius $R = 1/\kappa$ and center of the circle (x_c, y_c) in the transverse plane. In a second step the dip angle λ and the z position of the starting point z_0 are determined by a fit in the s_{xy} vs z plane. The knowledge of the helix parameters allows to calculate the momentum information

$$\begin{aligned} p_T &= qB/\kappa \\ p_z &= p_T \tan\lambda \\ p &= \sqrt{p_T^2 + p_z^2} \end{aligned} \tag{4.3}$$

In the experimental environment there are several effects to take into account which influence the curvature and thus the momentum. First of all the tracks loose energy while traversing the TPC gas, an effect which will be discussed later in more detail. The energy loss implies a momentum loss, and the curvature changes slightly along the particle trajectory in the TPC. To correct for this a *global refit* of the track is performed using a Kalman filter which takes the energy loss into account and calculates helix parameters both at the inner- and outermost position of the track. An additional input to the Kalman filter are the errors on the cluster position which are used to weight each cluster position by its relative measurement uncertainty. In this way also outliers, i.e. clusters falsely added to the track by the pattern recognition algorithm, can be removed to further improve the momentum determination.

A much more challenging experimental effect are distortions in the magnetic field or the electric drift field of the TPC which distort the position of the clusters used in the track finding. One has to remember that the online cluster finding is done in the TPC hardware coordinates, i.e. time bin, padrow and pad number. The distortions can thus be corrected in the mapping algorithm from hardware coordinates to the global Cartesian coordinate system.

Obviously distortions which affect mainly the x, y-plane are most critical since they influence the transverse momentum measurement. First to mention here are distortions due to the field cages. The inner field cage (IFC) is miss-aligned by 140 μm with respect to the outer field cage (OFC) which defocuses the tracks near $z = 0$ cm. In addition the IFC had a short between two stripes in the years 2003 and 2004, causing a big effect. To reduce the effect an additional resistor was added at the end of the resistor chain of the IFC. Tracks near $z = 0$ cm are also distorted by a non-perfect central membrane. It was designed to be flat, however miss-alignments of the order of 200-400 μm have been measured. The central membrane is tilted from the top to the bottom which is additionally pulled towards one end of the TPC. Further distortions are caused by the sector boundaries. As mentioned in section 3.2.1 each TPC half is divided into inner and outer sectors. The ground plane at this radius has a gap of 1.6 cm, causing sizeable distortions mainly to the clusters of the 13th padrow, the last one of the inner sectors. Corrections for all these effects are implemented ion the STAR reconstruction software, however tracks close to the central membrane still show some effects when compared to the data of other detectors, e.g. the RICH.

One of the biggest distortions in STAR are the ones caused by $E \times B$ effects. In principle the magnetic field B is aligned with the electric field E. However the magnetic field is not perfect and has a non-zero radial component which causes the electrons to develop a transverse velocity due to the $v \times B$ term in the Lorentz force equation. The distortions caused by this effect are less than 1 mm and position dependend, they are largest at large radius and near the central membrane. To correct for this, the STAR magnetic field was mapped before the TPC was inserted, allowing to calculate the expected distortions due to this effect. Related to this are deviations in coordinate transformations due to the non-perfect alignment of the TPC and magnet coordinate systems. The TPC is twisted and the west end out of alignment by 0.85 mm (0.30 mm) horizontally (vertically). This is accounted for in the applied corrections.

Common to all the distortions discussed so far is that they are static, i.e. depending only on the geometry. This is not the case for the distortion caused by space charge build-up in the TPC. Space charge is caused by the intrinsic difference in the drift velocity of electrons and ions, which move $\sim 10,000$ slower. This results in a net positive charge build-up in the TPC as result of the ionization process of the charged particles crossing the TPC volume. Obviously this correction dependens on the number of particles crossing the TPC volume. They can have two sources, the first one being of course the collisions itself which would cause a luminosity dependence. The other source are particles produced in (upstream) beam-gas interactions which enter the TPC, they should scale with the beam intensity. The charge distribution in the TPC is flat in z and scales approximately like $1/r^2$ in the transverse direction. Some non-uniformities in the ϕ distribution are expected, mainly due to the beam-gas interactions. This can however be neglected since the space charge caused by the collisions turned out to be dominant. During the 2003/2004 beam period the achieved luminosity was for the first time high enough to make this the largest distortion in STAR, with position shifts up to several mm. Given the sagitta of high p_T tracks (see below) this is sufficient to loose any momentum (and even charge sign) information. The dynamic nature of this distortion make the correction quite difficult, especially since sizeable fluctuations in the strength of the effect are observed on the sub-second level.

Ions from the amplification process itself leaking through the gating grid could be another source of space-charge in the TPC. None has been observed and also calculations show that one can neglect this compared to the space charge caused by the processes discussed above. However the grid coverage is not hermetic, causing ions to leak into the TPC volume. Places where this happens are the inner and outer end of the TPC supersectors and in between the inner and outer sectors. The distortions caused by this effect can reach up to 1 mm at the border between inner and outer sector and at the inner radius of the TPC. Also this effect is luminosity depended, requiring a "dynamic" correction.

Less critical are distortions which affect mainly the drift direction, i.e. the drift velocity. Such distortions are the gas composition, the barometric pressure, pressure changes as function of height in the TPC and temperature gradients in the TPC. Running at the peak of the drift velocity curve (see figure 3.6) reduces the sensitivity to small changes in the gas composition and the barometric pressure. In addition the drift velocity is controlled by regular "laser runs" where the ionization caused by the laser beams at precisely known positions is used to determine the drift velocity.

A further improvement of the momentum measurement can be achieved by adding the collision vertex as an additional fit point with generally small error and long lever arm ($\sim$ 60 cm from the first measured TPC point) to the track. The determination of the vertex position is the task of the *vertex finder* for which different algorithms are used, depending on the collision system. A common feature is the use of the tracks found so far to locate the vertex position. The tracks get extrapolated to the center of STAR and the point with the minimal summed distance to the track positions is determined and called the *primary vertex*. The different vertex finding algorithms differ in the choice and the weighting of the tracks used in the vertex finding. In general high-p_T tracks is given more weight than low p_T ones due to their reduced sensitivity to multiple scattering effects. While this approach works very well for heavy-ion collisions with more than $\sim$ 50 tracks, the vertex finding precision decreases in p+p and low multiplicity heavy-ion collisions due to the reduced number of tracks used in the fit, the increased sensitivity to secondary tracks, i.e. particles from weak decays of particles produced in the primary collision, and in the case of $p + p$ and low A ions also by pileup, i.e. tracks from earlier collisions whose ionization electrons have not yet drifted out of the TPC volume. Tracks with an extrapolated distance to the so found primary vertex of less than 3 cm are refitted using the Kalman filter described above and called *primary tracks*. The momentum at the primary vertex position is determined by the Kalman fit and stored for further analysis.

Another limiting factor for the momentum determination is the path length measured by the TPC. Only a small arc of the large radius circles of high momentum particle can be observed, making the curvature determination more and more difficult, increasing the sensitivity to distortions. Figure 4.1 shows the radius R as function of the particle momentum and the sagitta of tracks measured in the TPC.

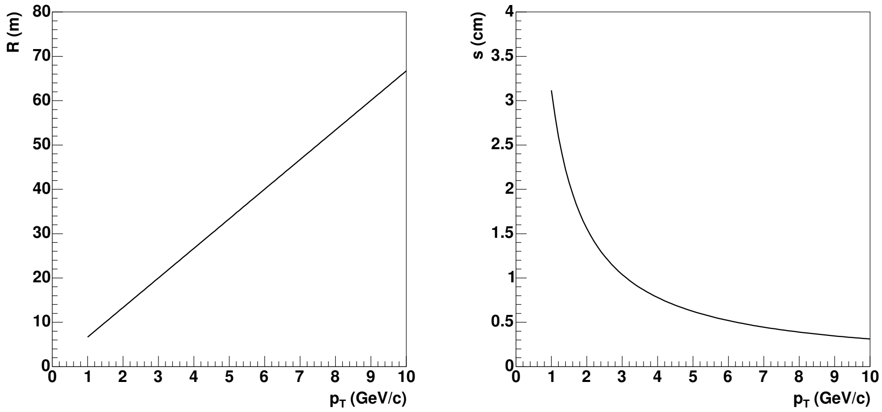

Figure 4.1: Radius R (left) and sagitta s in the TPC (right) of particles with momentum p passing through the STAR magnetic field.

The actual achieved momentum resolution is determined using the embedding technique. Simulated tracks with known momentum are superimposed on real events and the difference in the reconstructed momentum is calculated. The results of such an analysis are shown in figure 4.2 for both global and primary tracks for full field data[3]. Shown is the curvature resolution $\Delta\kappa/\kappa$ since it is gaussian following equation 4.2. The transverse momentum resolution $\Delta p_T/p_T$ can be simply calculated from it and parametrized as $\Delta p_T/p_T = 0.013p_T + 0.012$ for global tracks and $\Delta p_T/p_T = 0.005p_T + 0.01$ for primary tracks.

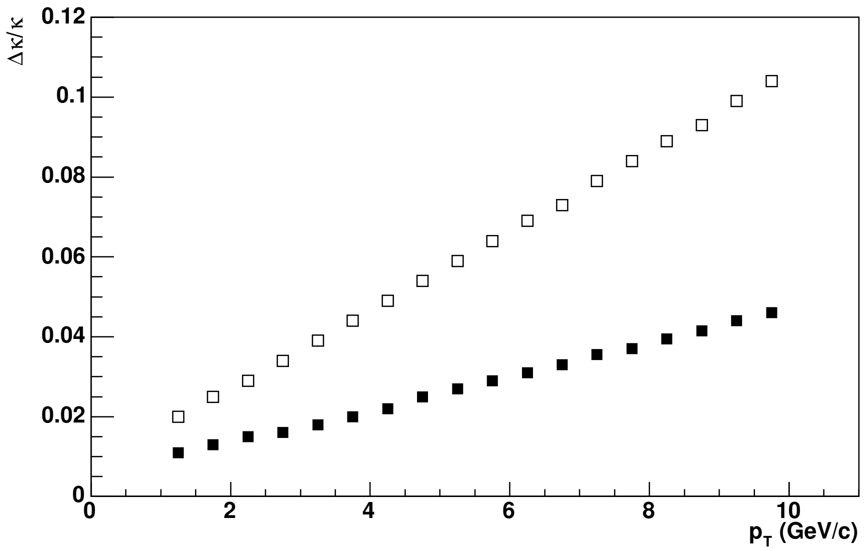

Figure 4.2: Curvature resolution $\Delta\kappa/\kappa$ as function of particle transverse momentum p_T for primary (closed symbols) and global tracks (open symbols).

[3]Obviously a dependence on the magnetic field is expected since the curvature at the same momentum is smaller. In addition the electrons diffusion during the drift process is higher at lower magnetic field. This results in a factor ~ 3 worser momentum resolution for half field.

However not all the particles passing through the TPC can be reconstructed. The path of some particles is inside the gap between the (readout) sectors and thus no clusters get reconstructed. In addition the pattern recognition algorithm might miss some of the tracks which are in principle reconstructable, especially in the high density environment of a central heavy-ion collision. These losses are calculatetable with the embedding method already used to determine the transverse momentum resolution. The tracking efficiency ϵ_{rec} gets defined as

$$\epsilon_{\mathrm{rec}} = \frac{N_{\mathrm{rec}}}{N_{\mathrm{embedded}}} \tag{4.4}$$

where N_{embedded} is the number of simulated tracks and N_{rec} the number of these tracks which get reconstructed by the pattern recognition algorithm. The tracking efficiency depends on transverse momentum as well as pseudorapidity of the particles and has therefore to be determined differently. It is also dependent on the quality cuts imposed in the later analysis, here the quality cuts from section 5 are used. The results are shown in figure 4.3 which shows the projections of ϵ_{rec} on transverse momentum p_T and pseudrorapidity η. Above $p_T = 2$ GeV/c the efficiency stays roughly constant at 83%. The pseudorapidity distribution shows a small dip close to midrapidity and a strong decrease when approaching the TPC borders at $\mid \eta \mid = 1$. All the results presented here are for minimum bias Au+Au collisions. As mentioned earlier a dependence on the event multiplicity is expected. Typical values for (pile-up free) $p+p$ collisions are a few percent higher ($\sim 86\%$) while in central Au+Au collisions ϵ_{rec} decreases to 81%.

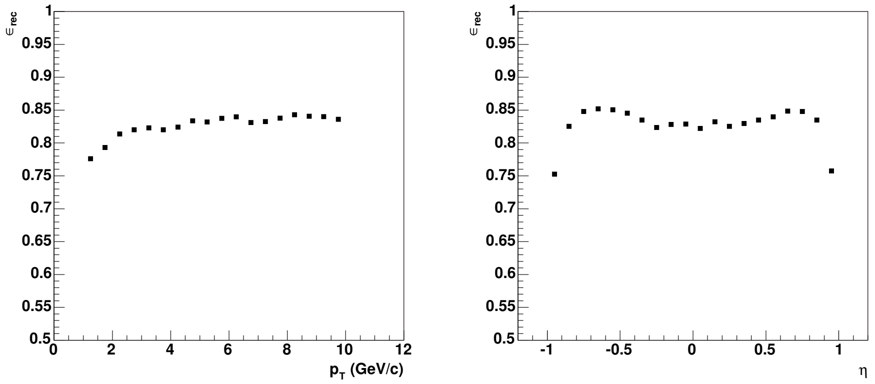

Figure 4.3: Track finding efficiency ϵ_{rec} as function of transverse momentum p_T (left) and pseudorapidity η (right) for minimum bias Au+Au collisions.

Reconstructing the momentum allows further charged particle identification by analyzing the amount of energy deposited in the TPC gas. The mean deposited energy is approximately described by the Bethe-Bloch equation

$$\frac{\mathrm{d}E}{\mathrm{d}x} = Kz^2 \frac{Z}{A}\frac{1}{\beta^2}\left[\frac{1}{2}\ln\frac{2m_e c^2\beta^2\gamma^2 T_{\max}}{I^2} - \beta^2 - \frac{\delta}{2}\right] \tag{4.5}$$

with A, Z the atomic mass and number of the gas, $K = 4\pi N_A r_e^2 m_e c^2$ and δ the density effect correction for which usually the Sternheimer parametrization is used. $T_{\max}$ is the maximum kinetic energy which can be imparted to a free electron in a single collision and can be calculated as

$$T_{\max} = \frac{2m_e c^2\beta^2\gamma^2}{1 + 2\gamma m_e/M + (m_e/M)^2} \tag{4.6}$$

for particles with mass M and momentum $M\beta\gamma c$. The mean excitation energy I is estimated based on experimental stopping-power measurements, its determination is the main uncertainty in calculation of the expected mean energy loss. However the $\mathrm{d}E/\mathrm{d}x$ of particles with $\beta\gamma \sim 0.1$ to $\beta\gamma \sim 100$ is well described within a few percent by the Bethe-Bloch equation. The energy loss reaches a minimum around $\beta\gamma \approx 3$.

For all practical purposes the energy loss $\mathrm{d}E/\mathrm{d}x$ is just a function of particle velocity β. This together with the momentum measurement allows to distinguish particles with different masses. The expected mean energy loss as function of the momentum is shown in figure 4.4 for different particle species which can be clearly distinguished.

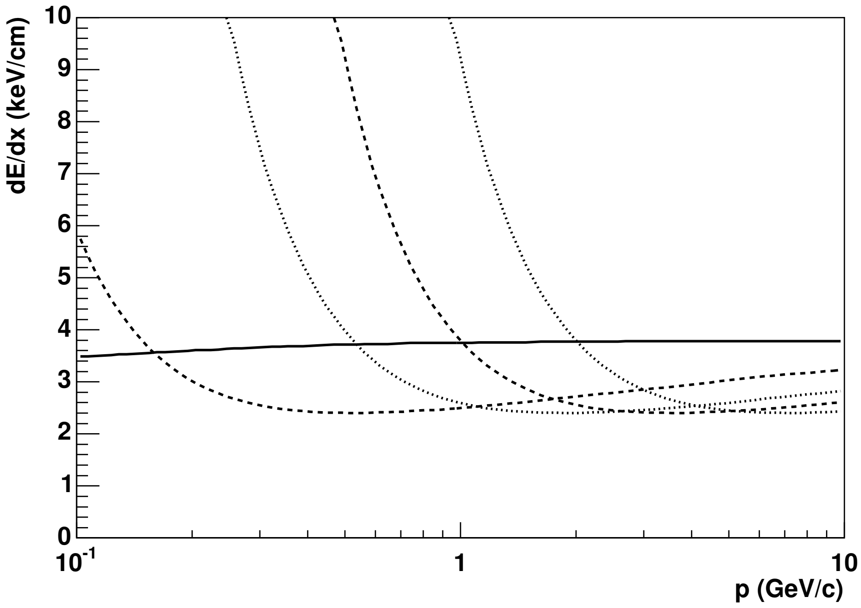

Figure 4.4: Expected mean $\mathrm{d}E/\mathrm{d}x$ for electrons (solid line) and π, K, p, d in the TPC gas versus particle momentum.

The experimental determination of the mean energy loss is made difficult by the stochastic nature of the involved processes. The probability distribution function describing the distribution of energy loss Δ in absorber thickness x is usually called the Landau distribution. More recent calculations of the probability function made by Bichsel are used in STAR. Common to all these probability distribution functions is that the most probable energy loss Δ_p is much smaller than the mean energy loss $\mathrm{d}E/\mathrm{d}x$ calculated from equation 4.5 and that the distribution has a long tail to high Δ/x values. The actual ratio $(\Delta_p/x)\,/\,(\mathrm{d}E/\mathrm{d}x)$ depends weakly on $\beta\gamma$ for $\beta\gamma > 1$ and is approximately 0.6 as described by the Bichsel functions.

The experimental $\mathrm{d}E/\mathrm{d}x$ value is calculated using the Truncated-Mean-Method. The energy deposition in each padrow as calculated by the cluster finder is interpreted as a single measurement. The lower 10% and upper 40% are discarded, the mean of the remaing is calculated and used as approximation of Δ_p/x, which will be called $\mathrm{d}E/\mathrm{d}x$ afterwards.

The number of $\mathrm{d}E/\mathrm{d}x$ measurements is obviously limited to the 45 padrows of the TPC for non-curling tracks which limits the available resolution. This is made even worse by discarding a significant fraction of the clusters in the truncated mean method. The nominal track length of ≥ 130 cm in the TPC is reduced to roughly the half for the $\mathrm{d}E/\mathrm{d}x$ calculation. The achieved $\mathrm{d}E/\mathrm{d}x$ resolution at 60 cm track length is $(\Delta\mathrm{d}E/\mathrm{d}x)\,/\,(\mathrm{d}E/\mathrm{d}x) = 8.7\%$ and is inversely proportional to the used track length, e.g. it decreases to 7.1% for 100 cm used tracks length. Figure 5.19 shows the experimentaly measured distribution for comparison.

The knowledge of the $\mathrm{d}E/\mathrm{d}x$ resolution allows to calculate the distance between electrons and pions, kaons and protons as the most abundant particles in units of standard deviation $\sigma(e)$ =dE/dx $(e,p) \times (\Delta\mathrm{d}E/\mathrm{d}x)\,/\,(\mathrm{d}E/\mathrm{d}x)$ as function of the particle momentum p. The results are shown in figure 4.5. Below $p = 2$ GeV/c the expected $\mathrm{d}E/\mathrm{d}x$ for hadrons cross the $\mathrm{d}E/\mathrm{d}x$ for electrons and thus no or negligible separation is achieved. When the hadrons have $\beta\gamma\ \sim 3$, their expected $\mathrm{d}E/\mathrm{d}x$ value following equation 4.5 reaches a minimum, and thus the separation to the electrons whose $\mathrm{d}E/\mathrm{d}x$ stays roughly constant over the momentum range shown here, is maximal at $\sim 4\sigma(e)$. With further increasing momentum (or $\beta\gamma$) the expected $\mathrm{d}E/\mathrm{d}x$ of the hadrons rises and thus the separation power is reduced to $\sim 2\sigma(e)$ for 10 GeV/c pions.

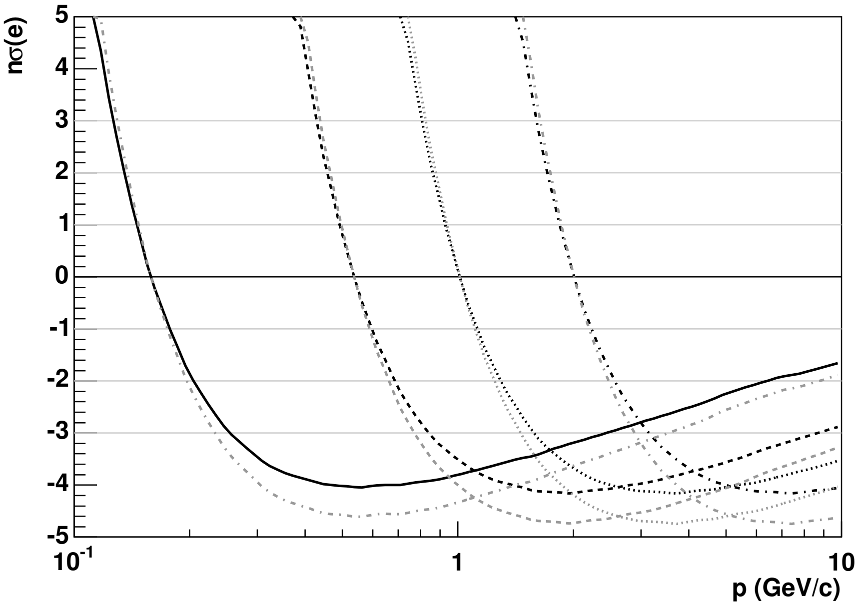

Figure 4.5: Distance of pions (solid line), kaons (dashed line), protons (dotted line) and deuterons (dashed-dotted line) mean $\mathrm{d}E/\mathrm{d}x$ to electron mean $\mathrm{d}E/\mathrm{d}x$ in units of standard deviations as function of particle momentum for 60 cm (black lines) and 100 cm (gray lines) sampled track length.

What matters for the electron identification in the end is the fraction of hadrons and electrons which are accepted by a cut on the measured energy loss $(\mathrm{d}E/\mathrm{d}x)_{\mathrm{min}} \leq \mathrm{d}E/\mathrm{d}x \leq (\mathrm{d}E/\mathrm{d}x)_{\mathrm{max}}$. Since the $\mathrm{d}E/\mathrm{d}x$ values depend on the measured track lengths it is more convenient to use a $\sigma(e)$ cut which takes the resolution already into account $n_{\mathrm{min}}\sigma(e) \leq \sigma(e) \leq n_{\mathrm{max}}\sigma(e)$. To quantify the effect of the cut, the particle identification efficiency ϵ_{PID} is introduced as the number of particles of a given species (e.g. electrons, hadrons) which are accepted by the $\mathrm{d}E/\mathrm{d}x$ cut:

$$\epsilon_{\mathrm{PID}} = \frac{\sum N_i \mid_{n_{\min} \leq \sigma(e) \leq n_{\max}}}{\sum N_i} \tag{4.7}$$

The also commonly used hadron rejection factor is given by inverse of the hadron efficiency, i.e. $\mathcal{R}_h = \sum_{\text{hadrons}} f_i 1/\epsilon_{\mathrm{PID}}(i)$ with f_i the fraction of hadrons of species i to all hadrons.

Figure 4.6 shows the pion identification efficiency $\epsilon_{\mathrm{PID}}(\pi)$ as function of the particle momentum for different $n\sigma(e)$ cuts. The corresponding electron identification efficiencies $\epsilon_{\mathrm{PID}}(e)$ can be easily calculated, given the gaussian form of the $\mathrm{d}E/\mathrm{d}x$ distribution. The results are tabulated in table 4.1. Smaller identification efficiencies (i.e. higher rejection factors) are achieved for the other hadrons due to their larger separation to the electrons.

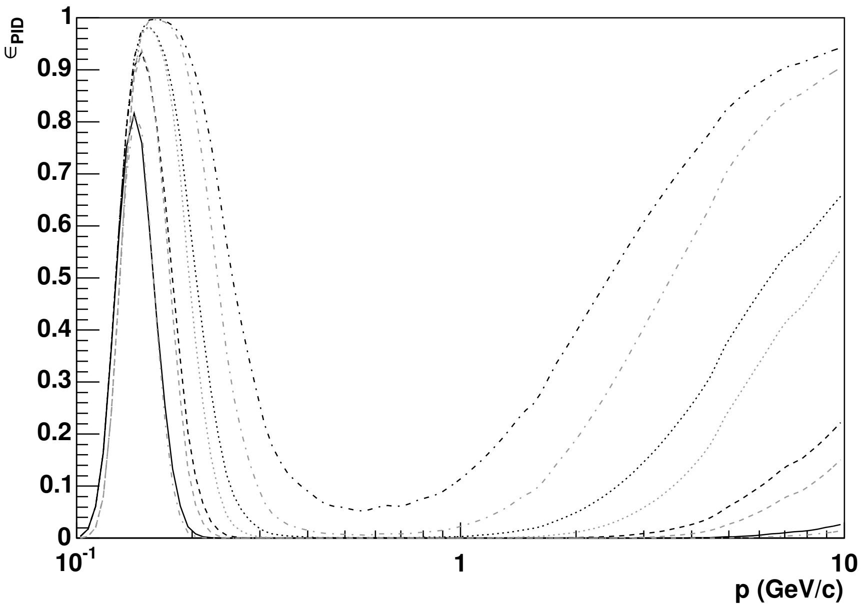

Figure 4.6: Pion identification efficiency $\epsilon_{\mathrm{PID}}(\pi)$ as function of particle momentum p for different $\sigma(e)$ cuts (solid line $0 \leq \sigma(e) < \infty$, dashed line $-1 \leq \sigma(e) < \infty$, dotted line $-2 \leq \sigma(e) < \infty$ and dashed-dotted line $-3 \leq \sigma(e) < \infty$) for 60 cm (black lines) and 100 cm (gray lines) sampled track length.

4.1.2 Electron Identification with the Barrel Electromagnetic Calorimeter

As mentioned in the introduction to this chapter, the STAR barrel electromagnetic calorimeter (BEMC), described in 3.2.2, provides additional electron identification capabilities. It measures the energy deposited by the particles traversing its volume. Together with the momentum measurement of the TPC a further electron/hadron discrimination is possible.

Electrons entering the BEMC develop an electromagnetic cascade in which they deposit their energy in the calorimeter material. They loose most of their energy by

$n_{\min}\sigma_e$	$\epsilon_{\mathrm{PID}}(e)$	$\epsilon_{\mathrm{PID}}(\pi)$ [A]	$\epsilon_{\mathrm{PID}}(\pi)$ [B]	$\epsilon_{\mathrm{PID}}(\pi)$ [C]
-3	$\sim$ 99%	52%	78%	87%
-2	$\sim$ 97%	15%	33%	52%
-1	$\sim$ 84%	2%	5%	14%
0	50%	$<$ 1%	$<$ 1%	1%
		[A] 2 GeV/$c \leq p \leq$ 4 GeV/c [B] 4 GeV/$c \leq p \leq$ 6 GeV/c [C] 6 GeV/$c \leq p \leq$ 8 GeV/c		

Table 4.1: Average pion identification efficiency $\epsilon_{\mathrm{PID}}(\pi)$ for different $n_{\min}\sigma(e)$ cuts and momentum ranges. The corresponding electron identification efficiency $\epsilon_{\mathrm{PID}}(e)$ is shown as well. See also figure 4.6.

radiation via bremsstrahlung which produces high energy photons. These photons then produce an electron-positron pair by pair-production in the Coulomb field of the nuclei of the detector material or produce Compton electrons. These electrons and positrons, in turn, radiate again photons which decay again into electrons and positrons and so on, a process called cascade shower or multiplicative shower. The cascade shower ends when the produced photons and electrons have low momenta (below few hundred keV). The remaining photons produce then low energy electrons via the photoelectric effect and via Compton scattering. The low momentum electrons energy loss gets more and more dominated by collision energy. In this way the incoming particle energy is absorbed by the calorimeter medium.

The length of the shower development in the calorimeter medium is usually expressed in units of radiation length X_0 which represents the mean-path length of an electron in a material. It can be calculated from

$$X_0 = \frac{X_{g0}}{\rho} \quad \text{with} \quad \frac{1}{X_{g0}} = 4\alpha\frac{N}{A}Z(Z+\varsigma)r_e^2 \ln\frac{183}{Z^{1/3}} \tag{4.8}$$

with ρ the density of the medium, α the fine-structure constant, N the Avogadro constant, A, Z the atomic weight and mass number of the medium and r_e the classical electron radius [LR00]. ς is a correction for the contribution from atomic electrons to the overall bremsstrahlung process. The calculated values can be found in [E$^+$04]. The natural unit for the shower development lateral to the incident particle direction is given by the Molière radius

$$R_M = \left(\frac{E_M}{\epsilon_c}\right) X_0 \tag{4.9}$$

with $E_M = \sqrt{\frac{4\pi}{\alpha}}m_e = 21.2$ MeV and ϵ_c the critical energy at which electrons lose as much energy in collisions as in radiation (7.42 MeV for Pb).

Curcial for an electron energy measurement are mainly the calorimeter depth and radius which contain the incident electron shower. According to an approximation by Rossi [Ros64], 98% of the incoming particle energy are deposited in

$$L(98\%) \approx 3t_{cg} \quad \text{where} \quad t_{cg} = 1.01\left[\ln\left(\frac{E}{\epsilon_c}\right) + d\right] \tag{4.10}$$

is the shower depth at which half of the particle incident energy has been deposited with E the electron energy, ϵ_c the critical energy and $d = 0.4$. For the STAR electromagnetic calorimeter a radiation length of 20 X_0 at $\eta = 0$ and further increasing with η has been calculated[4], therefore the whole longitudinal shower will be con-

[4] X_0 for Pb 0.56 cm

tained in the detector material. The 95% radial electron shower containment R_e is given by

$$R_e(95\%) = 2R_M \tag{4.11}$$

The typical individual tower size of the BEMC has been chosen to fullfill this requirement[5][6] for electrons which hit the tower in its center.

Hadrons in contrast show a much more complex shower development. It is driven mainly by the production of a wide spectrum of secondary hadrons which interact themself with the detector material. An important fraction of secondaries produced are electromagnetic decaying particles (e.g. π^0), where the decay photons or electrons produce an electromagnetic cascade as described above. The hadrons themself loose energy mainly by ionization and nuclear breakup.

The longitudinal development of an hadronic showers is characterized in units of interaction length

$$\lambda_A = \frac{A}{[N\rho\sigma_{nA(\mathrm{inelastic})}]} \approx 35\frac{A^{1/3}}{\rho} \tag{4.12}$$

with A, N, ρ the atomic weight, the Avogadro constant and the density of the calorimeter material[7]. $\sigma_{nA(\mathrm{inelastic})}$ is the inelastic cross section of a particle of species n with a nucleus with atomic weight A. A typical approximation at which calorimeter depth the hadron has lost 95% of its energy is

$$L_{95\%} \approx t_{max} + 2.5\lambda_A \tag{4.13}$$

where $t_{max} \approx 0.2\ln(E) + 0.7$ is the cascade maximum depth with a following exponential decay described by λ_A. The 95% radial containment is given by

$$R_{95\%} \approx \lambda_A \tag{4.14}$$

The different longitudinal and radial development of electromagnetic and hadronic showers allows to distinguish electrons and hadrons by measuring their energy deposition distribution. The BEMC provides two measurements of the longitudinal energy distribution, the total energy deposited in a tower[8] and the energy deposited in the first $(1 - 1.5)\,X_0$ of the tower (preshower (BRPS) measurement). Following equation 4.10 electrons deposit all their energy in the tower while hadrons deposit only a fraction of their energy according to equation 4.13. Hadrons with significant energy deposition in the towers typically produced a leading π^0 in the first collision which decays into photons which in turn develop electromagnetic showers which are still mainly contained in the BEMC. In comparison to electrons a smaller fraction of the total energy is deposited in the preshower part of the tower, allowing a further electron/hadron discrimination for these special cases. Unfortunately the BPRS was not operational for the data analyzed in this thesis and is thus not further discussed.

The BEMC response for electrons and hadrons with momentum 4 GeV $\leq p \leq$ 6 GeV from GEANT detector simulations is shown in figure 4.7. As expected the measured energy is quite different for hadrons and electrons. This becomes more clearly visible in figure 4.8 which shows the energy deposited in the BEMC E_{bemc} compared to the particle energy E. The electrons peak at $E_{\mathrm{bemc}}/E = 1$ while the

[5] Due to the projective geometry of the BEMC this is only true for electrons originating from the center of STAR

[6] $R_M = 1.6$ cm for Pb

[7] $\lambda_A = 17.1$ cm for Pb

[8] $\Delta\eta = 0.05 \times \Delta\phi = 0.05$, see section 3.2.2 for details

hadrons show a broad structure around 0.5 for particles starting to shower in the calorimeter, and at < 0.1 for particles just traversing it. Antiprotons show a slightly different response depositing on average a larger fraction than the other hadrons due to the additional annihilation channel.

The width of the electron peak allows to calculate the energy resolution $\Delta E/E$, which is typically parametrized for calorimeters as $\Delta E/E = a \oplus b/\sqrt{E}$ where $\oplus$ represents an addition in quadrature. While a accounts for detector non-uniformity and calibration uncertainties, b represents statistics related fluctuations such as intrinsic shower fluctuations, photoelectron statistics, dead material at the front of the calorimeter and sampling fluctuations. The expected values from test beam data for the BEMC where $a = 2\%$ and $b = 16\%$ which are also reproduced by the detector simulations with $a = 1.5\%, b = 14\%$ from photoelectron statistics alone. The resolution currently achieved in data is slightly worser with $b < 18\%$.

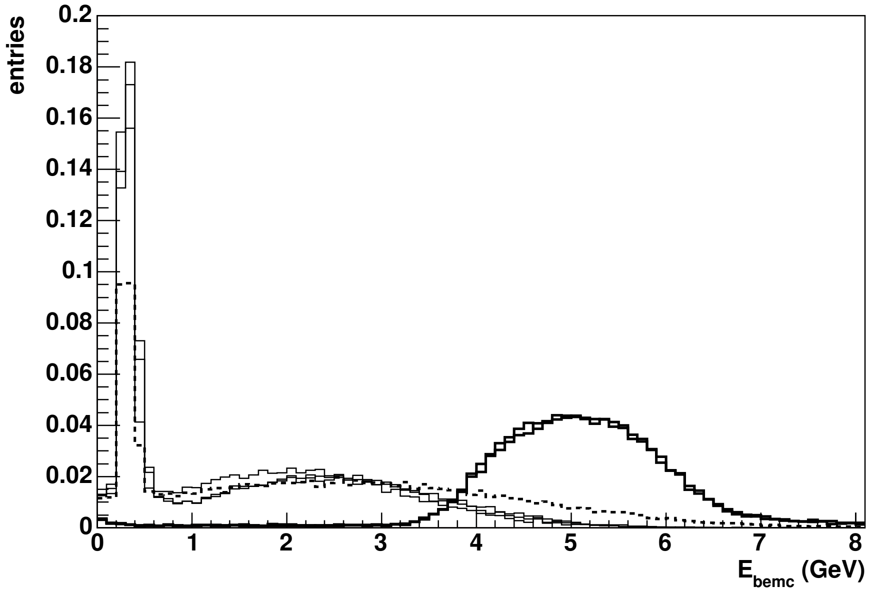

Figure 4.7: BEMC response for electrons (e^+, e^-, thick solid line), selected hadrons (π^+, π^-, p, solid lines) and antiprotons (dashed line) with energy $4 \leq E \leq 6$ GeV.

The energy of the incident particle is of course unknown for particles in the experiment. What is known from the TPC measurement is their momentum. Experimentally accessible is therefore the E_{bemc} to momentum p ratio[9] which is shown in figure 4.9. As expected the electrons still peak at 1 since their energy is well approximated by their momentum due to the small electron mass. The hadron distributions shift to slightly larger values but are still clearly distinguishable from the electron distribution, at least in this relatively high momentum region.

The electron/hadron discrimination so far has only used the differences in the longitudinal shower development. However as mentioned earlier there are also significant differences in the radial shower development, as obvious from equations 4.11 and 4.14. Some use of this information is implicit by the mechanical

[9]The E/p ratio is chosen because the error on the energy measurement is Gaussian in E while the error on the momentum measurement is Gaussian in $1/p$ as the momentum is determined by the curvature κ, see section 4.1.1.

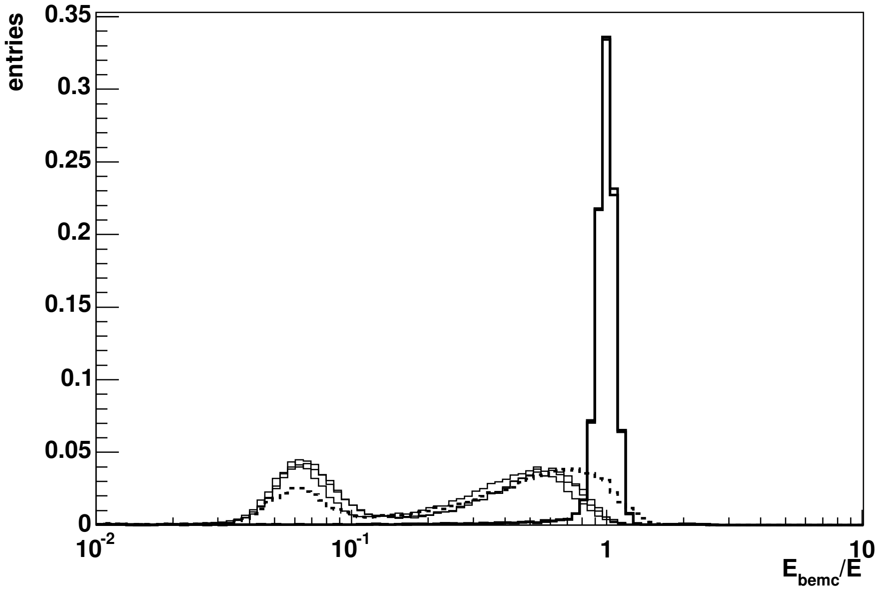

Figure 4.8: Ratio E_{bemc}/E of energy measured in the BEMC to energy of the particle for electrons and hadrons ($e^{\pm}$ thick solid lines, $\pi^{\pm}, p$ solid lines and $\overline{p}$ dashed line).

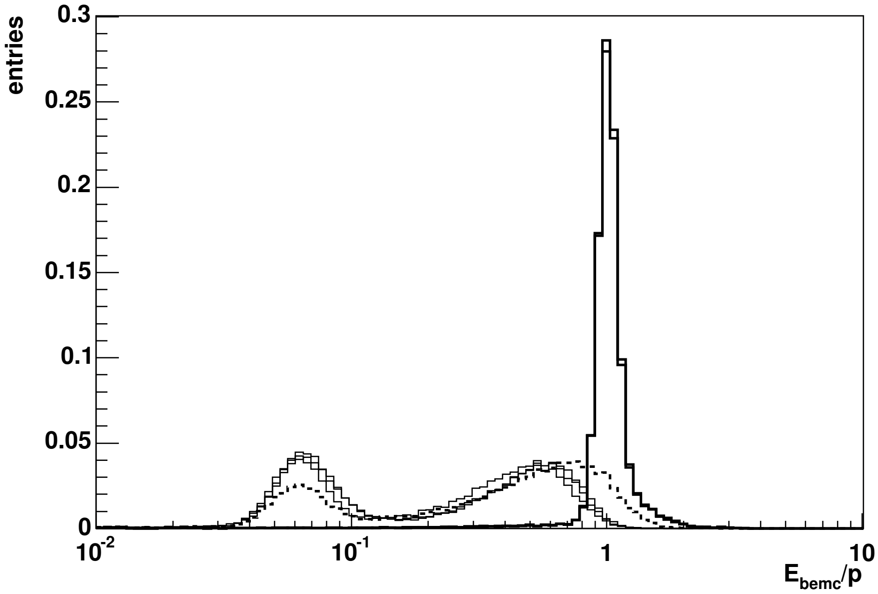

Figure 4.9: E_{bemc}/p ratio for electrons (thick solid line), pions and protons (solid lines) and antiprotons (dashed line) with momentum $4 \leq p \leq 6$ GeV/c .

structure of the BEMC which is segmented into towers as mentioned earlier. The experimentally measured quantity is the energy deposited in a tower E_{tower} and not the total energy deposited by the particle E_{bemc} used so far. The individual tower size was chosen to be much larger than the Molière radius and a typical electromagnetic shower deposits most of its energy in it. However the tower size is still small compared to the radial size of a fully developed hadronic shower and thus only a fraction of its energy is measured, further enhancing the different energy depositions between electrons and hadrons. More information on the radial shower development and shape can be gained with the Shower Maximum Detector information (BSMD) which provides detailed information on the shape of the energy deposition at ≈ 5.6 radiation lengths. However significant parts of the BSMD could not be properly operated during the data taking period analyzed for this thesis and thus this information is not used further.

Turning back to the enhanced electron/hadron separation by exploiting the different radial shower development using the tower structure of the BEMC, one has to realize that this depends on the assumption that the electron deposits all of its energy in a single tower. While this is true for electrons hitting the tower in its center, it becomes wrong for electrons hitting close to the borders since only part of the containment area of equation 4.11 is still within the tower. Some leakage to neighboring towers has to be expected. To demonstrate this effect the distance between the particle incident position and the tower center in pseudorapidity-azimuthal angle space gets defined as:

$$d = \sqrt{\left(\eta_{\text{tower}} - \eta_{\text{particle}}\right)^2 + \left(\phi_{\text{tower}} - \phi_{\text{particle}}\right)^2} \tag{4.15}$$

Figure 4.10 shows the electron E_{tower}/p ratio for three different distance d bins. Already the first bin with $d \leq 0.01$ has a shift to smaller E_{tower}/p values compared to the E_{bemc} peak and starts to develop a shoulder on the left side, indicating that some energy is lost already at small distances. As the distance of the incident particle to the tower center increases further, the peak position shifts to even smaller values. At the same time the distribution develops a large tail to low E_{tower}/p values.

A possibility to deal with this leakage effect is to accept a varying electron identification efficiency as function of the distance between tower center and particle hit position and correct for it during analysis. The single electron spectra analyzes in STAR [Sua04] used this method so far. But it has the disadvantage that using BEMC only information (i.e. without track information from the TPC), the electron energy is systematically and uncorrectable underestimated due to the unknown distance to the tower center. However to get a reasonable number of Upsilons on tape a good energy approximation already on the trigger level as to be achieved (i.e. with BEMC information only) as shown in section 4.3.

An experimentally accessible way to get close to the goal of a measured electron energy independent of the particle hit to tower center distance is a technique called *clustering*, i.e. adding the energy which leaked into neighboring towers to the energy of the incident tower. The algorithm used here takes the 8 neighboring towers, sorts them by energy and adds the energy of the $n-1$ highest energy towers to the energy of the incident tower to calculate a n-tower cluster:

$$\begin{aligned} &E_{\text{cluster}}(1) = E_{\text{tower}} \\ &E_{\text{cluster}}(n) = E_{\text{tower}} + \textstyle\sum_{i=2}^{i=n} E_{\text{tower}}(i) \quad \text{with} \quad n \geq 2, E_{\text{tower}}(i) \leq E_{\text{tower}}(i+1) \end{aligned} \tag{4.16}$$

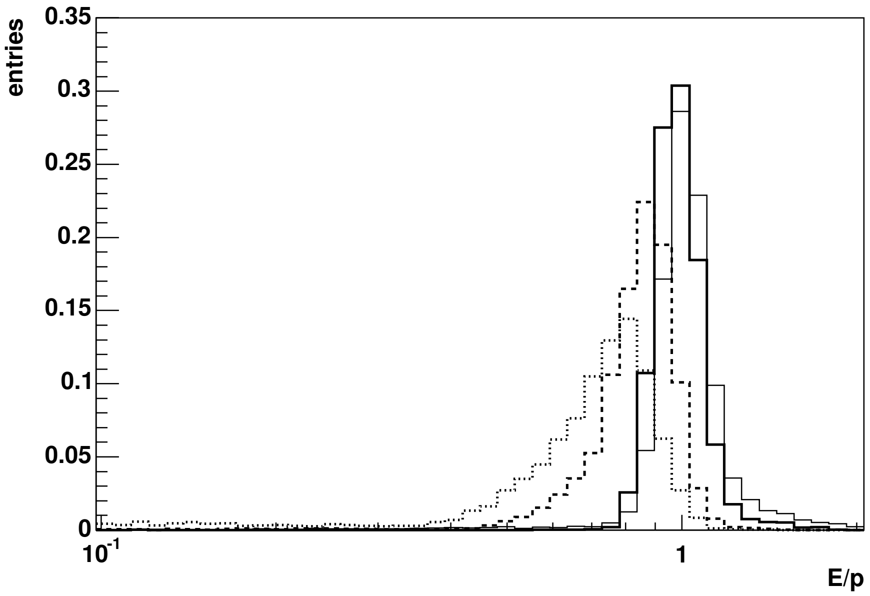

Figure 4.10: E_{tower}/p ratio for three different distance bins: $d \leq 0.01$ (thick solid curve), $0.02 \leq d \leq 0.025$ (dashed curve) and $d \geq 0.025$ (dotted curve). For comparison the E_{bemc}/p distribution is also shown as small solid curve.

Figure 4.11 shows the results of this algorithm for different number of towers per cluster and the three distance between tower center and particle hit position already used in figure 4.10. The most probable E_{cluster}/p value is calculated for each cluster and then normalized to the most probable value of the total energy to momentum ratio E_{bemc}/p.

The one tower per cluster ratio $E_{\mathrm{cluster}}(1)/p$ is by definition equal to the single tower ratio E_{tower}/p and indeed we see for $n = 1$ the shifts already observed in figure 4.10. What becomes obvious here is that even for electrons which hit the tower close to its center a small fraction of the energy leaks into neighboring towers. Since the nominal BEMC calibration uses the E_{tower}/p ratio and forces this to be one, the energy measured by the clustering algorithm will be always larger than the electron energy by a few percent.

A possible caveat of the clustering algorithm is the background energy from other particles in neighboring BEMC towers, which results in an overestimate of the electron energy. The mean value of background energy and the fluctuations of this quantity depend of course on the studied collision system and also on details of the physics process. The fragmentation of high energy partons (i.e. jets) for example will result in many particles close to each other in the calorimeter and the cluster algorithm will produce slightly larger energy measurements for electrons in jets than for e.g. decay electrons. One can minimize the effect by choosing the minimum number of towers per cluster that still gives a good energy approximation independent of the particle hit to tower center distance. While the deviations for 2 tower clusters are still quite large, the deviations for three tower clusters are below 3% as shown in figure 4.11. Three tower clusters will therefore be used for the further analysis.

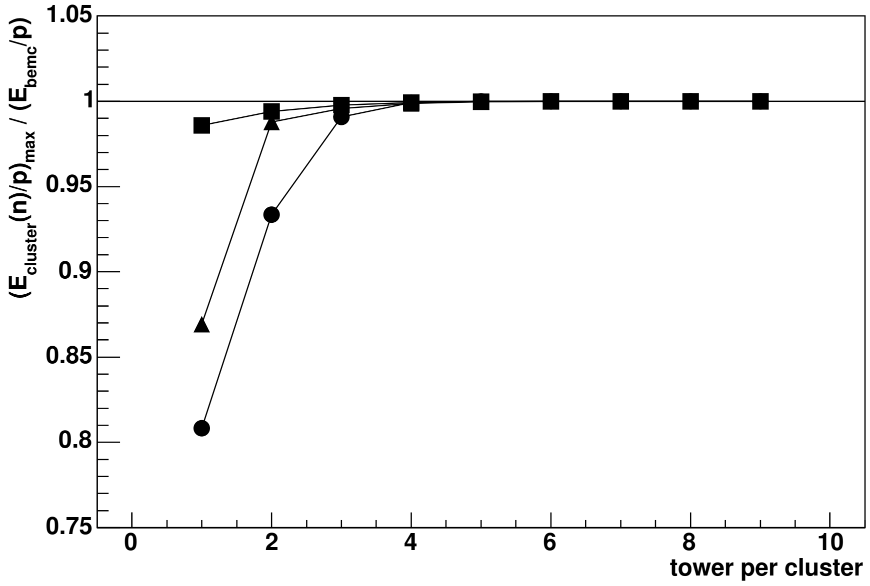

Figure 4.11: Position of the $E_{\text{cluster}}(n)/p$ peak relative to the E_{bemc}/p peak position for different number n of towers per cluster. Boxes show the result for particles which have a distance $d \leq 0.01$ to the tower center, triangles for particles with $0.02 \leq d \leq 0.025$ and circles $d \geq 0.025$.

Coming back to the original question how well electrons can be distinguished from hadrons, the particle identification efficiency ϵ_{PID} gets defines in analogy to the previous section 4.1.1 as the number of particles of a given species (e.g. electrons, hadrons) which are accepted by the PID cut, i.e. the E/p cut:

$$\epsilon_{\text{PID}} = \frac{\sum N_i \mid_{(E/p)>(E/p)_{\text{cut}}}}{\sum N_i} \tag{4.17}$$

The also commonly used hadron rejection factor $\mathcal{R}_h$ is then given by inverse of the hadron identification efficiency, i.e. $\mathcal{R}_h = \sum_{\text{hadrons}} f_i 1/\epsilon_{\text{PID}}(i)$ with f_i the fraction of hadrons of species i to all hadrons. The goal is to find an $E/p \mid_{\text{cut}}$ setting which accepts most of the electrons, i.e. high particle identification efficiency for electrons, while at the same time accepts only few of the hadrons, i.e. a low particle identification efficiency for hadrons.

Figure 4.12 shows ϵ_{PID} for electrons, pions, protons and antiprotons as function of the $E_{\text{cluster}}(n)/p$ cut for 1 and 3 tower cluster and three different momentum bins. As expected the electron identification efficiency stays high for $E/p \mid_{\text{cut}}$ values up to unity. In contrast the hadron identification efficiency drops quite fast when increasing the $E/p \mid_{\text{cut}}$ value. Both for the single tower and the three tower case the identification efficiency for hadrons at the same $E/p \mid_{\text{cut}}$ decreases with increasing momentum, as expected from the improved energy resolution of the calorimeter and the change of the shower shapes.

More relevant for this work are however the hadron identification efficiencies $\epsilon_{\text{PID}}(h)$ at high electron identification efficiencies $\epsilon_{\text{PID}}(e) \geq 90\%$ due to the expected low Υ yield. Figure 4.13 shows ϵ_{PID} as function of $\epsilon_{\text{PID}}(e)$ for pions, protons and antiprotons. Except for the antiprotons ϵ_{PID}, values of less than a few percent hadron identification efficiency are achieved for $\epsilon_{\text{PID}}(e) = 90\%$, as expected further decreasing with increasing particle momentum. Surprinsigly the use of the energy calculated by 3-tower clusters results in significantly smaller hadron identification efficiencies at high electron identification efficiencies, in contrast to the behaviour at low $\epsilon_{\text{PID}}(e)$ where better results are achieved with the single tower energy. The antiproton identification efficiency is significantly higher due to the additional anihaltion channel, with $\epsilon_{\text{PID}}(\overline{p}) \approx 25\%$ at low momentum. The $E/p\,|_{\text{cut}}$ values for $\epsilon_{\text{PID}}(e) = 90\%$ and 95% as well as the hadron identification efficiencies for these cuts are listed in table 4.2.

Further improvement of the hadron misidentification, i.e. lower hadron identification efficiency, is expected by the future use of the BPRS and BSMD subdetectors. Unfortunately they were not operational during the 2003/2004 run and could therefore not be used for the data analysis presented in chapter 5. The results in this subsection are based on single particle simulations only. However in the real data also other particles are present, whose showers may overlap, resulting in an increased energy deposit in the tower, in turn influencing the efficiencies and cut positions just calculated. The largest effect is obviously expected for the high multiplicity environment of central heavy ion collisions. Especially challenging are here π^0s and the large number of photons from hadronic decays which also deposit all of their energy in the BEMC. Studies of simulated HIJING events as well as of particles embedded into real central $Au + Au$ events have shown an increase of the hadron identification efficiencies of up to a factor 2-3 for momenta around 2 GeV/c, see also the analysis of the $Au + Au$ data from the 2003/2004 run presented in chapter 5.

In summary the BEMC in combination with the TPC achieves a hadron rejection factor ~ 50 ($\epsilon_{\text{PID}} \approx 2\%$) in the momentum region of the Upsilon daughter electrons, while at the same time accepting 90% of the electrons. Applying the $E/p\,|_{\text{cut}}$ cut to the data thus enhances the electron to hadron ratio by a factor 45, which will prove to be crucial in reducing the background from hadronic combinations in the Upsilon mass region. It is also interesting to note that using energies calculated from 3 tower-cluster results in a better performance than using the energy from only one tower, at least at the high electron identification efficiencies required by the Upsilon reconstruction.

$\epsilon_{\text{PID}}(e^{\pm})$	$(E/p)_{\text{cut}}$	$\epsilon_{\text{PID}}(\pi^{\pm})$	$\epsilon_{\text{PID}}(\overline{p})$	$(E/p)_{\text{cut}}$	$\epsilon_{\text{PID}}(\pi^{\pm})$	$\epsilon_{\text{PID}}(\overline{p})$
	single tower			$n = 3$ tower cluster		
2 GeV/$c \leq p \leq$ 4 GeV/c						
90%	0.65	6%	25%	0.93	3%	27%
95%	0.53	12%	37%	0.81	6%	36%
4 GeV/$c \leq p \leq$ 6 GeV/c						
90%	0.65	4%	12%	0.93	2%	10%
95%	0.53	10%	21%	0.87	3%	13%
6 GeV/$c \leq p \leq$ 8 GeV/c						
90%	0.7	2%	5%	0.93	1%	5%
95%	0.53	8%	13%	0.87	2%	7%

Table 4.2: Hadron identification efficiencies for pions and electrons at an electron identification efficiency of 90 and 95% using single tower and three tower cluster.

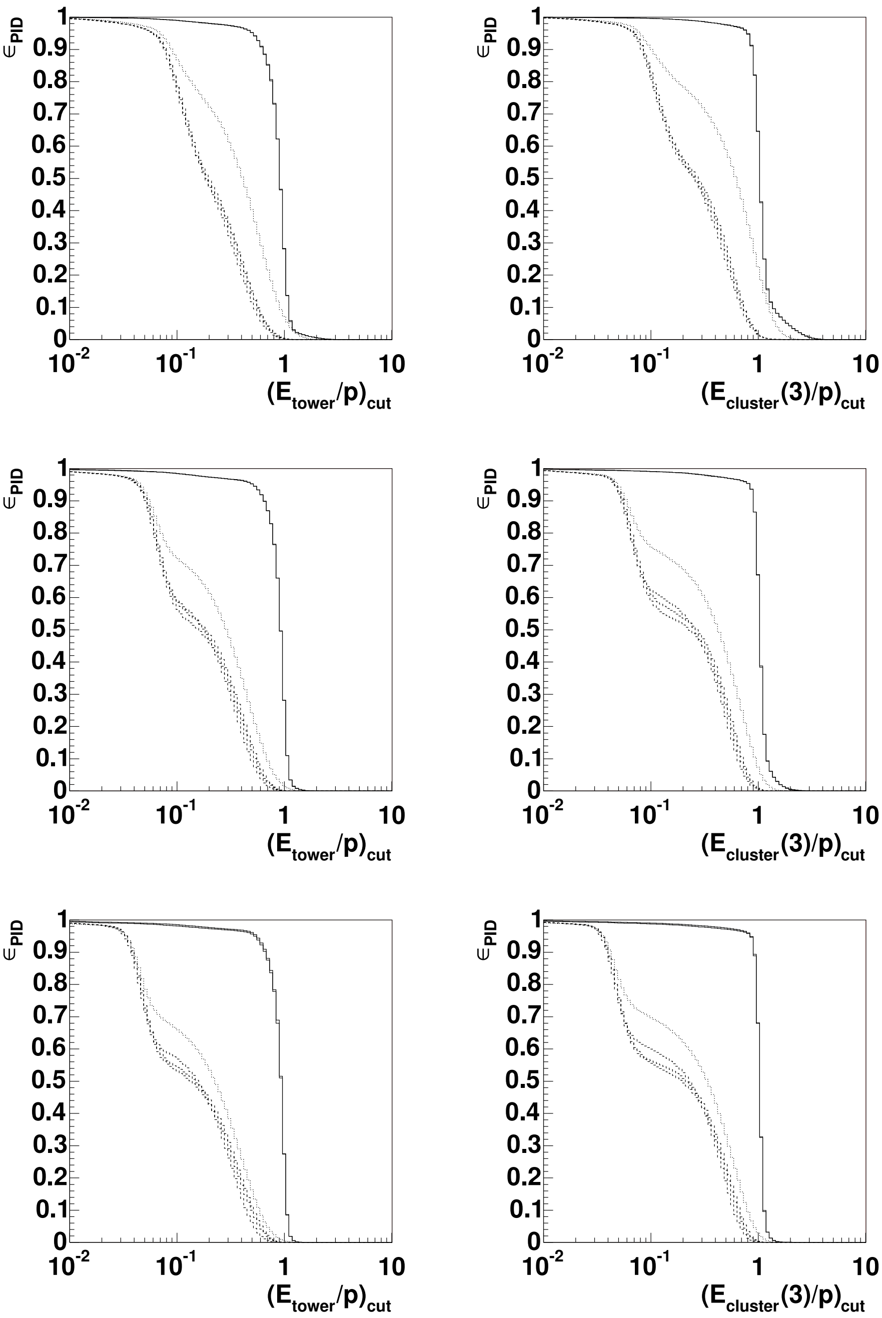

Figure 4.12: Particle identification efficiency for electrons (solid line), pions, protons (dashed lines) and antiprotons (dotted line) as function of the $E_{\mathrm{cluster}}(n)/p$ cut. Left column uses $n = 1$, i.e. the single tower energy E_{tower}, the right $n = 3$. Three different particle momentum bins are shown, 2 GeV/$c \leq p \leq$ 4 GeV/c in the first row, 4 GeV/$c \leq p \leq$ 6 GeV/c in the second row and 6 GeV/$c \leq p \leq$ 8 GeV/c in the last row.

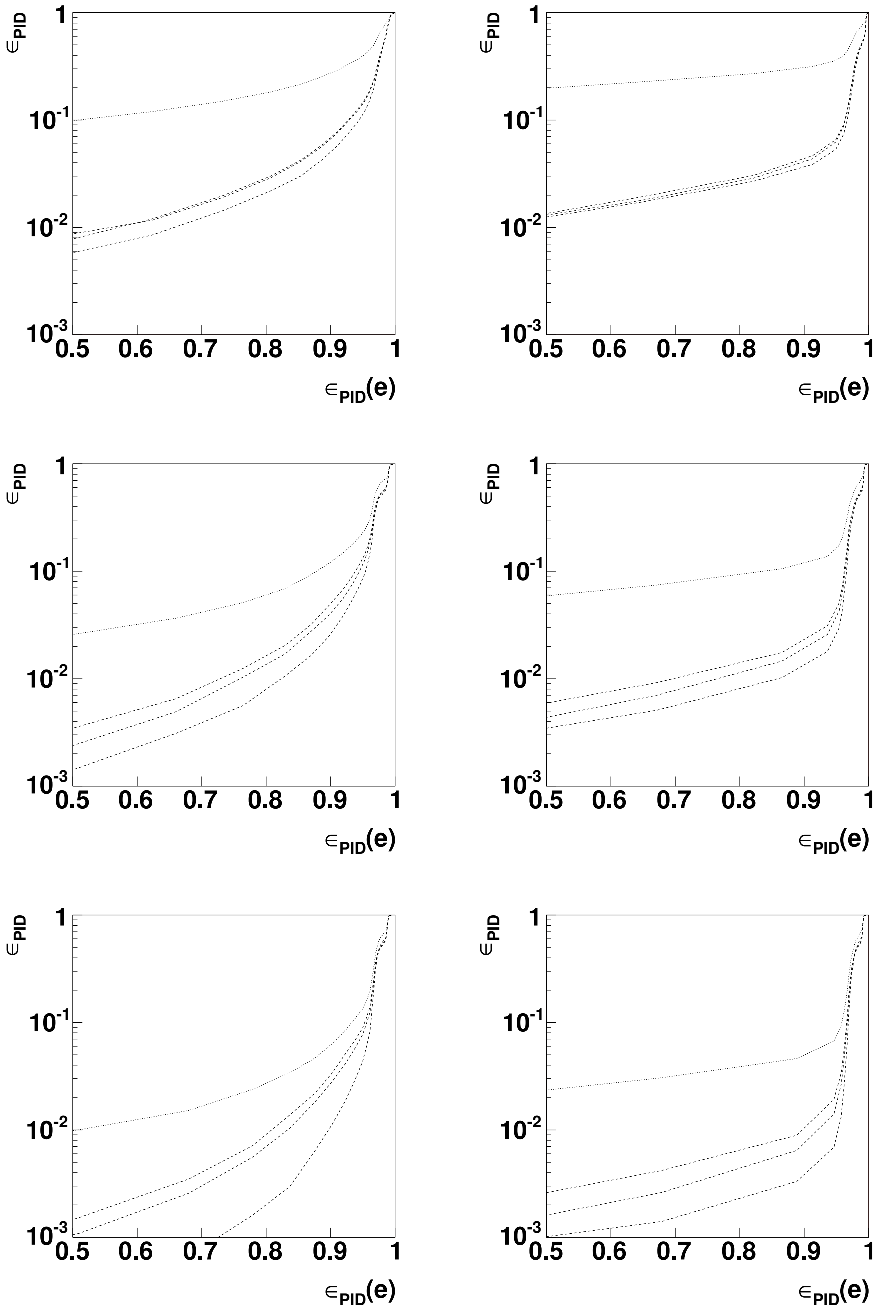

Figure 4.13: Particle identification efficiency as function of the electron identification efficiency for pions, protons (dashed lines) and antiprotons (dotted line) for two EMC cluster settings, left column single tower only, right column three tower cluster. Three momentum bins are shown, upper row 2 GeV/$c \leq p \leq 4$ GeV/c , middle row 4 GeV/$c \leq p \leq 6$ GeV/c and lower row 6 GeV/$c \leq p \leq 8$ GeV/c .

4.2 Upsilon Reconstruction

The reconstruction of the Upsilon decays into two electrons in STAR is made using the *invariant mass* reconstruction technique. It exploits the energy and momentum conservation of the Υ decay. By measuring the four-vectors v_i for both daughters and building *invariant mass pairs* (v_{e+}, v_{e^-}) one can thus reconstruct the four vector of the Upsilon candidate by a simple addition:

$$v_\Upsilon = \begin{pmatrix} p_x \\ p_y \\ p_z \\ E \end{pmatrix}_\Upsilon = \begin{pmatrix} p_x \\ p_y \\ p_z \\ E \end{pmatrix}_{e^+} + \begin{pmatrix} p_x \\ p_y \\ p_z \\ E \end{pmatrix}_{e^-} = v_{e^+} + v_{e^-} \tag{4.18}$$

Using the metric of the Lorentz space the mass of the reconstructed particle is then given by $m = |v_\Upsilon| = \sqrt{p_x^2 + p_y^2 + p_z^2 - E^2}$.

Combinations of electrons which did not originate from an Upsilon decay will e.g. not give the right mass and can thus be distinguished from real decays. There will be however some invariant mass pairs which by chance get reconstructed with a mass in the Upsilon region and thus result in *background counts* under the Upsilon signal. To extract the number of Upsilon events an estimate of the number of these background entries in the signal region is needed and thus an understanding of the different background sources. To first order they separate into two classes, the first one consisting of correlated electron-positron pairs originating from other physical processes (e.g. Drell-Yan pairs, correlated electrons from semileptonic charm and bottom decays), the second class containing random combinations from electrons and positrons originating from different processes[10].

The background entries belonging to the second class are also called *combinatorical background*. To estimate the background counts one can use the fact that all signal pairs, i.e. the Upsilon decays, have daughters with unlike sign electric charge (e^+e^-). Background pairs from random combinations are however not sensitive to the sign of the daughters, i.e. will have both pairs with the same sign and with unlike sign. Under the assumption that the ratio between electrons and positrons is roughly unity, one can estimate the number of unlike sign pairs from the number of like sign pairs:

$$N_{e^+e^-} \approx 2\mathcal{R}\sqrt{N_{e^+e^+} \times N_{e^-e^-}} \tag{4.19}$$

where the factor $\mathcal{R} \approx 1$ was introduced to account for e^+/e^- ratios not exactly equal to unity and differences in the electron and positron momentum distributions. Subtracting this approximated number from the signal distribution should eliminate the combinatoric background.

This whole procedure of *likesign background subtraction* works of course only if the assumption that there are no correlated, i.e. signal, pairs where both daughters have the same sign. It has been pointed out [CBM02] that semileptonic decays of B mesons which produce a D meson which later also decays semileptonic, might produce correlated signal pairs and one thus might overestimate the combinatoric

[10] Electrons and positrons in this section refers to all particles identified as electrons/positrons by the particle identification methods discussed in section 4.1.1 and 4.1.2. Since the identification is not perfect, e.g. there remains some low probability to also select hadrons, the sample is not a pure electron/positron sample but contains some hadrons. The exact fraction depends strongly on the PID cuts and is not further discussed here. Due to the small e/h ratio the uncorrelated background will however be affect by this contamination, making random combinations of electrons with hadrons or even hadron-hadron correlations a significant background source.

background. As long as a clear signal is observed this might not be relevant but might become important for upper limit estimates.

An alternative to like-sign background subtraction is *event mixing*. In this technique all e^+ from one event are mixed with all e^- from another event and the invariant mass pairs are calculated. Obviously there can not be any correlated unlike-sign pairs and the invariant mass pair spectrum is an estimator of the uncorrelated background. The main advantage of this method is the reduced statistical error on the background spectrum since the particles of every event can be mixed with the ones from several others, resulting in pairs from $2N_{\text{events}}\,(N_{\text{events}}-1)$ events instead of pairs from only N_{events} events. The main drawback of the method is the sensitivity to the exact event characteristics. It has been demonstrated that only events of same multiplicity and primary vertex z position can be mixed and that the event ensemble from which the background spectrum is calculated has to have the same multiplicity and vertex z distribution as the original ensemble. Also the correct normalization remains debated.

The case of the Υ analysis is even more complicated. As discussed later in section 4.3 sufficient signal statistics can only be accumulated by the use of a special trigger. This trigger condition needs to be also fullfilled in the mixed events. Otherwise the bias on the invariant mass distribution would not be correctly reproduced, especially since the trigger algorithm uses also correlations between both daughter particles of the invariant mass pair for its decision. This results in another huge cut in available event statistics, reducing further the advantage of the mixed-event technique over the like-sign technique. The analysis of the (very statistics limited) data from the 2003/2004 run described in chapter 5 did not result in a single mixed event which fullfilled the trigger conditions but produced at least a like-sign background entry, demonstrating the difficulties. The mixed-event method is thus not further discussed but it might be worthwhile to try it again if much more statistics is accumulated, at least as a cross check of the like-sign method.

As mentioned earlier another source of background entries originates from correlated electron-positron pairs from physical processes other than the Upsilon decays. These background counts represent a signal by themself and can thus not be removed by any of the techniques mentioned above. The most important process which result in electron-positron pairs in the Upsilon invariant mass region are:

- Drell-Yan pairs: $q\bar{q} \rightarrow \gamma^* \rightarrow l^+l^-$
- Electrons from decays of heavy hadrons from fragmentation of heavy quark (c,d) jets

The electrons from the decay of heavy hadrons produced in the fragmentation of heavy quark jets might be a significant source because fragmentation functions show that heavy flavor mesons retain a large fraction of the momentum of the primordial heavy quark. The subsequent semileptonic decay of the $D(B)$ mesons might result in a correlated electron-positron pair with relative high momentum and high invariant mass. PYTHIA simulations have however shown that the background yield from both processes under the Υ peak is less than a few 10^{-1} of the signal yield, making it insignificant for an Υ yield measurement. These simulations only reflect the situation in $p+p$ collisions, how this ratio is modified by nuclear effects in a heavy ion collision remains to be seen (there is some indication that heavy mesons out of heavy quark jets are suppressed at high p_T compared to $p+p$). Also both processes produce a monotonic mass distribution, any remaining background from these sources can thus be estimated by analyzing the entries above the Υ peak(s).

Common to both signal and background counts is the question how many and how well the invariant mass pairs are reconstructed. Following equation 4.18 the answer to these questions will be dominated by the momentum determination of the daughter particles. Due to the limited detector acceptance only daughter electrons at midrapidity are measured and thus only a fraction of all Upsilon decays as determined in the next subsection 4.2.1. In addition the momentum measurement with both TPC and/or BEMC has a non-negligible resolution as discussed in 4.1.1 and 4.1.2. While this results only in a smearing of the (continuous) background, the peak width of the Upsilon will significantly increase as shown in 4.2.2.

4.2.1 Geometrical Acceptance

Turn first to the question which fraction of the Upsilon decays will have both of the daughter electrons in the combined TPC+BEMC acceptance and can thus be reconstructed. To quantify this, the *geometrical acceptance* ϵ_{geo} gets defined as

$$\epsilon_{\text{geo}} = \frac{N^{\text{rec}}_{\Upsilon \to e^+e^-}}{N^{\text{prod}}_{\Upsilon \to e^+e^-}} \tag{4.20}$$

with $N^{\text{prod}}_{\Upsilon \to e^+e^-}$ the number of produced and $N^{\text{rec}}_{\Upsilon \to e^+e^-}$ the number of reconstructable Upsilons.

To determine the number of reconstructable Upsilons the GEANT simulation of the STAR detector system is used again. An Upsilon is called reconstructable if both of the decay electrons traverse the full TPC, i.e. have more than 40 hits and leave through the outer field cage, and hit the BEMC. No selection on the deposited energy in the BEMC or the energy loss in the TPC have been made. The Upsilon decay itself is simulated using the decay function of the PYTHIA simulation package. The resulting particles are then used as input to the detector simulation.

The number of reconstructable Upsilons depends on many variables, the most noteable ones being

- the Upsilon phasespace distribution,
- the BEMC coverage,
- the position of the primary collision vertex in beam direction.

The momenta of the decay electrons depend obviously on the Upsilon momentum, thus one has to assume some Upsilon momentum distribution. Using the approximate symmetry of the STAR detector in ϕ, one can express the Upsilon momentum using rapidity y and transverse momentum p_T by integrating over the full ϕ range. The Upsilon distribution in y, p_T is a priori unknown, but one can use theoretical predictions and the experimental results from lower and higher energies presented in section 2.2 as guidance. Based on them, the phasespace region, in which the geometrical acceptance is studied, is limited to $-2 \leq y \leq 2$ and 0 GeV/c $\leq p_T \leq$ 10 GeV/c.

Figure 4.12 demonstrates the used procedure. Upsilons are first generated flat in y, p_T as shown in the upper left panel of the figure. These Upsilons are then decayed and the number $N_{\Upsilon}^{\mathrm{rec}}$ of reconstructable Upsilons determined as explained above as functions of y and p_T, shown in the upper right panel. This information allows to use equation 4.20 to calculate the geometrical acceptance ϵ_{geo} which is shown in the lower plot. For these plots a complete BEMC was assumed, a vertex $z_{vtx} = 0$ cm position and 1,000,000 Upsilon decays were simulated. One should note that for the calculation of the phasespace-integrated geometrical acceptance the results need to be reweighted with a more realistic Upsilon phasespace distribution.

As expected only Upsilons produced around midrapidity are accepted, but the acceptance there is quite high, around $\approx 50\%$. It drops then significantly at higher rapidities and is 0 for $\mid y \mid \geq 1$. Only a very weak p_T dependence is visible. This is seen more clearly in figure 4.15 which shows the geometrical acceptance as function of p_T for several rapidity bins. The dependence of the acceptance on p_T is on the level of few percent. Thus only the geometrical acceptance as function of rapidity is studied in the following, integrating over all p_T.

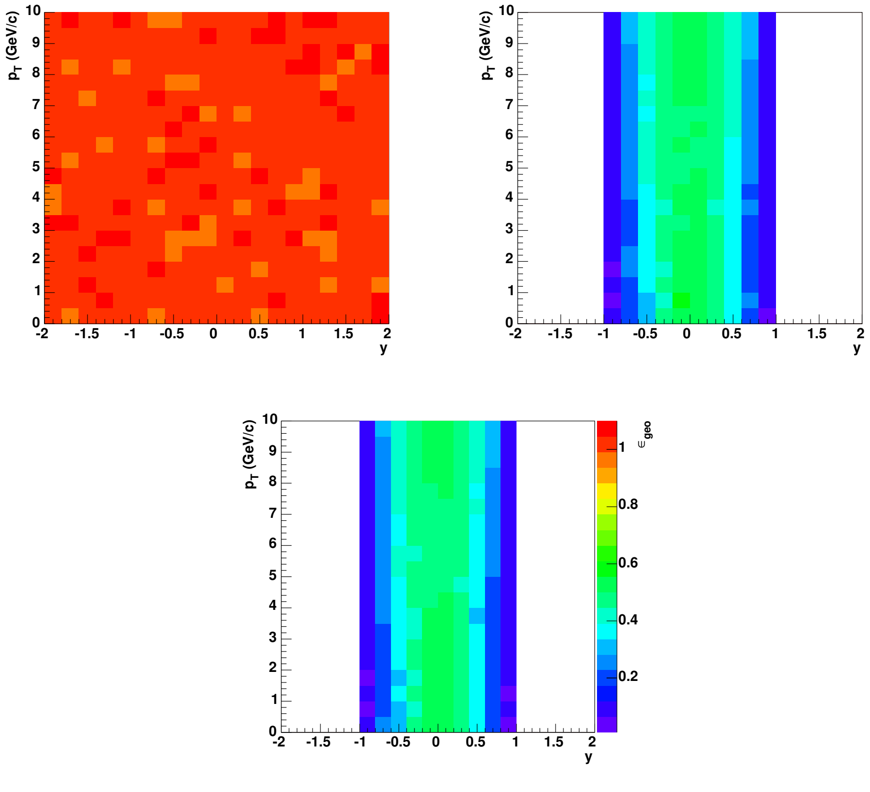

Figure 4.14: Upsilon geometrical acceptance calculation for the full BEMC configuration. The input phasespace distribution is shown in the upper left, the phasespace distribution of accepted Upsilons in the upper right panel. The lower plot shows the resulting geometrical acceptance ϵ_{geo}.

Another variable mentioned earlier which has a huge influence on the geometrical acceptance is the BEMC coverage. As already mentioned in section 3.2.2 the BEMC construction was staged over several years, with four different foreseen configurations:

I	full BEMC	120 modules
II	FY04 goal, 3/4 BEMC	90 modules (60 modules west, 30 modules east)
III	reduced FY04 goal	72 modules (60 modules west, 12 modules east)
IV	west half	60 modules

Case I shows the capabilities of STAR once the BEMC construction is completed, which is currently forseen for the FY06 run[11]. Configuration II was the goal for the FY04 run, which will be analyzed in chapter 5, but this was reduced shortly before the run started to configuration III due to delays in electronic production caused by funding problems. A operational west half (case IV) was already achieved during the FY03 run and thus represents a lower limit for the acceptance.

Figure 4.16 shows the geometrical acceptance as function of Upsilon rapidity for the four different BEMC coverages. The maximal acceptance decreases by nearly a factor 2 from $\approx 50\%$ for the full BEMC to $\approx 30\%$ for an instrumented west half only and shifts from $y = 0$ to $y = 0.5$. At the same time the covered rapidity interval decreases from $-1 \leq y \leq 1$ to $0 \leq y \leq 1$. The configurations II and III show a non-symmetric acceptance as one would expect. The approximate p_T independence of the acceptance for a given rapidity shown in figure 4.15 for configuration I holds for all other configurations as well. For judging the effect of the reduced coverage one has to keep in mind that these acceptance functions don't include the other effects mentioned above.

As mentioned, also the position of the primary collision vertex along the beam direction z_{vtx} is expected to have some influence on the geometrical acceptance. As discussed in section 3.1 z_{vtx} is not well constrained by the collider, with sizeable number of collisions still happening at $z_{vtx} = 75$ cm. To show the effect the geometrical acceptance is studied for five different z_{vtx} positions: -100 cm, -50 cm, 0 cm, 50 cm and 100 cm. The results are shown in figure 4.17 for the four BEMC configurations. Again one would have to fold these distributions with the Upsilon rapidity distribution to assess the effect on the overall acceptance. But already from these plots it is quite obvious that even for the most extreme case of $\mid z \mid = 100$ cm a large fraction of Upsilons is still accepted.

So far a flat rapidity and transverse momentum distribution of the Upsilons was assumed. To get the total integrated geometrical acceptance for Upsilons in the rapidity region $-1 \leq y \leq 1$, a realistic Υ phasespace distribution and a vertex z distribution have to be assumed. The Υ phasespace distribution is of course unknown however using the guidance from section 2.2, several assumptions about the form of the rapidity and p_T distribution can be made. The difference between the geometrical acceptances calculated from these assumptions can then be used to estimate the error on the acceptance. The same procedure is followed for the vertex z distribution where two different distributions were used, gaussians with $\sigma = 30$ cm and 60 cm. The so calculated geometrical acceptances for the four assumed BEMC coverage classes are listed in table 4.3. With a full BEMC 32% of all Upsilons produced in the rapidity interval $-1 \leq y \leq 1$ are accepted. This decreases by a factor ~ 2 for the original FY04 goal of a 3/4 BEMC and a factor ~ 4 if only the west half of the BEMC can be used.

[11] Mechanical completion was achieved for the FY05 run, but due to limited availability of readout electronic not all installed modules could be used.

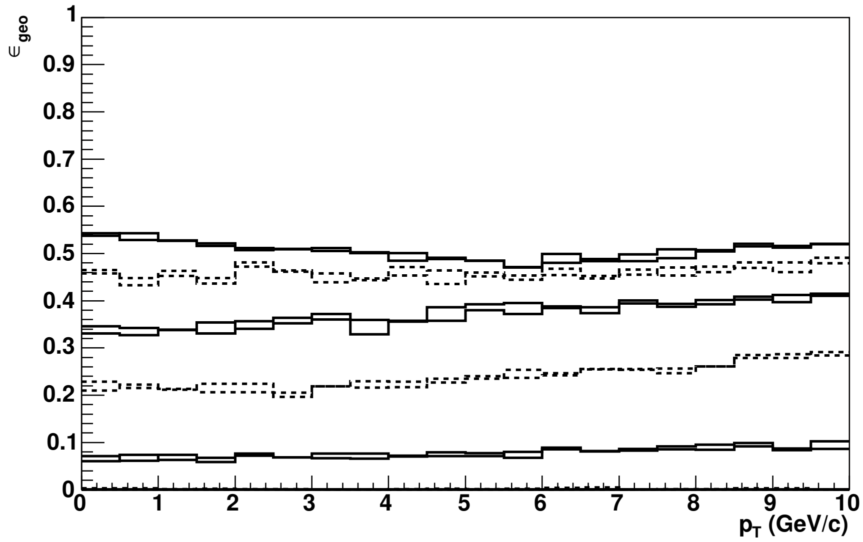

Figure 4.15: Upsilon geometrical acceptance versus p_T for different rapidity bins calculated from figure 4.14. From top: $0 \leq | y | < 0.2, 0.2 \leq | y | < 0.4, 0.4 \leq | y | < 0.6, 0.6 \leq | y | < 0.8, 0.8 \leq | y | < 1$ and $| y | \geq 1$.

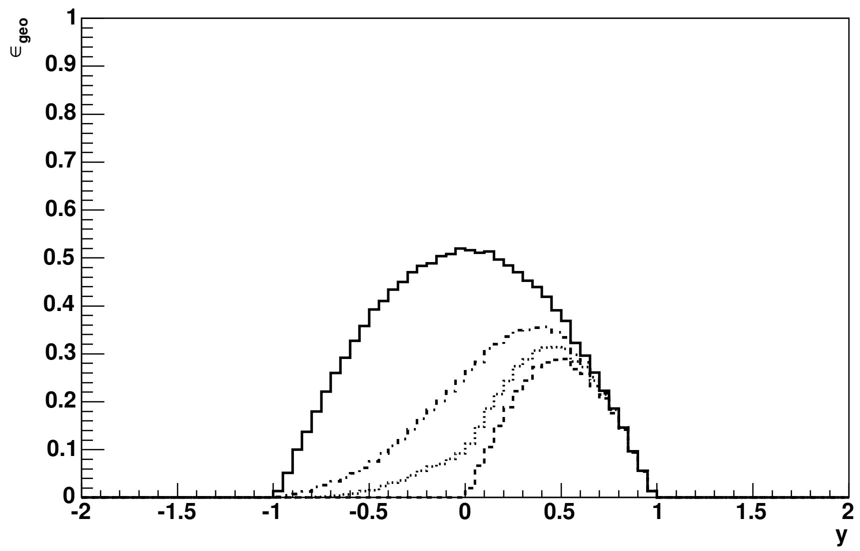

Figure 4.16: Geometrical acceptance $\epsilon_{\rm geo}$ as function of the Upsilon rapidity y for four different BEMC configurations: solid line full BEMC (I), dashed-dotted line 3/4 BEMC (II), dotted line reduced FY04 goal (III) and dashed line west half (IV).

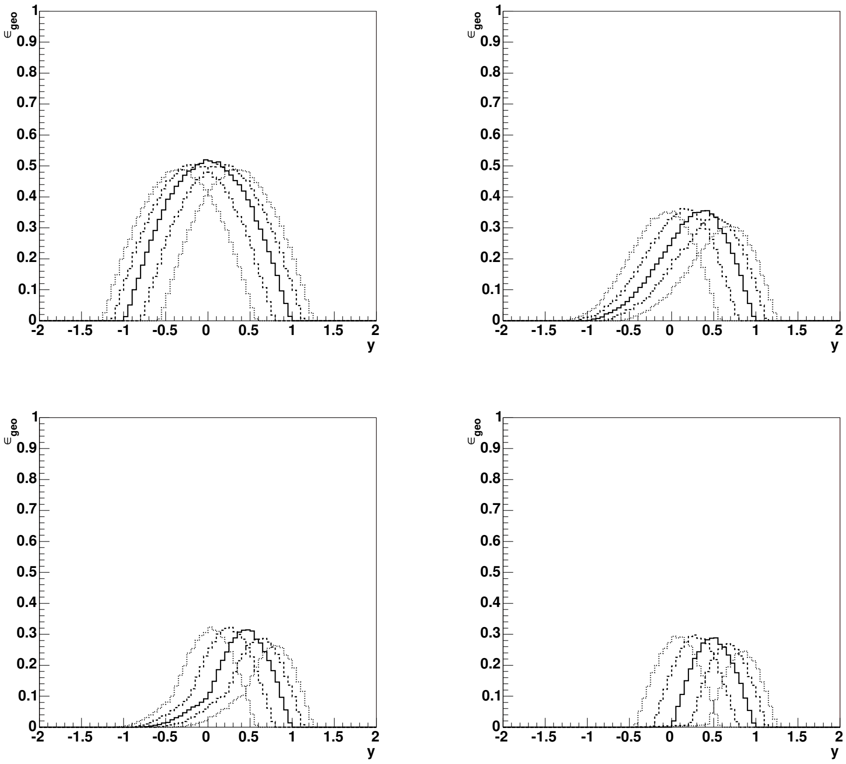

Figure 4.17: Geometrical acceptance ϵ_{geo} as function of the Upsilon rapidity y for different collision vertex z positions: from left to right z_{vtx} =-100 cm, -50 cm, 0 cm, 50 cm and 100 cm. Shown are the results for four BEMC configurations, full BEMC (I) upper left, FY04 goal (II) upper right, reduced FY04 goal (III) lower left and west half only (IV) lower right.

BEMC Coverage	I	II	III	IV
ϵ_{geo}	(32.0 ± 3.0) %	(16.1 ± 1.5) %	(10.9 ± 0.7) %	(7.8 ± 0.4) %

Table 4.3: Total geometrical acceptance ϵ_{geo} for the four different BEMC configurations defined in section 4.2.1. The values are integrated over p_T and the rapidity interval $-1 \leq y \leq 1$.

4.2.2 Mass Resolution

As demonstrated in the previous subsection, STAR can reconstruct a sizeable fraction of all Upsilon decays, roughly 30% for the completed detector. But how well is the reconstruction of the Upsilon momentum-energy vector? From equation 4.18 it is obvious that this depends on the accurancy of the daughter Lorentz vectors.

In the electron identification chapter 4.1 the momentum and/or energy resolution achievable with the TPC and the BEMC was already discussed. These results are summarized in figure 4.18 which shows the energy resolution for TPC primary and global tracks and the BEMC. Two different curves for the BEMC are shown, the lower one the expectation for a perfectly calibrated EMC from simulations and test beam studies, the other the one currently achieved in year 3 and year 4 data analysis.

Typical momenta of the Upsilon decay electrons are 2 GeV/c to 10 GeV/c range (see e.g. figure 4.21). The best momentum resolution in this region is provided by the primary TPC tracks which are thus used for the further analysis. In addition one has to take into account the energy loss suffered by parts of the electrons while passing through the SVT and inner field cage of the TPC discused in 4.1.1.

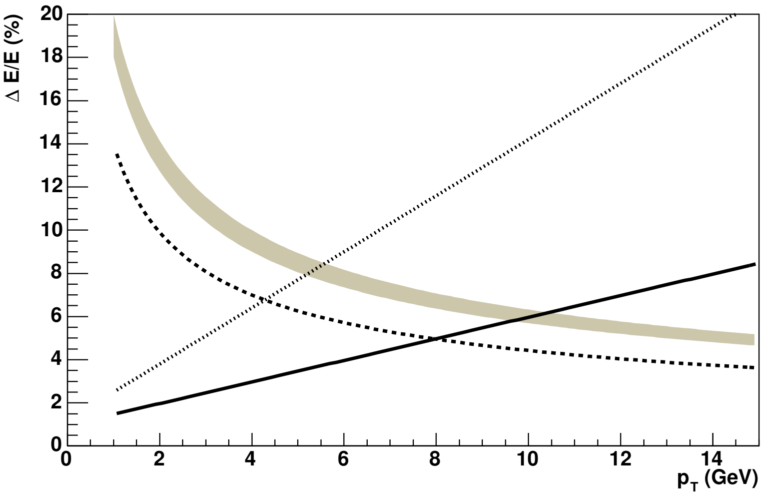

Figure 4.18: Electron energy resolution of the different STAR detectors as function of p_T. The resolution provided by the TPC is shown for both global (dotted line) and primary (solid line) tracks. The nominal BEMC resolution is shown by the dashed line, the one achieved in 2004 by the gray band.

The position and shape of the reconstructed Upsilon mass is one of the most sensitive variables to check the quality of our reconstruction. The natural width of 20-50 keV is so small that a momentum resolution in the sub-permille level for the daughter electrons would be need to reconstruct it, an order of magnitude smaller than the one achieved in STAR. The experimental momentum resolution of the daughter electrons is thus the dominating factor. The p_T depended momentum resolution and the correlation between electron momenta and parent Upsilon momentum will cause an increasing measured width for higher Upsilon transverse momenta and we thus have to determine the shape separately for different $p_T(\Upsilon)$ bins. The GEANT detector simulation is used to determine the expected position and shape.

The Upsilon input distribution was flat in $0\ \mathrm{GeV}/c \le p_T \le 10\ \mathrm{GeV}/c$ and $-2 \le y \le 2$, as already used for the acceptance calculation. The shape of the invariant mass peak depends strongly on details of the simulation, i.e. how well the electron bremsstrahlung is simulated in GEANT. A dominant input factor is the geometry and material budget of all detector components in front of the TPC. The current implementation has quite some uncertainties describing the SVT and SSD support structures and cables.

Focusing on the $\Upsilon(1S)$ resonance first, the expected invariant mass distribution is shown in the upper left panel of figure 4.19. As expected the peak shape is asymmetric with a long tail to lower mass values due to the energy loss of the electrons in the material in front of the TPC. To quantify this a gaussian was fitted to the mass peak in the region $8\ \mathrm{GeV/c^2} \le m_{ee} \le 10\ \mathrm{GeV/c^2}$. The fit results are shown in the upper right and lower left panel. A systematic shift of the mean reconstructed peak position by 150 MeV is visible, roughly independent of the original Upsilon p_T. In contrast the width of the fitted gaussian is increasing from 300 MeV for Upsilons at rest to 370 MeV for $p_T = 10$ GeV Upsilons, reflecting the decreasing momentum resolution for the increasing daughter electron momenta. This has been already taken into account for the invariant mass shape shown in the upper left panel of figure 4.19 by summing the expected mass shapes for different Upsilon p_T bins, weighted by the $p_T\,(\Upsilon(1S))$ spectrum from the PYTHIA simulations in section 2.3.

Extracting the Upsilon cross section is made difficult by the asymmetric peak shape. In principle the right way would be to fit the shape obtained from the simulations plus a background distribution to the experimentally measured mass spectrum. However with the expected low statistics such a fit will be quite difficult. Another possible way is to concentrate on the peak region and treat all reconstructed pairs with lower invariant mass as efficiency loss. To quantify this, the Upsilon mass reconstruction efficiency ϵ_{mass} get defined as

$$\epsilon_{\mathrm{mass}} = \frac{\int_{m_{low}}^{m_{high}} dN/dm_{ee}}{\int dN/dm_{ee}} \tag{4.21}$$

with $m_{low(high)}$ the lower (higher) mass threshold. The lower right plot of figure 4.2.2 shows a first example, with thresholds set to $m_{low} = m_{peak} - 3\sigma$ and $m_{high} = m_{peak} + 3\sigma$. The mean position of the peak and the width were obtained using the gaussian fit described above. A nearly constant Upsilon mass reconstruction efficiency of $\epsilon_{\mathrm{mass}} \approx 0.7$ is observed.

One of the physics goals is the distinction between the different Upsilon states. Given the small mass differences between the different Upsilon states of $m_{\Upsilon(2S)} - m_{\Upsilon(1S)} = 563\ \mathrm{MeV/c^2}$ and $m_{\Upsilon(3S)} - m_{\Upsilon(2S)} = 332\ \mathrm{MeV/c^2}$ the achieved resolution will certainly not be enough to clearly separate them. What makes it even more challenging is the asymmetry to lower invariant masses which moves even more of the yield from the higher mass states under the $\Upsilon(1S)$ peak. This can be clearly seen in figure 4.20 which shows the expected mass distribution for the first three Upsilon states on the left. What enters here as parameters are the ratios of the different Upsilon states. Using the approximate energy independence of these ratios as shown in table 2.3 they are set to $\Upsilon(2S)/\Upsilon(1S) = 0.27$ and $\Upsilon(3S)/\Upsilon(1S) = 0.13$. A clear separation of the different states is not possible.

As in the case of the Upsilon(1S) discussed above one faces the challenge of the long tail to lower invariant mass values. The possible approach is to limit oneselve to the region with a clearly visible peak. To decide on the borders of the mass window, the mass reconstruction efficiency ϵ_{mass} is calculated for two inter-

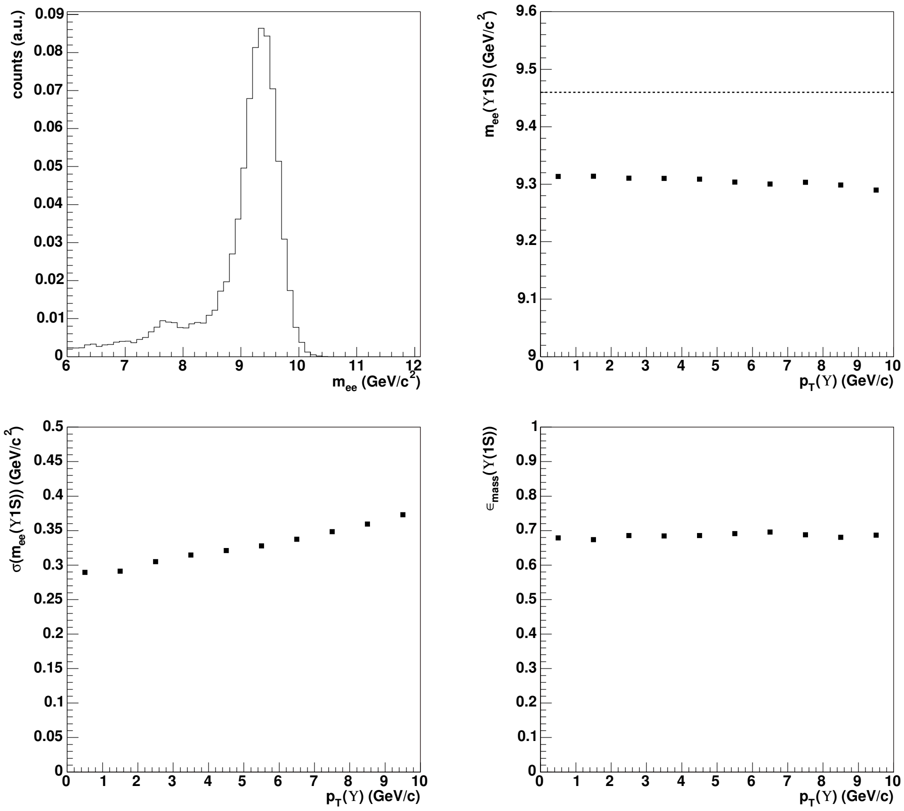

Figure 4.19: The expected invariant mass shape for the Υ(1S) is shown in the upper left figure. Results of a gaussian fit in the range 8 GeV/c^2 $\leq$ 14 GeV/c^2 are shown in the upper right (mean peak position) and lower left panel (peak width) as function of p_T. The lower right plot shows the identification efficiency ϵ_{mass} in a $[-3\sigma, 3\sigma]$ interval.

vals, $m_{low} = m_{ee}^{cut}, m_{high} = \infty$ and $m_{low} = 0, m_{high} = m_{ee}^{cut}$. The results are shown in the right panel of figure 4.20. We first concentrate on the case without an upper limit, i.e. the thick solid line. Even for a 6 GeV lower mass cut one would be able to reconstruct only 93% of all Upsilons. An 80% mass reconstruction efficiency is reached with a lower cut at $\sim$ 8.4 GeV/c^2. The dependence on the assumed Upsilon p_T distribution is quite small as can be seen from the results for Upsilons with $p_T = 0$ GeV/c and $p_T = 10$ GeV/c which differ only by a few percent (thin solid lines). The results for the interval without lower bound are shown by the dashed line, we still have a nearly perfect efficiency at 10.7 GeV. For an eventual extraction of the Upsilon production cross section later on, the mass interval 8.4 GeV/c^2 $\leq m \leq$ 10.7 GeV/c^2 will thus be used.

4.3 An Upsilon Trigger for STAR

It has been demonstrated in the previous section that STAR has a large acceptance and sufficient mass resolution to attempt an Upsilon measurement. However accumulating sufficient statistics will be quite challenging due to the very small Upsilon production cross section. This is especially demanding as STAR is nominally a slow

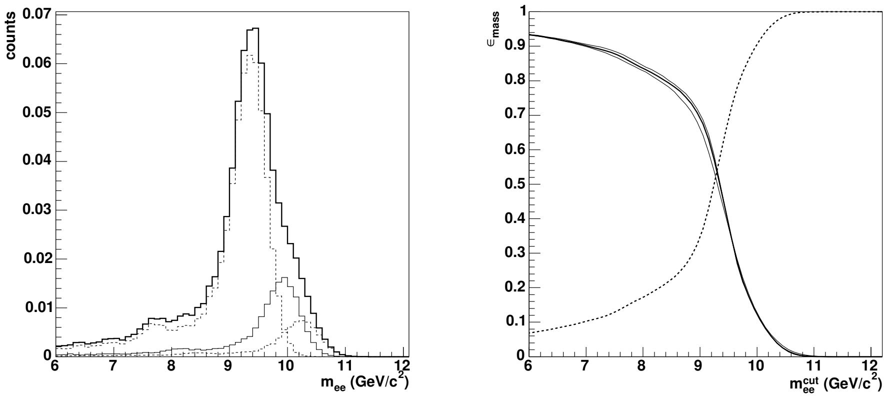

Figure 4.20: Expected invariant mass shape for the combined Upsilon states (left panel). The dotted lines show the contributions from the individual 1S,2S and 3S states. The detection efficiency ϵ_{mass} for $\left[0, m_{ee}^{cut}\right]$ (dashed) and $\left[m_{ee}^{cut}, \infty\right]$ (thick solid line) intervals is shown on the right. The dependence on the assumed Upsilon momentum dependence is shown by the detection efficiency for Upsilons with $p_T = 0$ GeV/c and $p_T = 10$ GeV/c (thin solid lines).

detector, i.e. TPC, SVT and DAQ limit the maximum event rate to ~ 100 Hz, a factor 100-1000 lower than the typical collision rates provided by RHIC[12].

The selection to determine for which collisions the *slow detectors* are read out is made by the STAR trigger system[13], based on the input data from the *fast* or *trigger detectors*. If it would be possible to define a trigger which selects primarily events containing an Upsilon decaying into electrons, the available statistics would be increased by a large amount compared to randomly selecting every n^{th} event.

The demands on the trigger algorithm are set by

- the physics involved in the Upsilon decay, mainly the space and momentum distribution of the electrons we want to detect,
- the technical limitations of the STAR trigger and detector system, e.g. maximum read out rate of the slow detectors and maximum time until a trigger decision is reached and
- some *"soft"* limitations caused by the need of integration into the overall STAR running scheme.

It turns out that the most stringent demands on the Upsilon trigger or any special trigger are set by the last item. STAR as a large collaboration pursues many different physics goals simultaneously and achieving a maximal scientific output requires integration of often competing demands into a single running scheme. Many analyzes pursued in STAR for example require a "min-bias" dataset, i.e. no or as low as possible selection of the collisions written to tape. The maximum number of events for such a dataset would be achieved when running the detector 100% dead, i.e. taking events using the maximum rate substained by the slow detectors and DAQ. On the other hand running in this mode reduces the rate of every other trigger

[12] The collision rate in RHIC depends on the particle species, typical values are 10 kHz for Au+Au and 100 kHz for p+p collisions, see also chapter 3.1.

[13] See section 3.2.3 for a description of the trigger system.

to zero, thus eliminating the physics opportunities opened by them. The negotiation of the running scheme is quite a complex process, starting with the specification of the physics goal by the different physics working groups within STAR several months before a run starts, followed by a weighting of the STAR management and physics working group convenors which results in a first rough running scheme. The actual fine tuning is then done on the operations level, i.e. trigger board and operation meetings which focus also more on the technical limitations present in the system. It should by now be clear that the determination of the running scheme is a very dynamic and flexible process, thus the limitations imposed by it are "soft", i.e. negotiable in the different stages of the decision process.

From this discussion follows immediately that these "soft" limitations change for different collision systems or even during the run with the commissioning of new detector components and are thus difficult to take into account in the algorithm design. But some general limitations exist which secure the maximum interoperability of an Upsilon trigger with the most common other triggers and thus increase the probability of sufficient detector ressource allocation for it. Most of them are connected to the technical limitations of STAR which will be discussed now, mentioning the more stringent "soft" limitations where appropriate.

The most important technical limitation is the triggered rate. The L0 trigger system is capable of examining all RHIC bunch crossings, i.e. 9.3 MHz. The first limiting factor is the L2 trigger system which can handle a maximum of a few kHz, i.e. a factor 1000 less. A technical and to some extent also soft limitation limits this rate further, namely the opening rate of the TPC gating grid. While technically possible with more than 1 kHz, worries about the increased chamber current have to be taken into account. Larger accumulated currents result in faster aging of the TPC as well as in the increased possibility of anode wire trips. Thus the maximum input rate into L2 should be less than 500 Hz. Taking the other concurrently running triggers into account, one has to limit maximum L2 trigger rate to 300 Hz for the Upsilon trigger[14].

The next limiting factor in the datapath is the TPC (or the slow detectors) readout speed of maximal 100 Hz. What becomes here important is the dead time issue, running with 100 Hz would mean running with close to 100% dead and therefore no rare triggers would be taken. Thus the event rate is typical limited to $\sim$ 50 Hz[15], from which roughly 5 Hz are dedicated to special, i.e. non min bias or central, triggers. Due to the concurrently running other special triggers (e.g. high p_T triggers using the EMC) a reasonable goal for the maximum Upsilon trigger rate is 1 to 2 Hz at maximum luminosity assuming a 50% dead time. The reduction to this rate has to be reached when the L2 decision is made[16].

A last limitation in the data path to physics analysis is the offline reconstruction time. For Au+Au collisions the total reconstruction time of one data taking period can reach 1 to 1.5 years for 100M events. For the Upsilon search (or every rare trigger analysis) only a very small fraction of these events is relevant. The *L3 express*

[14] This assumes that there are no other triggers running which need a significant fraction of the L2 bandwidth. The only other trigger envisioned so far which might need this is a J/ψ trigger.

[15] In real life STAR tries to optimize the use of the delivered luminosity by adjusting the event rate depending on the luminosity, i.e. run with low dead time and thus low event rates at the begining of a store when the luminosity is high and increase the dead time as the luminosity decreases. The specific share is again one of the soft limitations which get adjusted during the run. A more specific example can be found in section 5 which describes the trigger setup during the FY04 Au+Au run.

[16] The slow dector read out starts at the L0 accept as explained in section 3.2.3, L2 can then abort the read out.

streams introduced in section 3.2.4 offer the possibility to write the "interesting" events into a special data stream which can then be produced with priority. To really make use of this concept the number of events in these special streams has to be small, which translates into a rate of ≤ 1 Hz during data taking. Again one has to keep in mind that several triggers are sharing this rate, thus the goal for the Upsilon trigger is ≤ 0.5 Hz into the express stream.

To quickly summarize the maximum rates from the technical limitations inherent to the STAR trigger and detector system

- L0 trigger rate of ≤ 300 Hz.
- L2 trigger rate of 1-2 Hz.
- L3 trigger rate of ≤ 0.5 Hz.

with both L0 and L2 trigger rates goals assuming 50% deadtime. L3 is indepent of the deadtime assumption since it only introduces a negligible additional dead time.

The main demand on the Upsilon trigger is of course set by the physics one wants to achieve with it, i.e. measuring an Upsilon signal. This requires the Upsilon trigger to identify the (Upsilon decay) electrons and accepting every event with an Upsilon candidate, i.e. a dielectron pair in the Upsilon mass region.

The performance of the trigger algorithm relative to this goal can be specified by the *trigger efficiency* ϵ_{trg} defined as:

$$\epsilon_{\mathrm{trg}} = \frac{N_{\Upsilon(\mathrm{t}riggered)}}{N_{\Upsilon(\mathrm{m}easurable)}} \tag{4.22}$$

with $N_{\Upsilon(\mathrm{m}easurable)}$ the number of Upsilons with a reconstructed mass between 8.4 GeV/c^2 and 10.7 GeV/c^2, i.e. the mass window with a mass reconstruction efficiency of 80% as calculated in 4.2.2 and $N_{\Upsilon(\mathrm{t}riggered)}$ as the number of these Upsilons triggered.

The trigger efficiency alone is not sufficient to completely describe the actual performance of the trigger algorithm or a specific algorithm parameter set since it does not include the *trigger rejection rate* $\mathcal{R}$ necessary to reach the rate goals. One defines the rejection rate as the inverse of the trigger algorithm efficiency ϵ_{bkgd} for minimum bias events:

$$\mathcal{R} = \epsilon_{\mathrm{bkgd}}^{-1} = \frac{N_{\mathrm{events}}}{N_{\mathrm{triggered}}} \tag{4.23}$$

Both trigger efficiency and rejection rate can be calculated separately for each trigger level. This allows to judge if the rate goals at a given trigger level are reached, when the collision rate R_0 is known, with e.g. $R_i = R_{i-1}\epsilon_{\mathrm{bkgd},i-1}$. R_1 would then be the input rate to L1, R_2 to L2 and so on until R_4 which would be the rate to tape. The collision rate R_0 and the background rejection rates $\mathcal{R}$ depend of course strongly on the collision system, e.g. the collision rate in STAR varies between ~ 10 kHz for Au+Au to ~ 100 kHz for p+p and the background rejection rate relevant for the Upsilon algorithm is to first order a function of the number of binary collisions which increases from 1 in p+p to $\sim 197^{\left(\frac{4}{3}\right)}$ in central Au+Au. In addition background from beam-gas interactions, experimental noise etc also can have a huge influence on the rejection rate. This chapter describes thus only the possible trigger algorithms, their implementation and the trigger efficiency achievable with them. The discussion of the background rejection rate will be deferred to the next chapter where it is determined from data.

The main challenge on the trigger level will be to find a way to identify the electrons of the Upsilon decay. Obviously their phasespace distribution will have an influence on the chossen method. Figure 4.21 shows the correlation of the decay electron energy to the transverse momentum of Upsilons at midrapidity as well as the correlation between the decay electrons themself. For a decay at rest, both daughter electrons have an energy of ∼4.5 GeV as one would expect from the Q-value of the decay. Momentum conservation will change this with increasing Upsilon (transverse) momentum, e.g. one of the daughter electrons will get a boost in the direction of its momentum vector and thus an higher energy, the opposite will happen for the other electron. To make this more obvious we sort the daughter electrons by their energy; the one with the higher energy called e_h, the one with the lower energy e_l. The expect behavior with respect to the Upsilon transverse momentum is clearly visible in figure 4.21. The boost from the parent particle will also reduce the opening angle in the lab between the electrons, from the 180^o at rest to 100^o at $p_T(\Upsilon) = 10$ GeV.

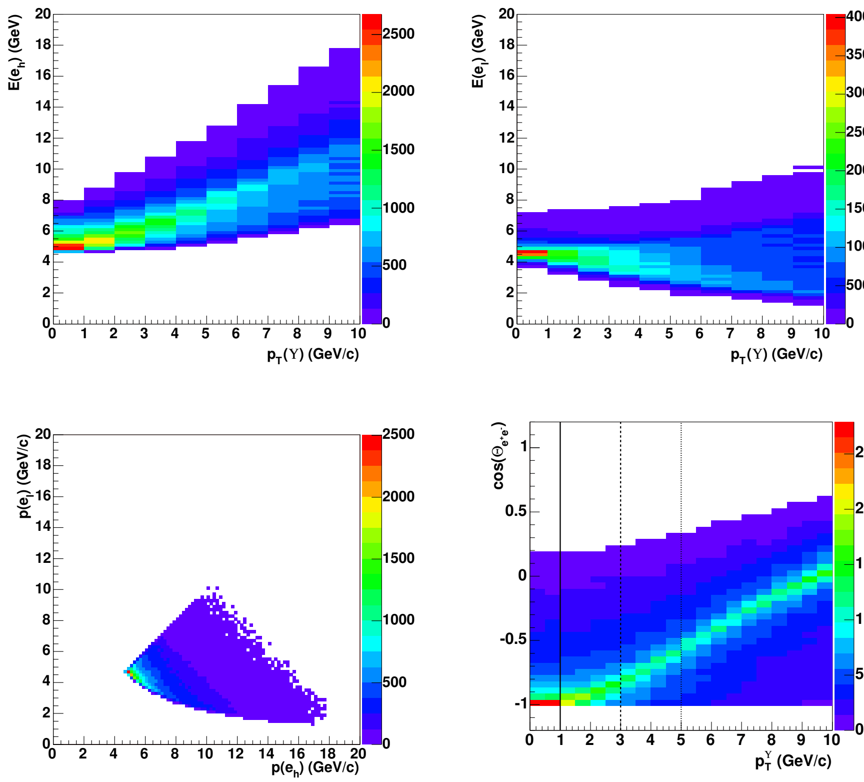

Figure 4.21: The energy of the decay electrons as function of the Upsilon transverse momentum is shown in the upper row. The upper left panel shows the distribution for the higher energy electron, the upper right for the lower energy electron. The correlation between the daughter electron momenta is shown in the lower left plot, the opening angle between them in the lower left plot.

Looking at the information available at the trigger level as described in 3.2.3 the only information usefull for electron identification on the lower trigger levels L0 to L2 is the BEMC tower data. Section 4.1.2 showed how to use it to identify electrons, however it was always assumed that the momentum is known from the TPC tracking. The task in the trigger system poses a slightly different challenge since only the BEMC information is available (or even only a subset of it on L0). On the other hand one does not need the same background rejection, i.e. can have higher hadron (mis-)identification efficiencies, as long as the rate goals outlined above are met.

4.3.1 L0 Trigger

Obviously one starts with the first trigger level L0. The complexity of the algorithms and also the available input data are quite limited due to its design and the need to issue a decision for every bunch crossing, i.e. with 9.4 Mhz. Two trigger primitives are sent from the BEMC electronic to the trigger, 300 high tower patches and 300 tower energy patches (see section 3.2.3). The information on the highest tower above threshold in a 4×4 high tower patch seems to be the most interesting, giving a first estimate of the electron energy. In principle the energy sum in the patch would be a better approximation of the electron energy as there is a energy sharing between the different towers. However at least in Au+Au collisions the background from other particles hitting the same patch would be much larger than the signal, leading to an overestimate of the electron energy. In addition the background fluctuations are quite large, reducing further the usefullness of the energy sum for electron identification. The Upsilon algorithms are thus based on the high tower patches as input data.

Two different algorithms were designed, implemented and tested:

1. The first algorithm concentrates only on the electron with the higher energy and select every event which has a tower above some transverse energy[17] threshold $E_{T,\mathrm{thresh}}$. The energy threshold is the only free parameter in this algorithm which allows to vary trigger efficiency and rejection rate. This algorithm will be refered to as the *L0 high tower* algorithm in the following. The algorithm is shown schematically in figure 4.22

2. In the second algorithm additionally the topology of the Upsilon decays is used, i.e. the large opening angle. For this one has to identify both daughter electrons and then calculate the opening angle. The relatively high complexity does not allow such an operation on all of the high tower patches. The 300 high tower patches are thus combined to 12 jet patches ($1 \times \pi/3$ coverage in $\eta\phi$) on the first two DSM levels of the BEMC subtree which are used as input data for the algorithm running on the third DSM. The algorithm requires two patches above an energy threshold $E_{T,\mathrm{thresh}}$ chosen low enough to also select the electron with the smaller energy. In addition it requires that these two patches are not adjacent to each other. This requirement assures that the minimum opening angle is the size of one patch, i.e. $\pi/3$. Figure 4.23 illustrates the algorithm. Assuming that the highest tower in the third jet patch is above the threshold, one would require that one of the non-adjacent jet patches is also above the threshold to accept the event. Also in this algorithm one just has

[17] The BEMC is (should be) calibrated in transverse energy E_T due to the demands of the high-p_T and spin working groups. The raw ADC values on which the L0 decision is based are thus also proportional to E_T. A conversion to E is not possible on the L0 trigger level. Due to the limited capabilities on the L0 trigger level the 10-bit ADC values are shifted and reduced to 6-bit values ADC_{trg}.

one free parameter, the common energy threshold for both patches[18]. This algorithm will be refered to in the following as the *L0 topology* algorithm.

What are the trigger efficiencies we can reach with each of these algorithms? As already mentioned the L0 high tower algorithm has just one free parameter, the threshold $E_{T,\mathrm{thresh.}}$ of the (transverse) energy deposited in a BEMC tower. Figure 4.24 shows the trigger efficiency as function of this threshold for three different Upsilon momentum bins. Due to the correlation between higher energy electron and the Upsilon momentum shown in figure 4.21 one gets $p_T(\Upsilon)$ dependend efficiencies, with the lowest efficiencies for Upsilons at rest. However high efficiencies of more than 90% for all $p_T(\Upsilon)$ are achieved in the range $E_{T,\mathrm{thresh.}} \leq 2.6$ GeV. We observe reasonable high trigger efficiencies (i.e. $> 50\%$) up to an energy threshold cut value of 4 GeV even for low momentum Upsilons.

The L0 topology algorithm has also just the transverse energy threshold $E_{T,\mathrm{thresh.}}$ as free parameter since the opening angle cut is fixed to $\pi/3$ by the L0 electronics design limitations. Figure 4.25 shows the trigger efficiency ϵ_{trg} as function of this parameter. More than 90% trigger efficiency is achieved for $E_{T,\mathrm{thresh.}} \leq 1.8$ GeV. The approximate anticorrelation between the lower energy electron causes a $p_T(\Upsilon)$ dependence of ϵ_{trg}, with decreasing trigger efficiency for higher momenta. Reasonable trigger efficiencies are achieved for $E_{T,\mathrm{thresh.}}$ values of less than 3 GeV.

Comparing both algorithms the first obvious difference is the transverse energy threshold needed to achieve the same efficiency, with the L0 high tower algorithm allowing roughly 1 GeV higher thresholds. A second difference is the observed dependence on the Upsilon transverse momentum. While the trigger efficiency increases with increasing momentum for the high tower trigger, it decreases for the topology trigger. The relative differences in efficiency for different $p_T(\Upsilon)$ are smaller for the topology trigger.

In summary both L0 algorithms are able to select Upsilons decaying into electrons with high efficiencies. The decision which one to use will depend on the background rejection factors they achieve which will be discussed in chapter 5 for Au+Au collisions. Will the difference in the energy threshold be large enough that the high tower algorithm achieves the higher rejection power at the same trigger efficiency? Or will the requirement of two towers above the threshold and a large opening angle between them give the topology algorithm the better rejection rate?

4.3.2 L2 Trigger

On L2 the ADC values of each BEMC tower are available and no hard limitations on the complexity of the algorithm have to be faced. The only constraint is the maximum time until a L2 decision has to be issued. As already discussed the time per event in L2 should be less than the 10 ms data transfer time from the TPC front end electronic to the DAQ system. To really make use of the system, the average time until a decision is issued should be much smaller, i.e. $(O)(1\text{ ms})$. The time an algorithm has to issue its decision is further reduced due to the overhead of the data transfer from BTOW to the L2 computer, the latencies in the system

[18] A possible extension of this algorithm would be to make use of the asymmetric energy of the two decay electrons, i.e. requiring one patch above a higher threshold and a second non-adjacent patch above a lower threshold. It's obvious that this extension would increase the rejection power for a given trigger efficiency. The complexity of this algorithm was however too large for an implementation on L0.

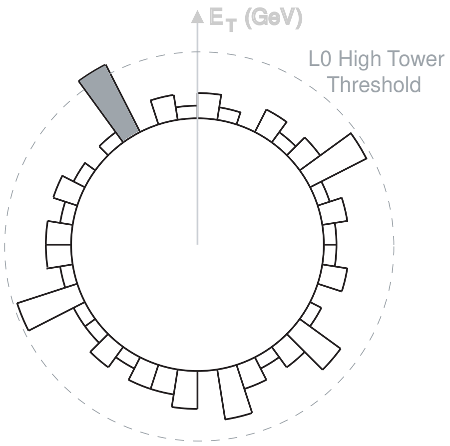

Figure 4.22: Schematic illustration of the L0 High Tower algorithm. The event is accepted because the filled tower is above threshold. For details on the algorithm see text.

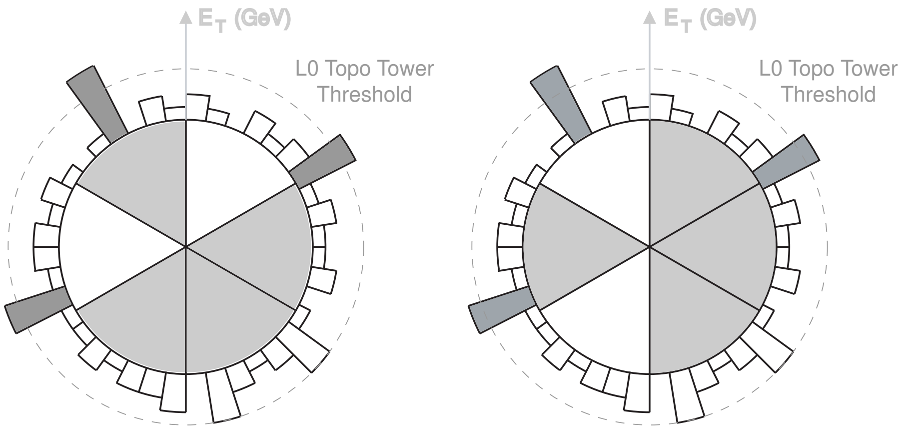

Figure 4.23: Schematic illustration of the L0 Topology algorithm. To illustrate the differences to the high tower trigger shown in figure 4.22 two different patch combinations of the same event are shown. In the right figure a tower in the upper left patch is above threshold. However no tower above the threshold is found in the non-adjacent patches (the gray shaded areas) and the event would not be accepted. However it gets still accepted by a different patch combination, as shown in the right figure. Both the tower in the lower left patch and the non-adjacent tower in in upper right patch are above threshold, satisfying the trigger condition. See text for details on the algorithm.

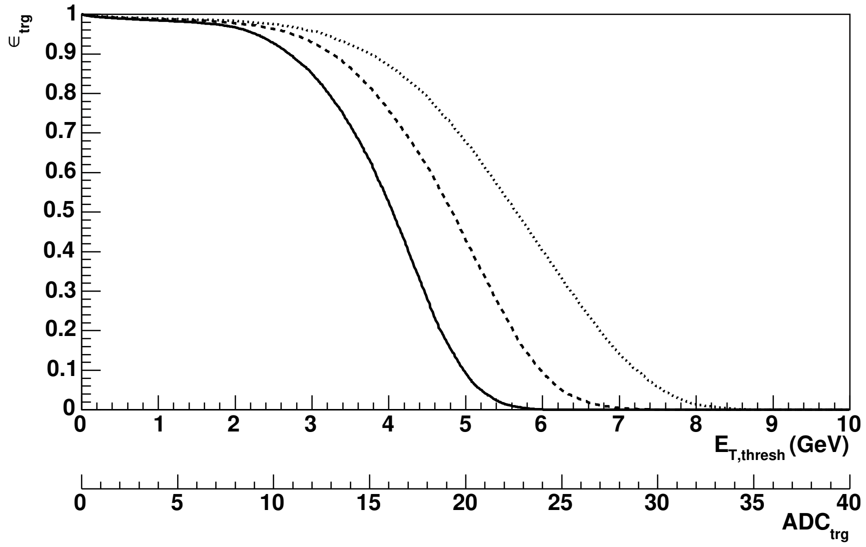

Figure 4.24: Trigger efficiency ϵ_{trg} as function of the energy threshold $E_{T,\text{thresh.}}$ for the Upsilon L0 high tower algorithm. Curves for different Upsilon momenta are shown, 0.5 GeV $\leq p_T(\Upsilon) \leq$ 1.5 GeV/c (solid), 2.5 GeV $\leq p_T(\Upsilon) \leq$ 3.5 GeV/c (dashed) and 4.5 GeV $\leq p_T(\Upsilon) \leq$ 5.5 GeV/c (dotted). The corresponding ADC_{trg} values are also shown assuming E_T = 32 GeV $\equiv$ 4096 ADC and a 5-bit shift.

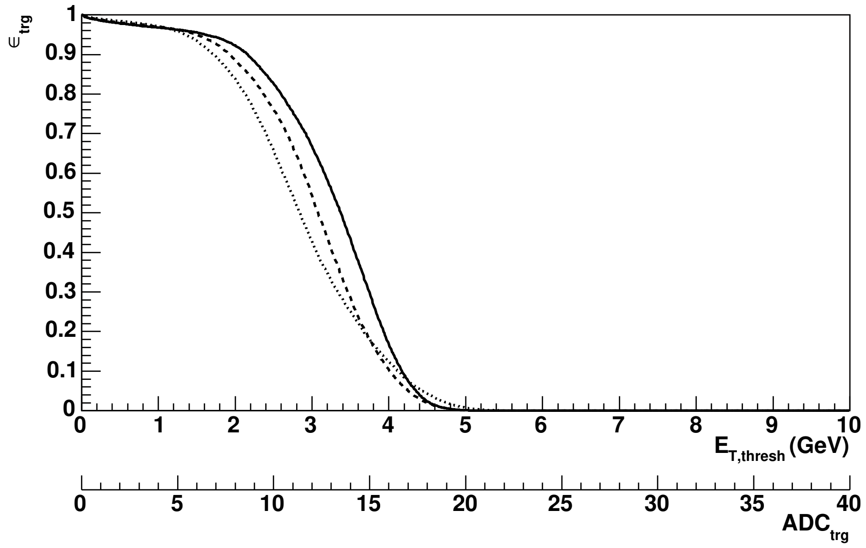

Figure 4.25: Trigger efficiency ϵ_{trg} for the L0 Topology trigger as a function of the energy threshold $E_{T,\text{thresh.}}$. Curves for different Upsilon momenta are shown, 0.5 GeV $\leq p_T(\Upsilon) \leq$ 1.5 GeV/c (solid), 2.5 GeV $\leq p_T(\Upsilon) \leq$ 3.5 GeV/c (dashed) and 4.5 GeV $\leq p_T(\Upsilon) \leq$ 5.5 GeV/c (dotted). The corresponding ADC_{trg} values are also shown assuming E_T = 32 GeV $\equiv$ 4096 ADC and a 5-bit shift.

and other concurrently running algorithms. A reasonable goal are $\leq 100\ \mu$s for the algorithm running time.

This time budget is large enough to attempt an online invariant mass reconstruction. As discussed in section 4.2 this requires the knowledge of the four-momentum vectors $v_e = (p_x, p_y, p_z, E)$ of both decay daughters. The BEMC tower data gives the energy of the electron and with the tower position also the direction of the momentum vector. Together with an assumption of the particle mass m this is sufficient to construct v_e. To simplify the calculation massless particles $m = 0$ GeV/c^2 are assumed. Using $E =\mid p \mid$ equation 4.18 can be rewritten as

$$m^2 = 2E_{e^+}E_{e^-}\,(1 - \cos\Theta) \tag{4.24}$$

where Θ is the opening angle between the decay daughters.

The main challenge is to get the "right" energy information from the BEMC. Figure 4.11 showed the dependence of the energy measured in a single tower on the distance of the particle hit position to the tower center. Only a fraction of the total energy is measured for non-central hits. In addition the fraction of lost energy fluctuates quite strong, making an average correction factor impossible. The way chosen in section 4.1.2 to deal with this challenge was to use clustering by adding the energy of multiple towers which removed the dependence of the energy on distance of the particle hit position to the tower center:

$$\begin{array}{l} E_{\text{cluster}}(1) = E_{\text{tower}} \\ E_{\text{cluster}}(n) = E_{\text{tower}} + \sum_{i=2}^{i=n} E_{\text{tower}}(i) \quad \text{with} \quad n \geq 2, E_{\text{tower}}(i) \leq E_{\text{tower}}(i+1) \end{array} \tag{4.25}$$

Also the angle between both daughters is needed for the invariant mass calculation, i.e. the direction of both daughter vectors v_e. Given the small curvature of high p_T tracks it can be approximated by the cluster position, calculated as the energy averaged tower position

$$\begin{array}{l} x_{\text{cluster}} = \left(\sum\left(x_{\text{tower}}\ E_{\text{tower}}\right)\right)/E_{\text{cluster}} \\ y_{\text{cluster}} = \left(\sum\left(y_{\text{tower}}\ E_{\text{tower}}\right)\right)/E_{\text{cluster}} \\ z_{\text{cluster}} = \left(\sum\left(z_{\text{tower}}\ E_{\text{tower}}\right)\right)/E_{\text{cluster}} \end{array} \tag{4.26}$$

where $(x_{\text{tower}}, y_{\text{tower}}, z_{\text{tower}})$ is the nominal position of the tower in the STAR coordinate system, i.e an event vertex at $(0, 0, 0)$ is assumed. While this is a good approximation in the transverse beam directions, it is questionable in the beam direction itself, given the large spread of the vertex distribution in z. The algorithm thus includes the option to calculate the position of the vertex z_{vertex} position from either the ZDC or BBC data and to correct the vectors used for the angle calculation for it: $p = (x_{\text{cluster}}, y_{\text{cluster}}, z_{\text{cluster}} - z_{\text{vertex}})$. The cosine of the angle Θ between the daughters can then be calculated as

$$\cos\Theta = \frac{\langle p_{e^+}, p_{e^-}\rangle}{\parallel p_{e^+} \parallel\parallel p_{e^-} \parallel} \tag{4.27}$$

with the scalar product in the three-dimensional cartesian space

$$\langle p_{e^+}, p_{e^-}\rangle = x_{e^+}x_{e^-} + y_{e^+}y_{e^-} + z_{e^+}z_{e^-} \tag{4.28}$$

However both clustering and $\cos(\Theta)$ computation are quite computing time intensive and ways to speed up the algorithm have to be found. To realize the necessary reduction in computing time several approaches are combined: reducing the number of calculated clusters, optimizing the time in the algorithm when the calculations are performed and optimizing the calculations itself. An example for the second class was the assumption of massless particles to simply equation 4.18 to equation 4.24 and thus reducing the computing operations from 27 to 5 for the calculation of the squared invariant mass[19].

Equation 4.27 includes the division by the product of the norms of the cluster position vectors. The $\cos(\Theta)$ calculation is performed for every cluster pair, i.e. each cluster is combined with multiple other ones. The length of the vector does of course not change while the event is processed. By normalizing the position vectors to 1 during the cluster calculation, equation 4.27 simplifies to

$$\cos\Theta = x_{e^+}x_{e^-} + y_{e^+}y_{e^-} + z_{e^+}z_{e^-} \tag{4.29}$$

and thus the computing amount for the $\cos(\Theta)$ calculation is significantly reduced to 5 arithmetic operations for each invariant mass pair. However the complexity of the clustering is increased by the calculation of the norm, i.e. 1 square root, 3 multiplications, 2 additions and 3 divisions.

Clustering is anyway the most computing intensive operation. To calculate a cluster, for each *seed tower* the 8 neighboring towers have to be found, sorted by energy and then added to the cluster to calculate the energy. Additionally the cluster position according to equation 4.26 has to be calculated and normalized to 1 to reduce the computing amount in the $\cos(\Theta)$ calculation. Finding the neighboring towers has been speed up using a lookup table which contains for each tower the IDs of the neighboring towers. The energy sorting is done using an insertation algorithm which is most efficient for small datasets like the one here. Further speedup of the clustering is only possible by reducing the number of calculated clusters, i.e. the number of seed towers. The natural choice is to introduce an energy threshold E_{seed} for the seed towers. This however means an effective energy cut on the energy of the cluster. Only clusters with $E_{\text{cluster}} \geq E_{\text{seed}} * n_{\text{towers/cluster}}$ are guaranteed to be calculated. However a more carefull examination of figure 4.11 shows that even electrons which hit a tower at its border still deposit a large fraction of their energy into this tower. The effective energy threshold set on the cluster by the seed tower energy threshold is thus much smaller. Figure 4.26 shows the ratio between the energy in a single tower E_{trg} and the $n = 3$ tower cluster energy $E_{\text{cluster}}(3)$. A reasonable cluster efficiency can be achieved with a E_{seed} setting of $\approx 0.5E_{\text{cluster}}(3)$.

Another constraint on the algorithm not discussed so far is that it must be a subset of the earlier L0 algorithm. In the case of the Upsilon algorithm that are either the L0 High Tower or the L0 Topology algorithm discussed in section 4.3.2. The reason behind this requirement is the trigger efficiency calculation. To illustrate this, lets assume a L0 HT triggered event with a single tower above the L0 threshold on which the L2 algorithm is now running. Several BEMC clusters get calculated, one around the one above the L0 high tower threshold, refereed to from here on as *L0 cluster*. All remaining clusters which do not fullfill the L0 trigger requirement will be called *L2 only clusters* afterwards. The invariant mass between all clusters gets calculated as described above. No combination of the L0 cluster with the L2 only clusters results in an invariant mass pair above threshold. However a combination of two L2 only clusters gives an invariant mass above the L2 threshold. The problem arising in the efficiency calculation is that one would need to know now the L0 trigger efficiency for one tower above the L0 threshold in coincidence with two other towers below threshold which however fullfill the L2 trigger condition. Obviously this strongly

[19]Not including the 5 operations needed to calculate $\cos(\Theta)$.

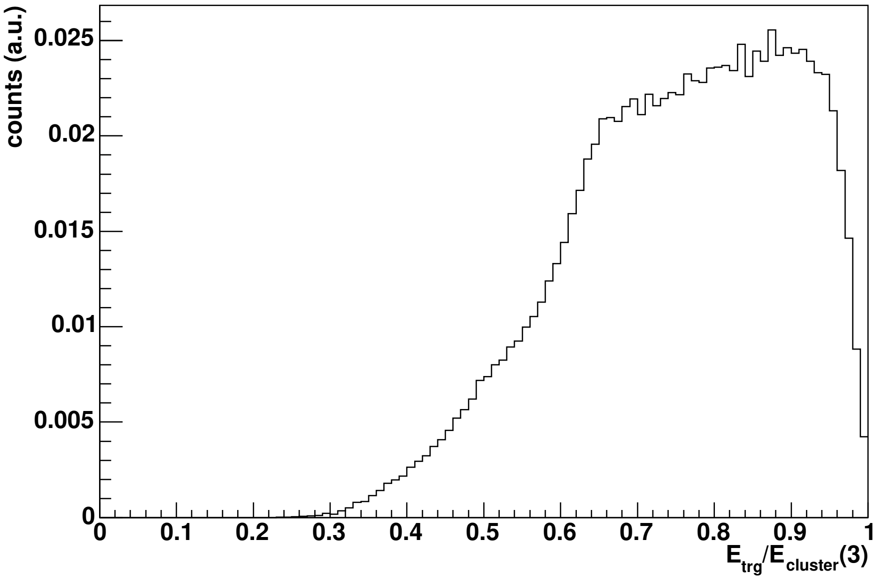

Figure 4.26: Ratio of energy deposited in the trigger tower, i.e. the tower with the highest energy share, to the energy in a 3 tower cluster for high p_T electrons.

depends on the exact event characteristics. Realistically it is impossible to calculate this quantity, even using particle production multiplicities from models as input. The only possibility to deal with this is making sure that events triggered by the L2 algorithm are a subset of the L0 triggered events.

This constrain is however easy to implement in the algorithm by introducing two cluster classes. One are the L0 clusters defined in the previous paragraph, the second one called *L2 clusters* includes all clusters calculated on L2[20]. In the invariant mass calculation according to equation 4.24 E_1 is required to be always a L0 cluster while E_2 is a L2 cluster. It is obvious that this fullfills the subset requirement in case of the L0 High Tower Trigger. However by setting both seed thresholds of the L2 algorithm to the same value, the requirement is also fullfiled for the L0 Topology Trigger. The necessary settings are listed in table 4.4.

L2 parameter	L0 High Tower Algorithm	L0 Topology Algorithm
L0 seed threshold	L0 Tower Threshold	L0 Tower Threshold
L2 seed threshold	not constrained	L0 Tower Threshold
$\cos(\Theta)_{\max}$ threshold	not constrained	$\leq \cos\left(60^O\right)$

Table 4.4: L2 Upsilon algorithm parameter settings necessary to fullfill the L0 subset requirement for both L0 triggers described in section 4.3.1.

Figure 4.29 to 4.31 show the efficiency of the L2 algorithm as function of various L2 cut parameters. The dependence on the minimum required energy of an L0 Seed Tower is shown in figure 4.29. The upper plot shows the dependence without any

[20]Note the difference between L2 clusters and the L2 only clusters defined above. While all clusters are either a L0 cluster or a L2 only cluster (i.e. the two sets are distinct), L2 clusters include all clusters calculated on L2 (i.e. L0 clusters and L2 only clusters are subsets of L2 clusters)

Parameter Name	Description	Run Control ID
L0 Seed Threshold	Threshold in trigger ADC above which a L0 cluster is calculated. It has to match the L0 threshold, see table 4.4 for more details.	I0
L0 Bit Shift	Bit shift from ADC to trigger ADC in L0 (defaults to 5)	-
L2 Seed Threshold	Threshold in ADC above which L2 clusters are calculated. It should be set in conjunction with the "L2 Energy Threshold" parameter so that all clusters with energies above this threshold get calculated. This is by construction guaranteed if the "L2 Energy Threshold" is converted into ADC and divided by the number of towers per cluster. Higher settings are possible, see text for details. Must be the same as the "L0 Seed Threshold" if the L0 Topology trigger is used, see table 4.4.	I1
Number of Towers/Cluster	Number of towers per cluster, 1 = single tower clusters	I4
Vertex z	Calculate vertex z position and correct cluster positions for it to get a better approximation of the angle between both daughters (0 = do not calculate,1 = vertex z position from ZDCs).	I3
CTB matching	Check if the CTB slat in front of the cluster has a hit from a charged particle. Might be used to reject clusters from neutral particles in low multiplicity events.	I2
L0 Energy Threshold	Minimum energy in GeV for L0 clusters. Minimum value is the energy to which the ADC value of the "L0 Seed Threshold" translates.	F0
L2 Energy Threshold	Minimum energy in GeV for L2 clusters.	F1
$\cos(\Theta)_{\max}$	Maximal cosine of the opening angle between the two clusters of a pair. Must be smaller then $\cos\left(60^0\right)$ if the L0 Topology trigger is used, see table 4.4 and text.	F2
$(m_{inv})_{\min}$	Minimum invariant mass	F3
$(m_{inv})_{\max}$	Maximum invariant mass	F4

Table 4.5: L2 Upsilon algorithm parameters.

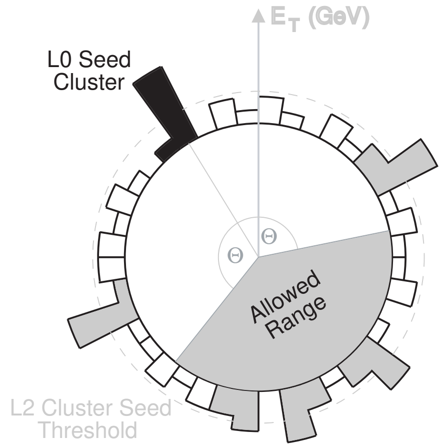

Figure 4.27: Schematic illustration of the L2 Upsilon algorithm. For details on the algorithm see text.

cut on L0, the lower assuming an L0 High Tower Trigger with an threshold of 3.5 GeV. The relative L2 efficiency for this case stays high up to ~ 4.5 GeV, with the higher threshold reducing the combinatorics from background particles by quite a bit.

The dependence of the L2 trigger efficiency on the L2 energy threshold parameter is shown in figure 4.30. Up to 2 GeV Upsilon p_T independent high efficiencies are achieved, further increasing the threshold reduces the efficiency for high-p_T Upsilons first as expected from figure 4.21. High efficiencies of more than 90% for low p_T Upsilons are possible up to an threshold of 3-3.5 GeV. The maximum opening angle cut $\cos(\Theta)$ does not influence the efficiency too much down to $\pi/2$ after which the efficiency starts to drop.

Finally the efficiency versus the required minimum invariant mass of the L2 cluster pair is shown in figure 4.32. One has to keep in mind that the efficiencies here are defined relative to accepted Upsilons (cf. section 4.2.2), i.e. Upsilons where the mass reconstructed from the TPC tracks is $m_{inv} > 8.4$ GeV/c^2. Upsilon decays where the electrons loose significant energy by Bremsstrahlung before entering the TPC are thus not included in the efficiency calculated here. Very high efficiencies of $\epsilon_{trg} > 95\%$ can be attained for cuts $min(m_{inv}) \lesssim 7.5$ GeV/c^2.

For the interpretation of the efficiencies just shown one has to keep in mind that the cut parameters are strongly correlated. The single efficiencies just shown can therefore not just be multiplied with each other to calculate the combined efficiency. For example the deviation from one for small cut values in figures 4.29, 4.30 and 4.32 originates from daughter electrons whose energy is severely underestimated. The efficiency dependence of the invariant mass cut is thus completely correlated with the product of the single efficiencies. However the dependence of the efficiency on the various parameters gives a first hint where to place the cuts and on the sensitivity to variations of the cut parameters, which proved to be very usefull during the trigger commissioning.

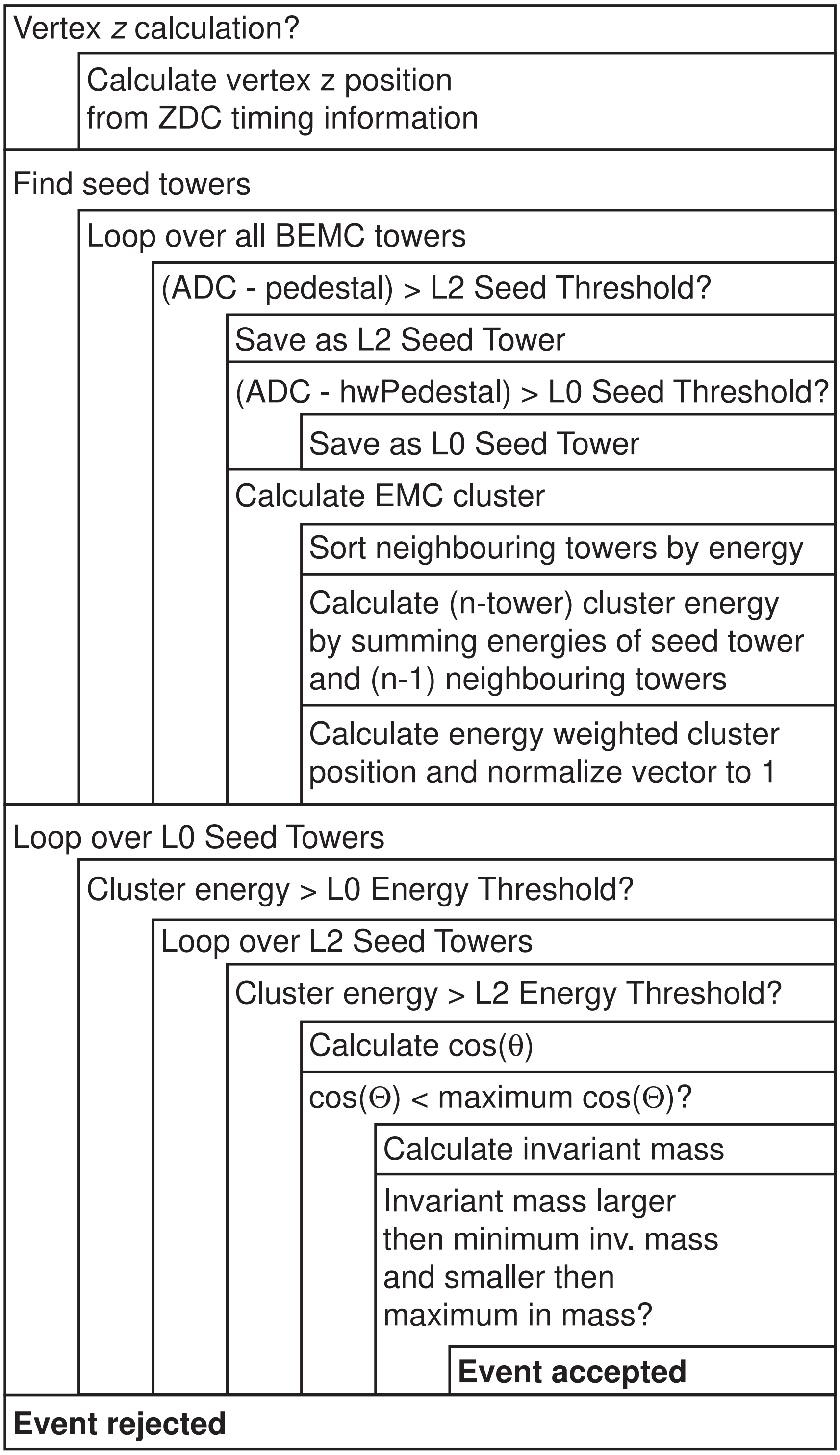

Figure 4.28: Logic of the L2 Upsilon trigger algorithm.

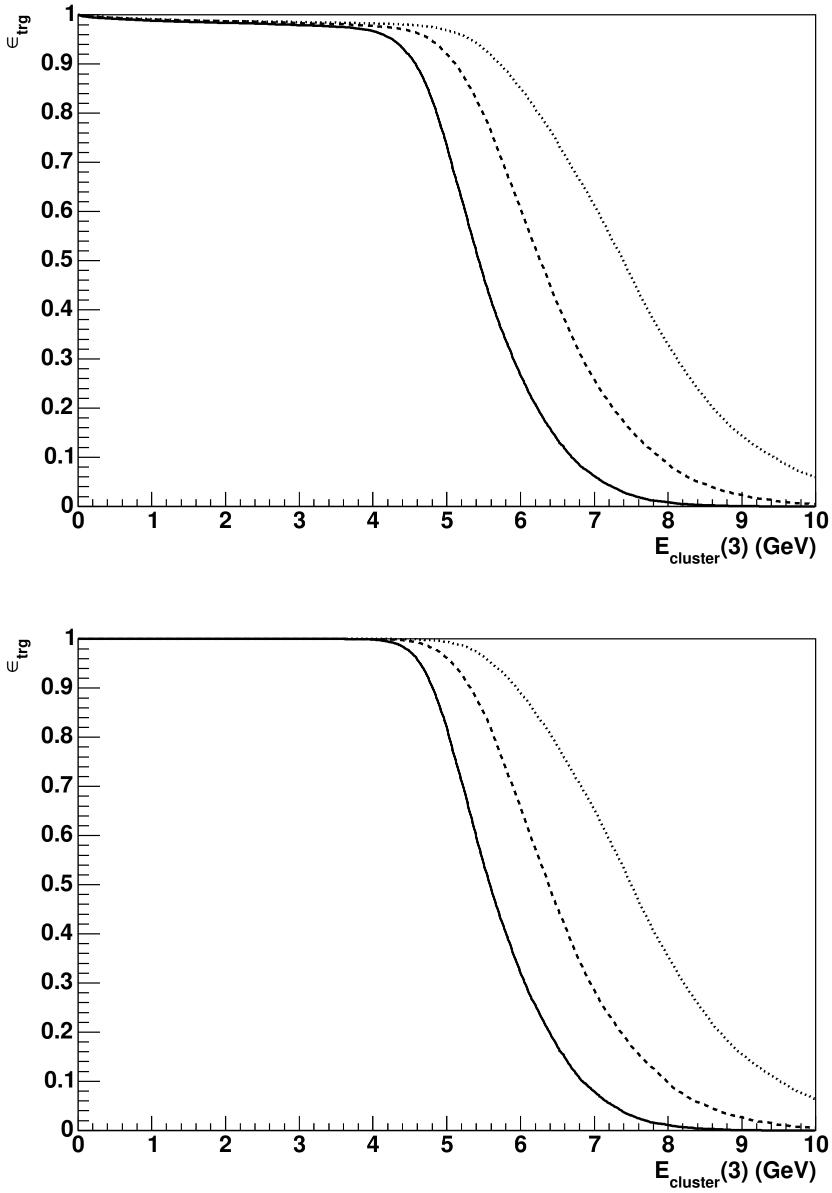

Figure 4.29: L2 trigger efficiency ϵ_{trg} as function of the "L0 Energy Threshold" cut parameter. While in the upper figure no L0 trigger condition has been assumed, an L0 high tower trigger with threshold $E_{\mathrm{L0}} = 3.5$ GeV was used for the lower plot. Results for different Υ momenta are shown, 0.5 GeV $\leq p_T(\Upsilon) \leq$ 1.5 GeV/c (solid), 2.5 GeV $\leq p_T(\Upsilon) \leq$ 3.5 GeV/c (dashed) and 4.5 GeV $\leq p_T(\Upsilon) \leq$ 5.5 GeV/c (dotted).

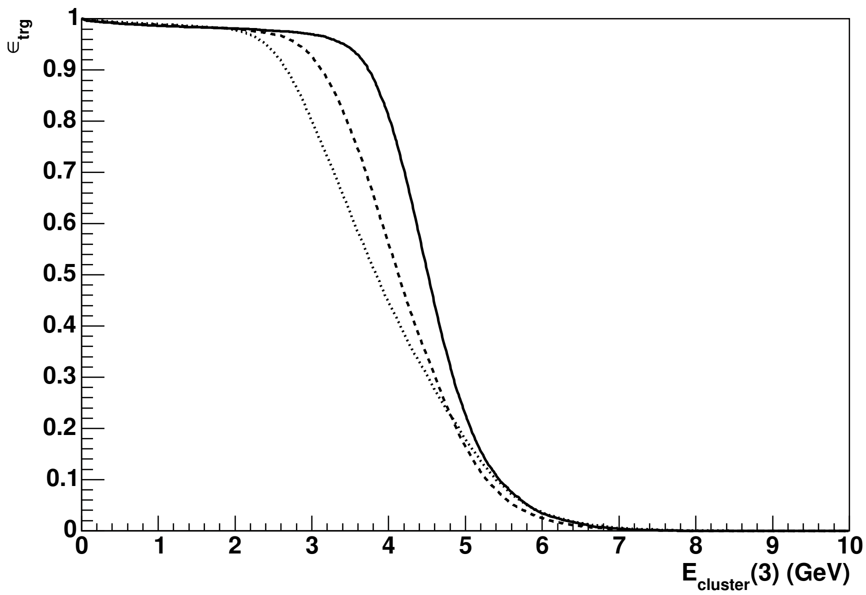

Figure 4.30: L2 trigger efficiency ϵ_{trg} as function of the "L2 Energy Threshold" cut parameter. Results for different Υ momenta are shown, 0.5 GeV $\leq p_T(\Upsilon) \leq$ 1.5 GeV/c (solid), 2.5 GeV $\leq p_T(\Upsilon) \leq$ 3.5 GeV/c (dashed) and 4.5 GeV $\leq p_T(\Upsilon) \leq$ 5.5 GeV/c (dotted).

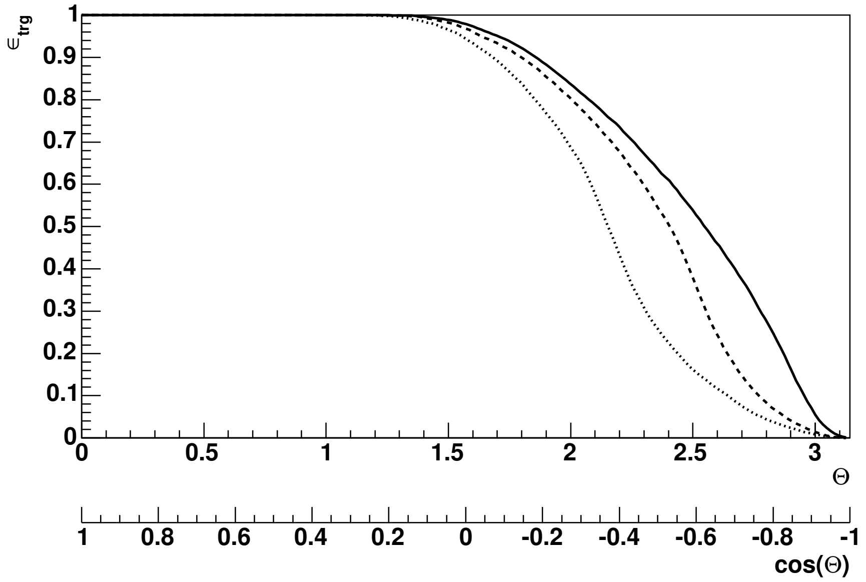

Figure 4.31: L2 trigger efficiency ϵ_{trg} versus a cut on the minimal opening angle Θ respectively the maximal $\cos(\Theta)$. Results for different Υ momenta are shown, 0.5 GeV $\leq p_T(\Upsilon) \leq$ 1.5 GeV/c (solid), 2.5 GeV $\leq p_T(\Upsilon) \leq$ 3.5 GeV/c (dashed) and 4.5 GeV $\leq p_T(\Upsilon) \leq$ 5.5 GeV/c (dotted).

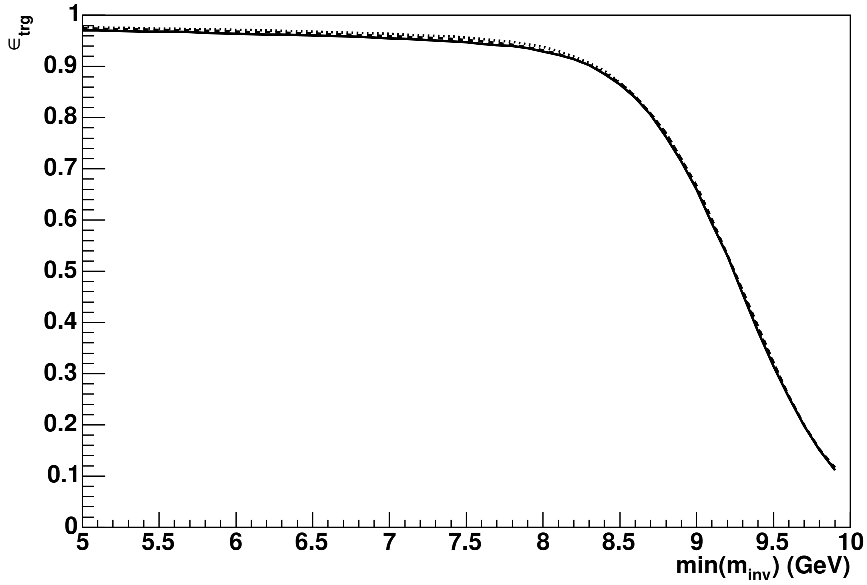

Figure 4.32: L2 trigger efficiency $\epsilon_{\rm trg}$ versus cut on the required minimal invariant mass. Note that this is relative to reconstructable Upsilons as defined in section 4.2.1. Results for different Υ momenta are shown, 0.5 GeV $\leq p_T(\Upsilon) \leq$ 1.5 GeV/c (solid), 2.5 GeV $\leq p_T(\Upsilon) \leq$ 3.5 GeV/c (dashed) and 4.5 GeV $\leq p_T(\Upsilon) \leq$ 5.5 GeV/c (dotted).

4.3.3 L3 Trigger

On Level 3 the TPC tracking information is additionally available to the BEMC information used so far. As in the case of the L2 algorithm just described it can only operate with the part of the event data which would have triggered the previous trigger level, in this case only with the invariant mass pairs calculated in the L2 algorithm which are above the thresholds. Since the L2 trigger saves only some quality information as output, the first step is to repeat the L2 algorithm to get a list of all invariant mass pairs present in the event which would have triggered it.

The combined BEMC and CTB data on L2 did not allow to distinguish between energy deposited in the BEMC by charged particles or neutral particles and photons. Given the large number of hadronic resonance decays which produce a photon and the large number of π^0s compared to electrons most of the invariant mass pairs are γ-γ combinations. The availability of TPC track data on L3 makes it possible to reject these pairs and thus to further increase the selectivity of the trigger.

For this the L2 algorithm was slightly modified. After all BEMC clusters are calculated, all $p_T > p_T^{\rm L3}$ L3 TPC tracks get extrapolated to the BEMC radius (with the trigger parameter $p_T^{\rm L3} = 1$ GeV/c). If the distance between the BEMC cluster position and an extrapolated L3 track is smaller then a trigger parameter $d_{\rm max}$ of typically 10 cm, the cluster is marked as a cluster potentially created by a charged particle. In the now-following calculation of invariant mass pairs in the L2 algorithm only pairs of clusters are calculated where both clusters are marked.

A considered extension of the algorithm was to calculate the invariant mass using the L3 track information. It turns however out that the L3 momentum resolution in the relevant region is worser then the one provided by the BEMC clusters and thus does not result in further event discrimination. This becomes obvious by looking at figure 4.19 and recalling from section 3.2.4 that L3 tracks are global tracks with a resolution typically a factor 2-3 worser than the one of offline tracks, i.e. the dotted line in the figure.

The idea to implement a cut on the ratio of cluster energy and track momentum as done in the offline electron identification with the BEMC (see section 4.1.2) was also not followed for the same reason. Since the momentum resolution enters in the cut position and some safety margin to allow a offline optimization of the cuts has to be included not much would be gained, but the offline analysis would be significantly complicated.

The efficiency ϵ_{trg} of this algorithm is thus just the squared tracking efficiency $(\epsilon_{\mathrm{rec}}^{\mathrm{L3,offline}})^2$ relative to offline, i.e. the fraction of tracks which offline would have reconstructed but L3 has not found. This fraction is heavily dependend on the exact cuts used in offline and on L3, but for "standard" settings (i.e. much looser cuts on L3 on e.g. the number of points on track) $\epsilon_{\mathrm{rec}}^{\mathrm{L3,offline}} = 0.85$ has been determined [Adl03, Fli03], resulting in $\epsilon_{\mathrm{trg}} = 0.72$.

In the calculation of the trigger efficiency above two effects were neglected. The L3 tracking efficiency relative to offline $\epsilon_{\mathrm{rec}}^{\mathrm{L3,offline}}$ gives the probability that the offline found track is also found on L3. It happens that L3 finds a track while offline does not find one, the probability for this is however low ($\sim 1\%$). However this might increase the trigger efficiency by 2%. The event might also be accepted if there is more than one track above p_T^{L3} in the matching radius d_{max} around the cluster. This results in an increasing trigger efficiency with increasing multiplicity but also means lower rejection rates of the algorithm. The excat L3 trigger efficiency can thus only determined from non-L3-triggered events (but with all previous trigger levels). An alternative is to require that only offline tracks are used where an matching L3 track was found which would trigger the event.

5 Search for Upsilons in Au+Au Collisions

The Upsilon trigger was first used in production mode during the 2004 Au+Au run. The accelerator worked remarkably well, reaching and even exceeding its design parameters for Au operation. The delivered luminosity was quoted by CAD to be 1270 μ^{-1}b, allowing for the first time to attempt an Upsilon measurement.

The operation of the STAR detector and especially its trigger capabilities were however severely affected by experimental difficulties encountered during the commissiong of the Barrel Electromagnetic Calorimeter. Although already used during the 2003 d+Au and p+p runs, it took the first half of the run before it could be included into normal data taking. But even then stable operation was never achieved, resulting in a reduced and varying coverage as well as corruption of the recorded data. This is discussed in detail in sections 5.1.1 and 5.1.3 respectively.

The operation of the BEMC based higher level (L2/L3) trigger algorithms was of course strongly affected by these problems. An additional limitation was the incapability to run L2 aborts with the full detector system. The Silicon Vertex Tracker (SVT) and the Calorimeter Shower Maximum Detectors (BSMDE,BSMDP) failed to treat aborts correctly. After it turned out that these systems could not be fixed during the run, the planned trigger strategy had to be modified. The Level 2 algorithm was completely dropped, shifting all decisions to L3. The rate of the L0 baseline trigger would have been however to high, severely reducing the lifetime of STAR and the ability to take concurrent minimum bias and central events. It was therefore decided to include a ZDC based vertex cut in the L0 baseline trigger. Also the L3 algorithm itself got modified. The high collision rates achieved by RHIC caused sizeable space charge distortions in the Time Projection Chamber. Since the effect on the online found tracks was not known during data taking, it was decided to not use the L3 tracking information in the algorithm decision. The rejection rates even without tracking turned out to be high enough to meet the rate goals for the express streams, allowing this simplification. The modified Upsilon trigger scheme is described in more detail in section 5.2.

The tagging of events for the express stream with Level 3 worked smooth besides the already mentioned problems with the BEMC data input. Four different tagging algorithms were run: the Upsilon trigger, a (very) high electromagnetic p_T trigger, an anti-helium trigger and a strangelet trigger; tagging a total of 384.225 events. The offline reconstruction of these events took one day while the production of the whole dataset is projected to take one year and will not be finished before this PhD thesis. Overall the whole concept of the L3/DAQ express streams outlined in 3.2.4 worked as planned, proving the usefullness of high level triggers in the challenging environment of heavy collisions. STAR will continue to use express streams in the coming years as a valuable tool to achieve high data quality and quick turn around times for specific rare probes.

The search for an Υ signal in the express stream events is described in 5.3. After applying QA cuts, mainly to remove the events affected by the above mentioned BEMC problems, 5,499 events out of a scanned luminosity of 34.3 μb^{-1} (237M events) had a valid Upsilon trigger. Very few counts are observed after requiring reconstructed TPC tracks pointing to the clusters of the trigger pair and even less after additional electron identification cuts. The extraction of an upper limit on Upsilon production in $Au + Au$ collisions is descriped in section 5.3.3, after calculating the efficiencies in section 5.3.2.

5.1 The Barrel Electromagnetic Calorimeter Performance in Run 4

5.1.1 Acceptance

The nominal BEMC coverage for run 4 was $\sim 3/4$, i.e. 72 modules out of the 120 total. Various failures reduced this coverage significantly. They can be roughly divided in two categories, one affecting single towers and being quite stable in the run. The second affects large areas at once and varies with time, we first focus on this effect.

As detailled in 3.2.2, the front end electronic for the 160 towers of $0.5 + 3 + 0.5 = 4$ modules is installed in the Tower Digitizer Crates. The power supplies of these crates developed a high failure rate during the run, with ~ 1 failure per week. The available spares and the time needed for repair of the broken power supplies would not have allowed to replace all failing ones. It was decided to drop the support of the east half, reducing the number of working modules to the 60 of the west half. With the freed power supplies of the east half crates enough power supply spares were available to replace the failing ones in the west half. The replacement was however only possible during the scheduled access periods every two weeks since the replacement procedure required roughly eight hours without beams. This resulted in extended periods with non-working crates and thus reduced BEMC coverage. The 160 towers of one crate correspond to $\sim$3% of all towers and $\sim$7% of the working towers. Ten periods with different working crate configurations where identified in the Upsilon trigger data taking period as listed in table 5.1. Two of them just consist of few runs. Dropping the data from these two short periods reduces the number of periods to six which we will use for the further analysis.

The other category of BEMC hardware failures affects single towers only. Several failure modes have been identified so far by analyzing the single tower ADC spectra in the recorded data:

- dead channels (no signal)
- hot channels (high values for every event)
- channels with very low/high gain (large shift of pedestal peak)
- noisy channels (large width of the pedestal peak)
- channels with bit failure (always set/never set)
- adjacent tower FEE channels giving the same ADC value for every event

Period	First run	Last run	Non-working crates	#working crates	#working towers
Ia	5044079	5047009	1-15	15	2195
	5047010	5047010	1-15,28	14	2042
Ib	5047032	5047064	1-15	15	2195
	5048018	5048047	1-15,30	14	2038
Ic	5040007	5053095	1-15	15	2195
II	5053112	5057039	1-15,26	14	2117
III	5064008	5066024	1-15,20	14	2041
IV	5066034	5068125	1-15,20,30	13	1884
V	5068126	5076096	1-15,20,28,30	12	1731
VI	5078030	5084023	1-15	15	2195

Table 5.1: BEMC tower status for the FY04 run.

Figure 5.1 shows the effect of these failure modes on the tower ADC spectra, a "normal" tower single ADC spectrum is shown as reference. A software tool was developed to automatically identify the affected towers which is now available in the STAR Software library as `StRoot/StEmcPool/CSMStatusUtils`. Since the analysis procedure is based on the ADC spectra of single towers, a large number of minimum bias events is needed. While this is no problem for a typical Au+Au run, the tagged events in the express streams do not allow for this.

To get an estimate of the affected towers, several days (86 - 91) at the end of the Au+Au running period were produced and analyzed[1]. Figure 5.2 shows the status for all towers as a function of the relative run number. A total of 203 towers out of the 2400 nominally working (8.4%) was found to not work properly. The large number of non-working towers visible around tower id 700 is the result of a broken PMT box, housing 80 PMTs. The number of affected towers is stable over the analyzed period of 5 days. It seems reasonable to use the single tower status determined at the end of the run as an estimate for the whole running period.

The relative position of the non-working towers has a large influence on the Upsilon trigger algorithm described in 4.3 since the L2 and L3 algorithms use the position and energy of two BEMC clusters (hits) to calculate the opening angle and invariant mass. Figure 5.3 shows the position of the working towers for the six run periods defined in table 5.1. The large holes of four modules caused by the failing crates are clearly visible. The effect of these tower failures on the Upsilon acceptance and the trigger efficiency will be discussed later in section 5.3.3 where the expected Upsilon yield is recalculated.

5.1.2 Tower Energy Calibration

During the data analysis another problem with the BEMC based triggers became visible: the individual tower calibration. Due to the accidental loss of the west half high voltage settings for the individual photomultiplier tubes between the FY03 and FY04 runs the whole calibration of the BEMC had to be redone in the first weeks of the FY04 run. The goal is a calibration in transverse energy, i.e. a measured ADC value translates to the same E_T independent of the actual tower. A proper

[1] The collision energy during these days was $\sqrt{s_{NN}} = 62.4$GeV but the BEMC hardware status should be independent of the collision energy or system.

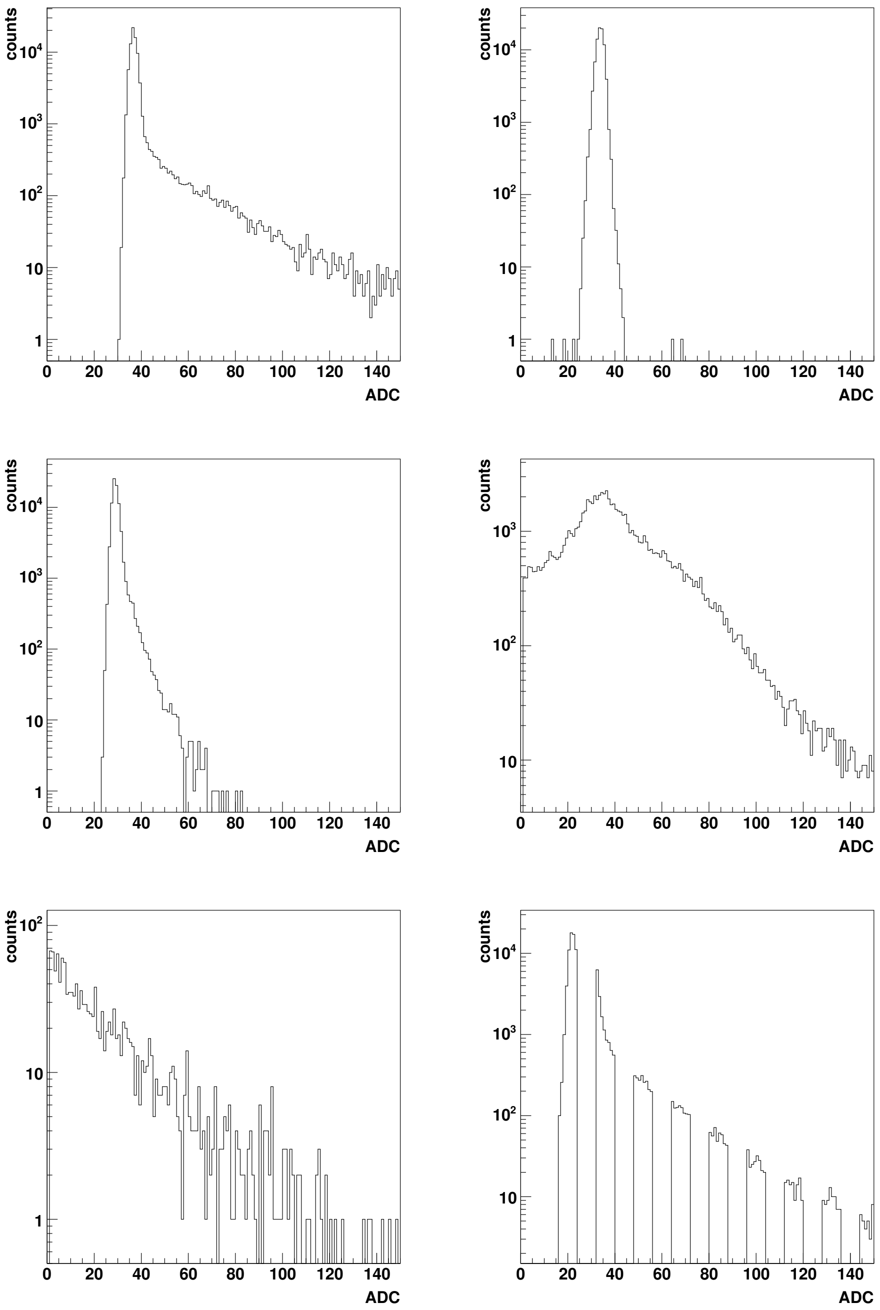

Figure 5.1: Examples of the effect of single tower failure modes on the ADC spectra. The upper left channel shows the a "normal" ADC channel as reference while the other five plots show various failure modes.

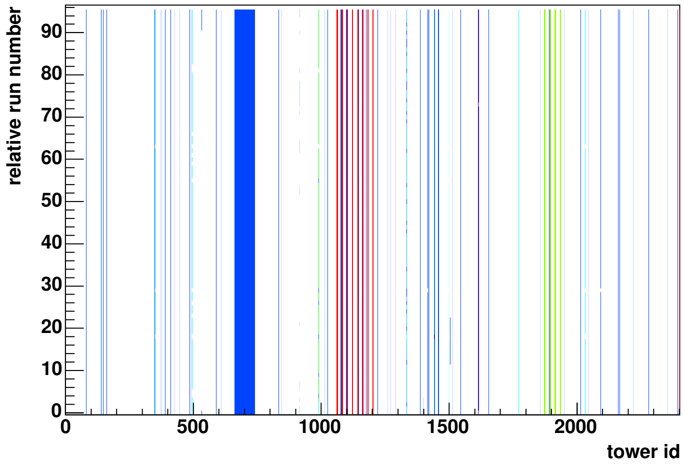

Figure 5.2: Tower status as function of the relative run number during days 86 to 91. Lines show periods with tower failures for the 2400 towers of the west side.

calibration is crucial for triggering as described in sections 3.2.3 and 4.3, especially on L0 where the raw ADC values are used as input. As will be shown later in this section the calibration for the FY04 run did not achieve this goal, decreasing the efficiency and increasing the analysis complexity.

The calibration scheme employed in STAR is based on ADC slope equilibration for the inter-tower-calibration and the BEMC response of minimum ionizing particles or electrons for setting the absolute energy scale. A typical ADC spectrum was already shown in the upper left plot of figure 5.1.

The calibration process starts by obtaining such ADC spectra for every (working) tower. To calibrate the towers relative to each other assumptions have to be made how the ADC spectra in neighboring towers relate to each other. Obviously the collisions are rotation symmetric in phi which allows to group the towers into rings of 120 towers in ϕ times 1 tower in η. After pedestal subtraction the slope of the ADC spectrum is fitted for each tower in the rings. The HV setting of the PMTs is then adjusted in an iterative process until the fitted slope are the same for each tower in the rings.

Calibrating the rings to each requires another assumption. It is known from earlier measurements that the transverse energy in an Au+Au collision is roughly independent of pseudorapidity η in the BEMC range $-1 \leq \eta \leq 1$. Thus equilibrating the fitted ADC slopes of all rings will result in the desired E_T calibration, i.e.

$$ADC \sim E_T = E \cdot sin(\Theta) \tag{5.1}$$

where Θ is the angle to the beam axis ($\eta = -\ln\tan(\Theta/2)$).

After this step all towers of the BEMC are calibrated relative to each other, i.e. they will give the same ADC value for the same deposited transverse energy E_T. What still needs to be done is a determination of the absolute energy scale. The STAR software supports not only a linear mapping but higher order corrections as

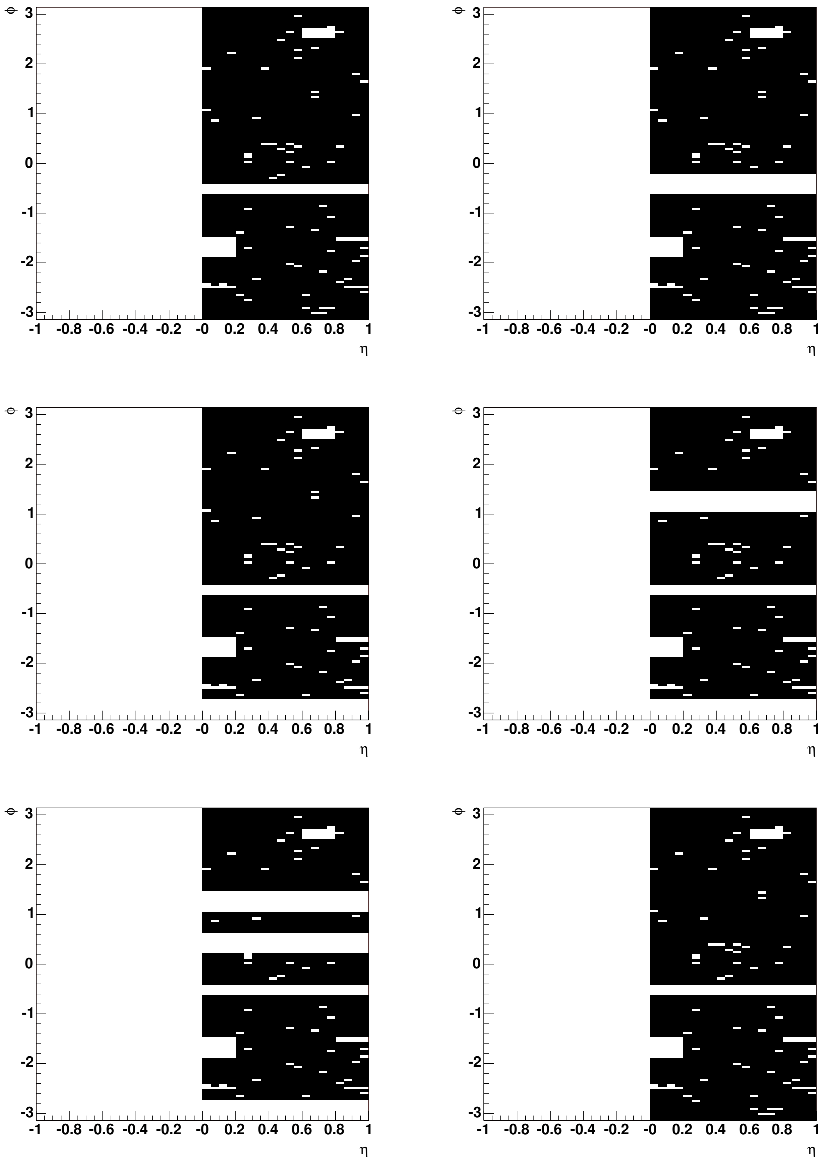

Figure 5.3: $\eta - \phi$ coverage of the BEMC for run periods I-VI, see table 5.1 for details.

well, leading to the equation

$$E = \sum_{i=0}^{4} (\mathrm{ADC})^i * c_i \tag{5.2}$$

to calculate the energy E from the measured ADC values using the calibration constants c_i for each of the 4800 towers. However currently only a linear mapping (i.e. only $c_1 \neq 0$) is used. The HV should be set that that the maximum energy is 64 GeV, a requirement for p+p jet spin physics at $\sqrt{s} = 500$ GeV. By mistake the actual calibration during the FY04 run was for a maximum energy of 32 GeV, which is still more than sufficient for heavy-ion collisions.

Two different methods are used in STAR to determine the energy scale: Both require a combination of particles measured in the TPC with the BEMC tower data. Either one selects electrons using the momentum and $\mathrm{d}E/\mathrm{d}x$ information (see section 4.1.1 and the adjusts the high-voltages so that the ratio of energy measured in the BEMC to the TPC momentum E_{tower}/p peaks at one. This requires however a large statistics dataset with both TPC and BEMC information due to the low number of (high-p_T) electrons in the collisions. This *electron calibration* is therefore only used for the offline calibration after the run.

During the run a different approach is used for the online calibration. It is based on the BEMC response of hadrons which do not shower in the calorimeter. By selecting particles with more than 1 GeV/c momentum, the energy loss in the BEMC material is essentially the one of minimum ionizing particles. However the observed structure is quite broad and thus the precision of this calibration is not as good as one achievable with the electron calibration discussed above. The big advantage is however the much smaller number of tracks needed. Such a calibration was done at the beginning of the FY04 run, using L3 tracking information, and used in the trigger levels L2 and L3.

After the run and the first data production enough statistics was available to perform an electron calibration which should result in better results due to the better determined peak shape and mean. A comparison of both calibrations is plotted in figure 5.4 the ratio between the calibration constants of both sets for all working towers:

$$\mathcal{R}^{\mathrm{calib}}_{\mathrm{bemc}} = c_1^{\mathrm{online}}/c_1^{\mathrm{offline}} \tag{5.3}$$

The first obvious observation is a large spread of the calibration constants with an RMS of 17%, giving an estimate of the online achieved energy resolution. What is a little bit more worrysome is the observed systematic shift to an mean value of 0.93 indicating a systematic underestimate of the deposited energy of 7%. Thus the energy cuts applied on the trigger levels were all significantly higher than intended, leading to a reduction in trigger efficiency.

As mentioned it was planned to calibrate the BEMC in transverse energy E_T and during the run it was assumed that this had happened. In this case the minimum transverse energy E_T triggered by L0 should be independent of η with some spread due to a non-perfect calibration. The left panel of figure 5.5 shows this distribution for the FY04 calibration with an L0 trigger ADC cut of 13. Obviously this distribution is far from being independent of η. Accidentally the BEMC group introduced an additional factor $\sin(\Theta)$ into equation 5.1 resulting in

$$ADC \sim E_T \sin(\Theta) = E \sin(\Theta) \sin(\Theta) \tag{5.4}$$

which is clearly visible in the figure. At $\eta = 1$ the effective energy threshold is increased by a factor $1/\sin(\Theta) = 1.54$, shifting it from $E_T \approx 3.5$ GeV at $\eta = 0$ to

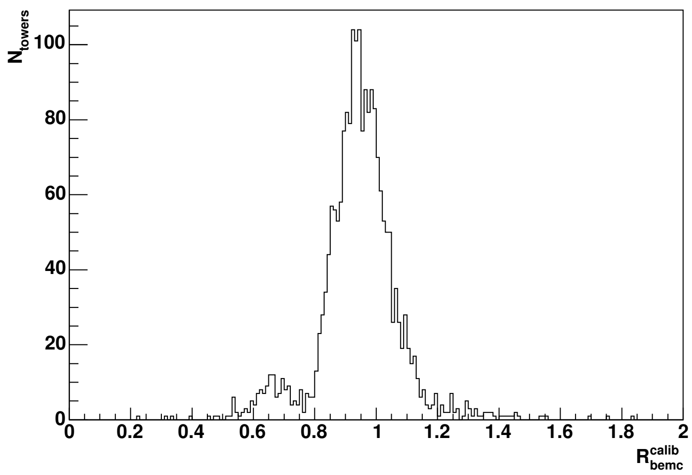

Figure 5.4: Ratio $\mathcal{R}_{bemc}^{calib}$ between the online and improved offline calibration.

$E_T \approx 5.4$ GeV at $\eta = 1$. The projections on the transverse energy axis shown in the right panel of figure 5.5 confirm this setting. Obviously such an unexpected shift in the trigger threshold will have a huge influence on the trigger efficiency of at least the L0 trigger. Steps have been taken to introduce additional QA measures during the run to prevent such a mistake in future. Another side effect is that the FY05 run has yet another set of BEMC PMT high voltages. The hit in the trigger efficiency for the Upsilon trigger will be quantified later in section 5.3.2. Yet another BEMC problem affecting the data and at least partly hiding the calibration problem in the online QA needs to be discussed first.

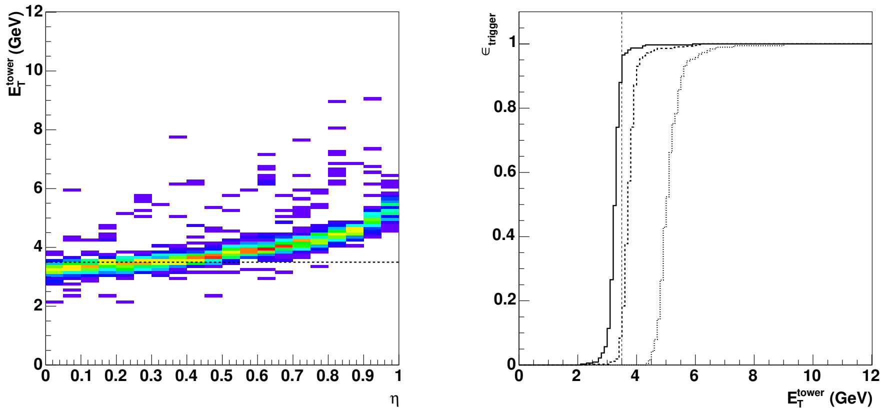

Figure 5.5: Left figure: Minimum transverse energy E_T^{tower} measured in an individual BEMC tower to get accepted by the FY04 L0 trigger. Right figure: Trigger efficiency $\epsilon_{trigger}$ as function of E_T^{tower} for three pseudorapidity bins ($0 \leq \eta \leq 0.1$ (solid line), $0.4 \leq \eta \leq 0.6$ (dotted line) and $0.9 \leq \eta \leq 1$ (dashed line)). For comparison both figures include a line showing the planned trigger threshold of $E_T^{\mathrm{tower}} = 3.5$ GeV.

5.1.3 Tower Data Corruption

An additional problem with the calorimeter was corruption of the data in the BEMC readout electronic. As mentioned in section 3.2.2 the tower digitizer crates which house the front end electronic send their data over fiber links to the tower data collector which collects the data for each event. The data is then transfered to the DAQ system and the L2/L3 triggers.

The data transfer between the tower digitizer crates and the tower data collector showed a relatively large fraction of malfunction, roughly 1% of all events. The most probable source of the failing transfers is a loss of synchronization with the STAR trigger clock. Attempts to improve the clock signal distribution in the Trigger Clock Distributor (TCD) were partly sucessfull, reducing the rate of corrupted events to 0.01% by the end of the Au+Au run.

The corrupted data transfers have a significant effect on the ADC spectra. The upper left plot of figure 5.6 shows the ADC spectrum of all towers in a minimum bias run taken at the beginning of data taking. While at the lower end the expected exponential decrease is observed, the higher part of the spectrum is completely dominated by suspicious entries.

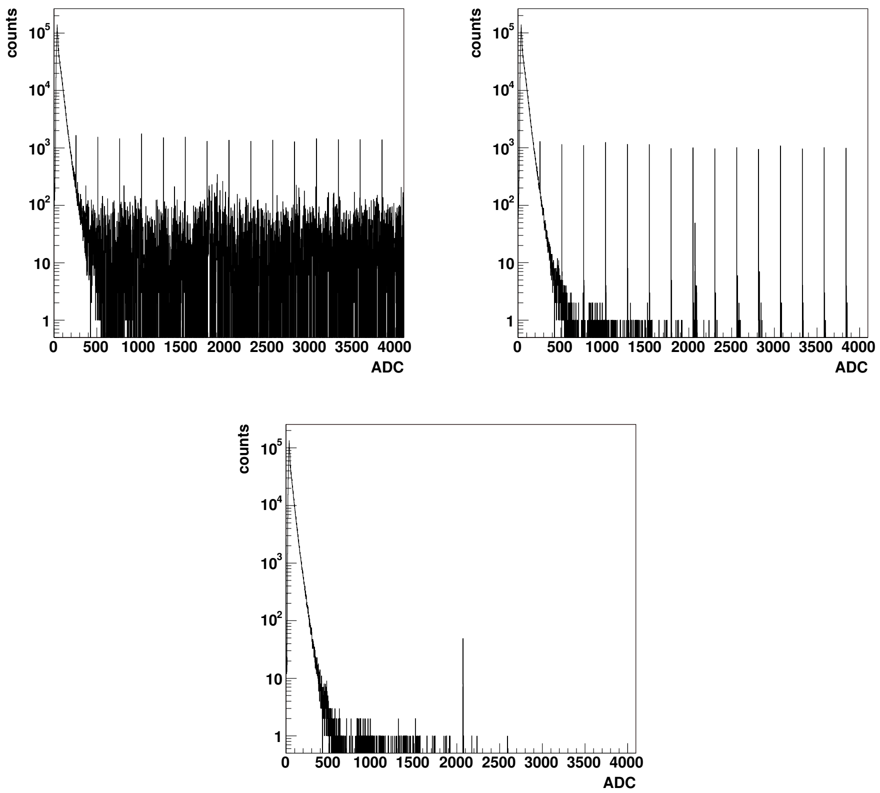

Figure 5.6: Effect of tower data corruption on ADC spectra: Upper left plot shows the spectrum of all recorded events, the upper right the ADC spectrum of crates with correct header, the lower one the ADC spectrum of events which have only correct headers.

Obviously the suspicious events need to be removed before any physics analysis. After the run it turned out that the data headers written by the BEMC Tower Data Collector for each crate can be used to detect the corrupted crates. The first two words contain the number of bytes transfered from the crate to the Tower Data Collector and a status flag. In a regular event the first word is always 164 and the second 0 for working crates. Non-installed crates have 4096 in both header words. Headers from corrupted crates have deviating entries, allowing to identify them.

After removing the data from corrupted crates, the ADC spectrum is much cleaner as can be in the upper right plot of figure 5.6. However there is still some unphysical structure remaining, i.e. peaks at $\sim n \times 256$ indicating persistent problems with the data transfer.

Further clean up is possible by not only removing the data from corrupted crates but the data from every event which has a corrupted event. The resulting ADC spectrum is shown in the lower plot in figure 5.6 and no artefacts indicating remaining problems with the data link are visible. The peak at $ADC \approx 2000$ is the result of a stuck bit in one single tower and gets removed by applying the status tables as described in the previous section. The here developed algorithm got integrated into the STAR offline and online frameworks, cleaning up any analysis and allowing to monitor the corruption level during data taking.

However the data corruption caused serious problems on the trigger level during the FY04 run. The lowest trigger level L0 has an own data path to the crates over which the trigger primitives are transfered as shown in figures 3.10 and 3.12. No data corruption could be identified on this data path and thus L0 triggered events are not affected by the crate data corruption. This changes for the higher trigger levels L2 and L3 which use the BEMC raw data collected by the tower data collector for their decision algorithms. Since the clean-up procedure was not available at the time of data taking, the trigger algorithms operated on the data shown in the upper left plot of figure 5.6. A significant fraction of these events fullfilled the trigger conditions of the Upsilon trigger, increasing the needed bandwidth by a substantial amount [2].

5.2 The Upsilon Trigger in the FY04 Au+Au run

As mentioned the Upsilon Trigger chain described in 4.3 had to be modified in the beginning of the run due to various detector problems. The most severe was the inability of the SVT and BSMD detectors to correctly handle L2 aborts. Fixing the L2 abort handling of the SVT would have required access to the detector itself, i.e. opening the magnet, removing BBC and FTPCs to be able to pull out the SVT cone. Obviously such an operation is not possible during the run. In the shutdown period between the FY04 and FY05 run a new software got installed in both detectors, resulting in working L2 aborts in FY05.

However for the FY04 run L2 could not be used, requiring a redesign of the Upsilon algorithm. The main challenge in this redesign was the limited TPC readout rate allocated to the Upsilon trigger chain. Without the additional rejection power of L2 the full rejection from the ~ 10 kHz collision rate had to be achieved with L0 alone. Reaching the original goal of 1-2 Hz Upsilon triggered TPC readout (i.e. a selectivity of 1 out of 10^4 events) was impossible without significantly increasing

[2]See section 5.3 for a more quantitative analysis.

the L0 high tower threshold, thus reducing the efficiency by a large amount (see section 4.3). To prevent this efficiency loss a much high fraction of the TPC readout rate and lifetime were allocated to the high tower triggers, up to 20-25 Hz at high luminosities. A side effect of this decision was that the same L0 threshold could be used for the high-p_T trigger, enhancing the statistics available for π^0 and jet analysis. However even with now $\sim$ 50% of the STAR event rate dedicated to the BEMC triggers another modification was necessary to get the required rejection rate. The most efficient way to gain rejection power was the introduction of a vertex cut based on the ZDC information like in the minimum bias trigger of STAR.

What also "helped" in getting the required rejection rate was the miscalibrated BEMC already discussed in section 5.1.2. As shown in figure 5.5 the calibration was in $E_T \sin(\Theta)$ instead of E_T, resulting in a larger effective threshold at high η. The trigger ADC cut value of 13 used in this figure is the one used during the FY04 run (BEMC Threshold 1), demonstrating the effect on the FY04 data. The E_T cut threshold varies from 3.5 GeV at $\eta = 0$ to 5.4 GeV at $\eta = 1$.

The L0 trigger definition (bemc-ht13) is summarized in table 5.2 together with the minimum bias trigger definition (mb-zdc-narrow). Several additional thresholds not discussed so far were set on the trigger detector data which will be briefly described in this paragraph. A set BY bit was required, indicating the passing of filled bunches in RHIC through each other in the STAR interaction region. Already mentioned were the ZDC based vertex cut implemented as three conditions on the L0 trigger level. Both ZDC must have registered a signal in the period set by the ZDC TAC coincidence (with 1 TAC count roughly 0.8 ns, i.e. a timing window of 160 ns). In addition the time difference between both signals must be in a 16 TAC count windows, resulting in a vertex z cut of ± 30 cm. The threshold values are determined by the formula 256 + TAC(west) - TAC(east) due to the implementation in the L0 DSM code where one tries to avoid signed values. The last L0 condition is a cut on the minimal multiplicity detected in the CTB counters in ADC values to reduce the number of triggered ultraperipheral events. It results in some inefficiency for very peripheral events but as will be discussed in section 5.3 the effect on the Upsilon trigger is small.

L0 bit	mb-zdc-nt	mb-zdc-narrow	bemc-ht13
CTB-Bit 1	75	75	75
ZDC TAC Difference	-	(248,274)	(248,274)
ZDC Coincidence	set	set	set
ZDC TAC Coincidence	(30,240)	(30,240)	(30,240)
BY	set	set	set
BEMC Threshold 1	-	-	13

Table 5.2: Definition of min bias and BEMC L0 triggers for the FY04 AuAu run. The threshold setting is listed in the parenthesis, two number specify a range. All triggers required CTB larger then CTB-Bit 1.

The L3 trigger was used in its event tagging mode, i.e. selecting events for a special handling by DAQ and offline as already explained in section 3.2.4. The increased trigger rate after L2, which was more than a factor 10 higher then planned, made the possibility to tag events for the "express stream" in DAQ even more important. Otherwise a timely production of the data would have been impossible.

The L3 algorithm worked as expected as soon as the BEMC was commissioned. Also the express streams in DAQ worked quite well, with the exception of the

RTS Parameter	Description	Value
I1	L0 HT threshold	13
I2	L2 seed tower threshold	150
I3	Use CTB matching	0
I4	Use ZDC vertex z position	0
I5	Number of towers per cluster	0
-	Use L3 tracking information	(1,0)
-	Minimal hits on L3 tracks	15
F1	Energy threshold L0 seed tower	4.5
F2	Energy threshold L2 seed tower	3.0
F3	Minimal invariant mass	7.2
-	Maximal invariant mass	25.0
F4	Minimal track p_T	2.0
-	Maximal track p_T	20.0
F5	Maximal opening angle ($\cos(\Theta)$)	0.5

Table 5.3: Upsilon Level 3 algorithm parameter settings during the FY04 AuAu run. Parameters without RTS Parameter were hardcoded in the algorithm. L3 tracking information was used until day 55 and switched off afterwards.

failure handling if L3 was not included in the run. In the original implementation every event with a L0/L2 base trigger, for which a L3 algorithm was configured, got written to the special stream, also when L3 was not running. This became obvious only weeks after data taking started when L3 had some network problems and could not be used for two days. The problem was fixed as soon as it was realized and no events get written to the express stream if L3 is not in the run. However for the later data analysis one has to keep in mind that a significant fraction of the express stream data is not correctly tagged.

The L3 algorithm parameter settings determined in section 4.3 had to be modified due to the modified L0 algorithm. The used parameters are listed in table 5.3. In the beginning also the tracking information of L3 was used to reject invariant mass pairs from photon-photon conversions as originally planned. However the high luminosities provided by RHIC caused sizeable space charge effects as discussed in section 4.1.1. The quality of the L3 tracking which does not include any corrections for space charge was therefore questionable, especially in the high transverse momentum region of interest for the Upsilon identification. The tracking part of L3 was therefore switched off shortly after data taking started to prevent any tracking problems. The rejection rates of the remaining part where large enough to permit this, the rate into the express streams was typically less than 0.1 Hz. This reduction by approximately a factor 100 was on the order of what was expected for the L2 algorithm from earlier simulations; as expected since the L3 algorithm is functionally identical to the L2 algorithms when the tracking information is not used.

A problem with the chosen parameters became obvious only after the run. By mistake the "Number of towers per cluster" parameter (I5) was set to 0, which is a debug setting to skip the cluster calculation. Only the energy of single BEMC towers and not the one of the intended 3-tower-clusters was used to calculate the invariant mass. This resulted in some underestimation of the electron energy and in turn lower invariant masses where calculated. The event tagging efficiency was strongly decreased by this as will be shown later. During data taking the wrong setting was not recognized due to the dominating problems with data from corrupted crates.

5.2.1 Sampled Luminosity

The determination of the Υ production cross section also requires the fraction of events select by the Υ trigger algorithm, i.e. out of how many minimum bias events were the 67,765 Upsilon trigger events selected?

This information is recorded by the trigger and DAQ scaler system described in section 3.2.3. The DAQ scaler records for every trigger the number of events N_{seen} which fullfill the L0 trigger detectors conditions (i.e. without the detector live requirement) and the number of events N_{rec} finally written to tape by DAQ. This information is saved for 2 minute intervals during the run in the database and additionally at the run stop.

Since the Upsilon trigger is based on the same conditions as the mb-zdc-narrow trigger (see table 5.2), with the exception of the BEMC high tower requirement, the scaler information for this trigger allows to calculate the number of minimum bias collisions scanned by the Υ trigger. A complication using the DAQ scaler information is that they count every fullfilled L0 trigger condition at each bunch crossing, independent of the detector status. What is needed to calculate the sampled luminosity is the number of events N_{live} where the slow detectors were alive, i.e. ready to record a new event. This number is however not saved in the DAQ scaler board.

However it can be calculated from the events recorded by DAQ, N_{rec}, using the prescale information for each run. The prescale factor PS determines what fraction of each trigger is recorded[3]. It is calculated at the beginning of each run based on the desired event rate to tape, the ZDC coincidence rate and the typical trigger frequency. The number of events seen with the slow detectors alive can then be calculated as

$$N_{\text{live}} = \text{PS} \cdot N_{\text{rec}} \tag{5.5}$$

and the lifetime t_L as

$$t_L = \frac{\text{PS} \cdot N_{\text{rec}}}{N_{\text{L0}}}. \tag{5.6}$$

As mentioned the bandwidth and lifetime allocated to the Upsilon trigger and the baseline L0 High Tower trigger got increased to offset the non-working L2 trigger level. To balance this with the need of minimum bias and central data taking three different trigger setups were used: productionHigh, productionMid and productionLow. Which one of these setups got used was determined by the luminosity provided by RHIC to STAR, at high luminosities productionHigh was run and then switched to the other trigger setups with decreasing luminosity. The main difference between these trigger setups were the detector lifetimes, as can be seen in figure 5.7. While productionHigh had a lifetime of ≈ 50 %, productionMid and productionLow had much smaller lifetimes of $\approx 30-35\%$. This was achieved by a stronger prescale of the minimum bias and central triggers in the productionHigh setup. The Upsilon trigger could thus benefit from the high luminosities at the beginning of the store while still sufficient minimum bias and central data could be accumulated. However the average lifetime was much smaller then planned before the run where $\approx 70\%$ detector live during the high luminosity phase and $\approx 50\%$ detector live during the medium and low luminosity phase were planned. This decrease in lifetime and thus number of sampled events by nearly a factor 1/2 was caused by the high L0 High Tower trigger rate, which was the direct result of the non-working L2 aborts.

[3]STAR allows prescales at each trigger level but only the L0 prescales were used.

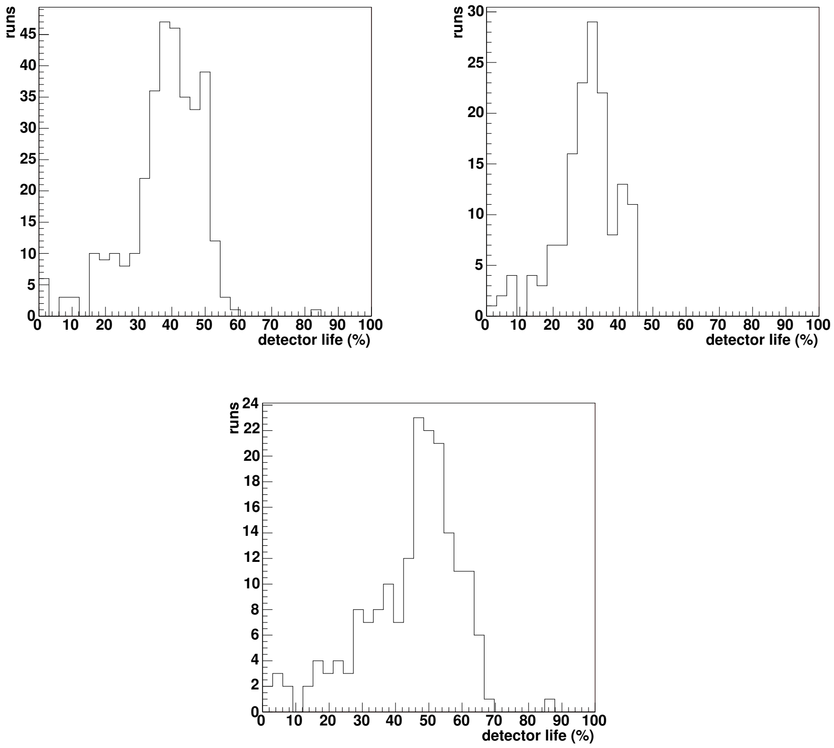

Figure 5.7: Percentage of detector life for the different trigger setups: productionLow (upper left), productionMid (upper right) and productionHigh (lower plot).

The number of minimum bias events N_{live} sampled by the Upsilon trigger per day, averaged over the different trigger setups, is shown in figure 5.8. Typically between $4 \cdot 10^6$ to $2 \cdot 10^7$ events were sampled[4]. There are however several days where significantly less events were sampled, most of them are due to the maintenance period every two weeks and maching development periods where no collisions were provided. The huge gap from day 57 to 63 is due to data taking with the magnet at half field, necessary to increase the low p_T acceptance for e.g. a D^* measurement. Since the gains of the PMT boxes might depend on the magnetic field, using the EMC for triggering would have required a recalibration (or at least a test that the old calibration is still valid) which was not possible in a week. Thus no BEMC based triggers where run. As a side effect this decision allowed to decrease the live time of the detector system, thus increasing the number of minimum bias events taken per time period.

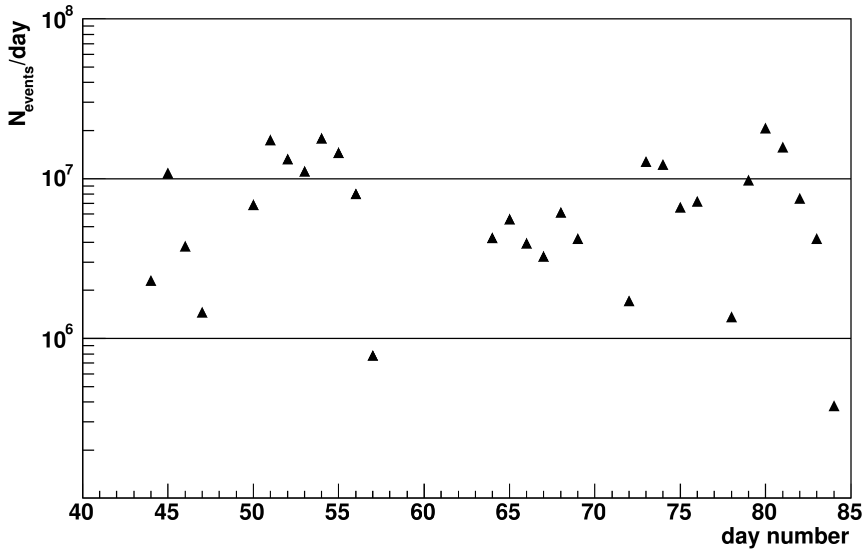

Figure 5.8: Number of min bias events N_{live} sampled by the Upsilon trigger versus day number.

As a cross check of the scaler information accuracy, also the number of recorded Upsilon events was determined from the scaler data. The number of events found in the offline analysis was 99.5 %, the missing 0.5% mainly caused by the one file which could not be restored from HPSS mentioned earlier. The scaler information seems thus to accurate on the percent level.

The periods without running Upsilon trigger are much clearer in figure 5.9 which shows the cumulative number of events scanned with the Upsilon trigger. What becomes clearly visible is the changing slope as the run progresses. The typical number of events scanned per day get slightly reduced. This is mainly due to an increase of the recorded minimum bias and central collision rate to achieve the STAR event goal for these trigger classes. In addition the ultra peripheral collision (UPC) triggers where switched on, decreasing the life time even further.

[4]For comparison, the total number of minimum bias events recorded by STAR during the complete run (i.e. ~ 80 days, twice the time the Upsilon trigger was running) was 50 million. The Upsilon trigger allowed to scan the same amount of data in five to six typical days

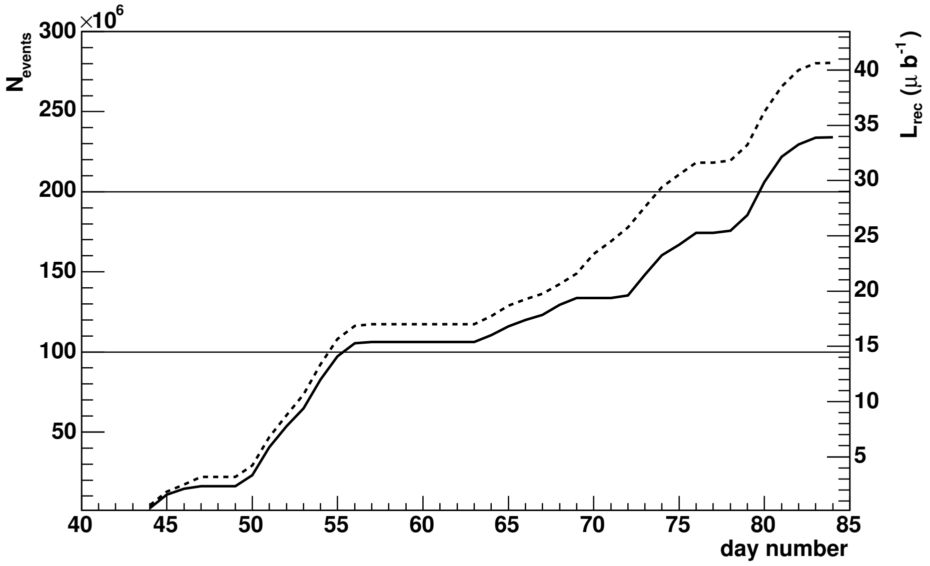

Figure 5.9: Integral of min bias events N_{live} (left scale) and luminosity (right scale) sampled by the Upsilon trigger versus day number (dashed curve before offline QA, solid curve after offline QA).

In total $237 \cdot 10^6$ events were scanned during the Au+Au run as shown by the solid curve. The dashed curve shows the number of events before the first offline QA described above, which removed nearly $50 \cdot 10^6$ events which were flagged useable by the shift crew. For the calculation of the number of expected Υs in section 5.3.3 also the number of events scanned in each of the BEMC acceptance periods defined in table 5.1 is needed, which are given in table 5.4.

Using equation 3.4 one can calculate the scanned luminosity from the number of scanned events using the hadronic cross section $\sigma_{AuAu} = 6.9$ barn:

$$\mathcal{L} = \frac{N_{\mathrm{live}}}{\sigma_{AuAu}} \tag{5.7}$$

resulting in a total scanned luminosity of 34.3 μb^{-1} as shown by the right scale in figure 5.9. The scanned luminosities for each of the BEMC acceptance periods are listed in table 5.4.

Period	N_{live}		$\mathcal{L}_{\mathrm{sampled}}$
I	63M	(62,932,152)	9.1 μb^{-1}
II	46M	(45,496,556)	6.6 μb^{-1}
III	12M	(12,387,820)	1.8 μb^{-1}
IV	8M	(8,381,806)	1.2 μb^{-1}
V	47M	(47,383,100)	6.9 μb^{-1}
VI	60M	(59,753,088)	8.7 μb^{-1}
total	237M	(236,334,528)	34.3 μb^{-1}

Table 5.4: Events and luminosity scanned in each BEMC coverage period, see table 5.1.1 for period definition.

5.2.2 Rejection Rates

Also the rejection rates of the Upsilon algorithm can be calculated using the scaler information. When introducing the Upsilon trigger in section 4.3, the rejection factor $\mathcal{R}$ got defined as the inverse of the trigger efficiency ϵ_{bkgd} for background events. Under the assumption that the number of signal events is very small compared to the number of minimum bias events, as it is the case for the Upsilon, the background trigger efficiency is simply the number of events triggered over the number of minimum bias events sampled.

The top plot of figure 5.10 shows the background trigger efficiency for the L0+L3 Upsilon trigger. There is some fluctuation visible in the beginning which will be discussed later. However the average background trigger efficiency is $\sim 10^{-4}$, i.e. $\mathcal{R} = 10^4$. This meets the rate goals defined earlier, it reduces the 10 kHz input rate to ~ 1 Hz, the bandwidth allocated to the Upsilon trigger.

The reason for the variation at the beginning is easier to understand by splitting the background efficiency into the ones achieved on the different trigger levels. The middle plot shows the one achieved by L0. It stays quite constant around 10^{-2}, i.e.. selects one event out of a hundred.

The lower plot of figure 5.10 shows the trigger efficiency achieved by L3 compared to its input rate. Here the variations in the trigger efficiency are much larger, changing by an order of magnitude. Several periods can be distinguished: At the beginning of data taking a drop of the background trigger efficiency from 10^{-2} to 10^{-3} until half field data taking starts at day 56. This drop is the result of the efforts to reduce the BEMC crate data corruption. By improving the trigger clock distribution to the BEMC the fraction of corrupted events dropped from several percent to less then a permille. Since the trigger efficiency of the Upsilon algorithm for corrupted events is quite high, its rate scales with the fraction of corrupted events.

As explained no BEMC data was taken during the half field running until day 64. After data taking resumed the background trigger efficiency rises back to 10^{-2}, where it stays constant until the end of the run. The two days with very high background trigger efficiencies are caused by the already mentioned problem in the interplay between L3 and DAQ. All events with L3 out of the run where wrongly written to the express stream and counted as Upsilon events. The rise after half field data taking resumed is caused by the decision to switch off the use of the L3 tracking information in the algorithm due to worries about the effect of the non-implemented space-charge correction.

In summary high rejection rates of 10^4 for the L0+L2 Upsilon trigger equivalent and 10^5 for the full L0+L2+L3 Upsilon trigger have been achieved, meeting the rate goals outlined earlier.

Anticipating some of the results of the offline analysis described in the next section, even higher rejection factors seem possible. As will be shown the use of better BEMC tower status tables, created with the methods described in section 5.1.1 will result in an additional rejection factor 10 for the L0+L2 Upsilon trigger. Meeting the goal of 10^4 even with the full BEMC and higher luminosities will thus be certainly possible. A reliable charged particle identification method would further suppress the rates by a factor 100, i.e. a factor 10 more than the one realized with L3 during FY04.

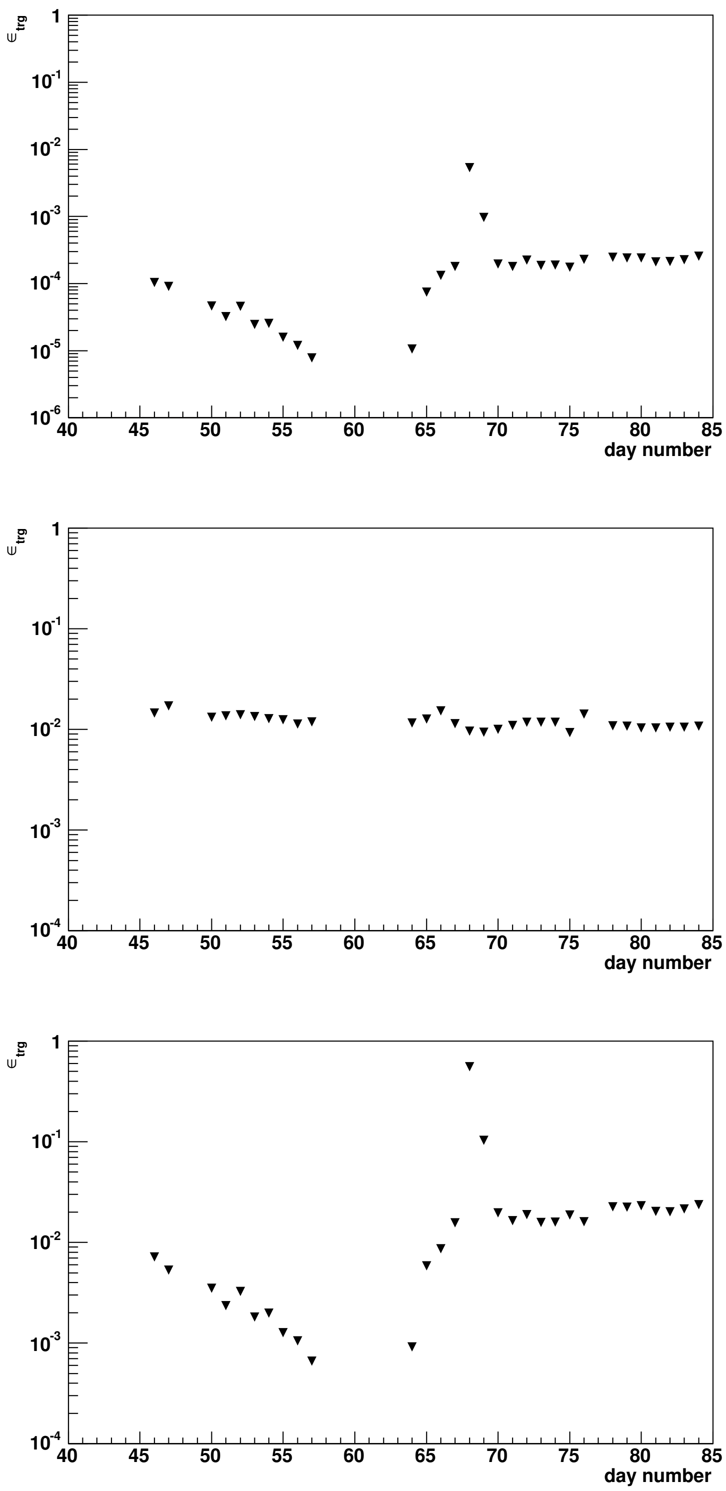

Figure 5.10: Trigger efficiency ϵ_{bkgd} for the combined L0+L3 upsilon trigger (upper plot), the L0 base trigger (middle plot) and the L3 trigger relative to the L0 base trigger (lower plot) versus day number. Note the change of scale between the upper plot and the two lower ones.

5.3 Analysis of the Express Stream Dataset

The various concurrently running L3 algorithms selected a total of 384.225 events for storage in the express streams and produced in offline afterwards[5]. Already included in this event count is a first round of quality assurance results. The first QA happens during data taking by the shift crew, using the plots of the online QA system. Both shiftleader and run time system operator have the possibility to mark a run as bad or questionable if they discover discrepancies. While these runs are still written to tape, they get never produced with the offline software. A second QA pass is made after the end of data taking by the offline reconstruction team which checks if all the information necessary for reconstructing the data is available. Such information includes e.g. magnetic field information which is recorded in the environment database based on data feed from RHIC systems (CDEV) or the TPC drift velocity in this store as measured by laser runs. If for some reasons not all information is available these runs are marked bad.

From the produced events 382,153 were analyzed, one reconstructed file was not restored from HPSS to disk and thus not available for the analysis. The decision in section 5.1.1 to restrict the analysis to six BEMC acceptance periods, dropping the short periods in-between, reduced the number of analyzable events further to 372,872.

From these events 261,369 have a trigger ID indicating that they were selected by the Upsilon trigger described in section 5.2. But only 67,765 have a valid L3 Upsilon algorithm information stored in the trigger data. This large discrepancy was caused by the the handling of events without a running L3 system in the DAQ/EVB system. Without L3 included in the run the EVB code assumed an L3 accept for every configured L3 algorithm. Thus all events that should have been analyzed by L3 were written in the express stream. During one weekend a failing BEMC crate caused problems in the L3 handling of the BEMC data and thus L3 was excluded from most of the runs as mentioned earlier. Both the L3 and the EVB code got fixed during that weekend and no further events of this type were observed. If should be obvious that one has to drop these events from the analysis.

The BEMC data corruption check described in section 5.1.3 was not available during the run. A sizeable fraction of the tagged events in the express stream thus include corrupted events. As shown earlier the whole event has to be discarded if one corrupted crate is present, reducing the number of useable events by 11% to 60,102. This rather large fraction compared to the $\leq 1\%$ in minimum bias data determined in section 5.1.3 is a side effect of the trigger algorithms. Events with corrupted crate data have a lot of towers with high energy, enhancing largly the probabilty of finding a cluster pair with high invariant mass and accepting the event.

As already mentioned in the introduction to this chapter and discussed in more detail in section 5.2 the non-working L2 aborts required the inclusion of an online ZDC based vertex cut in the trigger definition with an nominal cut position of $\mid z_{vtx} \mid \leq 30cm$. For the data analysis we require a found vertex in this range, reducing the number of events to 54,109 (90%). The bias caused by the ZDC resolution was determined to be negligible if one requires a found vertex [Dun04]. A summary of the event cuts described here and some more described later can be found in table 5.3.1.

[5] All the results presented here are based on the P05ib production of the express stream data, the latest available at the time of writing this thesis.

5.3.1 Offline Invariant Mass Analysis

The invariant mass technique to extract the Υ signal out of the recorded events was already described in section 4.2. The main remaining decision is the choice of particles which get combined in the invariant mass calculation.

The usage of the Upsilon trigger chain puts already quite some constrains on the particle selection. As discussed earlier in the trigger description in section 4.3, a proper event normalization requires that each trigger level is a subset of the previous one. Only combinations which would have passed the previous level are allowed to be used. The same principle also applies to the offline analysis described here. It can only use particle pairs which are selected by the Upsilon trigger.

Unfortunately not all of the necessary information from the trigger system is available at the time of offline data processing. The L2/L3 algorithms for example stop processing the event as soon as a cluster pair is accepted, even if there are more cluster combinations left which might also trigger the event. However in the offline analysis all valid cluster pairs in an event should be used since it is unclear which, if any, of the pairs accepted by the trigger comes from an Υ decay.

Furthermore the best invariant mass resolution can be achieved by using TPC primary tracks as discussed earlier. It is thus necessary to select only TPC tracks from particles which might have also created the BEMC clusters used in the trigger decision.

To fullfill the various requirements the following particle selection strategy has been chosen: As a first step the clustering part of the L2/L3 algorithm is repeated. Then "good" TPC tracks are selected, not yet with any electron identification. The clusters and tracks are "matched", i.e. it is checked if the cluster position and the extrapolated track position are close to each other. If this is the case it is assumed that the same particle created the TPC track and deposited the energy in the BEMC. Then all clusters with tracks attached to it in one event get combined to pairs. If the cluster pair passes the cuts of the L2/L3 Upsilon algorithm, the pair is marked as input for the invariant mass analysis. Figure 5.11 shows a schematic sketch of the strategy just described.

Calculate BEMC clusters
and BEMC trigger clusters
↓
Select TPC tracks
↓
Match clusters and tracks
↓
Find triggered cluster pairs
↓
Electron ID cuts
↓
Further cuts on invariant mass pairs
↓
Invariant mass spectra

Figure 5.11: Steps of the offline invariant mass analysis.

As mentioned the first analysis step is to repeat the online clustering. Figure 5.12 shows the energy spectrum of all calculated clusters. One should note that due to the choice of only one tower per cluster this spectrum is also the single tower spectrum. As obvious from its form and the comparison to figures 5.1 and 5.6 the spectrum is after removing corrupted crates and towers with bad status. Also the newer offline electron calibration has been used to convert ADC to energy. The fall-off below $1 - 1.5$ GeV is caused by the L2 seed threshold, no clusters with ADC values below the threshold get calculated. The number of clusters above the L2 seed threshold is shown in figure 5.13. On average 26 clusters per event out of the ~ 2400 possible get calculated in accepted events.

The energy cuts above which a cluster is called a L2 or L0 clusters are shown by the dotted and dashed lines in figure 5.12. A significant enhancement of clusters above the threshold compared to a minimum bias spectrum is observed (the "bumps" in the distribution). By construction every triggered event should contain at least one L0 and at least one additional L2 cluster[6]. The decision if a cluster is above the L0 (L2) energy threshold is made using the BEMC energy calibration used during data taking to be consistent with the L2 trigger decision.

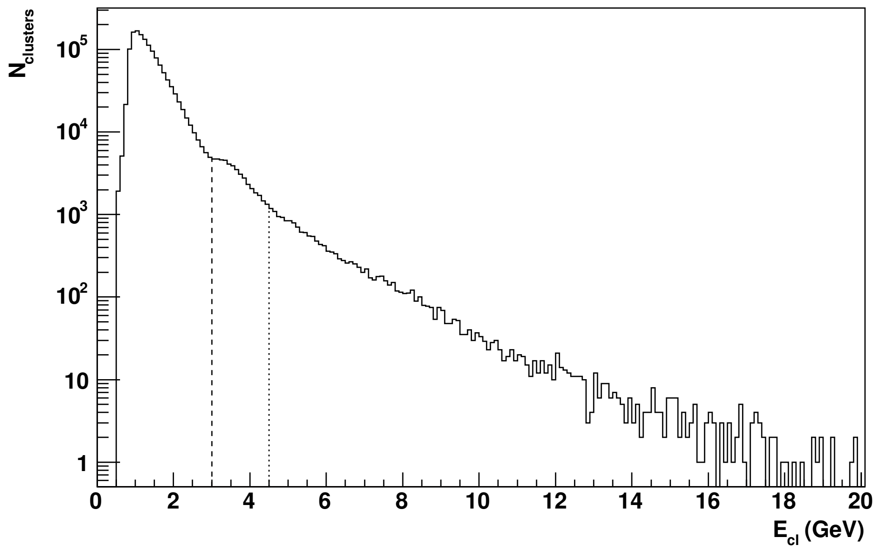

Figure 5.12: Cluster energy calculated for L2 seed towers. The online energy cuts for L0 and L2 clusters are shown by the dotted and dashed lines.

After finding the online BEMC clusters, the next step of the analysis strategy outlined above is the selection of "good" TPC primary tracks, i.e. tracks which are reasonably well reconstructed. The choice of these cuts follows the one used commonly in STAR analysis of high transverse momentum tracks. The first obvious quality cut is to use only tracks which the tracking software processed successfully, e.g. where all momentum fits terminated. This information is encoded in the status field of the tracks. To assure a good momentum resolution at least 22 TPC hits must have been used in the momentum fit. This cut also removes split tracks,

[6] However not every event in the data has at least one L0 and one additional L2 cluster. This originates from the tower status tables and corrupted event filtering already applied in the offline analysis and not during the online trigger decision, see also the discussion further below in this section

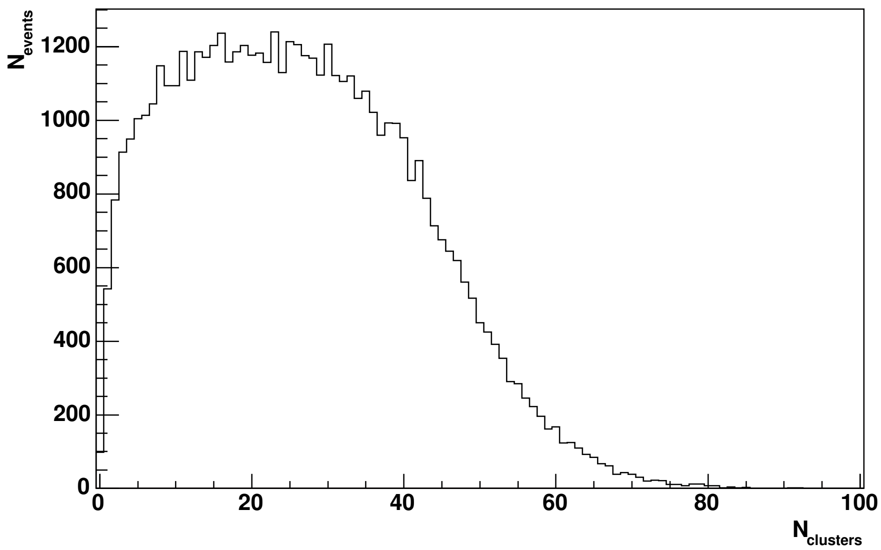

Figure 5.13: Number of cluster per event.

i.e. cases where the pattern recognition algorithm assigns the TPC hits created by one particle to two different tracks and thus reconstructs two instead of one tracks. Furthermore all tracks are required to pass the primary event vertex within a distance of 3 cm (distance of closest approach, DCA). This cut make obviously only sense in the case of global tracks where the primary vertex has not been used in the momentum fit and is thus applied to the global track partner of the primary track under consideration. In fact the decision when to create a primary track from a global track in STAR is based on that criterion, at least in the tracking implementation used for this analysis. Table 5.5 lists the fraction of tracks which pass the cuts just described.

Cut	
TPC tracks with tracking status flag OK	$\equiv$ 100 %
More than 22 TPC hits used in momentum fit	59 %
Extrapolated distance of global track to primary vertex less than 3 cm	59 %
Momentum larger than 2 GeV/c	16 %
Pseudorapidity less than 1.5	16 %

Table 5.5: Track cuts and percentage of tracks passing them.

Some more cuts are applied to reduce the number of tracks and thus the combinatoric in both the track-cluster matching and the invariant mass analysis. Only tracks with a momentum of more than 2 GeV/c and within a pseudorapidity of $\pm$1.5 units are used. For the interpretation of table 5.5 one has to keep in mind that most of the cuts discussed are strongly correlated, e.g. the pseudorapidity cut and the number of TPC hit cut are strongly correlated due to the TPC geometry. The number of tracks per event after all track quality cuts is shown in figure 5.14. An event has on average 18 accepted tracks.

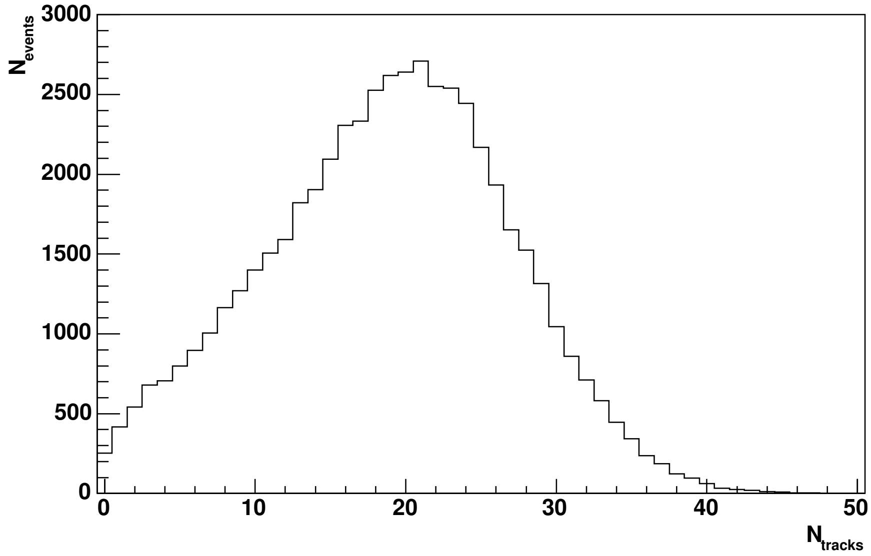

Figure 5.14: Number of tracks per event after track cuts.

The subsequent matching between tracks and clusters is done by calculating for each tower the distance between the extrapolated track position at the BEMC and the cluster position. As in section 4.1.2 the matching is done in the pseudorapidity-azimuthal angle space due to the projective geometry of the BEMC

$$d = \sqrt{(\eta_{\mathrm{cluster}} - \eta_{\mathrm{track}})^2 + (\phi_{\mathrm{cluster}} - \phi_{\mathrm{track}})}$$

The distribution of d is shown in figure 5.15. A clear correlation between the selected high energy tracks and clusters is observed. The observed correlation structure has to be compared to the BEMC towers size of 0.05 in both pseudorapidity and azimuthal angle. All track-cluster pairs with $d \leq 0.06$ are assumed to come from the same particle and the track is matched to the cluster.

The assumption that the cluster and the track originate from the same particle if the distance is below 0.06 is however questionable, there might be random combinations and also combinations from correlated particle production, e.g. jets. A further complication for the data analysis is that there might be multiple matches of tracks to clusters. Indeed this is the case as shown in figure 5.16. The probability for this to happen is not negligible on the level of a few percent. This has to be taken into account in the further analysis strategy. One possibility would be to select the "best" electron track based on e.g. the electron identification methods discussed in section 4.1.2. For this thesis a different strategy has been chosen: if after further electron identification cuts multiple matches to a trigger cluster remain, all matched tracks are used as input into the invariant mass calculation. A side effect of this method is that the same trigger-cluster pair might enter multiple times in the invariant mass distribution. However as will be shown later the electron identification cuts significantly reduce the number of tracks and multiple matches to an accepted trigger-cluster do not happen in the current data set.

Another feature visible in figure 5.16 is the very large fraction ($\sim 90\%$) of clusters without a matched track. This confirms the claim made earlier during the descrip-

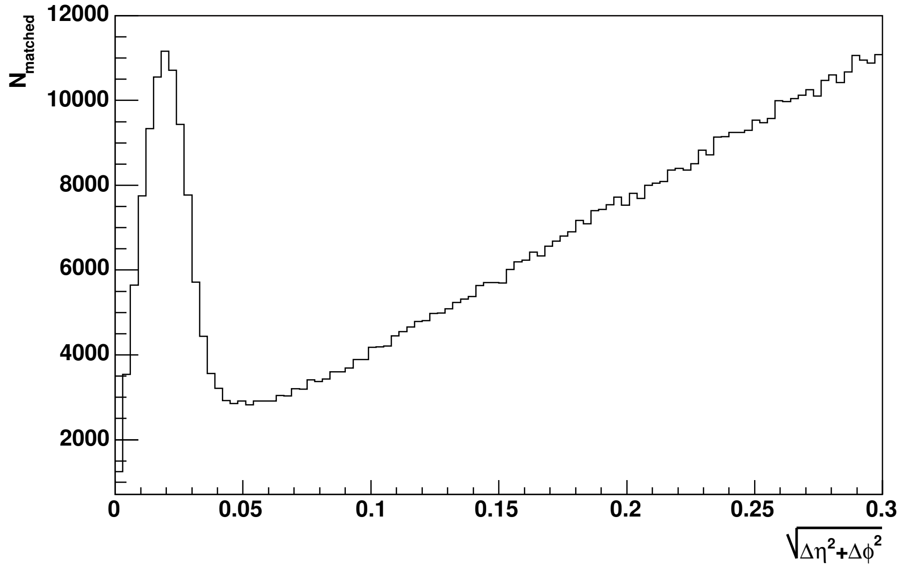

Figure 5.15: Distance between extrapolated track position at the BEMC and clusters in the event.

tion of the L3 algorithm in section 4.3.3 that most of the clusters come from neutral particles, mostly from π^0 and photons from hadronic resonance decays. The further background rejection power of a reliable charged track identification should be obvious.

The remaining step in the analysis strategy is the determination which cluster combinations in an event pass the L2 cuts. The energy cuts to determine the L0 and L2 clusters have been discussed earlier. What remains are the opening angle and invariant mass cuts. Figure 5.17 show the opening angle between L0 and L2 trigger clusters. The huge peak at 1 is the result of same cluster combinations[7]. The online cut value at 0.5 is shown by the dashed line. As expected the probability to find cluster pairs with opening angles below the threshold is increased, peaking at $\cos(\Theta) \approx -0.4$. However also some pairs above the threshold are visible. As explained earlier the tracks matched to these cluster pairs can not be used for the further analysis since otherwise the selected tracks would be not a subset of the ones selected by the trigger.

The same can also be observed in the (trigger-cluster pairs) invariant mass distribution shown in figure 5.18. While the threshold at 7.2 GeV/c^2 is clearly visible, there are some pairs below the threshold which can not be used for further analysis without violating the subset requirement.

By construction every event tagged by the Upsilon algorithm must have a valid trigger pair. However the invariant mass distribution in figure 5.18 has far fewer entries above 7.2 GeV/c^2 than the minimum of 54,109 one would expect. This discrepency is caused by the use of different tower status tables in the offline and online analysis.

[7]Every L0 cluster is by construction also a L2 cluster.

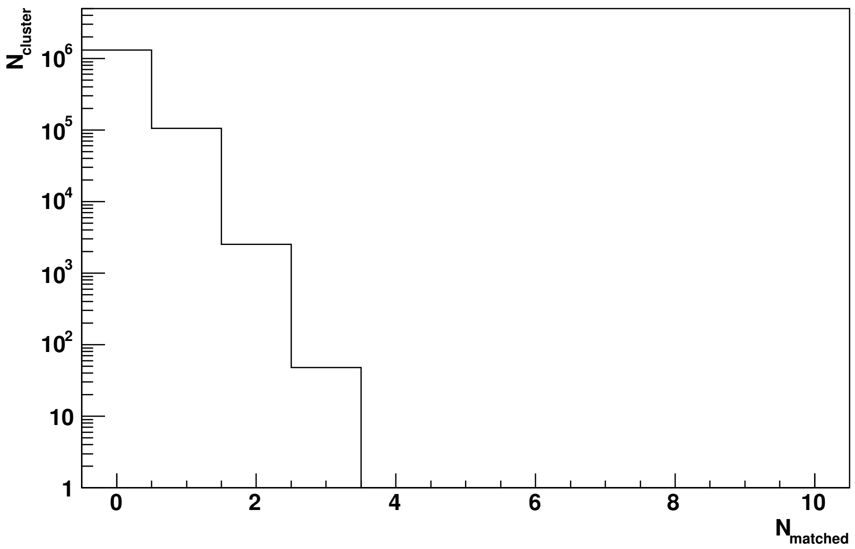

Figure 5.16: Clusters with N_{matched} matched tracks per cluster.

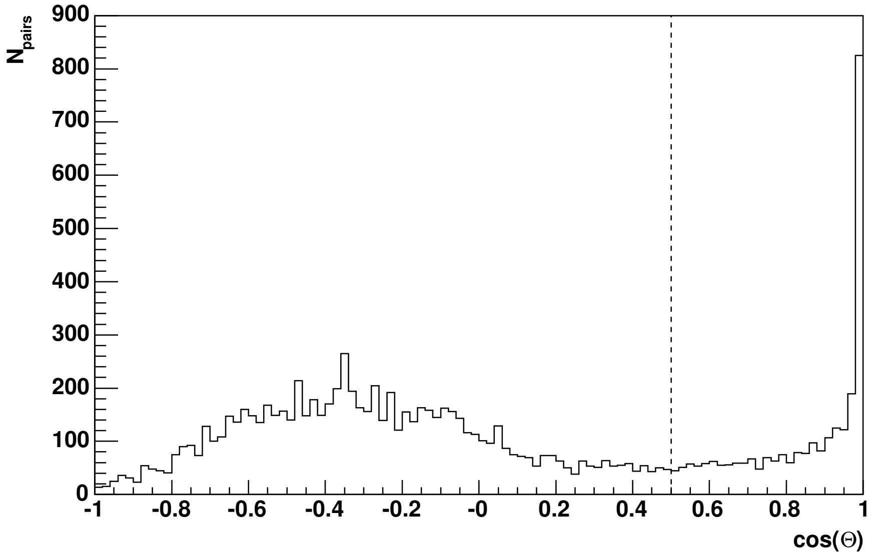

Figure 5.17: $\cos(\Theta)$ of offline reconstructed trigger pairs, the online cut at 0.5 is shown by the dashed line.

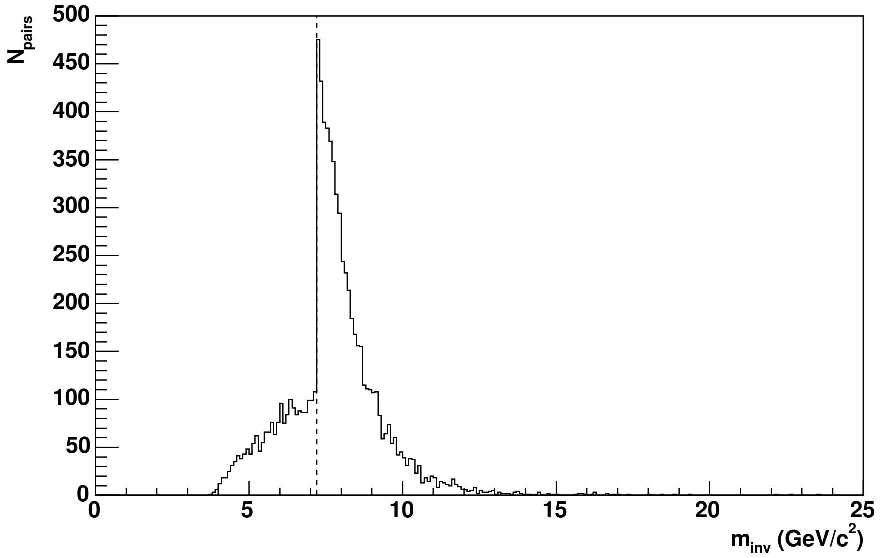

Figure 5.18: Invariant mass distribution of offline reconstructed trigger pairs, the online cut at 7.2 GeV/c^2 is shown by the dashed line.

The creation of the offline tower status table was described earlier in section 5.1.1, resulting in the six acceptance periods defined in table 5.1. Unfortunately the tower status information was not available during the run and thus also not properly working towers were used in the trigger decision, leading to fake triggers. Hot towers (i.e. towers with a non-normal frequency of high ADC values) turned out to cause many fake triggers. It is worthwhile to point out that the online tables were a subset of the offline tables used for this analysis. This guarantees that the subset requirement for the trigger pairs is fullfilled. For the final analysis only trigger decisions caused by towers with a good status can be used, reducing the number of events with a valid trigger cluster pair to 5,499. Table 5.3.1 summarizes the event numbers available for analysis after all cuts.

One should note that this number does not include any requirements on the trigger clusters themself above the ones used in the trigger itself. Most notably no matched tracks are required, making it directly comparable to the output of the combined L0+L2 trigger. $5,499 \times 1/\epsilon_{\text{vtx}} = 6,110$ is then the number of events a perfectly working trigger would have selected. A further factor 10 of rejection power on top of the ones achieved during the FY04 run seems possible, allowing to open up some of the trigger cuts. However the usage of 3-tower clusters instead of the 1-tower clusters will slightly enhance the background trigger efficiency.

So far none of the electron identification cuts discussed in section 4.1 have been used explicitly. Two complementary electron identification methods had been developed: one using the energy loss in the TPC, the second using a correlation between the momentum measurement in the TPC and the energy deposit in the BEMC.

Focusing on the energy loss in the TPC first, figure 5.19 shows the dE/dx distribution measured in minimum bias collisions in the FY04 run as function of the particle momentum. Also shown is the expected mean position of the electron band as calculated in 4.4. Especially at low momenta around 0.3 GeV/c the electron

	N_{Events}
Events in Express Stream	384,225
Events found on disk	382,153
BEMC acceptance periods	372,872
L3 Upsilon trigger ID	261,369
Valid L3 trigger	67,765
BEMC corruption check	60,102
Found event vertex	54,109
Only "good" BEMC towers used in trigger decision	5,499

Table 5.6: Number of useable events in the express stream after each event cut.

band is clearly visible, while in the relativistic rise region it merges with the other hadrons bands.

This becomes even more obvious in the lower plots of figure 5.19 which show the dE/dx distribution and the $\sigma(e)$ distribution for particles with 2 GeV/c momentum. The expected mean position of the electrons is shown by the dashed lines. The distribution is clearly dominated by hadrons as expected from the e/h ratio of order 10^{-3} at this momentum. The position of the hadron peak at $\sim -4\sigma(e)$ matches the expectations shown earlier in figure 4.5. The peak at large $\sigma(e)$ values originates from deuterons which are in the $1/\beta^2$ region at this momentum and have thus higher mean values then electrons.

The fraction of particles above a minimum $\sigma(e)$ cut $min(\sigma(e))$ is shown in figure 5.20. The pion and electron identification efficiencies as function of an $\sigma(e)$ cut were previously calculated in section 4.1.1 and tabulated in table 4.1. Assuming a dominance by hadrons a good agreement between the prediction and the measured distribution is observed.

The determination of the actual cut value must be based on a compromise between good hadron rejection (i.e. low hadron efficiency) and high electron efficiency. One has to keep in mind that the electron efficiency enters quadratically in the total efficiency due to the use of 2 tracks in the invariant mass analysis. Judging from table 4.1 the best compromise seems to be a $min(\sigma(e)) = -1$ cut. This gives a still quite high electron efficiency of $\sim$ 84% while the hadron efficiency is on the level of a few percent. To remove also deuterons and other reconstruction artefacts, also an upper cut on $\sigma(e)$ will be used, which is however not critical given the measured dE/dx distribution with few entries with higher dE/dx values. The final cuts choosen for further analysis are $-1 \leq \sigma(e) \leq 3$.

The electron identification capabilities provided by the BEMC have already been used in the trigger algorithms. Requiring a 1 tower-cluster of at least 3 GeV and a large invariant mass selects primarily particles which deposit large amounts of energy in the BEMC, i.e. electrons. At the same time most of the hadrons get removed. The additional requirement of a TPC track with at least 2 GeV/c pointing to it sets an E_{cluster}/p cut of 1.5, which following section 4.1.2 will unfortunately also remove most of the lower p_T electrons. Some electron selection is only possible if the E_{cluster}/p ratio drops below 1, i.e. for 3 GeV/c electrons, and good electron selection efficiencies are only reached if the ratio drops below 0.7, i.e. 4.3 GeV/c electrons. This will result in a hit of the L2 trigger efficiency which will be discussed in the next section.

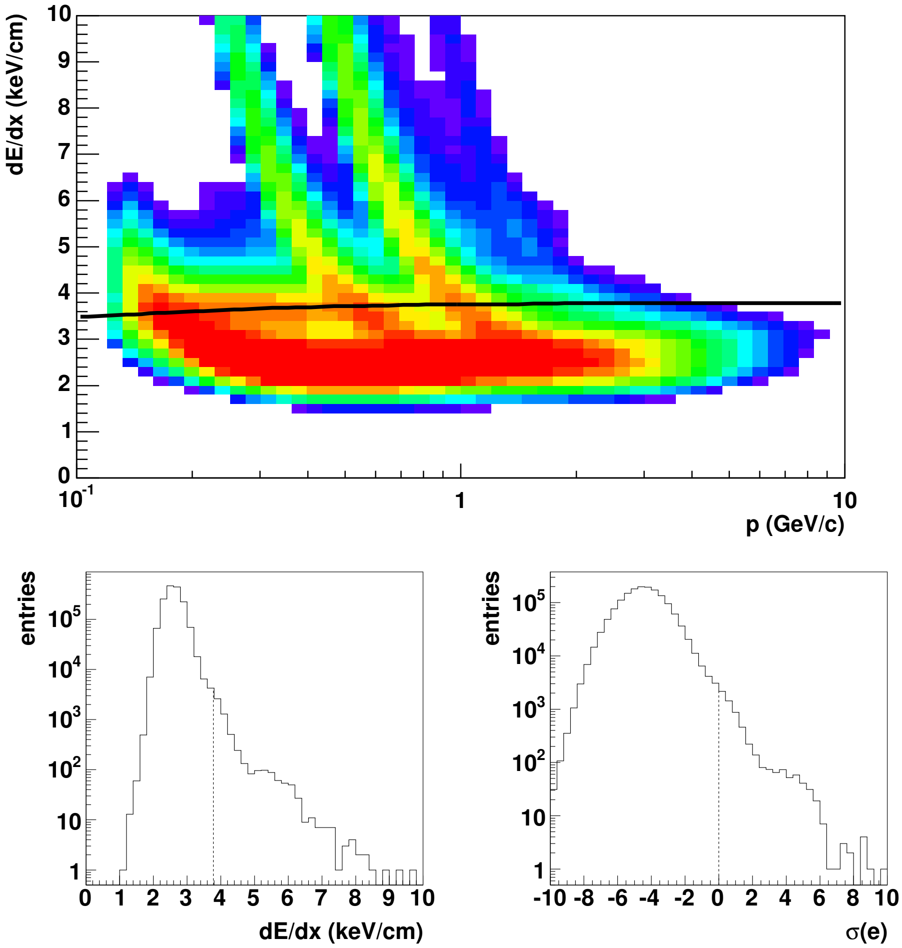

Figure 5.19: Upper plot: Energy loss dE/dx in the TPC versus particle momentum. The expected position of the electron band is shown by the solid line. The lower left plot shows the dE/dx distribution at a momentum of 2 GeV/c. The dashed line shows the expected electron position. The lower right plot shows the same projection however in units of standard deviation of the electron dE/dx resolution.

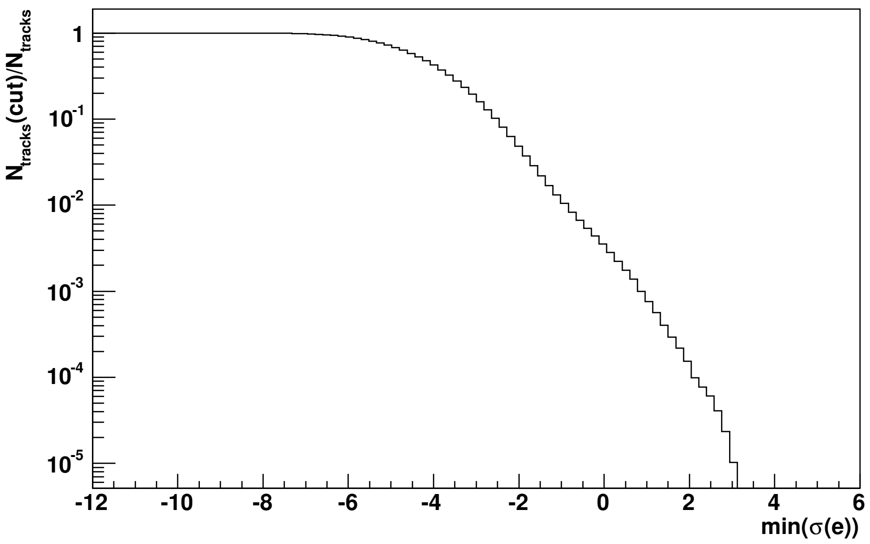

Figure 5.20: Fraction of tracks which pass the electron dE/dx cut as function of the cut value in units of standard deviation of the electron dE/dx resolution.

For the moment the interesting question is if the E_{cluster}/p ratio can be used to further reduce the hadronic contamination of the track sample. The left plot of figure 5.21 shows the ratio for particles from cluster pairs where both daughters where previously selected as electrons by the dE/dx method. The reader should note that for this plot E_{cluster} has been calculated using the planned 3 towers per cluster, in contrast to the 1 tower per cluster used on the trigger level and discussed so far. A clear peak at $E_{\text{cluster}}/p \approx 1$ is visible, indicative of electrons. The peak position is shifted to slightly larger values due to the background energy from low momentum particles present in the high-multiplicity environment of a $Au + Au$ collision.

There are no entries at small E_{cluster}/p values as expected from the above discussion on the implicit E_{cluster}/p cut made on the trigger level. However several entries which relatively large ratios of more than 2 are present. The origin of these entries can be understood as well from the combination of the selection of high energy clusters on the trigger level and the TPC momentum cut used in the analysis. There is some probability of a random match between a e.g. 2 GeV/c track and a high momentum cluster originating from a different source. This probability is further enhanced due to the correlation of particle production in jets. That this is indeed the case demonstrates the right plot of figure 5.21 which shows the E_{cluster}/p ratio for tracks selected as hadrons by the dE/dx method. A cut of $\sigma(e) < -4$ has been used which should have removed all electrons (c.f. figure 5.19 and the discussion above and in section 4.1.1). With this hadron selection the narrow peak at ~ 1 disappeared and a broad structure with a maximum around $E_{\text{cluster}}/p = 2$ appeared. The position of the maximum can be understood from the minimum cluster energy selected on the trigger level and the TPC momentum cut. Since both the tower energy spectrum as well as the track momentum spectrum are falling quickly with increasing energy (momentum), the probability for random cluster-track matches is largest for clusters and tracks close to the thresholds. As discussed above this means a minimum E_{cluster}/p value of 1.5 which is shifted to higher values due to the use of 3 tower-clusters in the figure.

The clear difference between the E_{cluster}/p plots of particles selected as electrons respectively hadrons by the $\mathrm{d}E/\mathrm{d}x$ method clearly demonstrates that the $\mathrm{d}E/\mathrm{d}x$ cut is quite efficient in selecting electrons and rejecting hadrons. A futher clean-up seems possible by a maximum cut on the E_{cluster}/p ratio. A cut of $E_{\text{cluster}}/p = 2$ has a very high electron identification efficiency[8], however removes quite some remaining low momentum tracks which, even if they are accepted by the $\mathrm{d}E/\mathrm{d}x$ method, are probably hadrons.

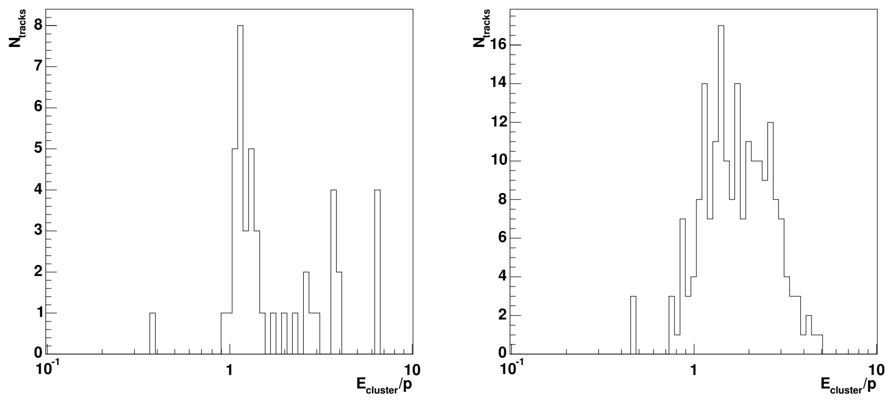

Figure 5.21: E_{cluster}/p distribution for particles selected by $\mathrm{d}E/\mathrm{d}x$ as electrons (left plot) and hadrons (right plot). E_{cluster} has been calculated by summing 3 towers, i.e. the original planned setting also for the trigger algorithms.

Figures 5.22 to 5.24 show the development of the invariant mass spectra for unlike-sign pairs, i.e with a positively and negatively charged daughter, and pairs where both daughters have the same charge as function of the electron identification cuts. Without any PID cuts except the ones already present on the trigger level a relatively large number of pairs is selected. Following equation 4.19 to calculate the background from the like-sign pairs, approximately the same number of background entries as unlike-sign entries is measured.

The $\mathrm{d}E/\mathrm{d}x$ cut removes, as expected, quite a lot of the invariant mass pairs. On the order of 5% of the pairs are accepted. An estimate of the background with the like-sign method becomes impossible since there are no pairs with two positivly charged daughters left. The E_{cluster}/p cut removes another 33% of the unlike-sign cluster pairs and nearly 75% of the $(--)$ pairs. After this cut 4 entries in the unlike-sign invariant mass spectrum and 1 $(--)$ entry are measured. Table 5.7 summarizes the number of entries in the invariant mass spectra after the particle identification cuts.

[8] In section 4.1.2 only the efficiencies for a lower E_{cluster}/p cut have been calculated. However from symmetry arguments (both the resolution of E_{cluster} and p are expected to be gaussian) the efficiency of an upper E_{cluster}/p cut can be easily calculated. Following table 4.2 95% electron efficiency is achieved for an lower E_{cluster}/p cut of 0.8. The same efficiency should be achieved for an upper E_{cluster}/p cut of 1.25. The choosen cut value of 2 has therefore high efficiency estimated to be $(98 \pm 6)\,\%$, even in the presence of background in high multiplicity $Au + Au$ collisions.

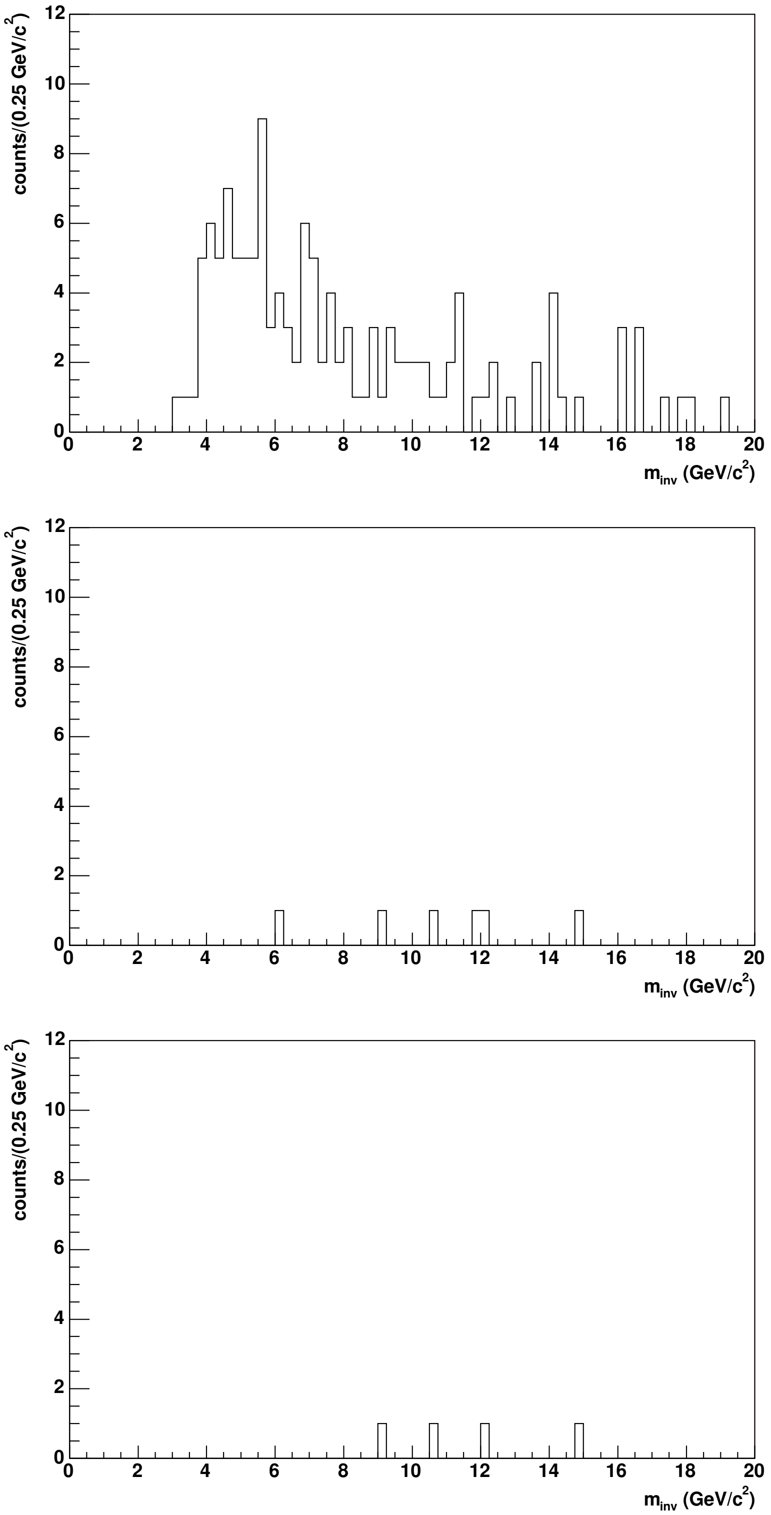

Figure 5.22: Unlike sign invariant mass spectra in the Upsilon triggered events. The top plot is without any electron identification cuts, the middle plot with a $\mathrm{d}E/\mathrm{d}x$ cut and the bottom one with $\mathrm{d}E/\mathrm{d}x$ and E_{cluster}/p cuts.

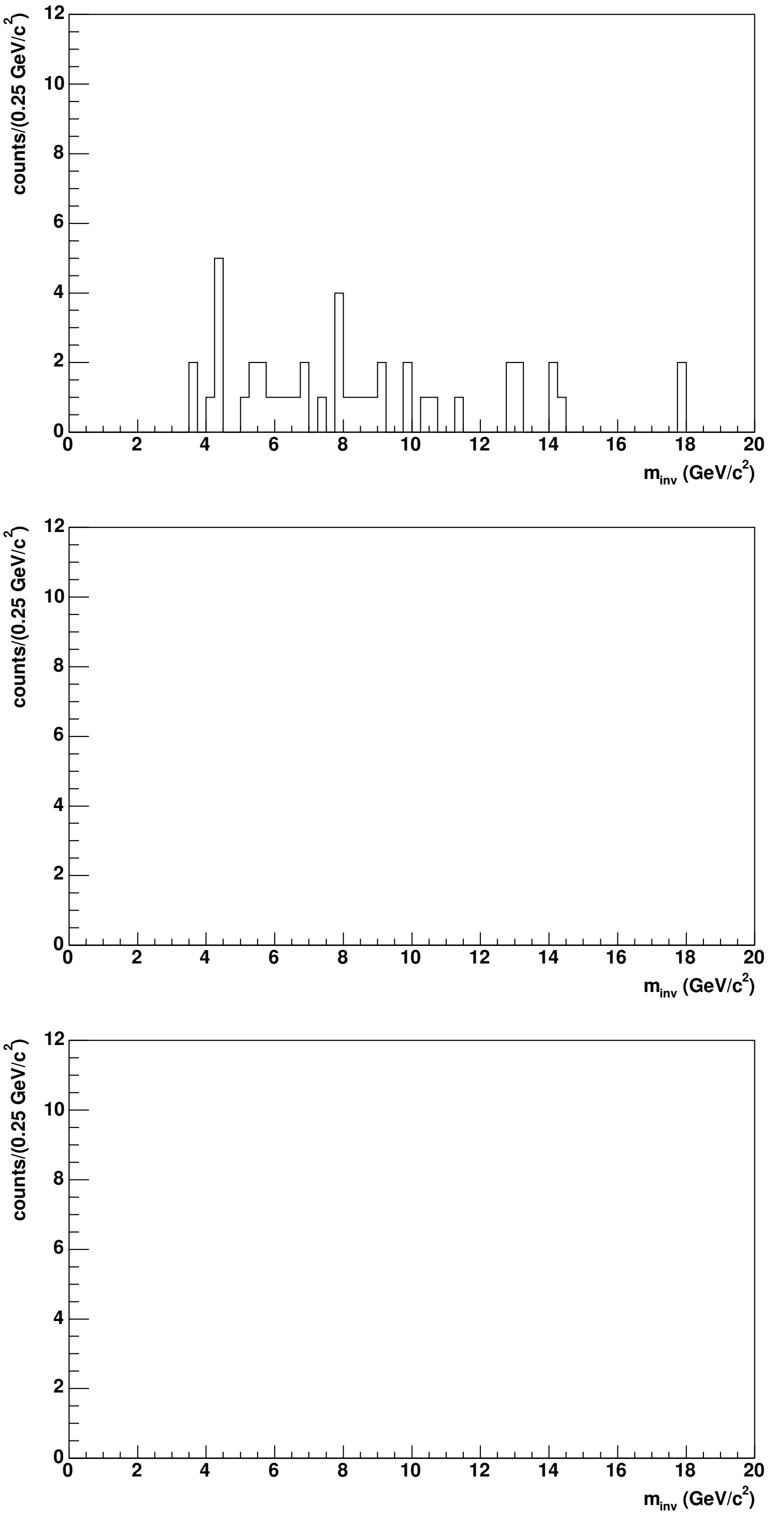

Figure 5.23: Invariant mass spectra of pairs with two positively charged daughters in the Upsilon triggered events. The top plot is without any electron identification cuts, the middle plot with a dE/dx cut and the bottom one with dE/dx and E_{cluster}/p cuts.

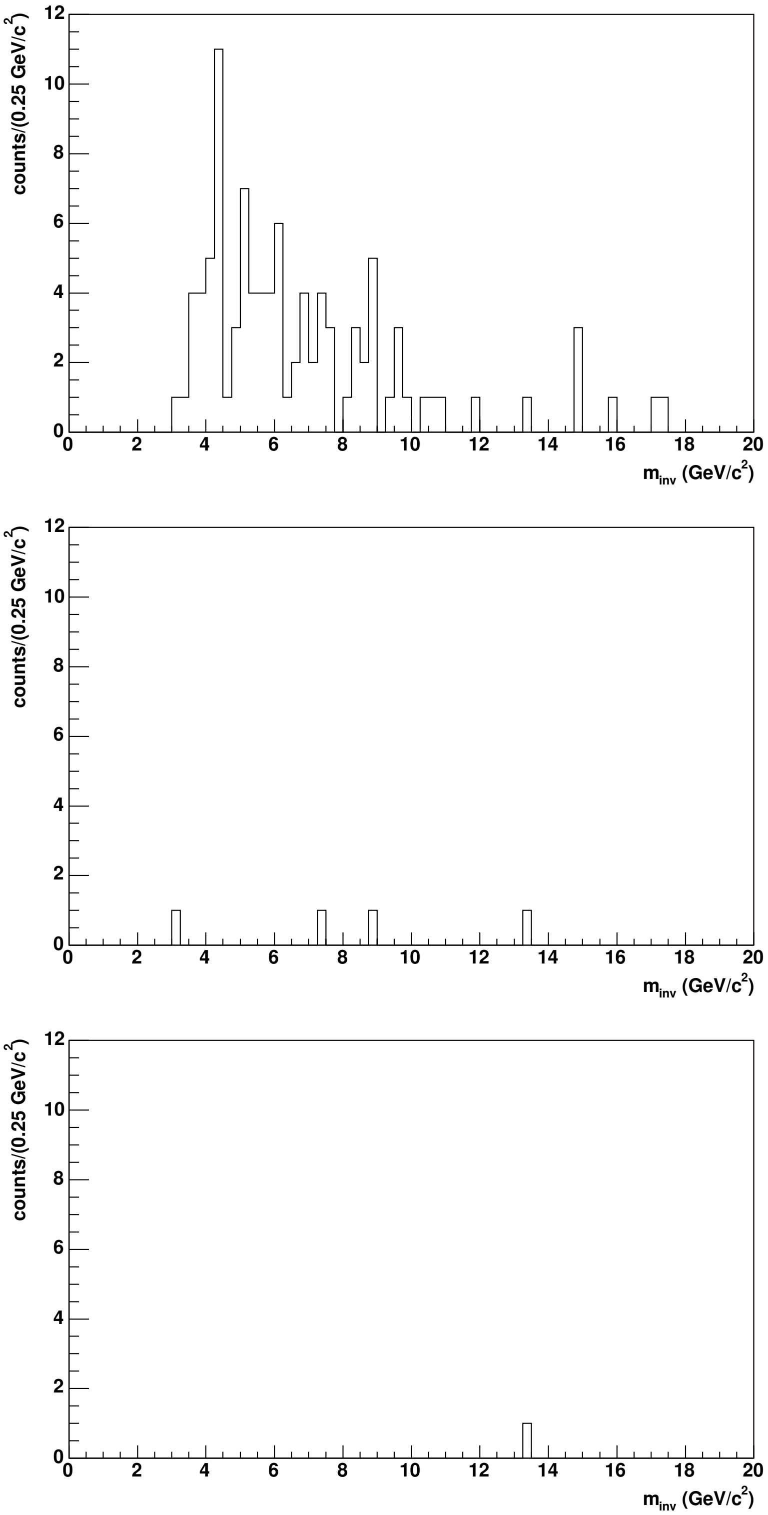

Figure 5.24: Invariant mass spectra of pairs with two negatively charged daughters in the Upsilon triggered events. The top plot is without any electron identification cuts, the middle plot with a $\mathrm{d}E/\mathrm{d}x$ cut and the bottom one with $\mathrm{d}E/\mathrm{d}x$ and E_{cluster}/p cuts.

Type	N_{pairs} no cuts	N_{pairs} dE/dx cut	N_{pairs} all cuts
$+\,-$	132	6	4
$+\,+$	44	0	0
$-\,-$	98	4	1
background (likesign)	131	0	0
background (summed)	142	4	1

Table 5.7: Number of entries in the invariant mass histograms and background estimates after the different cuts.

5.3.2 Υ Acceptance and Efficiency

The interpretation of the measured invariant mass entries requires also the geometrical acceptance as well as the trigger and Υ reconstruction efficiencies. The BEMC performance during the run and the necessary modifications to the Upsilon trigger make a recalculation of the values calculated in chapter 4 necessary.

The geometrical acceptance as well as the trigger efficiencies have to be calculated for the 6 BEMC coverage periods defined in table 5.1. Following the procedure described in section 4.2.1, Υ decays are simulated using the STAR GEANT simulation framework. An Upsilon is called reconstructable if both decay daughters traverse the full TPC and hit the BEMC at a tower with good status. No selection on the energy deposited in the BEMC is made. As discussed the phasespace integrated geometrical acceptance depends on the phasespace distribution of the Υ. The uncertainty due to this is taken into account by calculating the geometrical acceptance for various Υ phasespace distributions. The results are listed in table 5.8, the geometrical acceptance varies between 6.7% and 4.3% for the different BEMC coverage periods.

The rapidity and p_T dependence of the geometrical acceptance is shown in figures 5.25 and 5.26 for the five different BEMC coverage periods (BEMC coverage period I is identical with VI). The geometrical acceptance peaks at $y = 0.5$ and is approximately constant versus p_T.

The next quantity which needs to be recalculated is the L0 trigger efficiency ϵ_{L0}, i.e. how many of the accepted Upsilons are selected by the L0 trigger (c.f. section 4.3.1). The experimental difficulties which had to be overcome during the commisioning of the BEMC during the FY04 run have been alrady discussed extensively in the first part of the chapter. The mis-calibration will cause an pseudorapidity dependence of the L0 trigger efficiency, with lower values at high rapidities. In addition a higher threshold then planned had to be used to compensate for the non-working L2 aborts, which will further reduce the L0 trigger efficiency, especially at low Υ momentum.

The results from the detector simulation are shown in figure 5.27. In addition to the L0 trigger efficiency as function of Υ rapidity and transverse momentum also projections on the rapidity axis are plotted for $p_T = 1$ GeV/c and $p_T = 3$ GeV/c Upsilons. The expected effects from the discussion above are clearly visible.

The achieved L0 trigger efficiency is listed in table 5.8 for all BEMC coverage periods. To first order all BEMC coverage dependent effects should have been accounted for by the geometrical acceptance ϵ_{geo}. Indeed the L0 trigger efficiency stays constant at $\sim 75\%$ within errors.

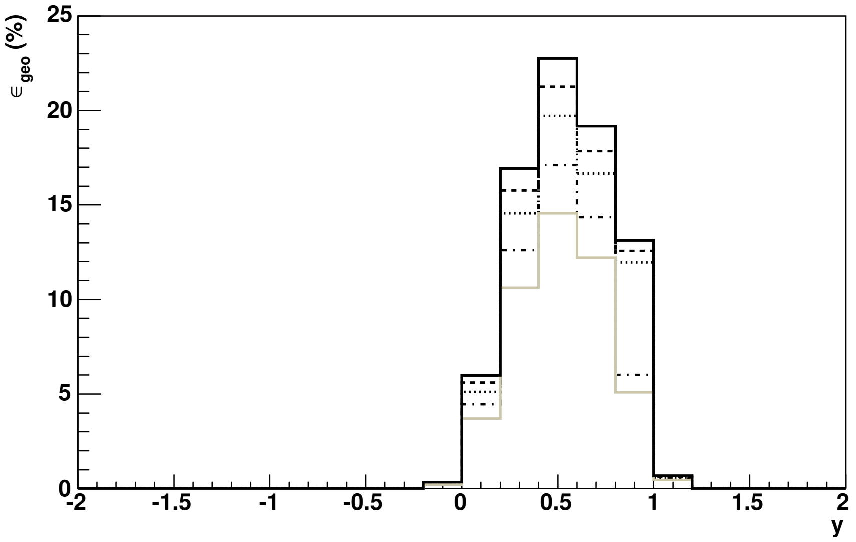

Figure 5.25: Dependence of the geometric acceptance ϵ_{geo} on the Upsilon rapidity y for the five different BEMC configurations (I to V from top to bottom).

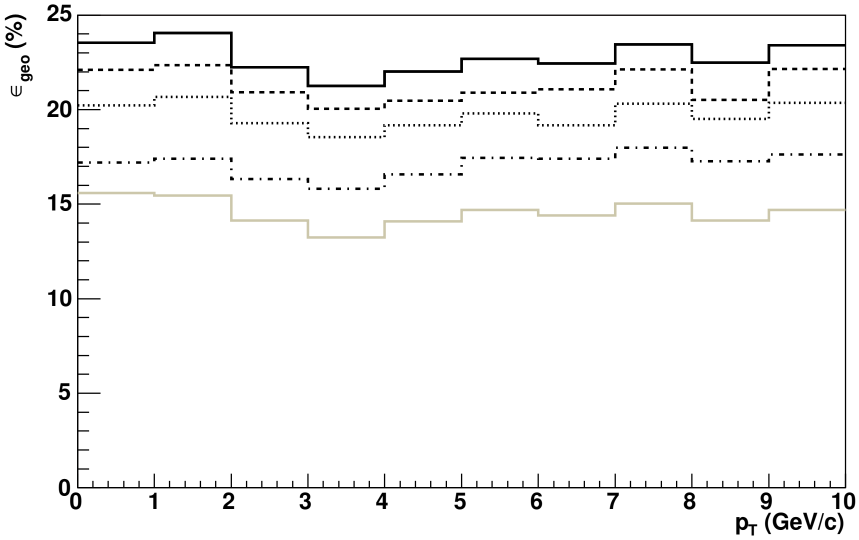

Figure 5.26: Dependence of the geometric acceptance ϵ_{geo} on the Upsilon transverse momentum p_T for the five different BEMC configurations (I to V from top to bottom).

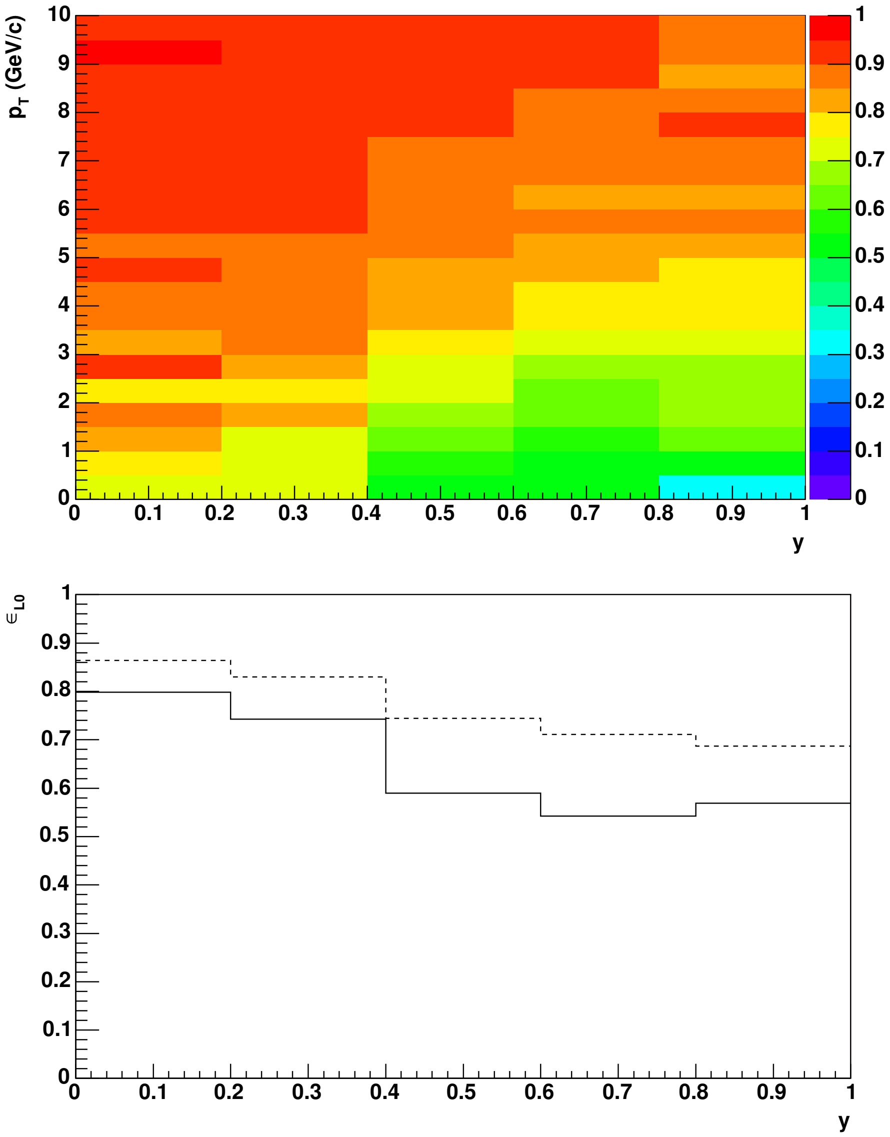

Figure 5.27: L0 trigger efficiency ϵ_{L0} as function of Υ rapidity y and transverse momentum p_T (upper plot). The lower plot shows the rapidity dependence of the L0 trigger efficiency for $p_T = 1$ GeV/c (solid line) and $p_T = 3$ GeV/c (dashed line) Upsilons.

The last part of the Upsilon trigger chain used in FY04 is the L3 trigger. Since the tracking information was not used in the decision, its trigger efficiency can be calculated without a full tracking simulation. The BEMC response simulation is sufficient, making the L3 efficiency calculation much less computing demanding.

It was already discussed that the BEMC corruption required the setting of higher energy threshold parameters then planned, which results in some reduction of the L3 trigger efficiency. At large rapidity this is partly compensated by the L0 mis-calibration. The higher effective L0 energy threshold triggered only towers well above the L0 energy threshold paramter of the L3 algorithm. In turn the relative efficiency of L3 to L0 is increased. This effect is strongest for low momentum Upsilons. A much harder hit is caused by the the fact that accidentally single tower-clusters where used instead of 3 tower-clusters. The reconstructed energy is thus severely underestimated and in turn also the reconstructed invariant mass is smaller. This will result in another reduction of the overall L3 trigger efficiency.

Figure 5.28 shows the results of the L3 trigger efficiency calculation as function of Υ rapidity and transverse momentum as well as the rapidity dependence of ϵ_{L3} for $p_T = 1$ GeV/c and $p_T = 3$ GeV/c Upsilons. The expected effects are clearly visible, with the efficiency at midrapidity reduced to only 40% to 50%. At higher rapidities ϵ_{L3} increased to $\sim 70\%$. The phasespace averaged L3 efficiency relative to L0 triggered events is $(56 \pm 4)\%$ and independent of the the BEMC coverage period.

As already discussed the efficiencies achieved by the different trigger levels are highly correlated. Figure 5.29 shows the combined L0+L3 trigger efficiency. The dependence on Υ rapidity and transverse momentum is largely reduced and is overall on the order of 40%.

To get the total efficiencies the combined L0+L3 trigger efficiency has still to be multiplied with the geometrical acceptance as well as the offline reconstruction efficiencies. The trigger efficiency times the geometric acceptance is given in the last column of table 5.8 for the different BEMC coverage periods. For the further analysis an averaged efficiency $(2.5 \pm 0.3)\,\%$ will be used, which is obtained by calculating the luminosity weighted average.

Period	$\mathcal{L}_{\mathrm{sampled}}$	ϵ_{geo}	ϵ_{L0}	ϵ_{L3}	$\epsilon_{\mathrm{geo}} \times \epsilon_{\mathrm{L0}} \times \epsilon_{\mathrm{L3}}$
I	9.1 μb^{-1}	(6.7 ± 0.4) %	(75 ± 5) %	(56 ± 4) %	(2.8 ± 0.3) %
II	6.6 μb^{-1}	(6.3 ± 0.4) %	(75 ± 5) %	(56 ± 4) %	(2.6 ± 0.3) %
III	1.8 μb^{-1}	(5.8 ± 0.3) %	(74 ± 5) %	(56 ± 4) %	(2.4 ± 0.3) %
IV	1.2 μb^{-1}	(4.9 ± 0.3) %	(74 ± 5) %	(56 ± 4) %	(2.0 ± 0.2) %
V	6.9 μb^{-1}	(4.3 ± 0.3) %	(74 ± 5) %	(56 ± 4) %	(1.8 ± 0.2) %
VI	8.7 μb^{-1}	(6.7 ± 0.4) %	(75 ± 5) %	(56 ± 4) %	(2.8 ± 0.3) %
Run	34.3 μb^{-1}	-	-	-	(2.5 ± 0.3) %

Table 5.8: Geometrical acceptance ϵ_{geo}, trigger efficiencies for L0 and L3 and combined efficiency $\epsilon_{\mathrm{geo}} \times \epsilon_{\mathrm{L0}} \times \epsilon_{\mathrm{L3}}$ for the different BEMC acceptance periods. The averaged total efficiency for the whole FY04 run is also given

The efficiencies entering the offline reconstruction efficiency have been already discussed in chapter 4. There is on one hand the Υ mass reconstruction efficiency to correct for the Upsilons lost due to Bremsstrahlung of the daughter electrons which leads to a too low reconstructed mass. However the main efficiency entering is the (squared) electron reconstruction efficiency. Since the measured FY04 data agrees

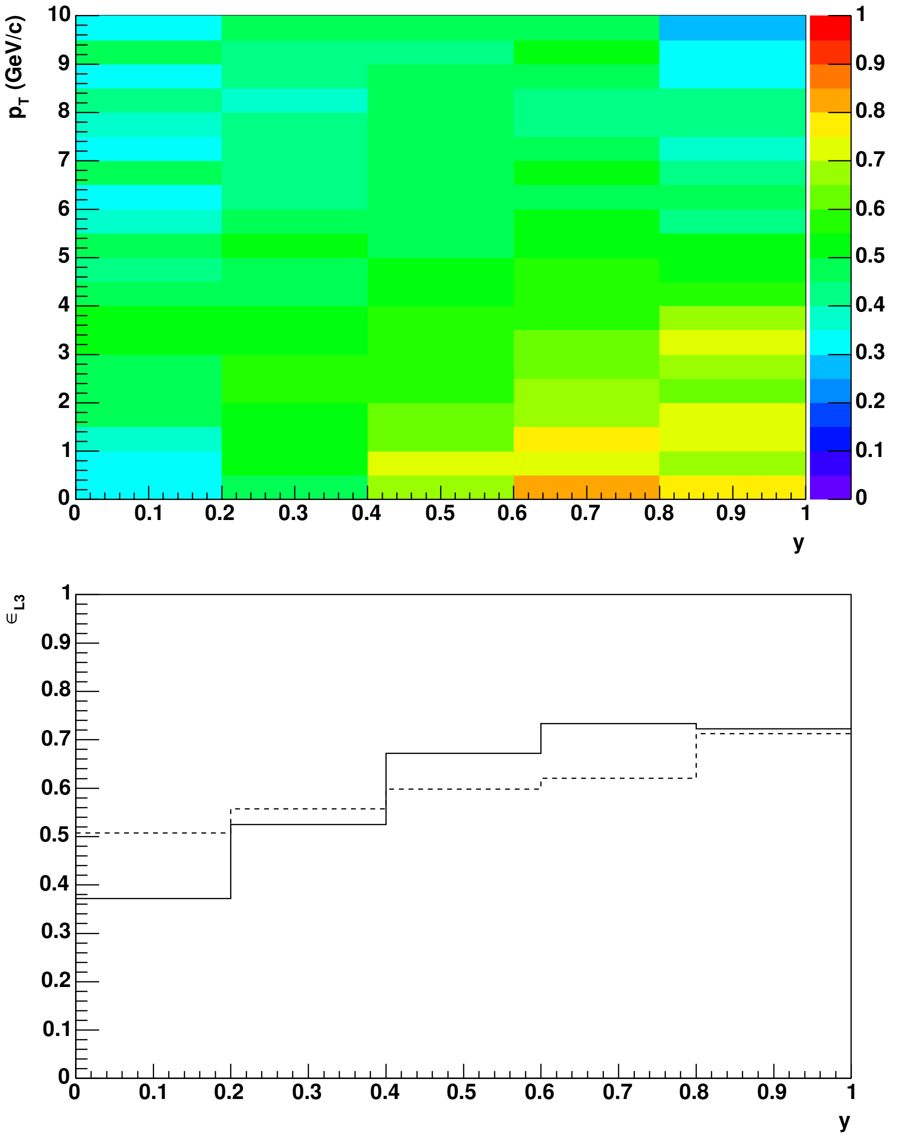

Figure 5.28: L3 trigger efficiency ϵ_{L3} as function of Υ rapidity y and transverse momentum p_T (upper plot). The lower plot shows the rapidity dependence of the L3 trigger efficiency for $p_T = 1$ GeV/c (solid line) and $p_T = 3$ GeV/c (dashed line) Upsilons.

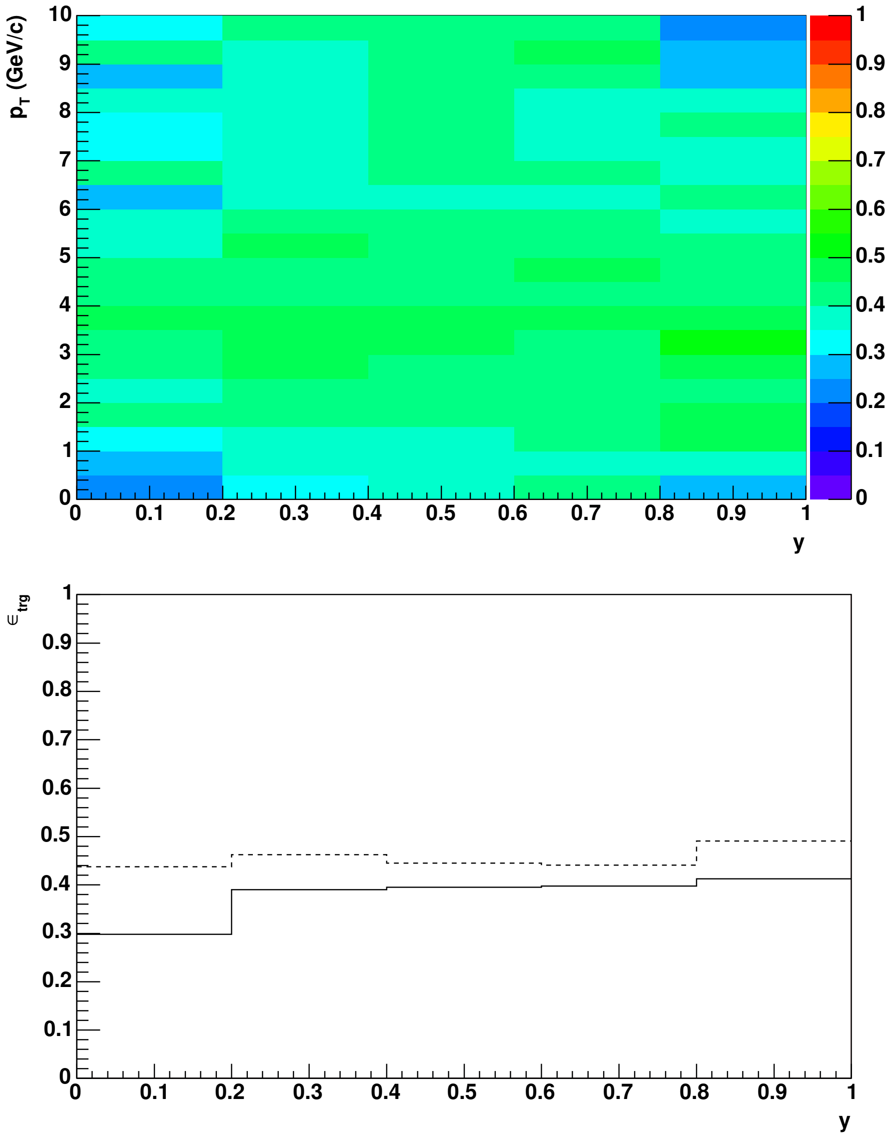

Figure 5.29: L0+L3 trigger efficiency $\epsilon_{\rm L0}$ as function of Υ rapidity y and transverse momentum p_T (upper plot). The lower plot shows the rapidity dependence of the L0+L3 trigger efficiency for $p_T = 1$ GeV/c (solid line) and $p_T = 3$ GeV/c (dashed line) Upsilons.

well with the predictions from chapter 4, the values listed there can be used. The assumptions entering into the efficiency of the E_{cluster}/p cut have been discussed above and were also verified with another detector simulation using simulated electrons embedded into real $Au + Au$ events.

Table 5.9 summarizes the efficiency calculation. The single electron reconstruction efficiency (after particle identification cuts) is $(68 \pm 6)\,\%$, which enters squared into the Υ reconstruction efficiency. The total Υ reconstruction efficiency for Upsilons decaying into an electron pair produced in the rapidity interval $-1 \leq y \leq 1$ has been determined to be $(0.9 \pm 0.2)\,\%$.

Electron Reconstruction Efficiency		
Tracking Efficiency	ϵ_{trk}	$(83 \pm 2)\,\%$
dE/dx PID Efficiency	$\epsilon_{\mathrm{PID}}(e)$	$(84 \pm 4)\,\%$
E_{cluster}/p PID Efficiency	$\epsilon_{\mathrm{PID}}(e)$	$(98 \pm 6)\,\%$
Electron Reconstruction Efficiency	$\epsilon(e)$	$(68 \pm 6)\,\%$

Υ Reconstruction Efficiency		
Combined Efficiency	$(\epsilon_{\mathrm{geo}} \times \epsilon_{\mathrm{L0}} \times \epsilon_{\mathrm{L3}})$	$(2.5 \pm 0.3)\,\%$
Squared e Reconstruction Efficiency	$(\epsilon(e))^2$	$(47 \pm 5)\,\%$
	ϵ_{mass}	$(80 \pm 8)\,\%$
Υ Reconstruction Efficiency	ϵ_{Υ}	$(0.9 \pm 0.2)\,\%$

Table 5.9: Electron and Upsilon reconstruction efficiencies.

5.3.3 Upper Limit on Υ Production in Au+Au Collisions

By now all the information necessary to calculate the Υ cross-section in $Au + Au$ collisions has been compiled. It is obvious from the invariant mass spectra shown in figures 5.22 to 5.24 that the accumulated statistics was not sufficient to observe a clear Upsilon signal. However it is still possible to calculate an upper limit from it. The obtained upper limit will be unique at RHIC and will be the foundation of the further assessment, presented in chapter 6, if a significant Υ measurement will be possible with STAR in the future.

The mass region of the Υ signal has been determined earlier as $8.4\mathrm{GeV/c}^2 \leq m \leq 10.7\mathrm{GeV/c}^2$. Integrating the mass spectra presented in figures 5.22 to 5.24 in this region results in the counts listed in table 5.10. Since no like-sign pairs are observed, it is assumed that the combinatorical background is negligible.

What remains to be done before the Υ cross-section can be calculated is an estimate of the remaining background present in the Υ mass region. As detailled in section 4.2, this might be e.g. entries originating from Drell-Yan pairs. Without a clear observed signal and without sizeable entries at higher invariant masses it is impossible to obtain this background by fitting expected mass shapes to the data. To nevertheless estimate an upper limit, the assumption that the number of background counts in the Υ region is the same as the number of counts in an interval of the same width at higher masses. The observed counts in the interval $10.7\ \mathrm{GeV/c}^2 \leq m \leq 13.0\ \mathrm{GeV/c}^2$ are also given in table 5.10. It is very likely that the assumption made is actually an underestimate of the background present in the signal region since the background is expected to increase with decreasing mass. A higher background in the signal bin would reduce the calculated upper limit. However without an measured background shape, it seems preferable to work with the assumption that the background in the signal mass range is equal to the one in the higher mass bin.

	$+-$	$++$	$--$
$N_{\text{pairs}}\left[8.4\ \text{GeV/c}^2 \leq m \leq 10.7\ \text{GeV/c}^2\right]$	2	0	0
$N_{\text{pairs}}\left[10.7\ \text{GeV/c}^2 \leq m \leq 13.0\ \text{GeV/c}^2\right]$	1	0	0

Table 5.10: Number of electron pairs with the given charge combination in different mass intervals.

To calculate the 90% and 95% confidence level (C.L.) intervals the procedure developed in [FC98] is followed. Two counts in the signal region with one expected background count are observed, as shown in table 5.10. The C.L. intervals given in [FC98] are $[0.00; 4.91]$ for 90% C.L. and $[0.00; 5.72]$ for 95% C.L. as also listed in table 5.11.

The corresponding confidence intervals for the Υ cross section at midrapidity times the branching ratio into electrons can be calculated using the total Υ reconstruction efficiency from above and the analyzed luminosity from section 5.2.1. The number of measured Upsilons N_Υ is given by

$$N_\Upsilon = \epsilon_\Upsilon\ \mathcal{B}\frac{\mathrm{d}\sigma}{\mathrm{d}y}\,|_{y=0}\ \ \mathcal{L}\ \Delta y \tag{5.8}$$

where $\Delta y = 2$ is the width of the rapidity interval for which the reconstruction efficiency ϵ_Υ was calculated. Using this equation a 90% C.L. upper limit of $\mathcal{B}\frac{\mathrm{d}\sigma}{\mathrm{d}y}\,|_{y=0}= 7.6\ \mu$b and an 95% C.L. upper limit of 8.8 μb are calculated. Table 5.11 gives also the corresponding confidence intervals on $\mathcal{B}\frac{\mathrm{d}N}{\mathrm{d}y}\,|_{y=0}$ where the uncertainty of the luminosity measurement has not to be included. The efficiency calculated in the previous section had an 20% uncertainty which needs to be added to the confidence given above. From the observed count one can calculate also the central value of $(1.5 \pm 0.3)\ \mu$b.

	Signal	90% C.L. interval[9]	95% C.L. interval[9]
N_{pairs}	1	$[0.00; 4.91]$	$[0.00; 5.72]$
$\mathcal{B}\frac{\mathrm{d}N}{\mathrm{d}y}\,\vert_{y=0}$	53 ± 10	$[0; 260]$	$[0; 303]$
$\mathcal{B}\frac{\mathrm{d}\sigma}{\mathrm{d}y}\,\vert_{y=0}$	$(1.5 \pm 0.3)\ \mu$b	$[0.0\ \mu\text{b}; 7.6\ \mu\text{b}]$	$[0.0\ \mu\text{b}; 8.8\ \mu\text{b}]$

Table 5.11: Number of electron pairs in the Υ signal region after background subtraction, number of Upsilons per rapidity unit at midrapidity and Υ cross section per rapidity unit at midrapidity (including branching ratio to electrons). Given are the measured number and the 90% and 95% confidence intervals.

The comparison to the expectations from chapter 2 are shown in figures 5.30 and 5.31. Figure 5.30 shows the 90% C.L. upper limit together with the prediction from figure 2.5 scaled to $Au + Au$ collisions assuming no nuclear effects ($\alpha = 1$ in equation 2.6) and assuming the same nuclear absorption of $\alpha = 0.96$ measured at

[9] The 20% uncertainty from the Upsilon reconstruction efficiency is not included in the calculation of the confidence intervals.

lower energies. The box around the central value shows the uncertainty from the trigger efficiency and luminosity determination. The width of the prediction bands is given by the difference between the different extrapolation of the $p+p$ cross section to the RHIC energy of $\sqrt{s_{NN}} = 200$ GeV. Figure 5.31 shows a different representation of the same data. The 90% C.L. upper limit from this work, scaled to elementary collisions with $\alpha = 1$, is added to the energy dependence figure 2.5. As can be seen in both figures, the upper limit is a factor 3 to 5 higher than the baseline predictions.

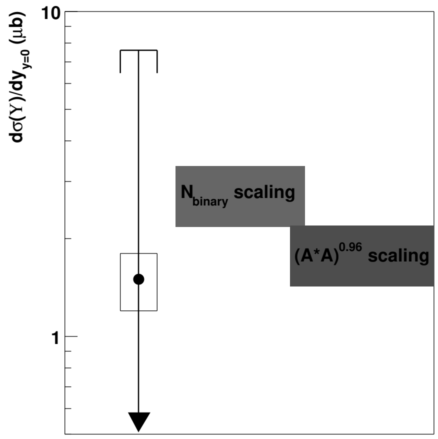

Figure 5.30: 90% C.L. upper limit on the Υ production cross section at midrapidity compared to the expect value from section 2.3. The predictions for two assumptions are shown: no nuclear effects, i.e. scaling with the number of binary collisions, and $\alpha = 0.96$ as measured at lower energy. The width of the prediction bands represents the uncertainty of the Υ cross section in $p+p$ collisions at $\sqrt{s_{NN}} = 200$ GeV due to the necessary extrapolation from other energies (see chapter 2.3).

In summary a first upper limit on the Υ production cross-section in heavy-ion collisions at RHIC has been set. The accumulated statistics is not sufficient to draw any conclusions about the predicted modification of Υ production in heavy-ion collisions. However it has been demonstrated that the necessary capabilities to sucessfully measure the Upsilon cross section at midrapidity with STAR have been developed, especially taking the various experimental difficulties encountered during the commisioning of the BEMC and the L2 trigger into account. The future prospects opened by this extension of the STAR capabilities will be discussed in the concluding chapter.

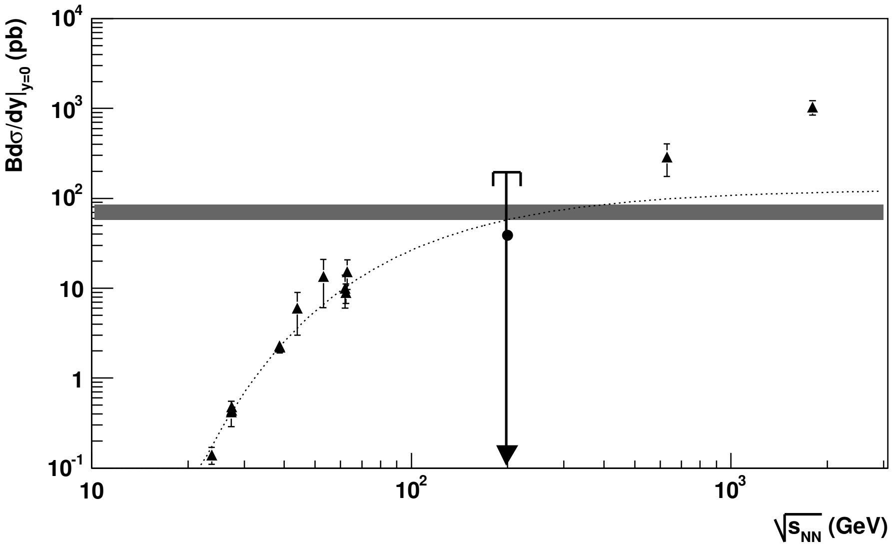

'

Figure 5.31: Energy dependence of the Υ cross section at midrapidity (figure 2.5) with the 90% C.L. upper limit from this analysis. The measured value has been scaled from $Au + Au$ collisions to elementary collisions assuming no nuclear effects ($\alpha = 1$).

6 Future Prospects for Upsilon Measurements with STAR

It has been demonstrated in the previous chapter that the Upsilon trigger algorithm chain developed in chapter 4 of this thesis fullfills its task and works successfully in the STAR environment. However its use during the 2003/2004 run was affected by the commissioning of several of its core components: the first ever use of the L2 trigger system and the continued commissioning of the BEMC.

The experimental difficulties encountered during this endeavor have already been discussed extensively. Several of them, also already present in previous runs, were highlighted by the Upsilon trigger as one of the most demanding trigger and BEMC applications in STAR. The experiences gained with the Upsilon trigger proved to be one of the key elements leading to a successfully and complete commissioning of the aforementioned systems.

The correct handling of L2 aborts in the BSMD was already implemented during the 2003/2004 run. The necessary modifications of the SVT followed in the shutdown period after the run when the inner cone was removed from STAR and the SVT electronic became accessible. The successfull operation of the L2 trigger system with aborts of the slow detector readouts could be successfully demonstrated during the 2004/2005 run. TPC readout trigger rates of up to 1,000 Hz in $Cu + Cu$ collisions have been demonstrated to be possible. L2 itself has been demonstrated to be able to process several kHz of collisions, however to limit the currents in the TPC long-term operation has been limited to 1 kHz. This is however more then sufficient for the needs of the Upsilon and other L2 triggers. Some setback in this trigger success story is the decommissioning of the L3 trigger system after the 2004 run. However the concept of the express streams demonstrated first with the L3 Upsilon trigger proved to be so usefull, that much higher express stream rates and even multiple streams have become a standard part of STAR operations. The background rejection power provided earlier by L3 is thus not anymore necessary for a successfull operation of the Upsilon trigger chain.

During the 2004 shutdown period and the 2004/2005 run significant progress has also been made with the commissioning of the BEMC, which got fully installed. To prevent the problems with failing crates, the power supplies were replaced with remote ones and no failures have been observed in the 2004/2005 run. Also the full BSMD got installed and commissioned, which will allow an even better particle identification. By rebuilding the trigger clock distribution to the BEMC also the data corruption during the transfer to the tower data collector got fixed, none was observed during large parts of the 2004/2005 run. In addition the detection methods developed in this work have been implemented as quality assessment in the DAQ system. In the 2005 shutdown period the full readout of the preshower detector BPRS got installed, further improving the particle identification system of the BEMC system. Last but not least the towers with bad status identified with the status tools introduced in the previous chapter got checked in the shutdown periods and a significant number of them could be repaired, further enlarging the acceptance of the system.

By now all components of the Upsilon trigger chain have thus the reached the maturity necessary for a stable operation, as originally envisioned in chapter 4. Consequently the Upsilon trigger has been established as a standard part of the STAR trigger mix. It remains the question if, based on the results obtained in this thesis, a successfully Upsilon measurement will be possible in future runs.

Key to answer this question are the efficiencies listed earlier in table 5.9 and the expected changes with the now fully working system. The first obvious change is in the geometrical acceptance, with the full BEMC available for use in the trigger it increases from 6% in the 2003/2004 run to the 32% calculated in table 4.3, i.e. by a factor 5!

The, now working, L2 aborts allow to lower the threshold of the L0 high tower trigger to the originally intended values, increasing its efficiency, which will be even further increased by the improved BEMC calibration. Certainly an efficiency of 90%, if not even higher, is possible, up from the 75% in the 2003/2004 run. Also the rapidity and transverse momentum dependence shown in the previous chapter will be strongly reduced. The improved quality of the BEMC data allows to relax the L2 threshold parameters further which, together with the use of 3 tower-clusters, will enhance the L2 trigger efficiency from 56% to $\sim$ 90%. All of this has been demonstrated already during the 2004/2005 run after the BEMC got commisioned. The combined effect on the trigger efficiency is an increase by a factor 2.

Also an increase of the accumulated statistics is expected. With BEMC and L2 based trigger now part of standard STAR operation, they are expected to get included in the trigger mix earlier in the run, while in the 2003/2004 run they were only included after more than half of the available beam time elapsed. This results in a trivial gain of another factor 2. The working L2 aborts have the additional benefit of allowing a larger STAR detector lifetime since the TPC readout rate can be significantly reduced.

In a future long run STAR will have a factor 10 more trigger efficiency and acceptance and an increase of more than a factor 2 in accumulated statistics, probably even more due to the improved luminosity in RHIC. What will additionally help the Upsilon analysis are the improved electron identification capabilities of the BEMC system with the BSMDs and the BPRS working. The, already now very small, background will be further decreased, with a factor 10 expected from simulation studies. However this will slightly reduce the efficiency of the electron identification to $\sim$ 90%.

Overall a factor 20 increase in the number of detectable Upsilons can be expected. This results in a significant improvement of the upper limit calculated in this work and very likely puts STAR in a position where the upper limit is comparable with the predictions of the different models outlined in chapter 2.

A key element for the interpretation and the success of the Upsilon program in STAR will be the better determination of the baseline. The planned future $p+p$ and $d+Au$ runs will probably allow this, reducing by a large amount the uncertainties in the baseline predictions shown in figure 5.30. The by-now available higher statistics data on J/ψ production additionally limits the uncertainty of the model prediction, in turn enhancing the selectivity of the complementary Upsilon measurement.

The expectations presented in this chapter so far were based on the present status of the STAR and RHIC system. Further improvements in the accumulated statistics can be expected from increased luminosities in RHIC, leading into the RHIC-II era with a factor 10 improvement compared to todays situation. In addition several modifications to the STAR detector have been proposed or are already in the construction phase which will further enhance STAR's capabilities. Currently a program is under way to replace the TPC readout electronic with the one developed for ALICE. The availability of data buffers already on the frontend chips results in a significant reduction of the dead time. It is expected that STAR will be able to run with livetimes close to 100%, resulting in a gain of accumulated luminosity compared to the present situation. The considered removal of the SVT reduces the material in front of the TPC and in turn the number of conversion electrons. Presently the ratio between conversion electrons and non-conversion electrons is 1:1. Any reduction of this ratio will further decrease the number of combinatorical combinations in the Upsilon region. In the long term a new inner tracking system is proposed to be installed in STAR. The pointing resolution of this new silicon tracking device will be good enough to reject also electrons originating from some resonance decays, again improving the combinatorical background. The Upsilon trigger itself will benefit from the approved installation of a Time-Of-Flight system and the availability of its data in the L2 system. As demonstrated a lot of the triggered pairs were caused by photons or other neutral particles. TOF will allow to tag charged particles in front of the towers, at least in non-high multiplicity collisions, reducing the number of triggered pairs with clusters from photons or neutral particles. To some degree it serves as replacement of the L3 functionality in the original trigger concept developed in this work.

In summary STAR has now developed the necessary capabilities for a successfull program of future Upsilon measurements, based largely on the foundations developed in this thesis. Together with the further expected improvements, STAR is on the advent of a promising multi-year program on quarkonia physics, with a potentially large impact on the understanding of the matter formed in heavy-ion collisions at RHIC.

Bibliography

[A+79] A. L. S. Angelis et al. A Measurement of the production of massive e+ e- pairs in proton proton collisions at s**(1/2) = 62.4-GeV. *Phys. Lett.*, B87:398, 1979.

[A+83] D. Andrews et al. The CLEO Detector. *Nucl. Instr. Meth.*, 211:47, 1983.

[A+87] C. Albajar et al. Beauty production at the CERN proton - anti-proton collider. (PAPER 1.). *Phys. Lett.*, B186:237, 1987.

[A+91] D. M. Alde et al. Nuclear dependence of the production of Y resonances at 800-GeV. *Phys. Rev. Lett.*, 66:2285–2288, 1991.

[A+95] F. Abe et al. Upsilon production in p anti-p collisions at s**(1/2) = 1.8-TeV. *Phys. Rev. Lett.*, 75:4358, 1995.

[A+99a] M. C. Abreu et al. J/psi and psi' production in p, O and S induced reactions at SPS energies. *Phys. Lett.*, B466:408–414, 1999.

[A+99b] S. Afanasev et al. The NA49 large acceptance hadron detector. *Nucl. Instrum. Meth.*, A430:210–244, 1999.

[A+00] T. Affolder et al. Production of Upsilon(1S) mesons from chi/b decays in p anti-p collisions at s**(1/2) = 1.8-TeV. *Phys. Rev. Lett.*, 84:2094–2099, 2000.

[A+02a] D. Acosta et al. Upsilon production and polarization in p anti-p collisions at s**(1/2) = 1.8-TeV. *Phys. Rev. Lett.*, 88:161802, 2002.

[A+02b] K. Adcox et al. Suppression of hadrons with large transverse momentum in central Au + Au collisions at s**(1/2)(N N) = 130-GeV. *Phys. Rev. Lett.*, 88:022301, 2002.

[A+02c] S. V. Afanasiev et al. Energy dependence of pion and kaon production in central Pb + Pb collisions. *Phys. Rev.*, C66:054902, 2002.

[A+03a] K. H. Ackermann et al. STAR detector overview. *Nucl. Instrum. Meth.*, A499:624–632, 2003.

[A+03b] J. Adams et al. Evidence from d + Au measurements for final-state suppression of high p(T) hadrons in Au + Au collisions at RHIC. *Phys. Rev. Lett.*, 91:072304, 2003.

[A+03c] J. Adams et al. Production of charged pions and hadrons in Au + Au collisions at s(NN)**(1/2) = 130-GeV. 2003. submitted to PRC.

[A+03d] J. Adams et al. Transverse momentum and collision energy dependence of high p(T) hadron suppression in Au + Au collisions at ultrarelativistic energies. *Phys. Rev. Lett.*, 91:172302, 2003.

[A+03e] C. Adler et al. Disappearance of back-to-back high p(T) hadron correlations in central Au + Au collisions at s(NN)**(1/2) = 200-GeV. *Phys. Rev. Lett.*, 90:082302, 2003.

[A+03f] C. Adler et al. The RHIC zero-degree calorimeters. *Nucl. Instrum. Meth.*, A499:433–436, 2003.

[A+03g] C. Adler et al. The STAR level-3 trigger system. *Nucl. Instrum. Meth.*, A499:778–791, 2003.

[A+03h] S. S. Adler et al. Absence of suppression in particle production at large transverse momentum in s(NN)**(1/2) = 200-GeV d + Au collisions. *Phys. Rev. Lett.*, 91:072303, 2003.

[A+03i] M. Anderson et al. A readout system for the STAR time projection chamber. *Nucl. Instrum. Meth.*, A499:679–691, 2003.

[A+03j] M. Anderson et al. The STAR time projection chamber: A unique tool for studying high multiplicity events at RHIC. *Nucl. Instrum. Meth.*, A499:659–678, 2003.

[A+04a] G. S. Adams et al. Measurement of the muonic branching fraction of the narrow Upsilon resonances at CLEO. 2004.

[A+04b] S. S. Adler et al. J/psi production in Au Au collisions at s(NN)**(1/2) = 200- GeV at the Relativistic Heavy Ion Collider. *Phys. Rev.*, C69:014901, 2004.

[A+05a] J. Adams et al. Experimental and theoretical challenges in the search for the quark gluon plasma: The STAR collaboration's critical assessment of the evidence from RHIC collisions. *Nucl. Phys. A*, 757:102–183, 2005.

[A+05b] K. Adcox et al. Formation of dense partonic matter in relativistic nucleus nucleus collisions at RHIC: Experimental evaluation by the PHENIX collaboration. *Nucl. Phys. A*, 757:184–283, 2005.

[A+05c] S. S. Adler et al. Centrality dependence of direct photon production in s(NN)**(1/2) = 200-GeV Au + Au collisions. *Phys. Rev. Lett.*, 94:232301, 2005.

[A+05d] S. S. Adler et al. J/psi production and nuclear effects for d + Au and p + p collisions at s(NN)**(1/2) = 200-GeV. 2005.

[A+05e] B. Alessandro et al. A new measurement of J/psi suppression in Pb - Pb collisions at 158-GeV per nucleon. *Eur. Phys. J.*, C39:335–345, 2005.

[A+05f] I. Arsene et al. Quark gluon plasma and color glass condensate at RHIC? The perspective from the BRAHMS experiment. *Nucl. Phys. A*, 757:1–27, 2005.

[ABMRS03] A. Andronic, P. Braun-Munzinger, K. Redlich, and J. Stachel. Statistical hadronization of charm in heavy-ion collisions at SPS, RHIC and LHC. *Phys. Lett.*, B571:36–44, 2003.

[AC98] N. Armesto and A. Capella. A quantitative reanalysis of J/psi suppression in nuclear collisions. *Phys. Lett.*, B430:23–31, 1998.

[ACF99] N. Armesto, A. Capella, and E. G. Ferreiro. Charmonium suppression in lead lead collisions: Is there a break in the J/psi cross-section? *Phys. Rev.*, C59:395–404, 1999.

[Adl03] C. Adler. *Der STAR Level-3 Trigger*. PhD thesis, University of Frankfurt, 2003.

[AHM00] Masayuki Asakawa, Ulrich W. Heinz, and Berndt Muller. Fluctuation probes of quark deconfinement. *Phys. Rev. Lett.*, 85:2072–2075, 2000.

[ALI95] ALICE. ALICE Technical Proposal. 1995. CERN-LHCC-1995-071.

[ALI04] ALICE. ALICE : Technical Design Report of the Trigger Data Acquisition High-Level Trigger and Control System. 2004. CERN-LHCC-2003-062, CERN-ALICE-TDR-010.

[B+79] J. Badier et al. First evidence for Upsilon production by pions. *Phys. Lett.*, B86:98, 1979.

[B+95] C. Baglin et al. psi-Prime and J/psi production in p W, p U and S U interactions at 200-GeV/nucleon. *Phys. Lett.*, B345:617–621, 1995.

[B+02] J. Berger et al. TPC data compression. *Nucl. Instrum. Meth.*, A489:406–421, 2002.

[B+03a] M. Beddo et al. The STAR barrel electromagnetic calorimeter. *Nucl. Instrum. Meth.*, A499:725–739, 2003.

[B+03b] M. Bedjidian et al. Hard probes in heavy ion collisions at the LHC: Heavy flavour physics. 2003.

[B+05] B. B. Back et al. The PHOBOS perspective on discoveries at RHIC. *Nucl. Phys. A*, 757:28–101, 2005.

[BCK+01] F. Becattini, J. Cleymans, A. Keranen, E Suhonen, and K. Redlich. Features of particle multiplicities and strangeness production in central heavy ion collisions between 1.7-A- GeV/c and 158-A-GeV/c. *Phys. Rev.*, C64:024901, 2001.

[BDM+97] R. Baier, Yuri L. Dokshitzer, Alfred H. Mueller, S. Peigne, and D. Schiff. Radiative energy loss of high energy quarks and gluons in a finite-volume quark-gluon plasma. *Nucl. Phys.*, B483:291–320, 1997.

[Ber03] J. Berger. *Anti-Proton to Proton Ratio in Au+Au Collisions at STAR*. PhD thesis, University of Frankfurt, 2003.

[BFL01] Eric Braaten, Sean Fleming, and Adam K. Leibovich. NRQCD analysis of bottomonium production at the Tevatron. *Phys. Rev.*, D63:094006, 2001.

[BGK+04] F. Becattini, M. Gazdzicki, A. Keranen, J. Manninen, and R. Stock. Study of chemical equilibrium in nucleus nucleus collisions at AGS and SPS energies. *Phys. Rev.*, C69:024905, 2004.

[BH97] F. Becattini and Ulrich W. Heinz. Thermal hadron production in p p and p anti-p collisions. *Z. Phys.*, C76:269–286, 1997.

[BLP+89] K. D. Born, E. Laermann, N. Pirch, T. F. Walsh, and P. M. Zerwas. Hadron properties in Lattice QCD with dynamical fermions. *Phys. Rev.*, D40:1653–1663, 1989.

[BM04] P. Braun-Munzinger. Relativistic nuclear collisions and the QCD phase boundary. 2004.

[BMCOR02] P. Braun-Munzinger, J. Cleymans, H. Oeschler, and K. Redlich. Maximum relative strangeness content in heavy ion collisions around 30-A-GeV. *Nucl. Phys.*, A697:902–912, 2002.

[BMMRS01] P. Braun-Munzinger, D. Magestro, K. Redlich, and J. Stachel. Hadron production in Au Au collisions at RHIC. *Phys. Lett.*, B518:41–46, 2001.

[BMS00] P. Braun-Munzinger and J. Stachel. (Non)thermal aspects of charmonium production and a new look at J/psi suppression. *Phys. Lett.*, B490:196–202, 2000.

[BMSW04] P. Braun-Munzinger, J. Stachel, and Christof Wetterich. Chemical freeze-out and the QCD phase transition temperature. *Phys. Lett.*, B596:61–69, 2004.

[BO89] J. P. Blaizot and Jean-Yves Ollitrault. On the Fate of a J/psi Produced in a Nucleus-Nucleus Collision. *Phys. Rev.*, D39:232, 1989.

[BP79] Gyan Bhanot and Michael E. Peskin. Short distance analysis for heavy quark systems. 2. Applications. *Nucl. Phys.*, B156:391, 1979.

[BR93] W. Blum and L. Rolandi. *Particle detection with drift chambers.* Springer, Berlin, 1993.

[C+85] S. Childress et al. Production dynamics of the Upsilon in proton nucleon interactions. *Phys. Rev. Lett.*, 55:1962–1964, 1985.

[C+03a] P. Cortese et al. Charmonia absorption in p A collisions at the CERN SPS: Results and implications for Pb Pb interactions. *Nucl. Phys.*, A715:679–682, 2003.

[C+03b] H. J. Crawford et al. The STAR trigger. *Nucl. Instrum. Meth.*, A499:766–777, 2003.

[C+04] H. Crawford et al. DSM Tree 2005. http://www.star.bnl.gov/... .../STAR/html/trg_l/TSL/Schematics/DSM_Tree_2005.pdf, 2004.

[Cam79] L. Camilleri. Production of heavy quark bound states in hadron hadron collisions. 1979. In *Batavia 1979, Proceedings, Lepton and Photon Interactions At High Energies*, 228-238.

[Cap04] A. Capella. Microscopic models of heavy ion interactions. *Lect. Notes Phys.*, 652:1–34, 2004.

[CBM02] P. Crochet and P. Braun-Munzinger. Investigation of background subtraction techniques for high mass dilepton physics. *Nucl. Instrum. Meth.*, A484:564–572, 2002.

[CCP+88] A. Capella, J. A. Casado, C. Pajares, A. V. Ramallo, and J. Tran Thanh Van. Nuclear effects in J/psi suppression. *Phys. Lett.*, B206:354, 1988.

[CKP01] A. Cucchieri, F. Karsch, and P. Petreczky. Propagators and dimensional reduction of hot SU(2) gauge theory. *Phys. Rev.*, D64:036001, 2001.

[CP75a] N. Cabibbo and G. Parisi. Exponential hadronic spectrum and quark liberation. *Phys. Lett.*, B59:67, 1975.

[CP75b] J. C. Collins and M. J. Perry. Superdense Matter: Neutrons or Asymptotically Free Quarks? *Phys. Rev. Lett.*, 34:1353–1356, 1975.

[Cra78] N. S. Craigie. Lepton and photon prodcution in hadron collisions. *Phys. Rept.*, 47:1, 1978.

[CS01] A. Capella and D. Sousa. Charged multiplicities and J/psi suppression at SPS and RHIC energies. 2001.

[DC05] H. Pereira Da Costa. PHENIX results on J/psi production in Au + Au and Cu + Cu collisions at s(NN)**(1/2) = 200-GeV. 2005.

[Die05] T. Dietel. *Azimuthal Correlations of high-p_T Photons and Hadrons in Au + Au collisions at STAR.* PhD thesis, University of Frankfurt, 2005.

[DPS01a] S. Digal, P. Petreczky, and H. Satz. Quarkonium feed-down and sequential suppression. *Phys. Rev.*, D64:094015, 2001.

[DPS01b] S. Digal, P. Petreczky, and H. Satz. String breaking and quarkonium dissociation at finite temperatures. *Phys. Lett.*, B514:57–62, 2001.

[Dun04] J. Dunlop. ZDC vertex bias. http://www.star.bnl.gov/protected/... .../common/common2004/trigger2004/, 2004.

[E+04] S. Eidelman et al. Review of Particle Physics. *Physics Letters B*, 592:1+, 2004.

[EGK+78] E. Eichten, K. Gottfried, T. Kinoshita, K. D. Lane, and Tung-Mow Yan. Charmonium: The Model. *Phys. Rev.*, D17:3090, 1978.

[EGK+80] E. Eichten, K. Gottfried, T. Kinoshita, K. D. Lane, and Tung-Mow Yan. Charmonium: Comparison with experiment. *Phys. Rev.*, D21:203, 1980.

[EHSW05] K. J. Eskola, H. Honkanen, C. A. Salgado, and U. A. Wiedemann. The fragility of high-p(T) hadron spectra as a hard probe. *Nucl. Phys.*, A747:511–529, 2005.

[EKS99] K. J. Eskola, V. J. Kolhinen, and C. A. Salgado. The scale dependent nuclear effects in parton distributions for practical applications. *Eur. Phys. J.*, C9:61–68, 1999.

[EQ95] Estia J. Eichten and Chris Quigg. Quarkonium wave functions at the origin. *Phys. Rev.*, D52:1726–1728, 1995.

[FC98] Gary J. Feldman and Robert D. Cousins. A Unified approach to the classical statistical analysis of small signals. *Phys. Rev.*, D57:3873–3889, 1998.

[Fli03] D. Flierl. *Two pion correlations at the STAR experiment* . PhD thesis, University of Frankfurt, 2003.

[FMNB03] R. J. Fries, B. Muller, C. Nonaka, and S. A. Bass. Hadronization in heavy ion collisions: Recombination and fragmentation of partons. *Phys. Rev. Lett.*, 90:202303, 2003.

[G+95] R. Gavai et al. Quarkonium production in hadronic collisions. *Int. J. Mod. Phys.*, A10:3043–3070, 1995.

[GFS+98] L. Gerland, L. Frankfurt, M. Strikman, Horst Stoecker, and W. Greiner. J/psi production, chi polarization and color fluctuations. *Phys. Rev. Lett.*, 81:762–765, 1998.

[GFS+01] L. Gerland, L. Frankfurt, M. Strikman, Horst Stoecker, and W. Greiner. Suppression of quarkonium production in heavy ion collisions at RHIC and LHC. *J. Phys.*, G27:695–702, 2001.

[GG99a] Marek Gazdzicki and Mark I. Gorenstein. Evidence for statistical production of J/psi mesons in nuclear collisions at the CERN SPS. *Phys. Rev. Lett.*, 83:4009–4012, 1999.

[GG99b] Marek Gazdzicki and Mark I. Gorenstein. On the early stage of nucleus nucleus collisions. *Acta Phys. Polon.*, B30:2705, 1999.

[GGB+99] J. Geiss, C. Greiner, E. L. Bratkovskaya, W. Cassing, and U. Mosel. Charmonium suppression with c anti-c dissociation by strings. *Phys. Lett.*, B447:31–40, 1999.

[GGJ88] S. Gavin, M. Gyulassy, and A. Jackson. Hadronic J/PSI Suppression in Ultrarelativistic Nuclear Collisions. *Phys. Lett.*, B207:257–262, 1988.

[GKL03] V. Greco, C. M. Ko, and P. Levai. Parton coalescence and antiproton/pion anomaly at RHIC. *Phys. Rev. Lett.*, 90:202302, 2003.

[GKR04] V. Greco, C. M. Ko, and R. Rapp. Quark coalescence for charmed mesons in ultrarelativistic heavy-ion collisions. *Phys. Lett.*, B595:202–208, 2004.

[GKSG01] M. I. Gorenstein, A. P. Kostyuk, H. Stocker, and W. Greiner. Statistical coalescence model with exact charm conservation. *Phys. Lett.*, B509:277–282, 2001.

[GKSG02] M. I. Gorenstein, A. P. Kostyuk, H. Stocker, and W. Greiner. J/psi suppression and enhancement in Au + Au collisions at the BNL RHIC. *Phys. Lett.*, B524:265–272, 2002.

[GM92] M. Gazdzicki and S. Mrowczynski. A Method to study 'equilibration' in nucleus-nucleus collisions. *Z. Phys.*, C54:127–132, 1992.

[GR01] L. Grandchamp and R. Rapp. Thermal versus direct J/psi production in ultrarelativistic heavy-ion collisions. *Phys. Lett.*, B523:60–66, 2001.

[GW73] D. J. Gross and Frank Wilczek. Ultraviolet behavior of non-abelian gauge theories. *Phys. Rev. Lett.*, 30:1343–1346, 1973.

[H+77] S. W. Herb et al. Observation of a dimuon resonance at 9.5-GeV in 400-GeV proton - nucleus collisions. *Phys. Rev. Lett.*, 39:252–255, 1977.

[H+03] H. Hahn et al. The RHIC design overview. *Nucl. Instrum. Meth.*, A499:245–263, 2003.

[Hag65] R. Hagedorn. Statistical thermodynamics of strong interactions at high- energies. *Nuovo Cim. Suppl.*, 3:147–186, 1965.

[Hei01] Henning Heiselberg. Event-by-event physics in relativistic heavy-ion collisions. *Phys. Rept.*, 351:161–194, 2001.

[HJ00] Ulrich W. Heinz and Maurice Jacob. Evidence for a new state of matter: An assessment of the results from the CERN lead beam programme. 2000.

[HKR95] Urs M. Heller, F. Karsch, and J. Rank. The Gluon propagator at high temperature. *Phys. Lett.*, B355:511–517, 1995.

[HKR98] Urs M. Heller, F. Karsch, and J. Rank. Gluon propagator at high temperature: Screening, improvement and nonzero momenta. *Phys. Rev.*, D57:1438–1448, 1998.

[HLO03] M. Harrison, T. Ludlam, and S. Ozaki. RHIC project overview. *Nucl. Instrum. Meth.*, A499:235–244, 2003.

[Huf52] D. A. Huffman. A method for the construction of minimum-redundancy codes. *Proceedings of the I.R.E.*, pages 1098–1102, 1952.

[JK00] S. Jeon and V. Koch. Charged particle ratio fluctuation as a signal for QGP. *Phys. Rev. Lett.*, 85:2076–2079, 2000.

[JOS86] Steve Jacobs, M. G. Olsson, and III Suchyta, Casimir. Comparing the Schrodinger and spinless Salpeter equations for heavy quark bound states. *Phys. Rev.*, D33:3338, 1986.

[K+80] C. Kourkoumelis et al. Characteristics of J/psi and Upsilon production at the CERN Intersecting Storage Rings. *Phys. Lett.*, B91:481, 1980.

[K+92] Y. Kubota et al. The CLEO-II detector. *Nucl. Instrum. Meth.*, A320:66–113, 1992.

[K+03] L. Kochenda et al. STAR TPC gas system. *Nucl. Instrum. Meth.*, A499:703–712, 2003.

[Kar02] Frithjof Karsch. Lattice results on QCD thermodynamics. *Nucl. Phys.*, A698:199–208, 2002.

[KLNS97] D. Kharzeev, C. Lourenco, M. Nardi, and H. Satz. A quantitative analysis of charmonium suppression in nuclear collisions. *Z. Phys.*, C74:307–318, 1997.

[KLP01] F. Karsch, E. Laermann, and A. Peikert. Quark mass and flavor dependence of the QCD phase transition. *Nucl. Phys.*, B605:579–599, 2001.

[Koc03] V. Koch. Some remarks on the statistical model of heavy ion collisions. *Nucl. Phys.*, A715:108c–117c, 2003.

[KS94] D. Kharzeev and H. Satz. Quarkonium interactions in hadronic matter. *Phys. Lett.*, B334:155–162, 1994.

[KS95] D. Kharzeev and H. Satz. Color deconfinement and quarkonium dissociation. 1995.

[KS96] D. Kharzeev and H. Satz. Charmonium composition and nuclear suppression. *Phys. Lett.*, B366:316–322, 1996.

[L+00] Micheal J. LeVine et al. The STAR DAQ receiver board. *IEEE Trans. Nucl. Sci.*, 47:127–132, 2000.

[L+03] J. M. Landgraf et al. An overview of the STAR DAQ system. *Nucl. Instrum. Meth.*, A499:762–765, 2003.

[LB+05] A. Ogawa L. Bland et al. STAR BBC Counters. http://www.star.bnl.gov/STAR/bbc/, 2005.

[Lis96] M. A. Lisa. The STAR TPC Clusterfinder/Hitfinder. STAR internal note 238, 1996.

[LR00] C. Leroy and P. Rancoita. Physics of cascading shower generation and propagation in matter: Principles of high-energy, ultrahigh-energy and compensating calorimetry. *Rept. Prog. Phys.*, 63:505–606, 2000.

[Lud03] T. Ludlam. Overview of experiments and detectors at RHIC. *Nucl. Instrum. Meth.*, A499:428–432, 2003.

[M+91] G. Moreno et al. Dimuon production in proton - copper collisions at s**(1/2) = 38.8-GeV. *Phys. Rev.*, D43:2815–2836, 1991.

[MS86] T. Matsui and H. Satz. J/psi suppression by Qark - Gluon Plasma formation. *Phys. Lett.*, B178:416, 1986.

[MV03] Denes Molnar and Sergei A. Voloshin. Elliptic flow at large transverse momenta from quark coalescence. *Phys. Rev. Lett.*, 91:092301, 2003.

[Pes79] Michael E. Peskin. Short distance analysis for heavy quark systems. 1. Diagrammatics. *Nucl. Phys.*, B156:365, 1979.

[Pol73] H. David Politzer. Reliable perturbative results for strong interactions? *Phys. Rev. Lett.*, 30:1346–1349, 1973.

[RL04] Fabrice Retiere and Michael Annan Lisa. Observable implications of geometrical and dynamical aspects of freeze-out in heavy ion collisions. *Phys. Rev.*, C70:044907, 2004.

[Ros64] B. Rossi. *High-Energy Particles.* Englewood Cliffs, NJ: Prentice Hall, 1964.

[Ros04] T. Roser. RHIC Collider Projections (FY2005 - FY2008). http://www.agsrhichome.bnl.gov/RHIC/Runs/RhicProjections.pdf, 2004.

[S+99] C. Spieles et al. Modelling J/psi production and absorption in a microscopic nonequilibrium approach. *Phys. Rev.*, C60:054901, 1999.

[SRS98] Misha A. Stephanov, K. Rajagopal, and Edward V. Shuryak. Signatures of the tricritical point in QCD. *Phys. Rev. Lett.*, 81:4816–4819, 1998.

[SSZ97] Heinz Sorge, Edward V. Shuryak, and Ismail Zahed. psi'/psi ratio in nucleus nucleus collisions: A measure for the chiral symmetry restoration temperature? *Phys. Rev. Lett.*, 79:2775–2778, 1997.

[Ste04] Mikhail A. Stephanov. QCD phase diagram and the critical point. *Prog. Theor. Phys. Suppl.*, 153:139–156, 2004.

[Sto99a] R. Stock. The parton-hadron phase transition in central nuclear collisions at the CERN SPS. *Prog. Part. Nucl. Phys.*, 42:295–309, 1999.

[Sto99b] Reinhard Stock. Quark Matter 99 summary: Hadronic signals. *Nucl. Phys.*, A661:282–299, 1999.

[Sto05] H. Stoecker. Collective Flow signals the Quark Gluon Plasma. *Nucl. Phys.*, A750:121–147, 2005.

[Str03] C. Struck. *Antinuclei Production in Central Au-Au Collisions at RHIC*. PhD thesis, University of Frankfurt, 2003.

[Sua04] A. A. P. Suaide. High-p(T) electron distributions in d + Au and p + p collisions at RHIC. *J. Phys.*, G30:S1179–S1182, 2004.

[TRG04] Simon Turbide, Ralf Rapp, and Charles Gale. Hadronic production of thermal photons. *Phys. Rev.*, C69:014903, 2004.

[U^+79] K. Ueno et al. Evidence for the Upsilon" and a search for new narrow resonances. *Phys. Rev. Lett.*, 42:486–489, 1979.

[VG02] Ivan Vitev and Miklos Gyulassy. High-p(T) tomography of d + Au and Au + Au at SPS, RHIC, and LHC. *Phys. Rev. Lett.*, 89:252301, 2002.

[VKR99] S. A. Voloshin, V. Koch, and H. G. Ritter. Event-by-event fluctuations in collective quantities. *Phys. Rev.*, C60:024901, 1999.

[Vog99] R. Vogt. J/psi production and suppression. *Phys. Rept.*, 310:197–260, 1999.

[Wie00] Urs Achim Wiedemann. Gluon radiation off hard quarks in a nuclear environment: Opacity expansion. *Nucl. Phys.*, B588:303–344, 2000.

[Won99] Cheuk-Yin Wong. The soft gluon emission process in the color-octet model for heavy quarkonium production. *Phys. Rev.*, D60:114025, 1999.

[Y^+78] J. K. Yoh et al. Study of scaling in hadronic production of dimuons. *Phys. Rev. Lett.*, 41:684, 1978.

[Y^+89] T. Yoshida et al. High resolution measurement of massive dielectron production in 800-GeV proton beryllium collisions. *Phys. Rev.*, D39:3516–3519, 1989.

[Yep96] P. Yepes. A fast track pattern recognition. *Nucl. Inst. Meth.*, A380:582–585, 1996.

Danksagung

Besonderer Dank gebührt meinem Doktorvater Reinhard Stock. Seine Begeisterung für und sein Wissen über – nicht nur – Physik, und insbesondere seine Fähigkeit, diese an seine Mitarbeiter weiterzugeben, waren ein steter Quell der Motivation und Inspiration während meiner Zeit in seiner Gruppe. Die von ihm eröffneten Freiheiten, sei es in der Wahl des Themas dieser Arbeit oder der Gestaltung der täglichen Arbeit, habe ich immer sehr zu schätzen gewusst. Es ermöglicht zu haben, längere Zeit vor Ort am Experiment zu arbeiten, war für diese Arbeit essentiell. Vielen Dank!

Harald Appelshäuser möchte ich für die Verlängerung der Stelle in Frankfurt danken, ohne die diese Arbeit nicht in dieser Form zu Ende gebracht hätte werden können.

Ohne die Unterstützung durch die Mitglieder der STAR Collaboration wäre diese Arbeit nicht möglich gewesen. Leider is es unmöglich, all jene aufzuzählen, die durch ihre Hilfe zum Gelingen beitrugen. Stellvertretend möchte ich mich bei einigen bedanken, die meine Tätigkeit in STAR besonders beeinflusst haben.

Hier wäre zunächst die Frankfurter Level-3 Gruppe zu nennen: Sören Lange, Thomas Dietel, Clemens Adler und Jens Berger.

Die intensive Zusammenarbeit mit den DAQ und Trigger Gruppen hat vieles in dieser Arbeit erst möglich gemacht – für die vielen Erklärungen und die Hilfe bei der Umsetzung meiner Ideen danke ich insbesondere Tonko Ljubičić und Hank Crawford. Bill Christie als STAR Operations Manager und Tim Hallman als STAR Spokesperson sei für das entgegengebrachte Vertrauen gedankt, es ist alles andere als selbstverständlich einem Doktoranden so große Einflußmöglichkeiten auf den Betrieb eines Experiments zu ermöglichen. Tim Hallman möchte ich außerdem für die finanzielle Unterstützung meines Aufenthalts am BNL danken.

Die Analyse der Daten profitierte von der engen Zusammenarbeit mit der STAR Computing Group und der Heavy Flavour Physics Working Group. Insbesondere sei hier Jérôme Lauret für die vielen Hilfestellungen und Gefallen im Computing gedankt.

Besonders gefördert und beeinflußt wurde die Idee, Upsilons in STAR zu messen von Thomas Ullrich. Ohne seine Hilfe wäre weder der Trigger möglich gewesen, noch hätte die Analyse der Daten die jetzige Qualität – vielen Dank!

Mein Dank gilt auch der Frankfurter IKF-Gruppe, vor allem Christoph Blume, Dominik Flierl, Peter Dinkelaker, Roland Bramm, Werner Amend, Marek Gaździcki, Herbert Ströbele, Ulrich Köpf, Boris Wagner, Wolfgang Sommer und Stefan Kniege für die gute Zusammenarbeit und die Hilfe bei vielen kleinen Problemen.

Bedanken möchte ich mich noch bei einigen Personen aus meinem privaten Umfeld. Ohne die Unterstützung meiner Familie wäre es nie zu dieser Doktorarbeit gekommen. Besonderer Dank gebührt meiner Freundin Anja; für die schöne gemeinsame Zeit auf Long Island, ohne Dich hätte die Zeit dort nicht annäherend so viel Spaß gemacht, und für die Geduld, als sich meine Rückkehr nach Deutschland immer weiter verschob und sich die Abgabe dieser Arbeit immer mehr hinzog. Vielen vielen Dank!